Chevron-Notch Fracture Test Experience

Metals and Non-Metals

Brown/Baratta
editors

ASTM

STP 1172

STP 1172

Chevron-Notch Fracture Test Experience: Metals and Non-Metals

Kevin R. Brown and Francis I. Baratta, editors

ASTM Publication Code Number (PCN)
04-011720-30

ASTM
1916 Race Street
Philadelphia, PA 19103

Library of Congress Cataloging-in-Publication Data

Chevron-notch fracture test experience—metals and non-metals/Kevin R. Brown and Francis I. Baratta, editors.
p. cm.—(STP; 1172)
Contains papers presented at the symposium held in Indianapolis, May 6, 1991, and sponsored by ASTM Committee E-24 on Fracture Testing.
"ASTM publication code number (PCN) 04-011720-30."
Includes bibliographical references and indexes.
ISBN 0-8031-1480-X
1. Fracture mechanics—Congresses. 2. Materials—Testing—Congresses. I. Brown, Kevin R., 1941– . II. Baratta, F. I. III. ASTM Committee E-24 on Fracture Testing. IV. Series: ASTM special technical publication; 1172.
TA409.C444 1992
620.1'126—dc20 92-24966
CIP

Peer Review Policy

Each paper published in this volume was evaluated by three peer reviewers. The authors addressed all of the reviewers' comments to the satisfaction of both the technical editor(s) and the ASTM Committee on Publications.

The quality of the papers in this publication reflects not only the obvious efforts of the authors and the technical editor(s), but also the work of these peer reviewers. The ASTM Committee on Publications acknowledges with appreciation their dedication and contribution to time and effort on behalf of ASTM.

Printed in Ann Arbor, MI
August 1992

Foreword

This publication, *Chevron-Notch Fracture Test Experience: Metals and Non-Metals*, contains papers presented at the symposium of the same name held in Indianapolis, Indiana on 6 May 1991. The symposium was sponsored by ASTM Committee E-24 on Fracture Testing. Symposium co-chairmen were Kevin R. Brown, Kaiser Aluminum and Chemical Corp., Pleasanton, CA, and Francis I. Baratta, Army Materials, Technology Lab, Watertown, MA.

Contents

Overview 1

STUDIES OF THE TEST METHOD

Some Observations in Fracture Toughness and Fatigue Testing with Chevron-Notched Specimens—JONATHAN A. SALEM, JOHN L. SHANNON, JR., AND MICHAEL G. JENKINS 9

Applicability of the Short Rod Fracture Toughness Test to New Microalloyed Bar Steels—T. C. TSCHANZ, D. K. MATLOCK, AND G. KRAUSS 26

Specimen Size and Orientation Effects in Chevron-Notch Fracture Testing of Aluminum Alloy Plate—J. MORRISON AND K. J. KARISALLEN 43

Analysis of Some Compliance Calibration Data for Chevron-Notch Bar and Rod Specimens—THOMAS W. ORANGE, RAYMOND T. BUBSEY, WILLIAM S. PIERCE, AND JOHN L. SHANNON, JR. 54

Fracture Toughness Evaluation of Ceramic Bonds Using a Chevron-Notch Disk Specimen—A. R. ROSENFIELD AND B. S. MAJUMDAR 63

Fracture Toughness of Composite Laminates and Metallic Materials Using a Modified CNSB Specimen—JAMES P. LUCAS 74

APPLICATIONS TO METALLIC MATERIALS

Fracture Toughness and Fractography of Corroded Dental Amalgams—HERBERT J. MUELLER 91

Aluminum-Lithium Alloys: Evaluation of Fracture Toughness by Two Test Standards, ASTM Method E 813 and E 1304—PATRICK T. PURTSCHER, J. DAVID McCOLSKEY, AND ELIZABETH S. DREXLER 110

Use of the Chevron-Notched Short Bar Test to Guarantee Fracture Toughness for Lot Release in Aluminum Alloys—JACK W. BRAY 131

Using Chevron-Notch, Short-Bar Specimens for Measuring the Fracture Toughness of a Martensitic Stainless Steel at High Hardness—CHARLES W. MARSCHALL, PAUL R. HELD, AND FRED J. DOLAN 144

APPLICATIONS TO NON-METALLICS

Chevron-Notched, Flexure Tests for Measuring the Elevated-Temperature Fracture Resistances of Structural Ceramics—MICHAEL G. JENKINS, MATTISON K. FERBER, ASISH GHOSH, JOUKO T. PEUSSA, AND JONATHAN A. SALEM 159

Short Bar Chevron-Notch Fracture Toughness of Bone Cement—SUSHIL K. BHAMBRI AND LESLIE N. GILBERTSON 178

Rock Fracture Toughness Determination with Chevron-Notched and Straight-Through-Notched Three-Point Bend Round Bar Specimens—WANG QIZHI AND XIAN XUEFU 191

Overview

The chevron-notched (CN) test specimen has been the subject of experimentation for over 15 years; however, it has had the status of an ASTM standard only since December 1989. The CN specimen and test procedure was the subject of another ASTM symposium held in 1983; and a volume of those proceedings was published as a Special Technical Publication, ASTM STP 855. It is hoped that the contents of this current STP, which include papers presented at the symposium on 6 May 1991, will serve to promote greater interest in this unique specimen configuration, help refine the test method, and hasten its further acceptance.

The purposes of the symposium were three-fold:

1. To gather together the range of experience by users of the E 1304 Test Method when the method was applied to a variety of materials, in particular to uncover any problems, deficiencies, or opportunities so that improvements can be made when the E 1304 document is revised in 1993, according to ASTM regulations.
2. To examine applications and geometries outside the current standard, to assess their usefulness, and to provide data for possible inclusion in future revisions of the standard.
3. To invite the investigation of many different materials, including ceramics, so that the resulting data would aid in the development of standard fracture toughness tests for such materials utilizing the chevron-notched beam, the short rod, and the short bar.

In these respects, the symposium was a success. The papers included a bewildering variety of materials, representing metals, rock, plastics composites, adhesives, and ceramics. There is a very high probability that in the near future engineers and researchers will find within the experience summarized in this volume: (1) guidance that will help in the testing of most structural materials, (2) improvement of the E 1304 test method, and (3) aid to those concerned in the development of fracture toughness test methods for brittle materials.

The chevron-notched specimen has several advantages over other fracture toughness test specimens in providing a measure of fracture toughness. The specimen need be only half the size of an equivalent K_{Ic} (ASTM E 399) specimen to develop plane strain conditions at the crack tip. Further, it needs no fatigue precrack, which frees it from the need for fatigue equipment that can be both capital intensive and expensive to run. In addition, the specimen is particularly attractive to researchers testing brittle materials, such as ceramics, because a CN specimen will self-precrack without specially designed fixtures or a stiff loading system. Also, the specimen will fracture in a stable manner, and the maximum load is obtainable at a predetermined crack length; thus, the parameters required for fracture toughness are readily determined for brittle materials having a flat *R*-curve.

The remaining questions relate to the significance, applicability, and relevance of the numerical value determined by the test. It has long been seen by many researchers as a substitute for the well-accepted K_{Ic} test (ASTM E 399), but with some scientific and engineering conjecture over how well it fits the role. Is it a substitute, or is it a successor, or is it neither? This symposium has helped to resolve some of these questions.

Several papers examined the range of application of the CN specimen and are therefore extremely useful in establishing or modifying the ranges for future revisions of E 1304. In that regard, the paper by Orange et al. provides more general formulas for a wide range of notch geometries for the short rod and short bar having geometries not included in E 1304. Three-point round bend bars having chevron notches and straight-through notches, as used by Qizhi and Xuefu, as well as the chevron-notched rectangular cross-sectioned beam tested by Jenkins et al. and Salem et al. are examples of potential standard geometries not included in the current standard. Further, they would be most appropriate as possible candidates for a standard fracture-toughness test method for both metals and more brittle materials.

Salem, Shannon, and Jenkins demonstrated that, although the CN toughness of metals and ceramics could agree well with those determined with other specimens, such as bend or compact tension, the CN specimen could give a nonconservative measure of toughness compared to established test methods, when "rising R-curve behavior" occurred, i.e., when toughness increased with crack extension. In some engineering endeavors, "nonconservative" translates to "possibly unsafe," so their conclusions should be indelibly noted.

The same observation is made by Bray, who correlated the results of ASTM E 399 and chevron-notched E 1304 testing on a wide range of aluminum alloys used in aerospace. He notes that the CN specimen yields a nonconservative measure of K_{Ic} or K_q, as the toughness level increases. In some instances he explains this in the same manner as Salem et al., i.e., a rising R-curve effect, but in some cases the higher values are due to sample heterogeneity. Surface-to-center toughness variations are common in heat-treated aluminum alloy plates.

Bray proposes using the E 1304 method for the release testing of aluminum alloys for aerospace use, but only after establishing the correlation between K_{Iv} and K_{Ic} to confidence levels adopted by Military Handbook 5E. Given his data and information on the relative economics of the two test methods, it would appear to be only a matter of time before ASTM E 1304, i.e., K_{Iv} testing becomes the most common method.

Whereas Bray compared the CN test results on aluminum alloys obtained with ASTM E 1304 with those obtained with ASTM E 399, i.e., K_{Ic} or K_q, Purtscher et al. made their comparisons with ASTM E 813, the J_{Ic} test method. They found that the CN specimens tended to give higher numerical measures of toughness, except in the case of lithium-aluminum alloys that suffered extensive interlaminar separation during fracture. In these alloys the delamination fracture mode is responsible for the relative changes in the measured toughness values.

The toughness of aluminum alloys was also the subject of the paper by Morrison and KarisAllen. Creatively, they compared the results of their side-grooved compact tension specimens (similar to those used to measure K_{Ic}) with the results of CN specimens. It is generally accepted that it is the inherent side grooving of the CN specimen that permits the use of a smaller specimen size than that of the CT specimen; why then would side-grooved CT specimens not give more comparable results? For aluminum-lithium alloy 8090, the comparisons were good, but for other aluminum alloys, the CT side grooves reduced R-curve effects.

The CN results compared well with the CT results for aluminum alloy 6061, but they were marginally higher for the other alloys tested. Morrison et al. speculate, as did Bray, that this may be a result of the different volumes of nonuniform metal sampled by the differently sized specimens.

Martensitic stainless steels of high hardness were the subject of the Marschall et al. paper of side-by-side comparisons of the results of CN and CT specimens. They found that the CN specimen consistently gave toughness values 18% higher than K_{Ic}, but, unlike Bray and Morrison et al., they could not attribute the difference to sample heterogeneity. They conclude that there is a different nature of the crack extension in the two specimens. In contrast, in a similar comparison of M-50 bearing steel, also of high hardness, Salem and coworkers found no difference in measured toughness between 14 replicate CT tests and 9 CN tests of three different geometries. This suggests that there is a material dependency of crack growth behavior, and it lends credence to the warning in E 1304 that K_{Ic} and K_{Iv} cannot be used interchangeably unless correlations have been established previously. These authors also attempted to use the CN specimen to measure the fatigue crack growth rates in this steel and concluded that the chevron-notched shape accelerated crack growth.

In contrast to these high hardness steels, Tschanz, Matlock, and Krauss used the CN geometry of ASTM E 1304 to examine the static fracture behavior at various temperatures of much softer microalloyed steels with harnesses in the range 25 to 30 Rockwell C. In room temperature tests, the CN specimen sizes they used were all invalid, as were most of their low temperature tests, but they consider much of the data to be significant after considering the microstructural processes at the crack tips. They claimed that the processes, such as martensite formation, invalidate the validity checks in E 1304, and that the appropriate values should be considered "valid." This is an interesting concept that could apply to other nonferrous materials. If they are correct, then such changes could be considered for future revisions of the standard test method; but more work would be required to understand and characterize those materials that are detrimentally affected by the present validity checks of E 1304.

A number of authors sought to apply the chevron-notched geometry to the determination of interface toughness, or of the toughness of thin layers of a material between two thicker materials; this is probably because of the ability of this geometry to restrict crack growth to the region of the interface.

Rosenfield and Majumdar used a disc-shaped specimen loaded diametrically in compression, similar to ASTM standards used to determine tensile strength of concrete (C 496) and rock core samples (D 3967). The specimen used by these authors acted as a chevron-notched specimen for only a limited range of crack extension while the crack was within the chevron ligament. For greater extensions, the crack occupied the full specimen thickness, and, because of the absence of side grooves and the specimen being biaxially stressed, it was free to change mode. In this way, mode 1, mode 2, and mixed mode fractures could be studied in both monolithic and bonded specimens. Nevertheless, for large crack extensions, the specimen is no more a chevron-notched specimen than is a compact tension E 399 specimen with a chevron-shaped fatigue crack starter.

Lucas used the geometry of the 1304 standard method to examine a sandwich construction he calls a hybrid specimen. He claims reasonable agreement between the measured mode 1 toughnesses of materials measured by monolithic and by hybrid CN specimens after corrections were made for the different moduli of elasticity of the materials in the hybrid specimens. Rosenfield and Majumdar made no such correction because they claimed that the elasticity moduli of the materials were quite similar, but they also reported good agreement with data from bend specimens.

Rosenfield and Majumdar also examined the fractography of the failed interfaces between dissimilar materials and established the significance of the measured values in terms of the component being fractured. The fractures in the study by Lucas were, with little doubt, entirely within the expected layer, which was relatively thicker than Rosenfield's interfaces or "adhesive" material. To avoid generating misleading data, an investigator using thinner layers would have to follow the example of Rosenfield and Majumdar and take the precaution of making a mechanistic fractographic study.

It is also likely that other hybrid systems may be influenced strongly by residual stresses, such as those generated in high-temperature bonding or heat treatment or by shrinkage of adhesives. In the systems studied above, the selection of materials has enabled these problems to be avoided, perhaps fortuitously, or perhaps by the skillful avoidance of complications by the experimenters.

With these caveats in mind, it seems that the authors have demonstrated clearly that chevron-notched specimens can be of use in measuring the fracture properties of interfaces.

The practical usefulness of the chevron-notched specimen is demonstrated in the paper by Mueller. He used the specimen to demonstrate the effect of corrosion on the toughness of dental amalgams. Dental amalgams are materials from which it is difficult to obtain fracture test specimens from field exposures, but which can easily be used to produce a cast CN specimen for laboratory exposure. Similar circumstances apply to the PMMA bone cements studied by Bhambri and Gilbertson, to the benefit of those with cemented implants. They examined the specimen size range over which useful data can be obtained, and they noted strain-rate effects that might affect the design of equipment for impact sports, but, tactfully, the authors stop short of imposing restrictions that might destroy the confidence of patients indulging in these activities.

A number of papers dealt with ceramics, another class of nonmetallics. Qizhi and Xuefu used three-point round bend bars containing straight and chevron-notches to measure the toughness of limestone. They found the chevron-notched specimen easier to control and obtain useful data because of the greater crack stability and the side groove constraint which kept the crack in the desired plane. They did observe a size effect in the CN specimen: the test value increased slightly with diameter, which was attributed to the *R*-curve effect. They also noted that the CN specimen gave higher values of toughness than the straight-through-notched specimen.

Jenkins et al. used the CN specimen to study the high-temperature fracture of a wide range of ceramics, both monolithic and reinforced. The three-point bend bar was chosen for simplicity of loading, which is an important consideration at elevated temperatures. They acknowledge the usefulness of the geometry for material comparisons and extend the range of parameters derived from the test to include *R*-curves and work of fracture. They conclude that these parameters are necessary to fully evaluate materials showing nonlinear behavior, an important point for those interested in developing a fracture toughness test for brittle materials, as well as a possible addition to the present E 1304 test method.

Salem et al. also used the CN beam at elevated temperatures and examined the range of geometry and sizes for which useful data can be obtained from the CN test. They concluded, as did Jenkins and his colleagues, that test results on materials with flat *R*-curves are independent of notch geometry and specimen size, but that this is not true for materials with rising *R*-curves.

The papers briefly outlined here should provide the latest information and innovative experimentation in the area of fracture-toughness testing using chevron-notched specimens. Greater detail is provided within this volume to the reader having an interest in specific papers.

Regarding the general but important questions posed earlier in this overview, i.e., is ASTM Test Method E 1304 a substitute for ASTM Test Method E 399, a successor, or neither? As with many general questions such as these, the answers are not clear-cut, but have to be qualified. The results from several papers indicate that indeed the CN specimen can be substituted if it is certain that the material being tested exhibits a flat *R*-curve response or if statistical correlations have been established. The first, of course, implies *a priori* knowledge of such material behavior. It also implies the employment of an *R*-curve test prior to the use of E 1304. Thus, as cautioned in the test method itself, earlier in this overview, and also by several authors, the E 1304 Test Method is neither a complete substitute for the E 399 Test Method nor a successor. Nevertheless, it can and does serve in many situations as a practical fracture-toughness test, as shown by all of the authors here.

Can a chevron-notched configuration be a candidate for a standard fracture toughness test of brittle monolithic materials? Again, from the results of several papers presented here (and of course elsewhere), it certainly appears so. Again; however, the same caveats are indeed applicable.

Kevin R. Brown
Kaiser Aluminum and
Chemical Corp.,
Pleasanton, CA

Francis I. Baratta
Army Materials
Technology Lab,
Watertown, MA

Studies of the Test Method

Jonathan A. Salem,[1] *John L. Shannon, Jr.,*[1] *and Michael G. Jenkins*[2]

Some Observations in Fracture Toughness and Fatigue Testing with Chevron-Notched Specimens

REFERENCE: Salem, J. A., Shannon, J. L., Jr., and Jenkins, M. G., "**Some Observations in Fracture Toughness and Fatigue Testing with Chevron-Notched Specimens,**" *Chevron-Notch Fracture Test Experience: Metals and Non-Metals, ASTM STP 1172*, K. R. Brown and F. I. Baratta, Eds., American Society for Testing and Materials, Philadelphia, 1992, pp. 9–25.

ABSTRACT: Chevron-notched specimens were used to test metallic and ceramic materials over a range of temperatures and testing conditions. The materials tested were M-50 bearing steel, alumina, silicon carbide, monolithic silicon nitride, and in situ toughened silicon nitride. Results were compared to measurements performed with compact-tension specimens, single-edge notched beam specimens, or single-edge precracked beam specimens.

Measured properties included fracture toughness, crack growth resistance, and fatigue crack growth rate. For materials with rising *R*-curves, the fracture toughness measured with chevron-notched specimens was dependent on specimen proportions and notch geometry, as related to the amount of crack extension to the measurement point. For materials with flat *R*-curves, the chevron-notch test is independent of notch geometry and specimen proportions.

KEY WORDS: silicon nitride, silicon carbide, alumina, bearing steel, crack growth resistance, fracture toughness, chevron notch, fatigue crack growth

Nomenclature

- a Crack length
- a_m Crack length corresponding to minimum stress intensity factor coefficient
- a_r Crack length corresponding to stable crack extension
- a_0 Initial crack length
- a_1 Length of chevron-notch at specimen surface (distance from line of load application to point of chevron emergence at specimen surface)
- Δa Crack extension: length of measured crack after application of load minus the initial crack or notch length, a_0
- B Specimen thickness
- b Crack front width
- da/dN Crack growth rate per fatigue load cycle
- H Specimen half-height
- K_c Measured fracture toughness
- K_I Applied stress intensity factor
- K_{Ic} Fracture toughness in accordance with ASTM E 399–83

[1]National Aeronautics and Space Administration, Lewis Research Center, Cleveland, OH 44135.
[2]Oak Ridge National Laboratory, Oak Ridge, TN 37831.

K_r Resistive stress intensity factor corresponding to stable crack extension (crack growth resistance)
ΔK_I Difference in maximum and minimum stress intensity factors applied in fatigue cycling
m Slope of the fatigue curve
P_{max} Maximum applied load in a fracture toughness or fatigue test
P_{min} Minimum applied load in a fatigue test
S_1 Major span
S_2 Minor span
W Specimen width
Y^* Dimensionless stress intensity factor coefficient for chevron-notched specimen
Y^*_m Minimum value of Y^*
α a/W
α_0 a_0/W
α_1 a_1/W

Introduction

Fracture toughness is a critical parameter in the design and life prediction of structural components made from metallic and ceramic materials. Both mature and developing material systems are applied over a range of temperatures and environments. Thus, fracture toughness test methodologies must consider and adequately account for ramifications of these environments in the measurement of fracture toughness. Desirable characteristics of a fracture toughness test specimen include simplicity, ability to withstand elevated temperatures, small specimen volume, and independence of the measurement on specimen geometry.

A major complication to fracture toughness measurements of brittle materials, such as ceramics, glass, and beryllium, has been the development of sharp "starter cracks." Many novel techniques have been developed [*1–9*], each having limitations when contrasted with the desirable characteristics mentioned previously [*8,9*].

The chevron-notched specimen solved precracking complications by developing the crack concurrently with the fracture toughness measurement [*10,11*]. Such crack growth, however, inherently promotes any naturally occurring damage mechanisms associated with monotonic crack extension. The use of different chevron-notch geometries and proportions results in different monotonic crack extensions to maximum load and a corresponding variation of measured fracture toughness for materials that exhibit damage mechanisms. Such dependencies are not all bad since they elucidate the initiation and plateau of damage mechanisms that may develop during the growth of a crack. The issue thus created is what crack extension history needs to be measured for design of components, material comparisons, and quality control. Most desirable is a measurement that will quickly and easily elucidate all aspects of a material's crack tolerance.

This paper presents positive and negative aspects of the chevron-notched fracture toughness specimen from an experimental viewpoint. Other approaches to fracture toughness measurement that could supersede it in standardization are also considered.

Test Procedures

Materials

Ceramic test materials were 96% alumina[3] exhibiting a rising *R*-curve [*12*], hot-pressed silicon nitride[4] exhibiting a flat *R*-curve [*13*], in situ toughened silicon nitride[5] exhibiting a

[3]ALSIMAG 614 96% alumina, G.E. Ceramics, Laurens, SC.
[4]NC-132 hot-pressed silicon nitride, Norton Co., MA.
[5]SN251 sintered silicon nitride, Kyocera Corp., Kyoto, Japan.

rising R-curve [*14*], and sintered α-silicon carbide[6] exhibiting a flat R-curve. The alumina was processed in isopressed, dry-pressed, and extruded forms. Each form exhibited slightly different properties. The only metallic material tested was quenched and tempered M-50 bearing steel conforming to AMS 6491. Typical microstructures are shown in Fig. 1, and a summary of material properties is given in Table 1.

Geometries

Chevron-notched short-bar (CNSB) and chevron-notched beam (CNB) specimens are illustrated in Fig. 2. The single-edge precracked beam (SEPB), single-edge notched beam (SENB), and compact-tension (CT) specimens were also tested for comparison. Details of specimen proportions, notch geometries, and testing procedures are described along with the application.

[6]Hexoloy SA α-silicon carbide, Carborundum, Niagara Falls, NY.

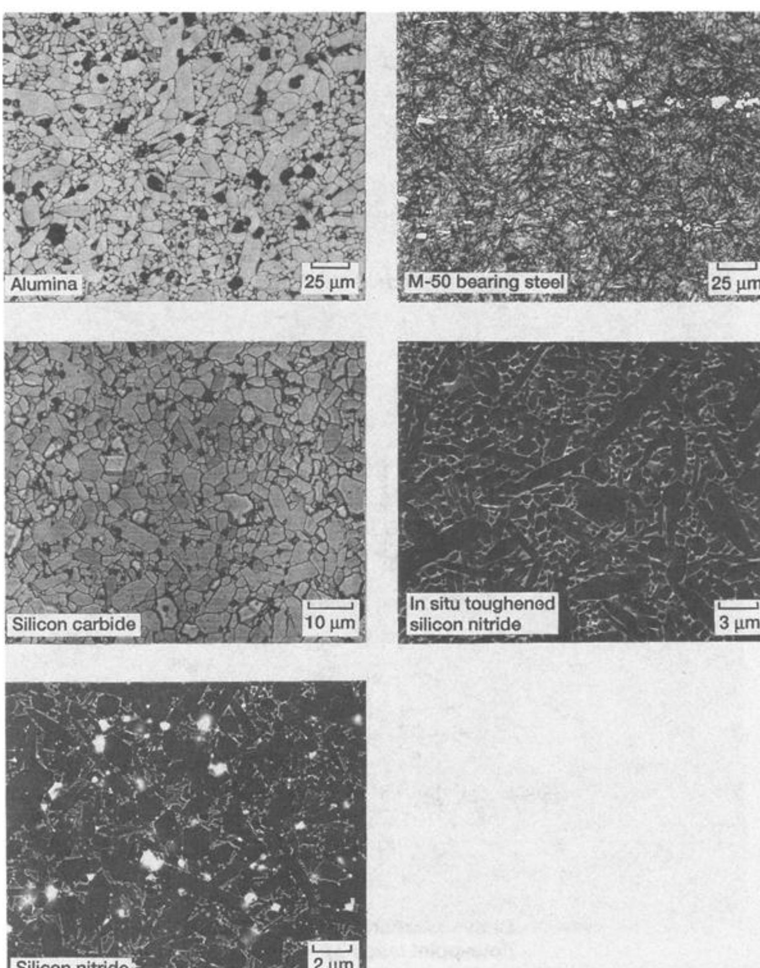

FIG. 1—*Microstructures.*

TABLE 1—*Material properties.*

Material	Density, g/cm^3	Grain Diameter, μm	Hardness,[a] GPa	Young's Modulus, GPa
Alumina				
Isopressed	3.74	6.2	10	324
Drypressed	3.74	11.3	...	...
Extruded	3.71	7.3	...	...
Silicon nitride (NC-132)	3.25	0.1 to 2.0	16	310
Silicon nitride (SN251)	3.4	...	15	299
Silicon carbide	3.16	4.2	25	397
M-50 steel	8.03	19	[b]62	203

[a]Vickers mean contact pressure hardness $H = 2P/d^2$.
[b]Rockwell C scale.

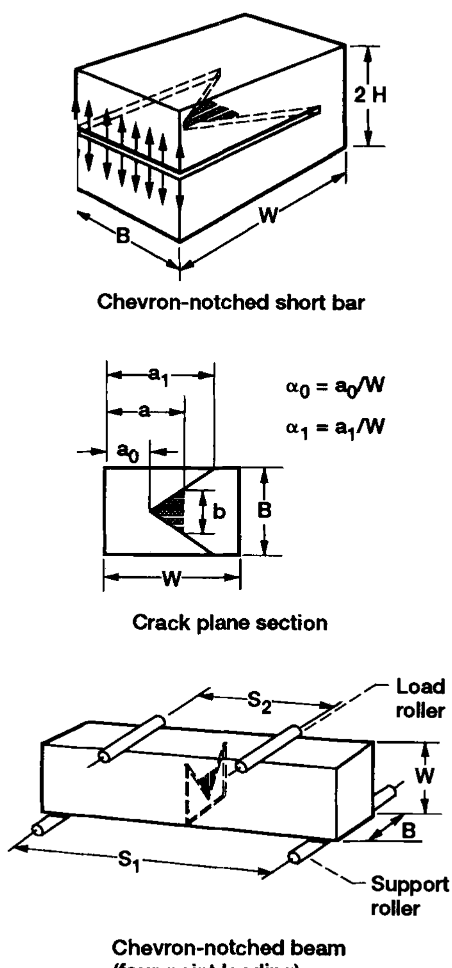

FIG. 2—*Chevron-notched specimens.*

Results

Specimen Proportions and Notch Geometry

The effects of notch geometry on fracture toughness were investigated with CNSB specimens made from the extruded alumina, silicon carbide, silicon nitride (NC-132), and M-50 steel. Aspects of notch geometry and specimen proportions considered included α_0, α_1, W/H ratio, and specimen size, since these influence the amount of crack extension and cracked area occurring during the test. Results were compared with those from CNB, CT, SEPB, and SENB specimens. Specimen-loading rates and proportions are listed in Tables 2 to 4.

The fracture toughness, K_c, of the chevron-notched specimens was calculated from the maximum test load, P_{max}, and the minimum coefficient of the stress intensity factor, Y^*_{min}.

$$K_c = \frac{P_{max} Y^*_{min}}{B\sqrt{W}} \tag{1}$$

TABLE 2—*Effects of specimen type and proportions on measured fracture toughness of silicon nitride and silicon carbide.*

Specimen Geometry	α_0	α_1	B,[a] m	W, mm	Number of Tests	Fracture Toughness,[b] MPa $\sqrt{m}$
			NC-132 SILICON NITRIDE			
CNSB	0.2	1	8.9	13.4	3	4.6 ± 0.1
	0.3	1	8.9	13.4	3	4.7 ± 0.2
	0.4	1	8.9	13.4	3	4.6 ± 0.2
	0.5	1	8.9	13.4	3	4.6 ± 0.1
	0.2	1	8.9	17.8	3	4.8 ± 0.3
	0.3	1	8.9	17.8	3	4.6 ± 0.01
	0.4	1	8.9	17.8	3	4.7 ± 0.2
	0.5	1	8.9	17.8	3	4.6 ± 0.2
					avg	4.7 ± 0.2
CNB[c]	0.2	1	3.5	5	2	4.8
	0.2	1	9.0	13	2	4.9
SEPB[d]	0.43	. . .	3	4	3	4.5 ± 0.4
			HEXOLOY SA SILICON CARBIDE			
CNSB	0.1	1	25.4	38	2	2.7 ± 0.1
	0.3	1	25.4	38	2	2.8 ± 0.01
	0.5	1	25.4	38	3	2.8 ± 0.3
	0.1	1	25.4	51	3	2.7 ± 0.02
	0.3	1	25.4	51	3	2.8 ± 0.1
	0.5	1	25.4	51	3	2.8 ± 0.1
	0.2	0.6	25.4	51	3	2.7 ± 0.1
	0.2	0.8	25.4	51	3	2.7 ± 0.02
	0.2	1	25.4	51	3	2.7 ± 0.02
					avg	2.8 ± 0.1
CNB[e]	0.44	1	6.5	6.5	3	2.9 ± 0.3

[a] $B = 2H$ for the CNSB specimens; stroke rate = 0.05 mm/min.
[b] Plus or minus one standard deviation.
[c] Stroke rate = 0.05 mm/min; four-point spans = 10 and 40 mm and 20 and 40 mm for W = 5 and 13 mm, respectively.
[d] Stroke rate = 0.2 mm/min; four-point spans = 10 and 18 mm.
[e] From Ref *18*; stroke rate = 0.01 mm/min; three-point test span = 40 mm.

TABLE 3—*Fracture toughness of NC-132 hot-pressed silicon nitride.*

Method	Reference	Fracture Toughness,[a] MPa $\sqrt{m}$
Controlled flaw (Knoop)		
Anneal, °C		
1000	[19]	4.6 ± 0.2
1200	[20]	4.6 ± 0.2
1300	[20]	4.5 ± 0.1
1400	[20]	4.3 ± 0.4
Indentation Fracture		
Evans calibration		
Load, kg		
5	[21]	5.1 ± 0.1
3	. . .[b]	5.0 ± 0.1
5	. . .[b]	5.3 ± 0.1
10	. . .[b]	5.8 ± 0.2
Anstis calibration		
Load, kg		
3	. . .[b]	3.8 ± 0.2
5	. . .[b]	3.9 ± 0.1
10	. . .[b]	4.1 ± 0.2
Double torsion	[22]	4.8 ± 0.3
Double cantilever beam	[6]	4.0

[a]Plus or minus one standard deviation.
[b]Salem, J. A., unpublished research.

TABLE 4—*Effects of specimen type and proportions on measured fracture toughness of M-50 bearing steel.*

Specimen Geometry	α_0	α_1	B,[a] mm	W, mm	Crack Length,[b] mm	Number of Tests	Fracture Toughness,[c] MPa $\sqrt{m}$
CNSB	0.2	1	24	50	15	3	20.1 ± 0.4
CNSB	0.5	1	24	50	10	3	18.8 ± 0.2
CNSB	0.2	0.4	24	50	15	3	20.4 ± 0.1
CT	0.4	. . .	7.4	25	12	14	19.3 ± 0.4

[a]$B = 2H$ for the chevron-notched specimens; stroke rate = 0.24 mm/min.
[b]Stable crack extension from a_0 to a_m for CNSB specimens and length of fatigue precracked region for CT specimens; stroke rate = 1.2 mm/min.
[c]Plus or minus one standard deviation.

where Y^*_{min} was determined from experimental and analytical techniques [15,16] for the short-bar and four-point bend specimens, respectively. Fracture toughness of the SEPB, SENB, and CT specimens was calculated with the equations given in Refs 15 and 17.

Flat R-*Curve Materials*—The results of chevron-notch geometry on fracture toughness of the hot-pressed silicon nitride (NC-132) and silicon carbide are tabulated in Table 2 and illustrated in Fig. 3 for the silicon nitride. There was no effect of specimen type or chevron-notch proportions on K_c. Use of a four-point configuration to test the silicon nitride and silicon carbide resulted in slightly higher mean values (4 and 5%, respectively), indicating

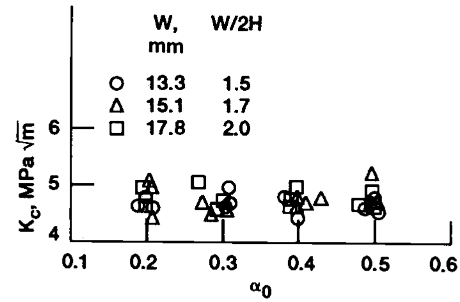

FIG. 3—*Effects of* α_0 *and* W/H *on the* K_c *of hot-pressed silicon nitride (NC-132) determined with chevron-notched short-bar (CNSB) specimens* [13].

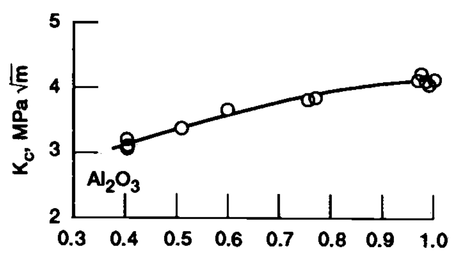

FIG. 4—*Effect of* α_1 *on* K_c *of alumina (extruded ALSIMAG 614) determined with chevron-notched short-bar (CNSB) specimens* [26]. B = *12.7 mm;* W/H = *4.0;* α_0 = *0.2.*

good correlation between vastly different configurations and proportions. It should be noted that the crack growth resistance of these materials is independent of crack extension [*13,18*].

Application of the SEPB technique to a different lot of NC-132 resulted in a slightly lower fracture toughness (4%) than the average value determined with the CNSB specimens (Table 2). These results are comparable with the results of most researchers [*6,19–22*],[7] as shown in Table 3. However, it should be noted that this hot-pressed β-silicon nitride exhibits texture. In one study of NC-132, the texture resulted in a 19% difference in average strength with test orientation [*23*] and differences of 21 and 19% in strength and fracture energy (9% in toughness) for another β-silicon nitride [*24*]. This may account for the large difference in value reported by Ref *6* and the low indentation strength results observed in this study. The calibration for the indentation fracture method given in Ref *6* was based on the double cantilever beam result of K_c = 4.0 MPa $\sqrt{m}$.

The measured fracture toughness of M-50 bearing steel was also independent of notch geometry as shown in Table 4. Measurement of the plane strain fracture toughness with the CT specimen in accordance with ASTM E 399 [*17*] indicated a K_{Ic} of 19.3 ± 0.4 MPa $\sqrt{m}$, in good agreement with the CNSB specimen results of 18 ± 0.2 MPa $\sqrt{m}$ to 20.4 ± 0.1 MPa $\sqrt{m}$, as tabulated in Table 4.

Rising R-*Curve Materials*—The alumina, which exhibited a rising *R*-curve, did show dependence of measured fracture toughness on notch geometry, as illustrated in Fig. 4 for the extruded form [*25*]. The dependence resulted from the rising *R*-curve of the material and the different crack extensions generated with each geometry, as shown in Fig. 5, where the fracture toughness is plotted as a function of the crack length at maximum load, a_m, less

[7]Salem, J. A., unpublished research.

	B, mm	W/2H	α_1	α_0
◇	25.4	2.0	1.0	0.21 to 0.43
◆	25.4	1.5	1.0	0.22 to 0.41
○	12.7	2.0	1.0	0.19 to 0.44
●	12.7	1.5	1.0	0.09 to 0.37
□	12.7	2.0	0.40 to 1.0	0.2

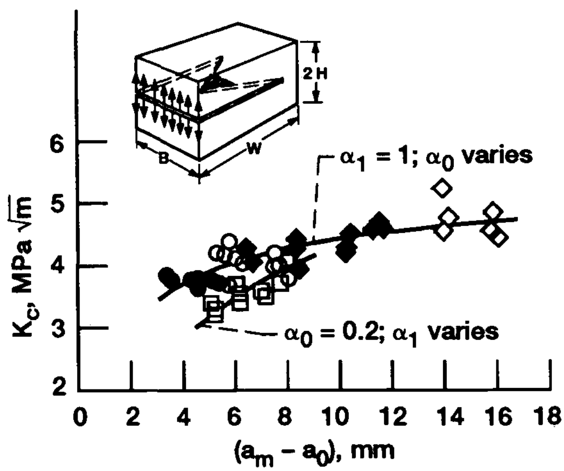

FIG. 5—*Variation in* K_c *of alumina (extruded ALSIMAG 614) with amount of crack extension to maximum load for chevron-notched short-bar (CNSB) specimens* [27].

the initial notch length, a_0. The different curves may result from the assumption of correspondence between maximum load and the minimum stress intensity factor coefficient, which may not be the case for materials with a rising crack growth resistance curve. Figure 5 also indicates that the R-curve is not only a function of crack extension, but depends on other geometric factors as well [*26*].

The effect of specimen size, without alteration in notch geometry, was determined with an isopressed version of the alumina. The fracture toughness increased by 7% from 3.67 ± 0.05 MPa $\sqrt{m}$ to 3.93 ± 0.04 MPa $\sqrt{m}$; the specimen size was more than doubled, as shown in Table 5. The use of the SEPB configuration with much shorter crack length resulted in 3.09 ± 0.17 MPa $\sqrt{m}$, lower by 16%. This specimen size dependence is expected for a material that exhibits R-curve behavior.

For the nominally brittle materials (i.e., fine-grained silicon nitride and M-50 steel that did not exhibit a rising R-curve), the notch geometry and specimen configuration did not affect the measured fracture toughness within the limits investigated; however, for a rising R-curve material, there was a discernable effect.

Elevated Temperature Measurements

The application of ceramic materials to advanced heat engines has generated interest in measurement of fracture toughness at temperatures as high as 1371°C. Such data are required

TABLE 5—*Effects of specimen type and proportions on measured fracture toughness of alumina (isopressed ALSIMAG 614).*

Specimen Geometry	α_0	α_1	B,[a] mm	W, mm	Crack Length,[b] mm	Number of Tests	Fracture Toughness,[c] MPa $\sqrt{m}$
CNSB	0.2	1	10	20	8	6	3.7 ± 0.1
CNSB	0.2	1	25	50	16	3	3.9 ± 0.1
SEPB[d]	0.2–0.5	...	3	6	1 to 3	10	3.1 ± 0.2
SEPB[e]	0.2–0.5	...	3	6	1 to 3	3	3.1 ± 0.1
DT[f]	...	...	...	...	...	...	3.8 ± 0.1

[a]B = $2H$ for the chevron-notched specimens; stroke rate = 0.05 mm/min.
[b]Stable crack extension from a_0 to a_m for CNSB specimens and length of rapidly precracked region in SEPB specimens.
[c]Plus or minus one standard deviation.
[d]Stroke rate = 0.2 mm/min; four-point spans = 10 and 18 mm.
[e]Stroke rate = 0.2 mm/min; four-point spans = 20 and 40 mm.
[f]From Ref *36*; double torsion; 5 mm/min, dry N_2.

for design and life prediction of components in which slow crack growth is governed by the ratio of the applied stress intensity factor and the materials fracture toughness [*27*]. The chevron-notched specimen has demonstrated applicability at such temperature [*28*], although some cautions are warranted.

At elevated temperatures, the intergranular phases in silicon nitrides soften, and crack extension changes from a mixture of intergranular and transgranular fracture to intergranular slow crack growth and creep. Such combined effects can affect test results as illustrated in the following paragraphs for the in situ toughened silicon nitride.

Fracture toughness was determined with the CNB, SEPB, and SENB methods in air with three-point bending. Specimens measured 3 by 4 by 30 mm in width, height, and span, and the chevron-notch parameters α_0 and α_1 were 0.625 and 1.0, respectively. The chevron stress-intensity factor coefficient was determined with a slice model [*16*] and an interlaminar shear factor of 1.453. The CNB specimens were tested at a displacement rate of 0.005 mm/min, and the SEPB and SENB specimens were tested at 0.05 mm/min. The low displacement rate was used for the CN to ensure stable crack extension. Such slow rates were successful in the testing of SiC/TiB_2 composites at elevated temperatures [*28*].

The resulting load-displacement diagrams and calculated fracture toughness values are illustrated in Fig. 6 and tabulated in Table 6, respectively. The fracture toughness decreased with increasing temperature to 1200°C. However, at 1371°C the fracture toughness appeared to increase substantially. The corresponding load-displacement behavior was severely nonlinear with a much higher maximum load than exhibited by lower temperature tests. This maximum was followed by a large, residual load-bearing ability and incomplete failure of the specimen.

Fractography of the CNB specimens tested at 1371°C indicated that the crack grew partially through the chevron and stalled, resulting in the ridge shown in Fig. 7*a*. The crack stalled because of hinging and deformation of the uncracked ligament. The stalled crack was oxidized (Fig. 7*b*), and the long grains oriented normal to the crack plane were pulled out by viscous deformation of the grain boundaries (Fig. 7*c*). These effects resulted in the high maximum and residual loads displayed and the high apparent fracture toughness. The grain pullout was indicative of crack tip deformation instead of bridging because high apparent fracture toughness was also observed for fine-grained monolithic and whisker-reinforced

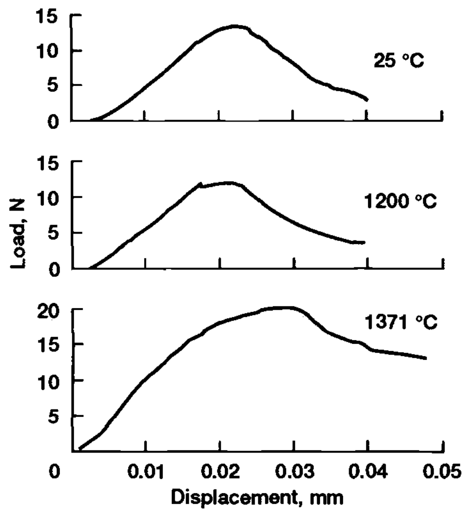

FIG. 6—*Load-displacement diagrams for silicon nitride (SN251) tested in three-point bending at room and elevated temperatures.*

silicon nitrides tested at 1400°C with loading rates of 0.05 mm/min and notch parameters of $\alpha_0 = 0.2$ and $\alpha_1 = 0.7$ [*29*].

The SEPB specimens, though convenient at room temperature, exhibited fracture toughness values dependent on heating rate and hold time at elevated temperature, as shown in Table 6. The heating rate and hold-time dependence of fracture toughness was due to healing of the precrack, which has a very small opening at the specimen surface (<5 μm). The SENB specimen with a 50-μm saw-notch width exhibited a fracture toughness in agreement with the trend of the chevron notch at temperatures up to 1200°C, as shown in Table 6. It

TABLE 6—*Effects of temperature and specimen type on fracture toughness of in situ toughened silicon nitride.*

Test Method	Temperature, °C	Number of Tests	Fracture Toughness,[a] MPa $\sqrt{m}$
CNB	25	5	7.9 ± 0.4
	800	5	7.1 ± 0.7
	1000	3	6.9 ± 0.4
	1200	4	6.0 ± 0.3
	1371	2	10.4 ± 0.5
SEPB	25	7	7.4 ± 0.5
	[b]1371	1	9.9
	[c]1371	1	9.0
	[d]1371	1	6.5
SENB	1371	4	6.1 ± 0.4

[a]Plus or minus one standard deviation.
[b]Heating rate of 12°C/min with soak time of 30 min.
[c]Heating rate of 12°C/min with soak time of 15 min.
[d]Heating rate of 20°C/min with soak time of 15 min.

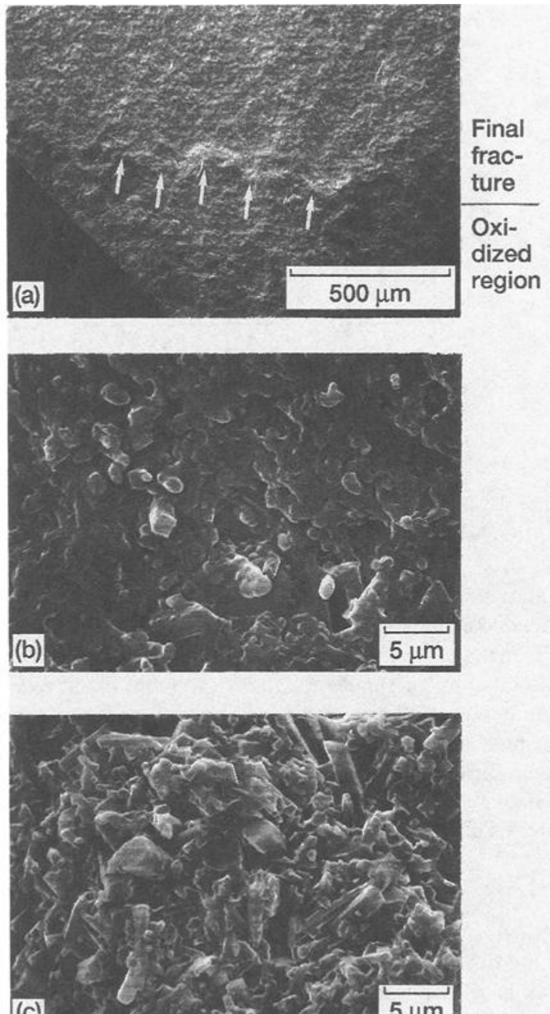

FIG. 7—*Fracture surface of a silicon nitride (SN251) chevron-notched bend specimen tested at 1371°C:* (a) *overall view;* (b) *oxidized wake region;* (c) *crack tip region.*

should be noted that the SENB typically overestimates room temperature fracture toughness unless the notch radius is sufficiently small, as shown in Fig. 8 for the drypressed version of the 96% alumina used in this study [*16*].

Crack Growth Resistance

The application of brittle materials as structural components has generated the need for increased fracture toughness and a degree of damage tolerance. Mechanisms that increase toughness and/or impart damage tolerance are thus being studied. One measurement that gives insight to toughening mechanisms is crack growth resistance. The inherent stability of

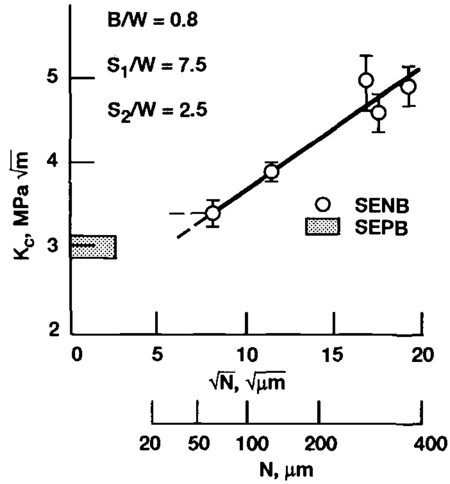

FIG. 8—*Effect of notch width,* N, *on* K_c *of alumina (drypressed ALSIMAG 614) for single-edge precracked beam (SEPB) and single-edge notched beam (SENB) specimens* [16].

the chevron notch allows measurement of crack growth resistance at room and elevated temperatures; however, the inherent stability may complicate results.

Quasistatic crack growth resistance tests were performed at room temperature by gradually loading CNSB specimens until a small increment of stable crack extension occurred, and then partially unloading to a small residual load. This sequence was repeated until the crack propagation became unstable. The crack growth resistance, K_r, was calculated from the maximum load sustained prior to unloading, P_r, and from the stress intensity factor coefficient, Y^*, for the corresponding crack lengths that were determined from the unloading load-displacement slopes and experimental compliance relations [*15*]

$$K_r = \frac{P_r Y^*}{B\sqrt{W}} \tag{2}$$

where B is the specimen thickness and W is the specimen width.

The resulting crack growth resistance curves for three geometries of CNSB made from M-50 steel are shown in Fig. 9, where the stress intensity factor is plotted as a function of the crack extension from the chevron-notch tip. Notch geometry did not affect the level or slope of the R-curve.

Crack growth resistance curves for alumina in the isopressed form are shown in Fig. 10. The CNSB data in Fig. 10 were generated with the method described previously; however, the CNSB specimens were loaded continuously in a dry nitrogen (10 ppm or less H_2O) atmosphere until the desired increment of stable crack extension occurred. The crack lengths were demarcated by injecting dye penetrant into the crack and reloading the specimen several times to one third of the maximum previous load. Load-displacement diagrams were recorded to ensure that no crack extension occurred during the reloading process. After drying the penetrant, the specimens were broken in air and the crack length was determined by averaging five optical measurements of the crack length. The optically measured crack lengths corresponded to crack lengths determined from the unloading slopes of the load-displacement diagrams and experimental compliance relations [*15*], as shown in Fig. 11. The crack growth resistance was calculated with Eq 2.

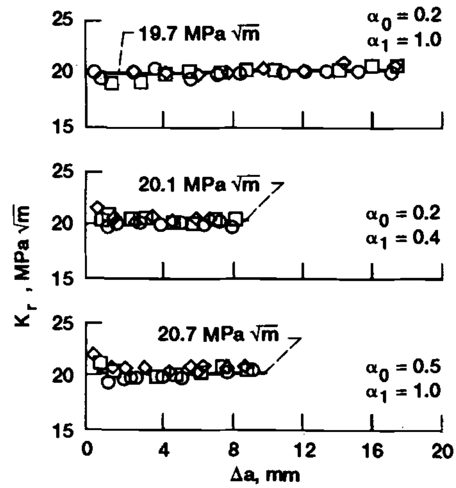

FIG. 9—*Effects of chevron-notched short-bar (CNSB) parameters* α_0 *and* α_1 *on the crack growth resistance of M-50 steel.*

The slopes and ranges of the *R*-curves in Fig. 10 depended on the chevron-notch parameters employed, although the range of K_r values measured was similar. For comparison, the indentation technique of Krause [*30*] was used to generate an *R*-curve in ambient air, as shown in Fig. 10. Although the range of K_r values measured was similar for the two methods, the crack sizes and extensions differed by two orders of magnitude. This indicates that additional crack parameters control the shape of the *R*-curve. The configuration of the crack controls the rate of crack growth resistance. For materials that exhibit crack growth resistance due to grain bridging behind the crack tip, the *R*-curve may be better plotted as a function of the size of traction zone, since the traction zone may be a more geometry-independent measure of the *R*-curve than crack extension.

Stability is another aspect affecting *R*-curve measurement with chevron-notched specimens. Stability of the specimen configuration may also influence the measured fracture toughness, if one assumes that the *R*-curve is a function of crack extension only. Chevron notches have a decreasing stress intensity coefficient with increasing crack length. This

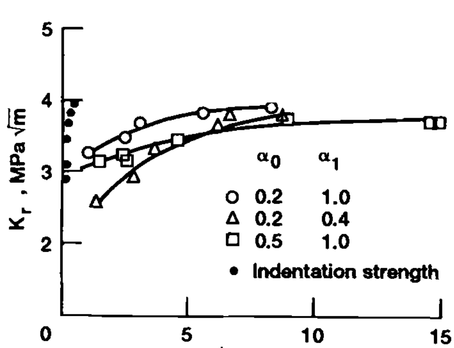

FIG. 10—*Crack growth resistance curves for alumina (isopressed ALSIMAG 614) determined with chevron-notched short-bar (CNSB) specimens and the indentation strength method.*

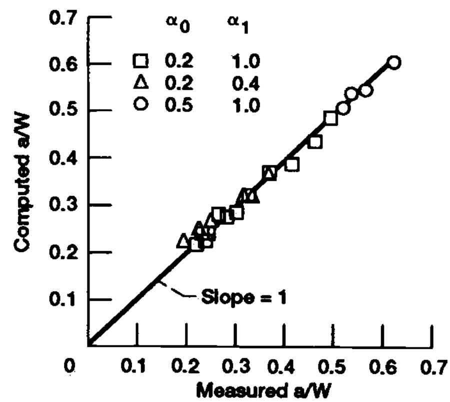

FIG. 11—*Comparison of normalized crack lengths* (a/W) *determined from optical measurement and the compliance method for alumina (isopressed ALSIMAG 614).*

characteristic allows more stable crack extension than commonly used test configurations such as the CT, SEPB, and SENB. For materials with a flat R-curve, the added crack extension in the stable test configuration will result in the same measured fracture toughness, as illustrated in Fig. 12*a*. For a material with a rising R-curve, the higher stability results in additional crack extension which in turn leads to higher measured fracture toughness values, as illustrated in Fig. 12*b*.

Ideally, if crack extension is used as the independent variable, the R-curve should be measured with cracks of the size, geometry, and stability that control component failure, thereby excluding the effects of other parameters. For ceramic components, critical crack lengths are about 1 mm. The CNB, the controlled flaw [*19*], and the SEPB specimens have crack sizes that correspond to this crack length; however, only the controlled surface flaw simulates crack shapes expected in real components.

Fatigue Crack Growth

Fatigue crack growth was conducted with M-50 steel at room temperature. Both CNSB and CT specimens were cyclically loaded in tension at 20 Hz in the load control mode. The crack length, a, and stress intensities K_I and ΔK_I were computed from compliance and stress intensity relationships [*31–33*], and the maximum and minimum loads (P_{max} and P_{min}) were adjusted to maintain an R ratio (P_{min}/P_{max}) of 0.1 with a constant ΔK_I.

CNSB specimens were fatigued at ΔK_I levels of 5.5 to 10 MPa $\sqrt{m}$. The cracks were propagated for a distance of 2.5 mm at each ΔK_I level, with each ΔK_I level being repeated at different points along the chevron. Fatigue cracking of the CT specimens was done at constant ΔK_I levels ranging from 4.1 to 16 MPa $\sqrt{m}$. The cracks were grown from an initial through-the-thickness relative crack length of $a/W = 0.4$.

Fatigue crack growth rates, da/dN, are plotted in Fig. 13. Each CT data point represents a single specimen fatigue cracked at a fixed ΔK_I. The data indicate that fatigue cracks propagate in hardened M-50 steel at ΔK_I as low as 4.1 MPa $\sqrt{m}$. The fatigue growth rates determined from the CT specimens compared well with the results of Rescalvo and Averbach [*34*], and the slope, m, of the fatigue curve was 3.2 in the Paris regime, in good agreement with the value of 3 reported by Rescalvo and Averbach [*34*].

The da/dN values for the CNSB specimen were consistently higher than the values obtained with CT specimens. In the CNSB specimen, for a fixed ΔK_I, da/dN decreased with increasing

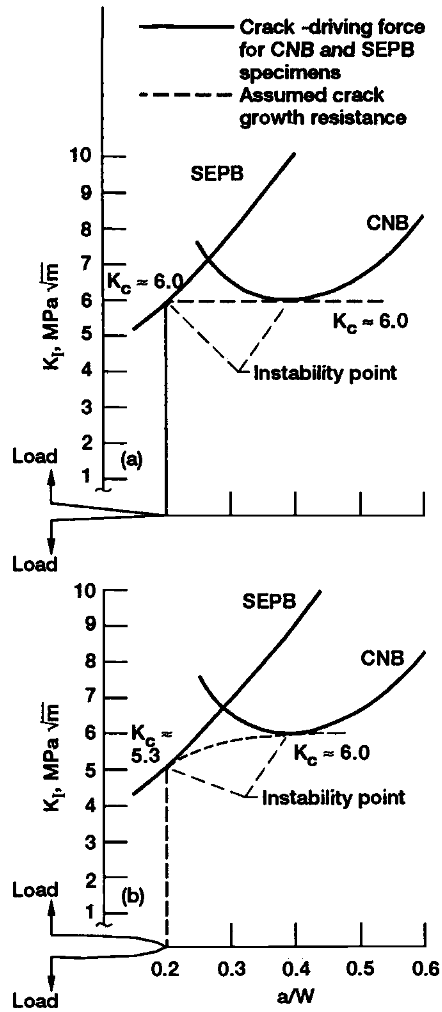

FIG. 12—*Dependence of instability points on specimen geometry:* (a) *Flat* R-*curve;* (b) *Rising* R-*curve.*

crack length and approached the CT specimen values as the crack length approached a_1 (the straight-through crack condition). The differences in crack growth rates were attributed to the large side grooving of the chevron notch, which increased constraint [*35*].

Conclusions

The chevron-notched specimen is very useful in fracture testing of a wide range of material geometries at room and elevated temperatures. The conclusions of this study follow:

1. For materials with a flat *R*-curve, the fracture toughness as measured with CNSB and CNB specimens was independent of proportions and notch geometry and was comparable to fracture toughness measured with SEPB or CT specimens.
2. For materials exhibiting rising *R*-curve behavior, the fracture toughness measured with

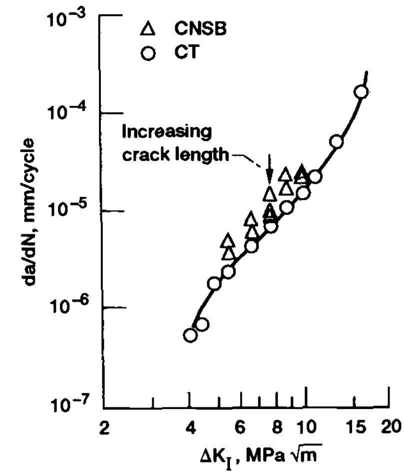

FIG. 13—*Crack growth rates in M-50 steel determined with chevron-notched short-bar (CNSB) and compact-tension (CT) specimens.*

CNSB specimens was dependent on specimen proportions and notch geometry. The dependence was not a function of crack extension alone.

3. Chevron-notch bend tests conducted at low loading rates and high temperatures can estimate fracture toughness to be greater than less stable configurations such as the SEPB and SENB.
4. Fatigue crack growth rates determined with chevron-notched specimens were greater than those determined with CT specimens. The growth rate decreased as the crack approached the straight-through crack condition.

References

[*1*] Jones, M. H., Bubsey, R. T., and Brown, W. F., *Journal of Testing and Evaluation*, Vol. 1, No. 2, 1973, pp. 100–109.

[*2*] Ewart, L. and Suresh, S., *Journal of Materials Science*, Vol. 22, No. 4, 1987, pp. 1173–1192.

[*3*] Warren, R. and Johannesson, B., *Powder Metallurgy*, Vol. 27, No. 1, 1984, pp. 25–29.

[*4*] Nose, T. and Fujii, T., *Journal of the American Ceramic Society*, Vol. 71, No. 5, 1988, pp. 328–333.

[*5*] Pabst, R. F., *Fracture Mechanics of Ceramics*, Vol. 2, R. C. Bradt, D. P. H. Hasselman, and F. F. Lange, Eds., Plenum Press, New York, University Park, PA, 1974, pp. 555–565.

[*6*] Anstis, G. S., Chantikul, P., Lawn., B. R., and Marshall, D. B., *Journal of American Ceramic Society*, Vol. 64, No. 9, 1981, pp. 533–538.

[*7*] Evans, A. G. in *Fracture Mechanics Applied to Brittle Materials, ASTM STP 678*, S. W. Freiman, Ed., 1979, pp. 112–135.

[*8*] Evans, A. G. in *Fracture Mechanics of Ceramics*, Vol. 1, R. C. Bradt, D. P. H. Hasselman, and F. F. Lange, Eds., Plenum Press, New York, 1974, pp. 17–48.

[*9*] Freiman, S. W. in *Fracture Mechanics of Ceramics*, Vol. 6, R. C. Bradt, D. P. H. Hasselman, and F. F. Lange, Eds., Plenum Press, New York, 1983, pp. 27–45.

[*10*] Tattersall, H. G. and Tappin, G., *Journal of Materials Science*, Vol. 1, No. 3, 1966, pp. 296–301.

[*11*] Barker, L. M., *Engineering Fracture Mechanics*, Vol. 9, No. 2, 1977, pp. 361–369.

[*12*] Salem, J. A., Shannon, J. L., Jr., and Bradt, R. C., *Journal of the American Ceramic Society*, Vol. 72, No. 1, 1989, pp. 20–27.

[*13*] Salem, J. A. and Shannon, J. L., Jr., *Journal of Materials Science*, Vol. 22, No. 1, 1987, pp. 321–324.

[*14*] Salem, J. A., Choi, S. R., Freedman, M., and Jenkins, M. G., NASA TM-103741, 1990.

[15] Bubsey, R. T., Orange, T. W., and Shannon, J. L., Jr., NASA TM-83796, not yet published.
[16] Munz, D., Bubsey, R. T., and Shannon, J. L., Jr., *Journal of the American Ceramic Society*, Vol. 63, No. 5–6, 1980, pp. 300–305.
[17] Plane-Strain Fracture Toughness of Metallic Materials. ASTM Standard Test Method E 399. *Annual Book of ASTM Standards*, Vol. 3.01, American Society for Testing and Materials, Philadelphia, PA.
[18] Ghosh, A., Jenkins, M. G., White, K. W., Kobayashi, A. S., and Bradt, R. C., *Journal of the American Ceramic Society*, Vol. 72, No. 2, 1989, pp. 242–247.
[19] Petrovic, J. J., Jacobson, L. A., Talty, P. K., and Vasudevan, A. K., *Journal of the American Ceramic Society*, Vol. 58, Nos. 3–4, March–April 1975, pp. 113–116.
[20] Quinn, G. D. and Quinn, J. B. in *Fracture Mechanics of Ceramics*, Vol. 6, R. C. Bradt, A. G. Evans, D. P. Hasselman, and F. F. Lange, Eds., Plenum Press, New York, 1983, pp. 603–636.
[21] Seshadri, S. G., Srinivasan, M., and King, L., *Ceramic Engineering and Science Proceedings*, Vol. 4, No. 9–10, 1983, pp. 853–863.
[22] Annis, C. G. and Cargill, J. S. in *Fracture Mechanics of Ceramics*, Vol. 4, R. C. Bradt, D. P. Hasselman, and F. F. Lange, Eds., Plenum Press, New York, 1977, pp. 737–744.
[23] Norton Company, Industrial Ceramics Division, Worchester, MA, 01606.
[24] Lange, F. F., *Journal of the American Ceramic Society*, Vol. 56, No. 5, October 1973, pp. 518–522.
[25] Bubsey, R. T., Munz, D., and Shannon, J. L., Jr. in *Ceramics for High Performance Applications III: Reliability*, E. M. Lenoe, R. N. Katz, and J. J. Burke, Eds., Plenum Press, New York, 1983, pp. 753–771.
[26] Munz, D. and Shannon, J. L., Jr. in *Chevron-Notched Specimens, Testing and Stress Analysis, ASTM STP 855*, J. H. Underwood, S. W. Freiman, and F. I. Baratta, Eds., 1983, pp. 270–280.
[27] Evans, A. G. and Weiderhorn, S. M., *International Journal of Fracture*, Vol. 10, No. 3, 1974, pp. 379–392.
[28] Jenkins, M. G., Salen, J. A., and Seshadri, S. G., *Journal of Composite Materials*, Vol. 23, No. 1, 1989, pp. 77–91.
[29] Salem, J. A., NASA TM-102423, 1990.
[30] Krause, R. F., *Journal of the American Ceramic Society*, Vol. 71, No. 5, 1988, pp. 338–343.
[31] Munz, D., Bubsey, R. T., and Srawley, J. E., *International Journal of Fracture*, Vol. 16, No. 4, 1980, pp. 359–374.
[32] Saxena, A. and Hudak, S. J., Jr., *International Journal of Fracture*, Vol. 14, No. 5, October 1978, pp. 453–467.
[33] Shannon, J. L., Jr., Bubsey, R. T., and Pierce, W. F., *International Journal of Fracture*, Vol. 19, 1982, pp. R55–R88.
[34] Rescalvo, J. A. and Averbach, B. L., *Metallurgical Transactions A*, Vol. 10A, September 1979, pp. 1265–1271.
[35] Shih, C. F., deLorenzi, H. G., and Andrews, W. R., *International Journal of Fracture*, Vol. 13, 1977, pp. 544–548.
[36] Bansal, G. K. and Duckworth, W. H., *Journal of the American Ceramic Society*, Vol. 60, No. 7–8, 1977, pp. 304–310.

T. C. Tschanz,[1] *D. K. Matlock,*[2] *and G. Krauss*[2]

Applicability of the Short Rod Fracture Toughness Test to New Microalloyed Bar Steels

REFERENCE: Tschanz, T. C., Matlock, D. K., and Krauss, G., "**Applicability of the Short Rod Fracture Toughness Test to New Microalloyed Bar Steels,**" *Chevron-Notch Fracture Test Experience: Metals and Non-Metals, ASTM STP 1172*, K. R. Brown and F. I. Baratta, Eds., American Society for Testing and Materials, Philadelphia, 1992, pp. 26–42.

ABSTRACT: The applicability of the short rod fracture toughness test to fracture analyses of new microalloyed bar steels, under consideration as substitutes for quenched and tempered steels, is evaluated. Data on two bainitic steels processed with microstructures of ferrite and austenite in which the austenite transforms to martensite with strain are compared to data on 4140 steel and 1045V steel. The applicability of the short rod fracture toughness test is discussed in conjunction with an analysis of the unique deformation behaviors of the four steels. Alterations to the test criteria for materials with microstructures which change with strain are suggested.

KEY WORDS: microalloyed bar steels, stress assisted martensite formation, strain assisted martensite formation, stress strain analysis, transition temperature, validity requirements

The use of new microalloyed steel grades offers significant potential cost savings in applications which require yield strength levels in the range of 560 to 700 MPa [*1–3*]. Some of the microalloyed steels exhibit deformation behavior, as summarized in the following sections, which differs significantly from conventional steels. Universal acceptance of the new microalloyed steels has been limited by a lack of a complete understanding of their fracture behavior. Many of the forged bar products under consideration have dimensions (e.g., <30 mm) that make use of standard plane strain fracture toughness tests inapplicable [*4*]. As a result, the Charpy impact test has been used to evaluate fracture properties. If full acceptance of these new steel grades is to be obtained, then design-oriented fracture toughness data obtained over the complete design temperature range are required. Therefore, the short rod test, which offers many advantages including adaptability to dimensional requirements and inexpensive specimen preparation, was evaluated.

Experimental Materials

Four bar steels were chosen for this study. The steels include two medium-carbon microalloyed bar steels processed with bainite microstructures (designated 0.24%C-Mn-Mo-V and 0.35%C-Mn-Mo-V), a microalloyed ferrite-pearlite steel (1045V), and a conventional quenched and tempered bar steel (4140). The steel processing histories and compositions are summarized in Tables 1 and 2 respectively. All steels were heat treated to produce hardnesses in the range of 25 to 30 HRC.

[1]Senior Materials Engineer, Martin Marietta Astronautics Group, Denver, CO 80201. Now metallurgical engineer, Metallurgical Services of Kentucky.
[2]Professor, Advanced Steel Processing and Products Research Center, Department of Metallurgical and Materials Engineering, Colorado School of Mines, Golden, CO 80401.

TABLE 1—*Summary of processing histories, microstructures, and hardness values of experimental steels* [4,5].

Alloy	Bar Diameter, mm (in.)	Heat Treatment	Microstructure	Hardness (HRC)
1045V	31.8 (1.25)	As-Received	Ferrite/Pearlite	27.8–28.4
4140	31.8 (1.25)	Austenitized 1 h @ 845°C Oil Quenched Temper 1 h @ 670°C Air Cool	Tempered Martensite	28.2–28.6
0.24C-Mn-Mo-V	30.2 (1.19)	Austenitized 1 h @ 1100°C Air Cooled	Bainite	25.3–28.4
0.35C-Mn-Mo-V	31.8 (1.25)	Austenitized 1 h @ 1100°C Air Cooled	Bainite	26.9–30.7

TABLE 2—*Chemical compositions, in weight percent, of the four experimental steels* [4,5].

Alloy	Element											
	Fe	Al	C	Cr	Cu	Mn	Mo	Ni	P	S	Si	V
1045V	bal.	0.019	0.45	0.21	0.14	0.79	0.03	0.18	0.022	0.022	0.26	0.22
4140	bal.	0.001	0.35	0.84	0.24	0.89	0.22	0.10	0.013	0.021	0.29	0.13
0.24C-Mn-Mo-V	bal.	0.001	0.24	0.13	0.44	1.78	0.22	0.17	0.016	0.028	0.41	0.13
0.35C-Mn-Mo-V	bal.	0.040	0.35	0.07	0.06	1.46	0.19	0.06	0.012	0.019	0.79	0.16

The 0.24%C-Mn-Mo-V and 0.35%C-Mn-Mo-V steels were processed by controlled cooling to produce steels with fine bainitic microstructures. In contrast to bainites which consist of ferrite and cementite, the microstructures of the bainite steels of this investigation consisted of ferrite and retained sustenite [5,6]. The 0.35%C-Mn-Mo-V steel had a higher volume fraction of retained austenite than the 0.24%C-Mn-Mo-V steel [5]. The ferrite-pearlite of the 1045V steel was composed of grain boundary allotriomorphs of proeutectoid ferrite and a high volume fraction of pearlite. The vanadium contributed to precipitation strengthening of the ferrite. The 4140 steel had a standard quenched and tempered martensitic structure. Complete summaries of the processing microstructures of the steels are presented elsewhere [4,5].

The mechanical properties as measured by standard Charpy V-notch testing, instrumented impact testing, and crack tip opening displacement (CTOD) testing were evaluated previously as a function of temperature [5]. The temperature-dependent tensile properties of the two bainitic steels differed significantly from both the ferrite-pearlite (1045V) and martensitic steel (4140). Figures 1*a* and 1*b* show the effect of test temperature on the 0.2% offset yield (σ_y) and ultimate strengths (σ_{UTS}), respectively. The temperature dependence of the yield strength for both the 1045V and 4140 steel decrease with an increase in temperature, a behavior which is common to most steels. In contrast, the yield strengths of the two bainitic steels decreased with decreasing test temperatures. All four steels exhibit similar effects of temperature on the ultimate tensile strength, an increase with a decrease in temperature.

Figure 2 shows two sets of schematic stress strain curves based on complete experimental stress-strain curves [5] and illustrates the effects of temperature on the overall deformation behavior of the four steels. Figure 2*a* illustrates the behavior observed for the bainitic steels, while Fig. 2*b* illustrates the behavior for the 1045V and 4140 steel. The schematic stress-strain curves in Fig. 2 clearly show that the temperature dependences of both the yield and ultimate tensile strengths shown in Fig. 1 translate into two distinctively different sets of flow curves. The stress-strain behavior shown in Fig. 2*b* illustrates the anticipated response of most alloy system with stable microstructures. In contrast, the behavior illustrated in Fig. 2*a*, where the stress-strain curves at various temperature cross at an intermediate strain level, reflects the effects of an unstable microstructure in which the microstructure changes with strain. The retained austenite in the bainitic steels transforms to martensite with strain. Austenite transformation with deformation occurs by either stress-assisted or strain-assisted mechanisms and is enhanced with a decrease in test temperature [7]. Therefore the decrease in yield strength with decreasing temperature for the bainitic steels reflects contributions of low-strain stress-assisted transformation of austenite to martensite. Transformation of austenite to martensite produces an extra increment in strain at stress levels less than the conventional macroscopic 0.2% offset yield stress. Thus the initial shape of the curve is altered to produce the behavior shown in Fig. 2*a* in which the proportional limit decreases with a decrease in temperature. Therefore conventional yield strength definitions (i.e., the 0.2% offset) lead to a decrease in yield strength with a decrease in temperature as shown in Fig. 1*a*. Note also for the bainitic steels that immediately after yielding, high strain hardening rates are observed, leading to low ratios of yield strength to ultimate tensile strength.

Most fracture criteria consider the yield strength a critical parameter as it can be used to assist in descriptions of crack tip constraint. However, conventional fracture toughness tests inherently assume that the stress-strain behavior is as illustrated in Fig. 2*b*; thus potential effects of the yield behavior illustrated in Fig. 2*a* must be incorporated in fracture criteria. In this study the effects of the different yielding and deformation behavior of the four steels on fracture behavior are considered.

a.

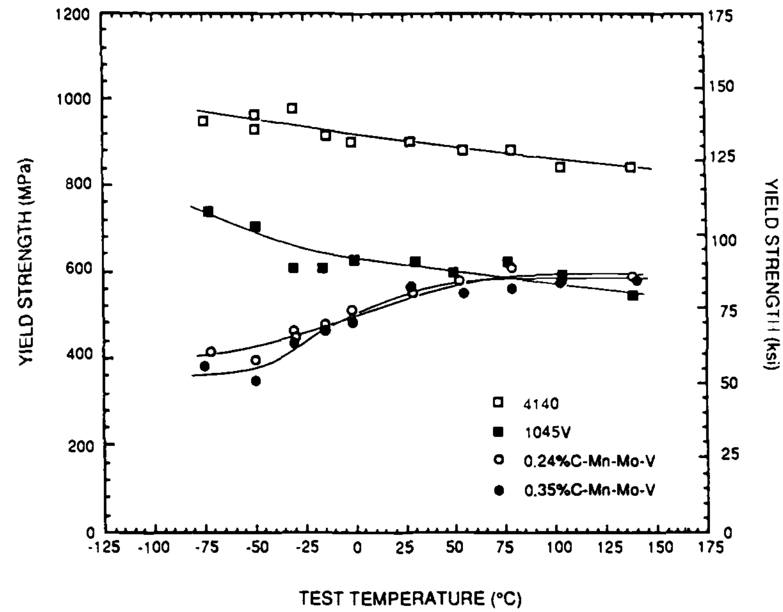

b.

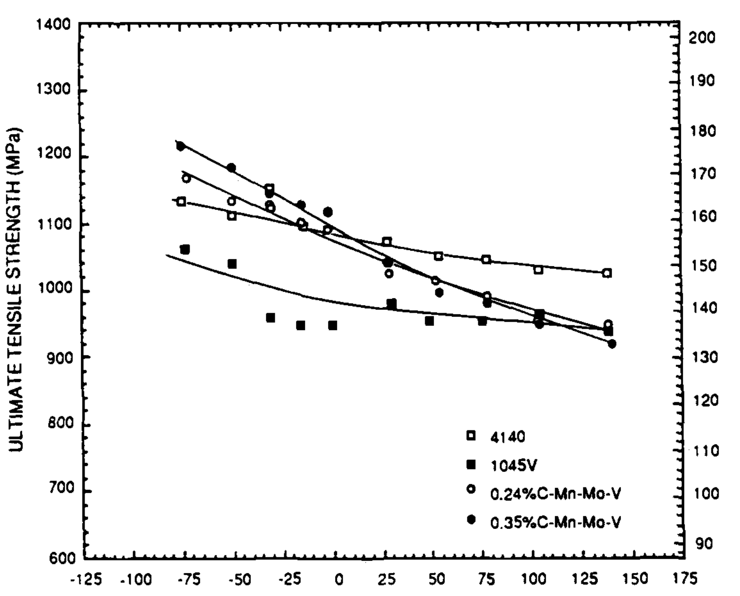

FIG. 1—*Effects of test temperature on the tensile properties of the four experimental steels.* (a) *0.2% yield stress.* (b) *Ultimate tensile strength* [5].

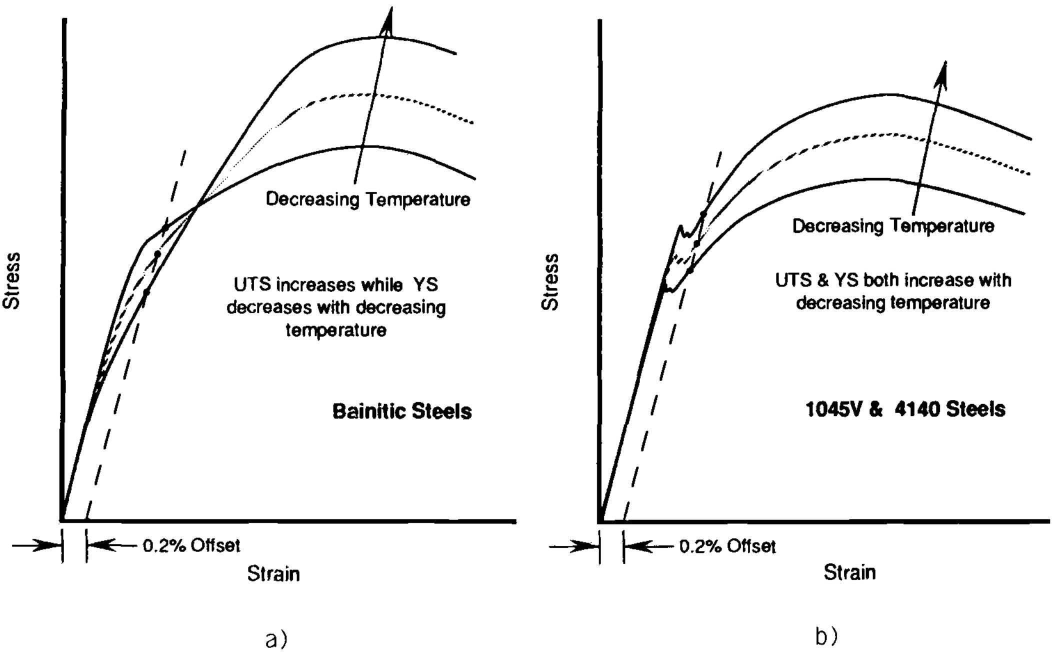

FIG. 2—*Schematic summary of the effects of test temperature on the stress-strain behavior of the four experimental steels. This figure is based on the experimental data of Grassl* [5]. (a) *0.24%C-Mn-Mo-V and 0.35%C-Mn-Mo-V bainitic steels.* (b) *1045V and 4140 steels.*

Experimental Procedure

Cylindrical short rod fracture toughness test specimens were machined and tested in accordance with ASTM Test for Plane-Strain (Chevron-Notch) Fracture Toughness of Metallic Materials (E 1304-89). Full sized (25.4 mm) and sub-sized (12.7 mm) diameter specimens were machined with the dimensions summarized in Table 3. According to the nomenclature for the test orientations summarized in ASTM Terminology Relating to Fracture Testing (E 616-89), full sized samples were machined in the R-L orientation while sub-sized samples were machined in both the R-L and L-R orientations. Fifteen full sized (25.4 mm) specimens were machined in the R-L orientation for each of the four steels and tested as a function of temperature. Eight sub-sized (12.7 mm) short rod specimens were also machined for each orientation (L-R and R-L). All the short rod specimens were removed from center of the heat treated bar stock.

Chevron notches were machined with either a diamond slitting saw or by electrical discharge machining (EDM). Slitting of the chevron notch with the diamond saw proved to be difficult and time consuming. Achieving proper slot alignment on both sides of the specimen was very difficult because the diamond blade warped due to overheating or misalignment.

As an alternative to slitting, the slots in the samples were machined by electrical discharge machining (EDM). After EDM, the depths of the chevron tip (a) were found to be slightly out-of-tolerance because of inconsistent grip groove depths (S in Table 3) which were used as a reference for a_o. The as-machined a_o measurements for the 25.4 mm diameter samples were out-of-tolerance with an average a_o of 11.58 mm. Even though the samples were slightly out-of-tolerance, the results, corrected with the method summarized below in the Discussion,

TABLE 3—*ASTM E 1304 dimensional requirements for short rod specimens (dimensions in mm).*

	25.4 mm Specimen		12.7 mm Specimen	
Symbol[a]	Dimension	Tolerance	Dimension	Tolerance
B	25.4	...	12.7	...
W	36.830	±0.254	18.415	±0.127
a_o	12.217	±0.127	6.109	±0.064
S	3.302	±0.254	1.651	±0.127
X	1.270	±0.076	0.635	±0.038
T	7.950	±0.127	3.975	±0.064
τ	≤0.762	...	≤0.381	...
ϕ	54.6°	±0.5°	54.6°	±0.5°

[a]B = Specimen Diameter
W = Length
a_o = Distance to Chevron Tip
S = Grip Groove Depth
X = Distance to Load Line
T = Grip Groove Width
τ = Slot Thickness
ϕ = Slot Angle

were included in this study and found to correlate directly with those on samples with acceptable dimensions.

In contrast to the machining of the 25.4 mm samples, in which the grip groove and chevron notch were machined in two steps, all machining was done in a single EDM step on the sub-sized samples. As a result, the dimensional tolerances of the sub-sized samples were acceptable according to ASTM E 1304 [*4*].

Machining of specimens within the dimensional tolerances specified by ASTM E 1304 for the sample geometries used in these steels (W/B = 1.45 and a_o/W = 0.332 configuration) may result in specimens which do not meet the tolerance for the chevron slot angle, ϕ. This point is demonstrated in Fig. 3, where ϕ is determined geometrically by assuming the maximum and minimum dimensions within the tolerance bands. For example, as summarized in Table 4, if W is at the high end of the tolerance band while a_o is at the low end of the band (i.e., W = 37.084 mm and a_o = 12.090 mm respectively), then the calculated ϕ is 53.9°. If the reverse conditions are chosen for W and a_o (i.e., W = 36.576 mm and a_o = 12.34 mm), then ϕ is 55.3°. Thus even though the dimensions are within the allowable specification, the calculated value of ϕ is outside the allowable range of 54.6° ± 0.5°. In practice direct measurement of ϕ is not made during machining, and the acceptability of a sample is based primarily on dimensions. Careful consideration of all the dimensions must be given to ensure that all specifications are satisfied.

Short rod testing was performed on a commercial short rod fracture toughness test unit equipped with computer control. The test unit meets the requirements of ASTM E 1304. Copper heating and cooling jackets were used for temperature control in the temperature range of −100°C to +125°C. For cooling, liquid nitrogen was sprayed though four nozzles into each corner of the copper jackets; for heating four resistance heaters were used. The jackets heat or cool the specimens through conduction. Two thermocouples were used: (1) a control thermocouple in the copper jackets near the heating/cooling elements, and (2) a monitoring thermocouple placed in the machined notch and held in place against the inside surface of the notch on the short rod specimen.

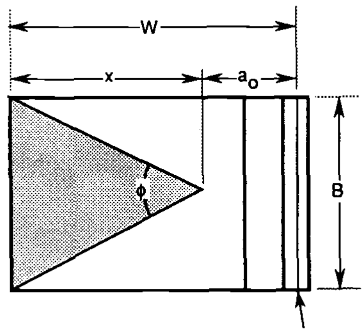

$x = W - a_o$

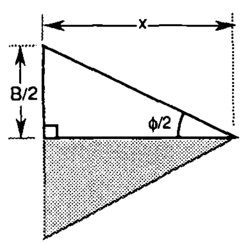

$\tan(\phi/2) = \text{opposite} / \text{adjacent}$

$\tan(\phi/2) = (B/2)/x$

$\tan(\phi/2) = (B/2)/(W-a_o)$

$\phi/2 = \tan^{-1}[(B/2)/(W-a_o)]$

$\phi = 2\tan^{-1}[(B/2)/(W-a_o)]$

FIG. 3—*Schematic drawing of chevron notch in the short rod test sample identifying the parameters used in the calculations summarized in Table 4.*

TABLE 4—*Calculated chevron notch angles based on tolerance extremes in ASTM E 1304.*

	Assumed Values			
Tolerance Case	B	W	a_0	Resulting ϕ
Ideal	25.400	36.830	12.217	54.6°
Worst (+, −)	25.400	37.084	12.090	53.9°
Worst (−, +)	25.400	36.576	12.344	55.3°
Worst (+, +)	25.400	37.084	12.344	54.3°
Worst (−, −)	25.400	36.576	12.090	54.8°

Results

Load-displacement data as a function of test temperature were obtained for the samples, and the results were used to calculate the critical stress intensity factors. In this paper selected data are discussed to illustrate the relationship between stress-strain behavior (as shown in Fig. 2) and calculated short rod fracture toughness data. A complete discussion of all the data is included elsewhere [*4*]. The resulting calculated stress intensity data for the 1045V steel and the two bainitic steels are shown in Figs. 4, 5, and 6. All three materials exhibit a decrease in toughness with a decrease in temperature. In contrast, the 4140 steel exhibited a slight increase in toughness with a decrease in temperature. As the load-displacement data

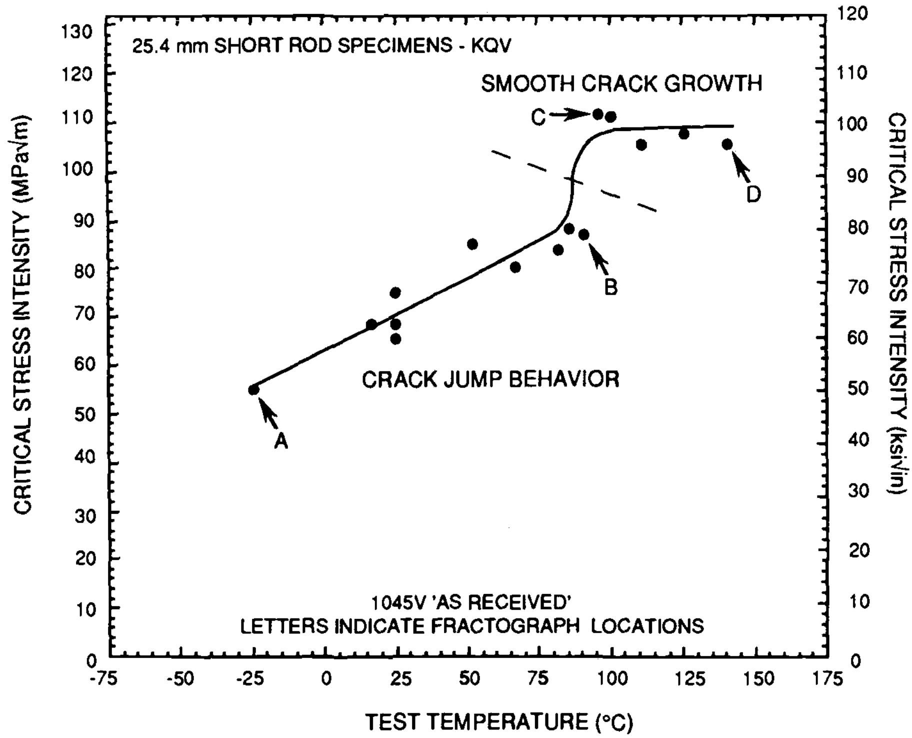

FIG. 4—*Effect of test temperature on the critical stress intensity factor for 25.4 mm diameter specimens of 1045V steel as measured with the short rod fracture toughness test. The arrows indicate the samples used for the fracture analysis summarized in Fig. 7. The dashed line marks the transition from crack jump to smooth crack growth behavior.*

for the 4140 steel differ significantly from the other steels, and the UTS data are higher, further analysis of the fracture toughness data are omitted from the discussion below.

Two different types of load-displacement data were observed: (1) incremental instabilities associated with "crack jump" and (2) smooth data associated with stable or ductile crack growth. Crack jump behavior is characterized by "pop-ins" associated with unstable growth. Unstable crack growth can occur several times within a single test, and at each point of instability the stress intensity reaches a critical value (K_{Ivj}) which is equivalent to the plane-strain fracture toughness. At lower test temperatures only incremental load drops were observed, while at higher temperatures only smooth crack behavior occurred.

The plane-strain fracture toughness was determined using different loads for different types of behavior:

$$K_{Iv} = Y^* m P_c / (B\sqrt{W}) \tag{1}$$

$$K_{Ivj} = Y^* P_n / (B\sqrt{W}) \tag{2}$$

where K_{Iv} is the toughness based on smooth crack growth behavior, K_{Ivj} is the toughness based on crack jump behavior, and P_c and P_n are the critical loads for smooth crack and

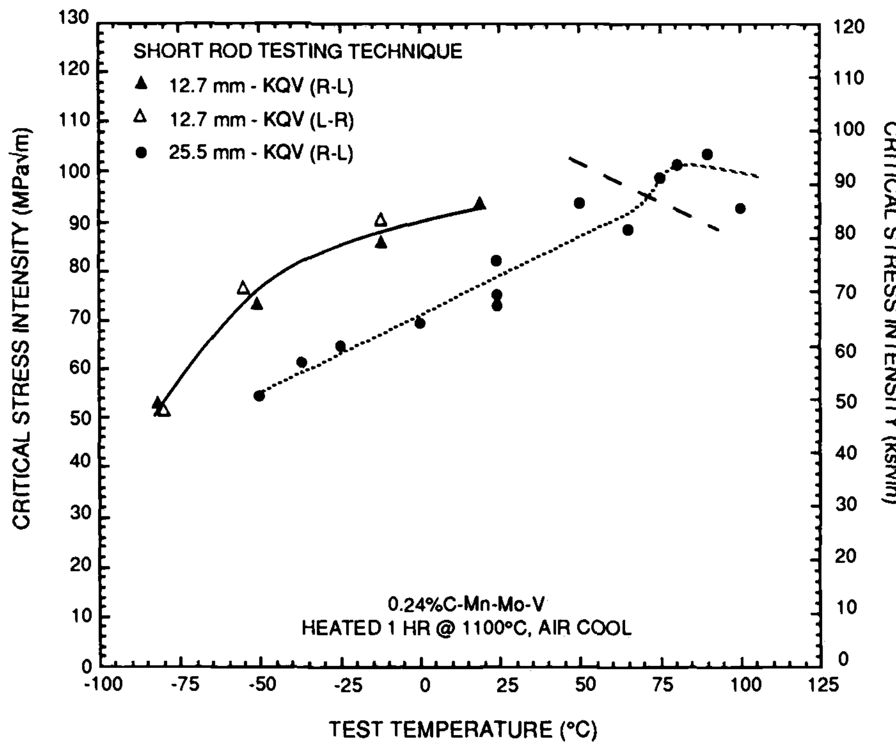

FIG. 5—*Effect of test temperature on the critical stress intensity factor for the 0.24%C-Mn-Mo-V bainitic steel as measured with the short rod fracture toughness test. Data for two specimen diameters (25.4 and 12.7 mm) and two orientations (R-L and L-R) are shown. The dashed line marks the transition from crack jump to smooth crack growth behavior.*

crack jump behavior, respectively. During a test both types of behavior require unloading and reloading, which measure the compliance through the unloading slope ratios, r.

The equation for the stress intensity coefficient (Y^*) as a function of the slope ratio is given in ASTM E 1304 by

$$Y^* = \exp(5.052 - 9.488r + 19.78r^2 - 18.48r^3 + 6.92r^4) \quad (3)$$

Furthermore, the minimum value of the stress intensity coefficient (Y^*_m) can be found by inserting the critical slope ratio (r_c) for a given specimen into Eq 3. For the short rod specimen in this study (i.e., a/B of 1.45 and a_o/W of 0.332) the critical slope ratio is 0.52, resulting in a Y^*_m value of 29.21. The accuracy of Eq 3 is estimated to be $\pm 0.5\%$ for slope ratios between 0.2 and 0.85. Generally, crack jump behavior indicates lower fracture toughness because the crack tends to grow in an unstable manner, whereas smooth crack behavior is associated with stable crack growth.

The transition from crack-jump to smooth crack growth with test temperature is indicated by the dashed line in Figs. 4, 5, and 6. All the load-displacement curves for the 4140 steel exhibited smooth crack behavior over the test temperature range (> -70°C).

The critical stress intensity data for the 25.4 mm diameter samples in Figs. 4 to 6 indicate similar behavior, a gradual increase with temperature followed by a transition region to an upper plateau. The observed transition in toughness is mirrored by a change in fracture surface appearance. For example, the fracture surfaces for the four 1045V steel samples,

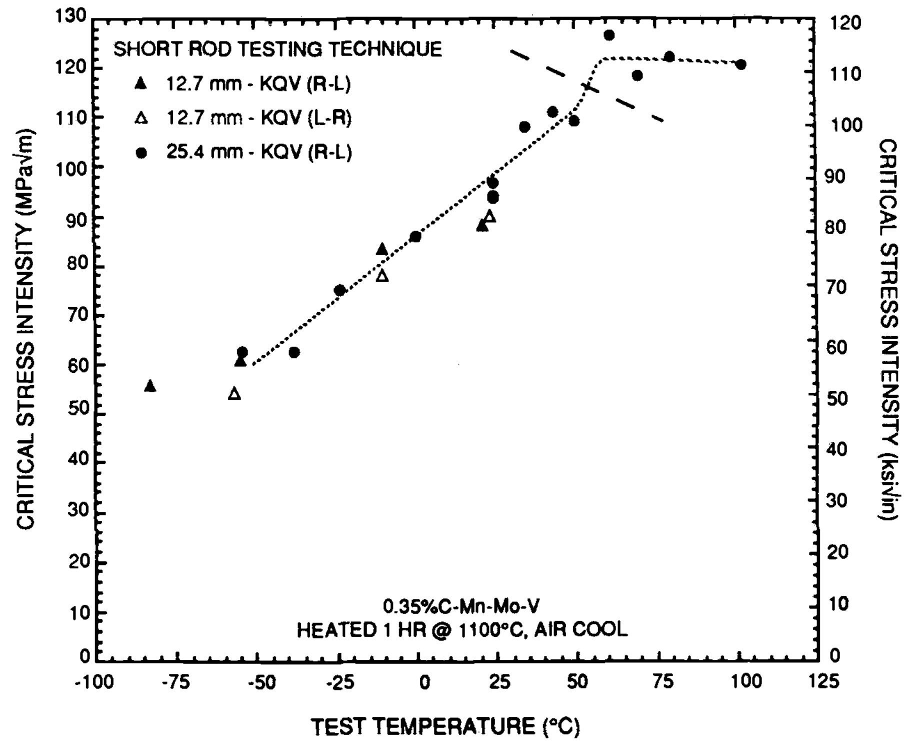

FIG. 6—*Effect of test temperature on the critical stress intensity factor for the 0.35%C-Mn-Mo-V bainitic steel as measured with the short rod fracture toughness test. Data for two specimen diameters (25.4 and 12.7 mm) and two orientations (R-L and L-R) are shown. The dashed line marks the transition from crack jump to smooth crack growth behavior.*

indicated by the letters *A*, *B*, *C*, and *D* in Fig. 4, are shown in Fig. 7. The scanning electron microscope fractographs in Fig. 7 were taken at the crack position which corresponded to the crack lengths used in the toughness calculations.

All fracture surfaces for samples tested below the transition region had a shiny faceted appearance when viewed without magnification. Figure 7*a*, for a specimen at the lowest test temperature (−25°C), exhibits primarily brittle cleavage fracture. The 90°C sample shown in Fig. 7*b* exhibits a mixed-mode cleavage fracture with increased microvoid coalescence. Between 90 and 95°C, the fracture toughness increased abruptly to a upper plateau. Above 95°C, the fracture surface consists of microvoid coalescence due to ductile rupture as shown by fractographs in Figs. 7*c* (95°C) and 7*d* (141°C). Thus the transition in toughness shown in Fig. 4 directly reflects a transition in fracture surface morphology and correspondingly a true transition temperature between 90 and 95°C. Below the transition region, the load versus displacement plots were characterized by crack jump or unstable behavior (between −25 to 90°C) and high strain rates. Within this 5°C range the load displacement curves were found to change from crack jump to smooth crack growth behavior. In other words, the upper plateau is characterized by smooth (stable) crack growth behavior (≥95°C) and low strain rates. Therefore the test record directly reflects the change in the fracture mode that accompanies the transition zone.

Similar correlations between the fracture surface and the load versus displacement records are demonstrated by the bainitic steels with 25.4 mm short rod specimens shown in Figs. 5

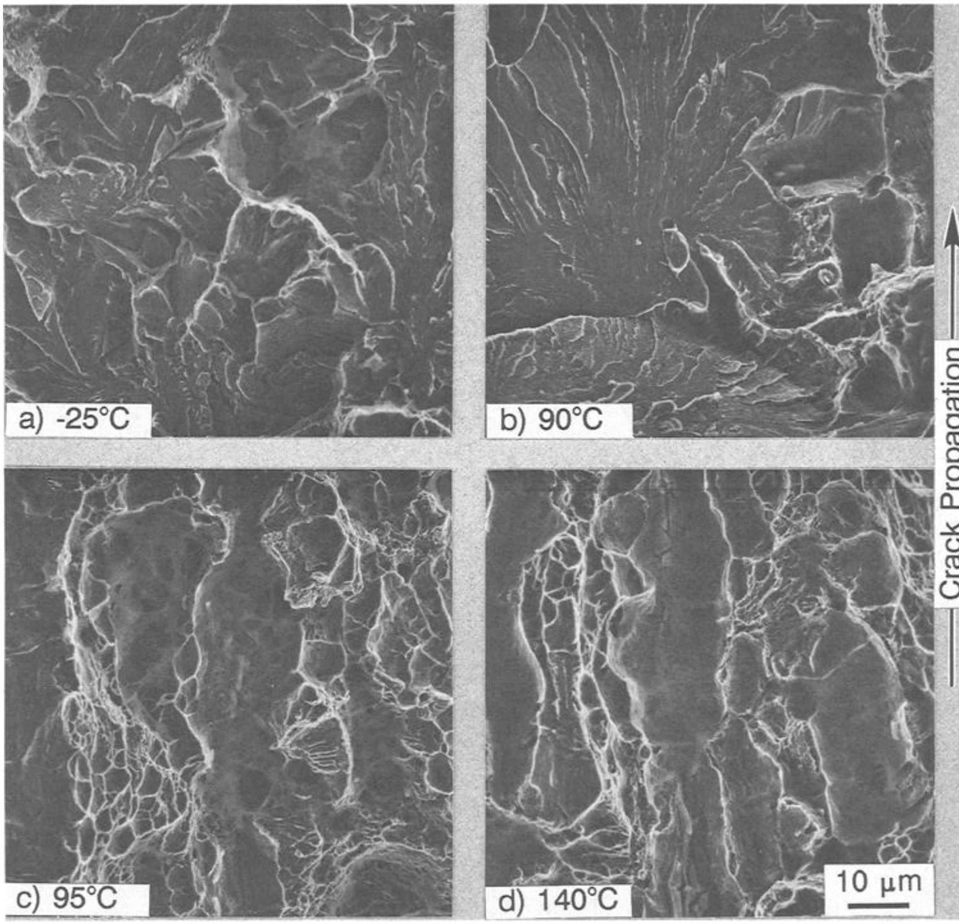

FIG. 7—*Scanning electron microscope fractographs of the 1045V steel at the temperatures indicated in Fig. 4.* (a) *−25°C.* (b) *90°C.* (c) *95°C.* (d) *140°C.*

and 6. Both steels demonstrated three different types of load versus displacement behavior as a function of temperature: 100% crack jump, mixed mode, and smooth crack growth behavior. At low temperatures, crack jump behavior was observed where the specimens displayed multiple small crack jumps in the valid slope ratio region. At intermediate temperatures the specimens displayed mixed mode behavior, where the initial portions of the load versus displacement plot showed smooth crack growth behavior (i.e., woody fracture texture) followed by crack jump behavior (i.e., shiny faceted texture) in the final portions of the test record. This smooth crack growth behavior occurred in the initial part of the load versus displacement data and accounted for a larger fraction of the test record as the temperature increased. An example of a specimen with both types of behavior and the corresponding fracture surface is shown in Fig. 8 for a sample of the 0.24%C-Mn-Mo-V steel tested at 70°C. The increasing load is associated with ductile tearing, while the abrupt load drop is associated with crack growth which leads to the observed brittle fracture (shiny regions).

The effect of sample diameter and orientation was evaluated with sub-sized samples (12.7

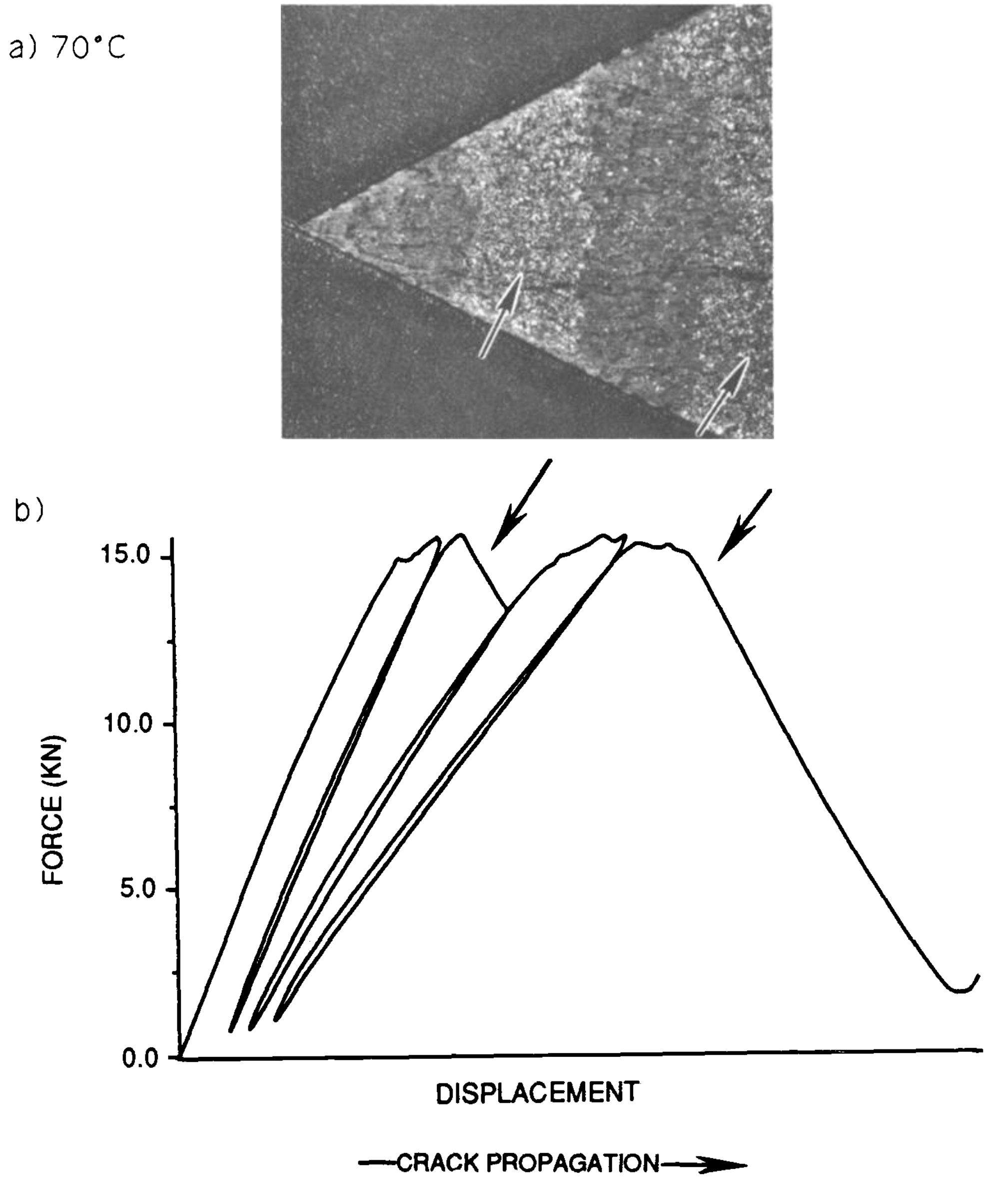

FIG. 8—*A comparison of the fracture surface* (a) *and the load-displacement trace* (b) *for a sample of 0.24%C-Mn-Mo-V steel tested at 70°C, a temperature near the transition temperature. The shiny cleaved regions in* (a) *correlate to the load drops indicated by the arrows in* (b).

mm diameter) for the four steels. The results for the bainitic steels are included in Figs. 5 and 6. All sub-sized samples of the 1045V steel exhibited bulk yielding except for the two L-R samples tested below −77°C. Calculated toughness values for these samples were significantly higher than the data shown in Fig. 4. For the bainitic steels there was no observable effect of orientation for either steel. However, the effect of sample size differed between the two steels. Data for the sub-sized samples of the 0.24%C-Mn-Mo-V steel in

Fig. 5 exhibited the same behavior as for the 1045V steel (i.e., higher toughnesses for subsized specimens). In contrast, there was no apparent sample size effect for the 0.35%C-Mn-Mo-V steel as shown in Fig. 6 where the data for the two sample diameters are superimposed. The significance of the sample size effects are discussed below in conjunction with a discussion of validity requirements.

Discussion

To interpret the fracture data shown in Figs. 4 to 6, it is necessary to evaluate the validity requirements described in ASTM E 1304 along with a consideration of the various stress-strain behaviors exhibited by the steels in this study. Two criteria, the specimen size requirement and the allowable compliance plasticity factor, may be influenced by the extent of stress-induced martensite formation in the plastic zone on loading. As indicated previously, the decrease in yield strength with a decrease in temperature (Fig. 1) was a result of increasing amounts of martensite formation with decreasing test temperatures. Furthermore, the retained austenite volume fraction was higher in the 0.35%C-Mn-Mo-V steel and as a result the extent of transformation was greater.

Specimen Size Requirement

The specimen size requirement given by ASTM E 1304 states that allowable diameters must be larger than the quantity, 1.25 $(K_{QV}/\sigma_y)^2$. Calculations based on the yield data shown in Fig. 1 indicate that valid toughness measurements on the 0.35%C-Mn-Mo-V steel require diameters of 61 to 70 mm, dimensions which are significantly greater than those used in this study. However, the coincidence of the fracture data for the two sample diameters shown in Fig. 6 suggests that both sets of data are valid; otherwise a measurable size effect would have been observed. The possible difference between the observed behavior and the prediction of the allowable diameter may reflect the value of the yield strength used in the dimension validity calculation. Most steels exhibit yield strengths of approximately $0.7\sigma_{UTS}$. However, the bainitic steels exhibit low yield strengths, as low as $0.3\sigma_{UTS}$, and high initial strain hardening rates. Thus, use of abnormally low yield strengths in the constraint requirement would predict larger than required diameters. Therefore it is concluded that the data shown in Fig. 6 are valid. This leads to the further conclusion that the size validity requirement is not applicable to the 0.35%C-Mn-Mo-V steel and needs to be modified. One possible modification is to use σ_F, an average flow stress defined by

$$\sigma_F = \frac{1}{2}(\sigma_y + \sigma_{UTS}) \quad \text{or} \quad \sigma_F = \frac{\sigma_y + \sigma_{UTS}}{2} \tag{4}$$

The average flow stress in Eq 4 would more realistically describe the constraint requirements.

In contrast to the behavior of the 0.35%C-Mn-Mo-V bainitic steel, the other three low steels exhibited fracture data which depended on specimen diameter, and the smaller diameter samples did not produce valid fracture toughness measurements. The 0.24%C-Mn-Mo-V steel, with its lower volume fraction of retained austenite, did not produce significant austenite transformation to offset the size effect.

Compliance Plasticity Factor

The austenite transformation may also influence analysis of the compliance plasticity factor. The compliance plasticity factor, p, is illustrated in Fig. 9 for materials that exhibit two different deformation behaviors. Idealized behavior in Fig. 9*a* obeys the basic principles

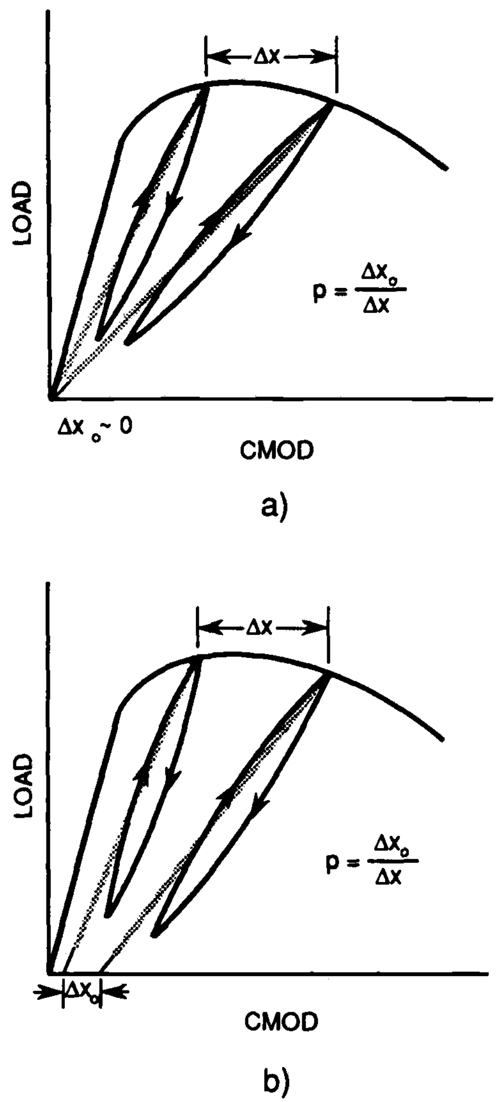

FIG. 9—*Schematic drawings of the load versus crack mouth opening displacement data used to evaluate the compliance plasticity factor as defined in ASTM E 1304-89.* (a) *Linear elastic behavior.* (b) *Elastic-plastic behavior.*

of linear elastic fracture mechanics (LEFM), which is displayed by linear unloading/reloading paths. If the material behaves in an elastic manner, the specimen would completely close when unloaded. In the case of elastic/plastic behavior, the formation of a plastic zone at the crack tip (and the resulting residual stresses) prevent the specimen from completely closing. This causes the slopes of the unloading/reloading cycles to deviate from the origin of the load versus crack mount as shown in Fig. 9*b*. Since LEFM requires negligible plasticity, an elastic-plastic validity check has been developed for short rod specimens to account for plasticity effects. The plasticity is measured by a sequence of unloading and reloading cycles, which allows graphical determination of the "plasticity" from load versus crack mouth opening displacements ratio, $\Delta x_o/\Delta x$, and must be between -0.05 and 0.1 for a valid short rod test. Values outside this range indicate excessive residual stresses ($p < -0.05$) or excessive plasticity ($p > 0.1$), which may indicate specimen failure by plastic tearing instead of crack extension. Thus the mouth opening or plasticity can be taken as a measure of the degree to which LEFM assumptions are violated.

The compliance plasticity factor (p) exceeded the maximum value of 0.1 by a large margin (0.33 to 0.41) for the 0.35%C-Mn-Mo-V bainitic steel and to a lesser extent (approximately 0.17) for the 0.24%C-Mn-Mo-V bainitic steel. However, the maximum load plasticity validity requirement was met (i.e., the $1.1P_c > P_m$ requirement). This indicates that the compliance plasticity factor (p) may be affected by austenite transformation in the plastic zone. The plasticity factor may be affected if the slopes of the compliance measurements are altered by crack closure effects due to martensite formation on loading. In other words, martensite formation may alter closure mechanisms as follows: (1) as stress and resulting induced strain is applied to the crack tip, the retained austenite transforms to martensite; (2) a volume expansion is associated with the transformation from austenite to martensite [5]; (3) the expansion produces compressive residual stress at the crack or notch tip; and (4) the compressive residual stress tends to increase the stress needed to propagate the crack (similar to crack closure effects in fatigue). This mechanism would be expected to decrease the CMOD and reduce the compliance or slope of the unloading/reloading, indicating a smaller crack length than actually exists. Therefore the formation of martensite may alter the appearance of the load displacement curve.

To illustrate the effects of martensite formation on load displacement data, Fig. 10 shows how the increased volume fraction of retained austenite affects load versus displacement records displaying smooth crack growth behavior and may affect the compliance for the various steels studied. These test records were taken just above the transition from crack jump to smooth crack growth behavior, so they can be directly compared without concern for additional plasticity due to elevated test temperatures. In the 4140 steel the load versus displacement record displays linear elastic behavior as shown in Fig. 10*a*. This steel has little or no retained austenite. For the 0.24%C-Mn-Mo-V steel in Fig. 10*b*, the test record demonstrates increased elastic/plastic behavior where the slopes of the unloading/reloading cycles deviate from the origin (i.e., as previously shown in Fig. 9*b*). The final test record for the 0.35%C-Mn-Mo-V steel, shown in Fig. 10*c*, demonstrates elastic/plastic behavior to even a greater extent than the 0.24%C-Mn-Mo-V steel in Fig. 10*b*. As previously mentioned, the 0.35%C-Mn-Mo-V steel has considerably larger volume fraction of retained austenite than the 0.24%C-Mn-Mo-V steel, which resulted in more martensite formation with strain. These results indicate two major changes in the load/displacement plots as the degree of martensite formation with strain increases: (1) the Δx_o term in Fig. 10 increases while the Δx term remains relatively constant for all the test records, and (2) the degree of elastic/plastic behavior increases. The increase of the Δx_o term relative to the Δx term would result in larger p values, which may be associated with the larger volume fraction of retained austenite which transforms to martensite on deformation.

This mechanism may also affect the toughness results in crack jump behavior, since the toughness is determined by evaluating the slope ratios of the critical load (i.e., $0.8r_c \leq r \leq 1.2r_c$). If the slope ratios or compliances are altered by austenite transformation to martensite, the critical loads (P_n) used to evaluate K_{Ivj} may also be altered.

Evaluation of Out-of-Tolerance Specimens

The short rod fracture toughness values were reported as apparent fracture toughness values, K_{Qv}, instead of true plane-strain values primarily due to specimens out-of-tolerance

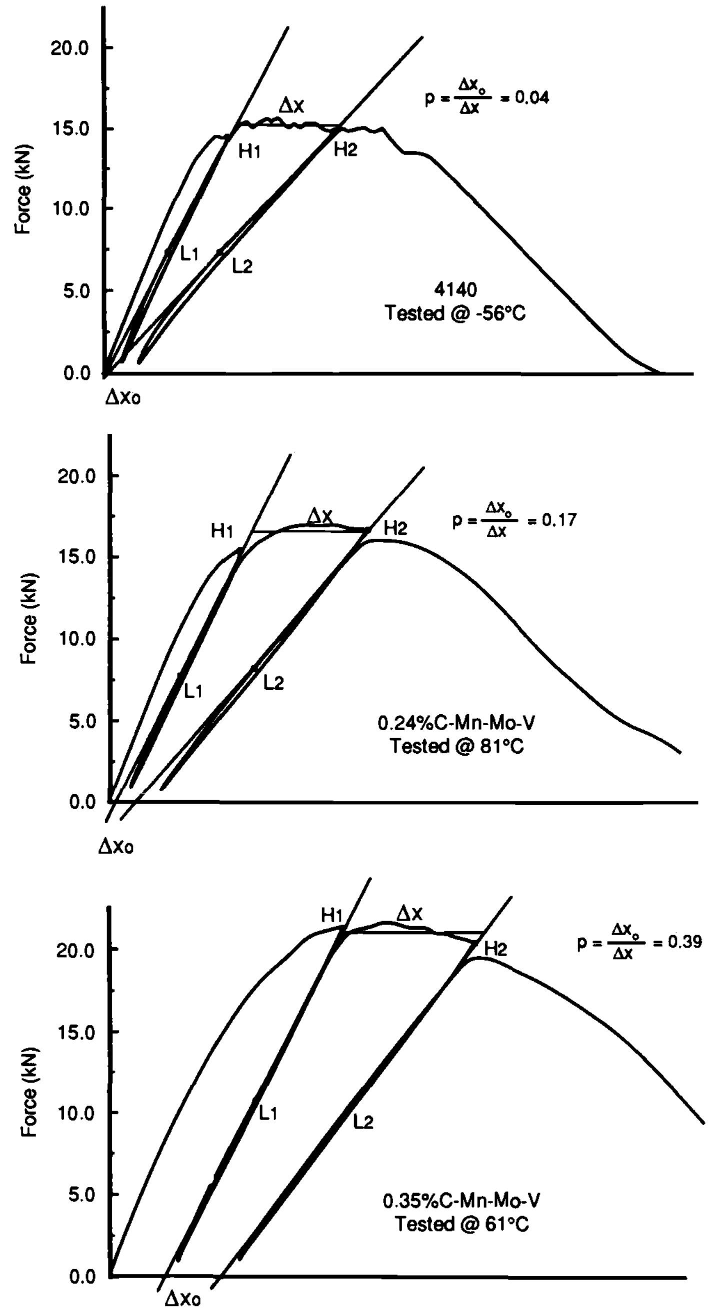

FIG. 10—*Direct traces of the load versus displacement test records for the 4140 steel in* (a) *and the two bainitic steels in* (b) *and* (c).

with respect to the machined notch depth, a_o. An analysis, presented elsewhere [4], showed that correction of the calculations based on the modified stress intensity coefficients determined by Bubsey et al. [8] indicated that the out-of-tolerance crack lengths contributed a maximum error of 4% to the toughness values. Errors of this magnitude are within the experimental measuring capability of most equipment. Thus it is concluded that coefficients in ASTM E 1304 result in conservative limitations to crack geometries, and that proper correction factors can be used to expand the dimension range for short rod samples which produce valid results.

Summary and Conclusions

The results of this study have shown that the short rod test is a viable test for the evaluation of the fracture behavior of several new bar steel grades if the steel microstructures are considered in the analysis. The specification, as written, is appropriate for steels with stable microstructures that exhibit conventional behavior (i.e., both yield and ultimate tensile strengths increase with a decrease in test temperature and the yield to tensile strength ratio is approximately 0.7). However, for steels with microstructures and properties as were exhibited for the bainitic steels, modifications to the validity requirements may be required in order to properly evaluate the fracture toughness.

Acknowledgments

Support by the Advanced Steel Processing and Products Research Center, an NSF-Industry Cooperative Research Center at the Colorado School of Mines, is gratefully acknowledged. The authors also thank Timken Company, Inland Steel Company, and Chaparral Steel Company for the experimental steels and Martin Marietta Company for use of the short rod mechanical test system.

References

[1] Grassl, K., Thompson, S. W., and Krauss, G., "New Options for Steel Selection for Automotive Applications," *SAE Technical Paper Series*, No. 890508, Society of Automotive Engineers, Warrendale, Pa., 1989.

[2] *Fundamentals of Microalloying Forging Steels*, G. Krauss and S. K. Banerjii, Eds., The Metallurgical Society, Warrendale, Pa., 1987.

[3] Krauss, G., "Microalloyed Bar and Forging Steels," in *Proceedings, 29th Mechanical Working and Steel Processing Conference*. Iron and Steel Society, 1987, pp. 67–77.

[4] Tschanz, T. C., *Short Rod Fracture Toughness Testing of Bar Steels*, M. S. Thesis No. T-3993, Colorado School of Mines, Golden, 1990.

[5] Grassl, K. J., *The Effects of Microstructure Type and Loading Rate on the Toughness of Forging Steels*, M. S. Thesis No. T-3797, Colorado School of Mines, Golden, 1990.

[6] Heitman, W. E. and Babu, P. B., "Influence of Bainite in the Microstructure on Tensile and Toughness Properties of Microalloyed Steel Bars and Forgings," in *Fundamentals of Microalloying Forging Steels*, G. Krauss and S. K. Banerjii, Eds., The Metallurgical Society, Warrendale, Pa., 1987, pp. 55–72.

[7] Olson, G. B., "Transformation Plasticity and the Stability of Plastic Flow," in *Deformation Processing and Structure*, G. Krauss, Ed., The Metallurgical Society, Warrendale, Pa., 1984, pp. 391–424.

[8] Bubsey, R. T., Munz, D., Pierce, W. S., and Shannon, J. L., Jr., "Extended Range Stress Intensity Factor for Chevron-Notched Short Bar and Short Rod Fracture Toughness Specimens," *International Journal of Fracture*, Vol. 19, 1982, pp. R55–R58.

J. Morrison[1] *and K. J. KarisAllen*[1]

Specimen Size and Orientation Effects in Chevron-Notch Fracture Testing of Aluminum Alloy Plate

REFERENCE: Morrison, J. and KarisAllen, K. J., "**Specimen Size and Orientation Effects in Chevron-Notch Fracture Testing of Aluminum Alloy Plate,**" *Chevron-Notch Fracture Test Experience: Metals and Non-Metals, ASTM STP 1172*, K. R. Brown and F. I. Baratta, Eds., American Society for Testing and Materials, Philadelphia, 1992, pp. 43–53.

ABSTRACT: Side grooving of specimens can have a pronounced effect on the fracture behavior of aluminum alloys during plane-strain fracture tests. The first part of this paper describes an investigation of the effect of different amounts of side grooving on K_{Ic} determined using compact specimens of varying thicknesses machined from a 6061–T651 plate. The results are also related to K_{Iv} measurements made on the same material and are discussed in terms of rising R-curve effects on compact and short-bar fracture specimens.

Chevron-notch fracture tests in accordance with ASTM E 1304-89 were also carried out on nominally 13-mm-thick plates of aluminum alloys 2024-T351, 7075-T651, and 8090-T8771. Various specimen orientations were used, including both in-plane and short-transverse loading. Tension and also, where possible, compact specimen fracture tests have also been carried out on the same plates.

Data are presented showing the variation in load-deflection behavior and measured toughness with alloy type, and also with specimen orientation. Correlations of toughness and strength with plate rolling direction have been made. Problems arising from the E 1304 test method are also highlighted.

KEY WORDS: fracture toughness, chevron-notched specimens, aluminum, fracture mechanics

During the development and standardization of ASTM E 1304[2] short-bar test procedure for plane-strain fracture toughness, a number of studies were made of its applicability to various aluminum alloys [*1–9*]. Results of particular interest included possible R-curve influences [*3,9*] and the effect of variations in fracture toughness through the thickness of the material [*2,5,6*], both of which were considered to lead to discrepancies between plane-strain fracture toughnesses measured on chevron-notched short bar and those measured on through-notched fatigue precracked specimens.

In an analysis of R-curve effects on chevron-notched and compact specimens, Barker [*9*] has suggested that the chevron-notched specimen is intrinsically independent of the rising portion of the R-curve. The rising R-curve effect is viewed as an increase in stress intensity resulting from the development of a crack-tip plastic zone. A valid K_{Iv} toughness is measured only after a considerable amount of crack extension and, correspondingly, full development of crack tip plasticity up to an R-curve plateau. Depending on the material behavior and the degree of crack-tip constraint in a bend or compact specimen E 399[3] test, the 5% secant

[1]Defence scientist, Defence Research Establishment Pacific, Victoria, British Columbia, Canada, VOS 1BO.
[2]Test Method for Plane-Strain (Chevron Notch) Fracture Toughness of Metallic Materials (E 1304).
[3]Test Method for Plane-Strain Fracture Toughness of Metallic Materials (E 399).

offset toughness measurement point may vary with specimen size as a result of a rising *R*-curve. The toughness might therefore be less than that measured on the corresponding chevron-notched specimen (ignoring any through-thickness toughness variation). This effect would be more pronounced in high toughness alloys, for example Alloy 2024, where the associated plasticity effects are more important.

In a recent study of specimen size effects in 6061-T651 [*8*], it was shown that 25 and 50-mm chevron-notched specimens gave equivalent K_{IvM} results in all E 1304 standard geometries, testifying to their inherent *R*-curve independence. In the same study, a limited number of standard compact specimens from the same plate were also tested. A dramatic effect of side grooving on the load-displacement behavior was observed, producing a maximum load instability rather than gradual ductile tearing. This paper describes some further side-grooving experiments on compact specimens of the same material aimed at clarification of the *R*-curve behavior. Since the *R*-curve is expected to rise more rapidly to a plateau value as the crack tip constraint is increased, side grooving should produce the same trend in K_{Ic} as increasing specimen thickness.

Heat-treatable aluminum alloys, typically in plate form, have usually been found to have lower strength and higher toughness at midthickness relative to the surface [*5–7*]. In certain orientations, therefore, higher toughness measurements can be expected from chevron-notched specimens than from through-thickness notched bend or compact specimens since the advancing crack will sample a greater proportion of the center of the plate. It is of interest to examine the relationship between K_{Ic} and K_{Iv} in an aluminum alloy with greater strength (and perhaps lower toughness) in the center than at the surface of the plate, and also with pronounced anisotrophy of mechanical properties within the rolling plane. As part of an evaluation of the suitability of the short bar procedure for testing relatively thin sections of 8090 aluminum-lithium alloy, a comparison has been made between short bar and compact specimen data, and also with conventional heat-treated aluminum alloys of the same thickness.

Materials and Procedure

Effect of Side Grooving on Toughness

The 63-mm-thick commercial plate had a center line transverse yield strength of 290 MPa, UTS of 320 MPa, and 15% elongation. The standard T-L oriented compact tension specimens had thicknesses of both 25 and 50 mm, the 25-mm-thick specimens being machined from the center of the plate. The specimens were side grooved a total of 0, 10, or 20% of the thickness, with equal material removal on each side and a maximum included angle of groove of 60°. Duplicate specimens, precracked to $a/W = 0.5$, were tested in accordance with the ASTM E 399 procedure, with K_Q measured from either maximum load or a 5% secant offset as appropriate. In calculating *K*, the expression provided in ASTM Standard E 813[4] was employed (using $\sqrt{B \cdot B_N}$, where *B* and B_N are the thicknesses before and after side grooving). Extensive chevron-notch short-bar test results are available from the same plate [*8*].

Effect of Specimen Orientation on Toughness

The conventional aluminum alloys 7075-T651 and 2024-T351 and also the lithium-bearing 8090-T8771 alloy were procured in the form of plate with thicknesses in the range 13 to 15 mm. The room temperature tensile properties of each plate in both the transverse and

[4]Test Method for J_{Ic}, a Measure of Fracture Toughness (E 813).

longitudinal orientations were measured using rectangular specimens with a 6 by 6-mm reduced cross section and 25-mm gauge length. The specimens were machined from the center of the plate and thus sampled approximately half of the thickness. In the case of Alloy 8090, because of its known directionality of properties, additional orientations were included with the long axis of the specimens at 30° intervals between 0 and 150° clockwise from the rolling direction. The tension test results are shown in Table 1. In all cases the highest yield strength and stiffness are obtained in the longitudinal (0°) direction. It has also been established [*10*] that, in contrast to published results on 7075 and 2024, center line strength in the 8090 plate is higher than that of the material closer to the surface. In addition to the in-plane directionality, there is also a tendency for longitudinal splits or delaminations to occur during tension testing of Alloy 8090. Table 1 also agrees with published reports that, in 8090 aluminum, minimum strength occurs at about 55° from the rolling direction [*11,12*].

For each of the orientations for which tensile data were obtained, duplicate fracture toughness tests were carried out at room temperature using both fatigue precracked compact and also chevron-notched short-bar specimens. In this case the orientation refers to the direction of crack extension; the yield stress of interest would, of course, be that for the corresponding loading direction.

The compact specimens had a nominal thickness of 13 mm with a width W of 51 mm and a through-thickness machined notch 23 mm long (nominal $a/W = 0.45$ before precracking). For these specimens the 0 and 90° orientations correspond to the T-L and L-T designations, respectively, using the standard crack plane orientation code. They were precracked to a/W equal to 0.5 in accordance with ASTM Standard E 399 at an R ratio of 0.1 and frequency of 10 Hz, and then side grooved 10% of the thickness on each side prior to the toughness determination.

As with the side-grooving experiments, toughness was measured as appropriate either from maximum load or the 5% secant offset load, using the K expressions of ASTM E 399 and modified net thickness in accordance with ASTM Standard E 813. In a standard plane-strain toughness test, the maximum K capacity of any of these specimens based on the $B \geq 2.5(K/\sigma_y)^2$ criteria would be 26 MPa$\sqrt{\text{m}}$ for the range of yield stress given in Table 1. Based on published values [*13*], none of the Alloy 2024 tests were expected to yield a valid

TABLE 1—*Tensile properties.*

	Orientation—Degrees Clockwise from Rolling Direction					
Alloy	0	30	60	90	120	150
2024-T351						
0.2% proof stress, MPa	395	...	...	355	...	...
UTS, MPa	490	...	...	490	...	...
Elongation, %	18	...	...	15	...	...
Young's modulus, GPa	73	...	...	67	...	...
7075-T651						
0.2% proof stress, MPa	535	...	...	510	...	...
UTS, MPa	575	...	...	580	...	...
Elongation, %	12	...	...	12	...	...
Young's modulus, GPa	71	...	...	67	...	...
8090-T8771 [*12*]						
0.2% proof stress, MPa	530	460	385	495	380	455
UTS, MPa	560	520	500	550	505	525
Elongation, %	6	9	14	9	13	9
Young's modulus, GPa	83	80	81	79	78	81

K_{Ic}, and the 7075 alloy results were expected to be borderline with respect to specimen thickness.

The standard chevron-notched short-bar specimens were 13 mm square with W/B equal to 2; the chevron tip was thus located at the midthickness of the plate. Both the through thickness and short transverse loading directions were investigated, with crack planes normal and parallel to the plate surface, respectively. In this case the 0° orientations correspond to the T-L and S-L designations, and the 90° orientations to the L-T and S-T designations. Tests were conducted in accordance with ASTM Standard E 1304. As a result of limitations in machining capability, difficulty was experienced consistently cutting the chevron slots to the required width (0.38 mm maximum) with the desired tip profile. A reproducible slot width of 0.48 mm was employed, and the lack of validity of the resulting data is indicated by the use of the K_{QvM} designation throughout. The maximum measurable K for the through-thickness notched specimens ranged between 25 and 38 MPa$\sqrt{m}$.

All of the toughness measurements in this and the previous subsection were carried out under ambient conditions in an automated servohydraulic testing machine using displacement control.

Results

Effect of Side Grooving on Toughness

The results of the compact specimen K_{Ic} tests are shown in Table 2 together with the toughness values determined from the same plate using chevron-notched short bar tests [8]. The minimum required thickness for a valid K_{Ic} test was 29 mm and half of this value for a valid K_{Iv}. However, even in the case of the 50-mm-thick compact specimens P_M/P_Q exceeded the 1.1 limit. Short bar toughness was determined using the unloading slopes procedure of E 1304, but only the W/B = 2 specimen data yielded a valid K_{Iv}. The effect of side grooving on the compact specimen load displacement curve was similar for both thicknesses and is shown in Fig. 1. There is a change from a slow ductile tearing (accompanied by the formation of large shear lips) to a sudden crack extension and load drop at maximum load. Side-grooved specimen toughness is therefore calculated from maximum load rather than a 5% secant offset. A small amount of plasticity (more evident in 10% side-grooved specimens than 20%) usually preceeded failure, and the fracture surface was flat.

In the absence of side grooving, there is a small but systematic trend to higher K_Q values with specimen thickness, whereas in short bar tests no consistent thickness effect is observed. Side grooving also increases K_Q to the extent that, in specimens with 20% grooving, the thickness effect disappears. The effects are small and might be more evident in higher

TABLE 2—*6061-T651 compact specimen and chevron-notch test results.*

COMPACT SPECIMENS, K_Q, MPa $\sqrt{m}$		
% Sidegrooved	B = 25 mm	B = 50 mm
0	29	31
10	30	31
20	32	32
CHEVRON-NOTCHED SPECIMENS, K_{Qv} (MPa $\sqrt{m}$) [8]		
Short Bar Type	B = 25 mm	B = 50 mm
W/B = 1.45, B/H = 0.5	31	31
W/B = 2	31	29

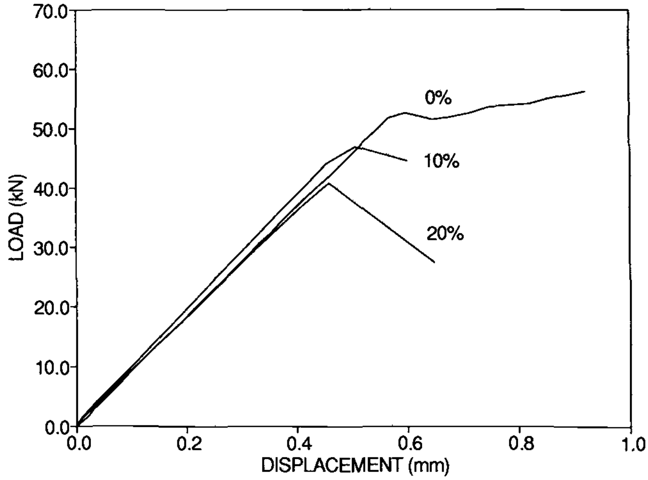

FIG. 1—Effect of side grooving on 6061-T651 load-displacement curves.

toughness aluminum, but they tend to confirm the greater R-curve influence on compact specimens.

Effect of Specimen Orientation on Toughness

The compact specimen test results are given in Table 3. The Alloy 7075 specimens failed abruptly at maximum load with little or no prior crack growth, while the tougher 2024 specimens slowly tore open (Fig. 2). Based on the above results, any R-curve effect would therefore be expected to be more pronounced in the 2024 rather than 7075 alloy. In both alloys, T-L and L-T specimens behave in a qualitatively similar manner. However, only the 7075 K_Q results meet the minimum thickness requirement for a valid K_{Ic} test.

The 8090 alloy shows both kinds of behavior depending on the orientation. The T-L specimens showed sudden crack extension at peak load, while, in orientations near L-T, gradual tearing was observed as well as a higher toughness (Fig. 3). After separation of the specimen halves, differences were also observed in the form of the fatigue precrack and the tendency of the crack to deviate from the intended plane. The T-L and L-T orientations showed a relatively large nonlinearity in load displacement during precracking, presumably as a result of crack closure, and also rough-surfaced fatigue cracks, the L-T having an inverted crack front (i.e., the precrack was longer at the surfaces than in the center of the specimen). The remaining orientations (those loaded in the lower yield strength directions) showed smoother, more thumb-nail shaped, fatigue cracks, particularly at 30 and 150°. Figure 4

TABLE 3—*Compact specimen fracture toughness test results.*

	Toughness K_Q, MPa $\sqrt{m}$ Crack Growth Direction—Degrees from Longitudinal					
Alloy	0	30	60	90	120	150
2024-T351	30	...	...	35	...	...
7075-T651	23	...	...	28	...	...
8090-T8771	28	33	36	36	36	30

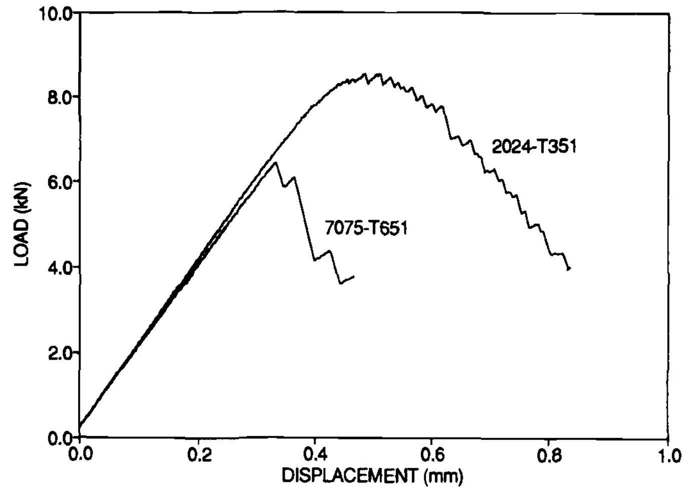

FIG. 2—*Compact specimen load-displacement curves.*

shows an example of each type. Some of these specimens also contained splits ahead of the precrack parallel to the plate surfaces. The T-L fatigue crack was the most prone to deviation from the intended path, whereas during the toughness test after sidegrooving, this orientation was the least inclined to wander.

Table 4 shows the results of the short-bar tests. A characteristic of the 2.0 ratio short bar specimen relative to the 1.45 ratio is frequently a longer flat region of stable tearing. Alloy 7075 specimens showed varying degrees of crack instability, from marked jumps in short transversely loaded specimens, to relatively small serrations in L-T specimens (Fig. 5). T-L specimens frequently showed a preliminary peak prior to a series of smaller instabilities, perhaps indicative of a lack of sufficient constraint at the notch root. Characteristically, Alloy 2024 showed relatively smooth stable tearing in all orientations (Fig 6). However, 2024 T-L specimens tended to tear out of plane.

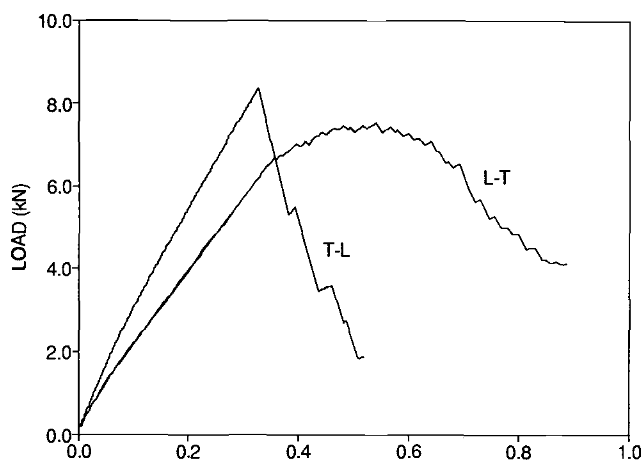

FIG. 3—*Compact specimen load-displacement curves for 8090-T8771.*

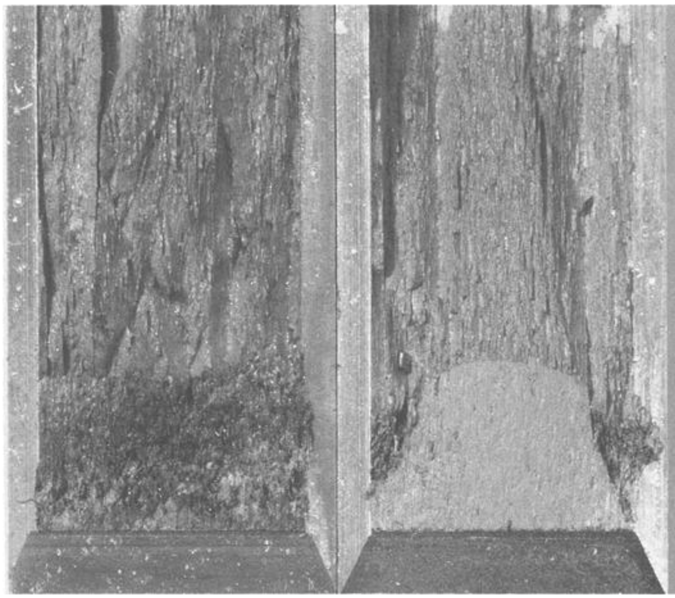

FIG. 4—*Effect of orientation on fatigue precrack appearance in 13-mm-thick 8090-T8771 compact tension specimens.*

Alloy 8090 showed a strong orientation effect. Short transverse specimens showed behavior similar to 7075, with relatively few big crack instabilities and a final sudden separation, the jumps being most pronounced at orientations with crack extension in close to the transverse direction. Specimens loaded in the plane of the plate showed relatively stable tearing, with a flat load-displacement curve at 0°/30°, but as the crack extension direction rotated away from the rolling direction, the crack plane deviated in a conical fashion as the crack extended. The corresponding load-deflection curve showed an initial peak followed by a large increase in load as the crack deviated. At the 120° orientation, the peak was hardly noticeable. L-T 2024 specimens also tore out of plane. The through-thickness notched broken specimens

TABLE 4—*Short bar fracture toughness test results (W/B = 2).*

Alloy	Toughness K_{QvM}, MPa $\sqrt{m}$ Crack Growth Direction—Degrees from Longitudinal					
	0	30	60	90	120	150
2024-T351						
Short transverse	30	...	...	33	...	...
Through thickness	40	...	...	46	...	...
7075-T651						
Short transverse	22	...	...	26	...	...
Through thickness	30	...	...	38	...	...
8090-T8771 [*12*]						
Short transverse	14	15	17	19	19	14
Through thickness	27	27	28[a]	32[a]	29[a]	28

[a]Prior to onset of out of plane tearing.

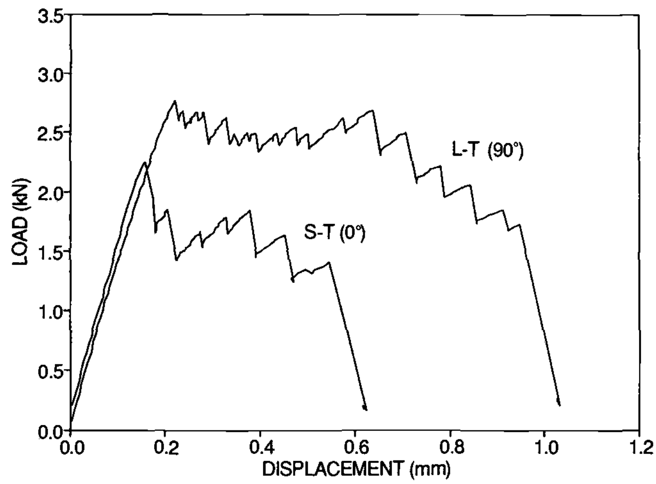

FIG. 5—*Short-bar specimen load-displacement curves for 7075-T651.*

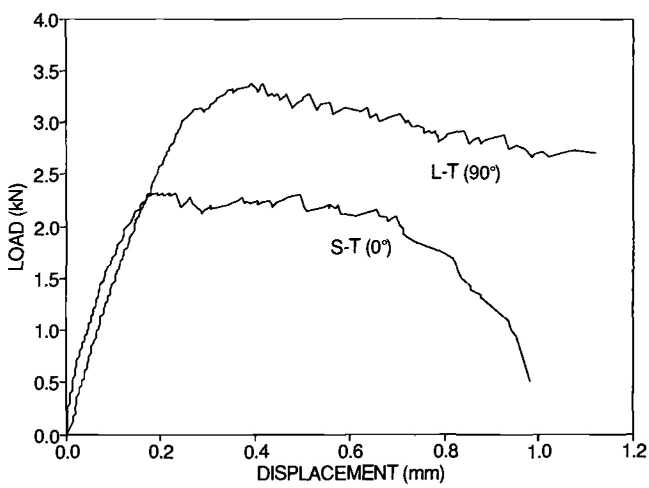

FIG. 6—*Short-bar specimen load-displacement curves for 2024-T351.*

of Alloy 8090 showed some delaminations, most noticeably at the quarter thickness positions. The short transverse specimen fracture surfaces in both 8090 and 7075 were much smoother than in Alloy 2024.

In order to present comparable data from the different alloys and orientations, toughness was calculated as K_{QvM} in accordance with ASTM standard E 1304. In the case of the through-thickness 8090 specimens oriented between 60 and 120°, where out-of-plane tearing inflated the load, the initial peak values are listed for reference. Obviously, these data do not meet the requirement that P_M occur after the 1.2 r_c point.

As expected, only the T-L 7075 alloy compact specimen tests met the ASTM E 399 thickness requirement. However, the rest of the 2024 and 7075 alloy compact specimen results are in good agreement with K_{Ic} values reported elsewhere [*13*]. The short-bar tests

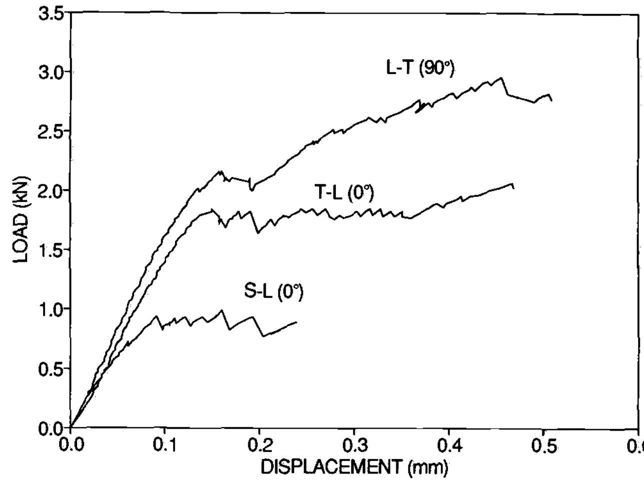

FIG. 7—*Short-bar specimen load-displacement curves for 8090-T8771.*

met the thickness requirement for 7075 and for most of the 8090 tests (marginal at the lowest strength orientations). However, the K_{QvM} for 2024 and 7075 are significantly higher than K_Q from compact specimens in the corresponding orientations. The fact that the short transverse results for these alloys are close to those from compact specimens indicates that they are also somewhat inflated.

In contrast, the 8090 data agree well with the manufacturer's K_Q values for 8090 of 28 MPa$\sqrt{m}$ for T-L and 31 MPa$\sqrt{m}$ for L-T. Table 4 indicates that the ratio of short transverse toughness to that in the plane of the plate is relatively low in Alloy 8090. There is a consistent trend to higher toughness as the crack growth direction moves away from the rolling direction.

Discussion

The results do not provide a clearcut rationale for the higher toughness in the short bar tests on 2024 and 7075 relative to the compact specimen results. A contribution may arise from the plate center being tougher than the outside in these alloys, the opposite trend being evident for Alloy 8090. This might be expected to be more noticeable in the case of 7075 than 2024, but such is not the case. On the other hand, the *R*-curve effect might be expected to be more evident in 2024, as was the tendency to tear out of plane in these specimens. In Tables 3 and 4 short-bar toughness shows an increase of about one third over the corresponding compact specimen toughness for both 7075 and 2024. Similar differences have been reported previously for aluminum alloys with K_{Ic} greater than 30 MPa$\sqrt{m}$ [*3*,*8*]. Munz [*3*] developed an empirical relationship to account for the *R*-curve discrepancy between K_{Ic} and K_{IvM}. His expression would account for about half of the differences found for Alloy 2024 in the present study, and about one third of those found for Alloy 7075. An additional contribution will arise from the limited specimen thickness available for this study; insufficient for a valid compact specimen toughness measurement. This is expected to reduce further the K_Q values. On the other hand, the insufficiently narrow and/or sharply contoured groove tip, which tended to promote an inflated initial load peak prior to crack extension, may continue to influence crack growth resistance as the crack extends.

In most cases 8090 short bar data are in reasonable agreement with those from compact specimens and show the pronounced toughness dependence on orientation characteristic of this alloy. It is interesting that the K_{QvM} values taken from an early peak prior to the out-of-plane tearing in some of these specimens are lower than the corresponding K_Q results. This arises in part from the fact that these K_{QvM} determinations were made at a shorter crack length and higher stress intensity factor coefficient than the standard calibration values. Short-bar tests are currently being carried out on thicker 8090 plate as a means of further evaluating the effect of through thickness strength and toughness variations.

Conclusions

A comparison has been made of compact and short-bar specimen fracture toughness for a variety of aluminum alloys. Chevron-notched specimen toughness has also been measured using both short-transverse and in-plane loaded specimens. Side-grooving compact specimens of Alloy 6061 resulted in a small increase in toughness, of the same order as increasing specimen thickness, indicating a small *R*-curve effect not observed in short-bar specimens. In Alloys 2024 and 7075, short-bar toughness was much higher than that from compact specimens, because, it is believed, of the combined effect of higher center-line toughness, a rising *R*-curve, and a tendency to out-of-plane tearing. Although most of the data were invalid, good agreement was found between toughnesses measured on both compact and short-bar specimens in Alloy 8090. The chevron-notched tests of Alloy 8090 have also been used to demonstrate this material's strong directionality of toughness and relatively low, short transverse fracture resistance. A further investigation of the relative importance of *R*-curve and through-thickness variability in these alloys is underway.

References

[1] Barker, L. M. and Baratta, F. I., "Comparisons of Fracture Toughness Measurements by the Short Rod and ASTM Standard Method of Test for Plane Strain Fracture Toughness of Metallic Materials (E 399-78)," *Journal of Testing and Evaluation*, Vol. 8, No. 3, May 1980, pp. 97–102.

[2] DeJong, H. F., "Thickness Direction Inhomogeneity of Mechanical Properties and Fracture Toughness as Observed in Aluminum 7075-T651 Plate Material," *Engineering Fracture Mechanics*, Vol. 13, 1980, pp. 175–192.

[3] Munz, D., "Determination of Fracture Toughness of High Strength Aluminum Alloys with Chevron-Notched Short Rod and Short Bar Specimens," *Engineering Fracture Mechanics*, Vol. 15, 1981, pp. 231–236.

[4] Guest, R. V., "Progress Report: The Effect of Specimen Size on Short Rod Fracture Toughness Measurements of Aluminum," in *Proceedings*, 26th National SAMPE Symposium, April 1981, SAMPE, Los Angeles, pp. 536–542.

[5] Barker, L. M., "Specimen Size Effects in Short-Rod Fracture Toughness Measurements," *Chevron-Notched Specimens: Testing and Stress Analysis, ASTM STP 855*, American Society for Testing and Materials, Philadelphia, 1984, pp. 117–133.

[6] Brown, K. R., "The Use of the Chevron-Notched Short-Bar Specimen for Plane-Strain Toughness Determination in Aluminum Alloys," *Chevron-Notched Specimens: Testing and Stress Analysis, ASTM STP 855*, American Society for Testing and Materials, Philadelphia, 1984, pp. 237–254.

[7] Eschweiler, J., Marci, G., and Munz, D. G., "Fracture Toughness of an Aluminum Alloy from Short Bar and Compact Specimens," *Chevron-Notched Specimens: Testing and Stress Analysis, ASTM STP 855*, American Society for Testing and Materials, Philadelphia, 1984, pp. 255–269.

[8] Morrison, J., Gough, J. P., and KarisAllen, K. J., "Comparison of Chevron-Notched Specimen Types for Fracture Toughness Testing of Aluminum," *Journal of Testing and Evaluation*, Vol. 17, No. 1, January 1989, pp. 14–19.

[9] Barker, L. M., "Chevron-Notched Specimens for Fracture Toughness Measurements Independent of R-Curve Effects," *Journal of Testing and Evaluation*, Vol. 17, No. 4, July 1989, pp. 218–223.

[10] Peel, C. J., "The Present Status of the Development and Application of 8090 and 8091 Alloys,"

Proceedings, ASM Aluminum-Lithium Symposium, Westec, Los Angeles, 1988, American Society for Metals, Metals Park, OH.

[*11*] Starke, E. A. and Quist, W. E., "The Microstructure and Properties of Aluminum-Lithium Alloys," AGARD Lecture Series No. 174 on New Light Alloys, AGARD-LS-174, Advisory Group for Aeronautical R&D, Neuilly Sur Seine, France, September 1990.

[*12*] Morrison, J. and KarisAllen, K. J., "Orientation Dependence of Fracture Toughness in 8090 Aluminum Alloy Plate Using Chevron Notched Specimens," *Proceedings*, ECF8, Fracture Behaviour and Design of Materials and Structures," Turin, Vol. II, 1990, pp. 327–333.

[*13*] *Damage Tolerant Design Handbook*, Vol. 3, Metals and Ceramics Information Center, Columbus, OH, 1983.

Thomas W. Orange,[1] *Raymond T. Bubsey,*[1] *William S. Pierce,*[1] *and John L. Shannon, Jr.*[1]

Analysis of Some Compliance Calibration Data for Chevron-Notch Bar and Rod Specimens

REFERENCE: Orange, T. W., Bubsey, R. T., Pierce, W. S., and Shannon, J. L., Jr., "**Analysis of Some Compliance Calibration Data for Chevron-Notch Bar and Rod Specimens,**" *Chevron-Notch Fracture Test Experience: Metals and Non-Metals, ASTM STP 1172,* K. R. Brown and F. I. Baratta, Eds., American Society for Testing and Materials, Philadelphia, 1992, pp. 54–62.

ABSTRACT: This paper presents a set of equations describing certain fracture mechanics parameters for chevron-notch bar and rod specimens. They are developed by fitting earlier compliance calibration data. Numerical differentiation must be used to determine the minimum stress intensity factor and the critical crack length, and the problem this presents for these specimens is discussed.

KEY WORDS: chevron-notch specimens, compliance calibration, stress intensity factor, critical crack length

Nomenclature (see Fig. 1)

a	Crack length (measured from load line)
a_0	Distance from load line to tip of chevron
a_m	Crack length at which Y^* is minimum
B	Specimen thickness
C	Specimen compliance, $C = EBV/P$
D	Diameter (rod), $D = B$
E	Elastic (Young's) modulus
K_I	Opening-mode stress intensity factor
K_{Iv}	Plane-strain fracture toughness for chevron-notch specimens
P	Applied load
V	Crack mouth opening displacement
W	Width
Y^*	Dimensionless stress intensity factor for a crack in a chevron notch, $K_I B W^{1/2}/P$
Y^*_m	Minimum value of Y^* as a function of α
α	a/W
α_0	a_0/W
α_m	a_m/W

[1]Research Engineer, retired, retired, and Branch Chief, respectively, NASA Lewis Research Center, Cleveland, OH 44135.

Introduction

This paper presents a set of equations describing certain fracture mechanics parameters for chevron-notch bar and rod specimens. They are developed by fitting previously reported experimental compliance calibration data. Their use will facilitate the testing and analysis of brittle metals and the tougher ceramics. The equations present the various parameters in forms suitable for determining fracture toughness from maximum load, for determining the crack-extension resistance curve (R-curve), and for setting instrument sensitivities. The data encompass the entire range of the specimen geometries most commonly used.

We first discuss briefly the background of the chevron-notch specimens and the experimental data to be used. Then we present a more extensive discussion on some particular characteristics of the chevron-notch specimens and their practical application. The fitted equations are presented and their fitting accuracies are discussed. Finally, problems in determining the minimum stress intensity coefficient and the critical crack length are discussed.

Background

The chevron-notch specimens are fairly recent additions to the field of fracture mechanics. Consequently they do not have the same historical background of extensive stress intensity and displacement analysis as do the more common specimen types. But, like the earliest specimen types, we can develop useful expressions using experimental compliance data.

Compliance data for the chevron-notch bar [*1*] and rod [*2*] specimens were previously reported. In each paper, one fitted equation was presented relating the minimum stress intensity factor to the initial crack length and to the specimen dimensions. A later paper [*3*] reported additional data for specimens having smaller initial crack lengths and also revised the previous equations to cover the wider range of crack lengths. But those equations alone are not sufficient for all analyses and tests involving high-toughness ceramics. To make them more complete and useful, a new set of generalized equations are presented in this paper. These equations are developed by fitting curves to the existing data. They are usable over a wide range of specimen dimensions.

Characteristics of Chevron-Notch Specimens

For most common fracture test specimens, the dimensionless stress intensity factor (Y) increases continually with increasing relative crack length (a/W). But due to the wedge shape of the unnotched material in the chevron-notch specimen, the corresponding factor (Y^*) reaches a minimum, denoted Y^*_m, as the crack length reaches a value denoted a_m. The values of Y^*_m and α_m are functions of specimen dimensions and notch geometry only and are independent of material properties.

If the material being tested has a crack growth resistance curve which increases rapidly to a relatively constant plateau (known as a "flat" R-curve), instability will occur at $a = a_m$ and $P = P_{max}$. Then the fracture toughness (K_{Iv}) can be calculated from

$$K_{Iv} = Y^*_m \frac{P_{max}}{BW^{1/2}} \tag{1}$$

and no other test measurements are necessary.

For some materials (even some ceramics), however, the R-curve does not reach a plateau but continues to increase with increasing crack extension (a "rising" R-curve). For such

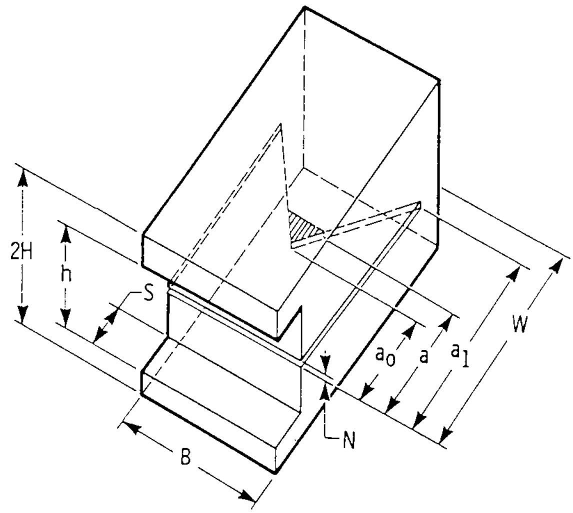

FIG. 1*a*—*Chevron-notch bar specimen.*

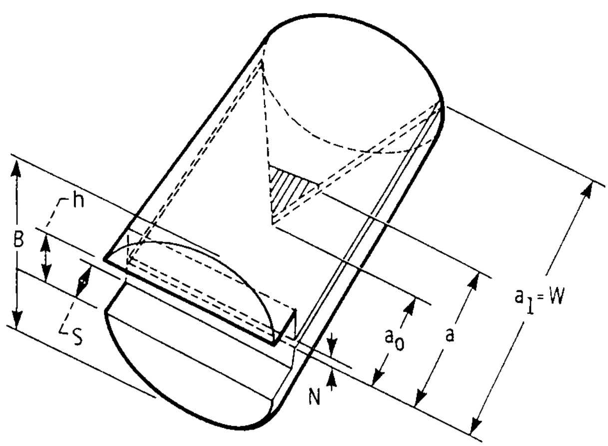

FIG. 1*b*—*Chevron-notch rod specimen.*

materials, Eq 1 does not apply and it may be desirable to determine the complete *R*-curve. In this case ASTM Practice for *R*-Curve Determination (E 561–86) may be used for guidance. If crack mouth opening displacement (CMOD) is measured during the test and appropriate compliance relations are available, one can calculate the instantaneous crack length. From crack length and load, one can calculate the crack extension resistance as

$$K_I = Y^* \frac{P}{BW^{1/2}} \tag{2}$$

A plot of crack extension resistance against crack advance is the *R*-curve.

Procedure

Experimental Procedure

The experimental procedure is described in detail in Refs *1* and *2*. The complete data are presented in Ref *4*. At least three replicate tests for each crack length were averaged to obtain the data reported here. For each specimen, 7 to 15 crack lengths (depending on the initial crack length) were tested.

Basic Data Reduction

Analysis of the data is based on the following equation [*1*] and its derivative with respect to α:

$$Y^* = \left[\frac{1}{2}\frac{\alpha_1 - \alpha_0}{\alpha - \alpha_0}\frac{d}{d\alpha}\frac{EBV}{P}\right]^{1/2} \tag{3}$$

In Refs *1* to *3* the logarithms of the basic compliance data ($C = EBV/P$) were fit with a fourth-degree polynomial in α. The fitted curve was differentiated and the values of Y^* calculated from Eq 3.

In Ref *1*, the reported values of Y^*_m and α_m corresponded to the minimum of that fitted curve. In Ref *2*, Y^*_m and α_m were determined in the same way, but the data range was restricted to seven points symmetrical about the value of α_m found by the first fitting. Reference *3* used still another procedure. Seven points were selected by the previous criterion. Then a fourth-degree polynomial was fit to the logarithms of the compliance derivatives. That second polynomial was used to calculate Y^*_m and α_m.

In the process of verifying these calculations, some general concerns arose concerning procedures for determining Y^*_m and α_m. These will be discussed later.

Development of Generalized Equations

The following expressions are useful for computing the plane strain fracture toughness K_{Iv} when the material has a relatively "flat" *R*-curve:

$$\alpha_m = A_0 + A_1\alpha_0 + A_2\alpha_0^2 + A_3\alpha_0^3 \tag{4}$$

and

$$Y^*_m = B_0 + B_1\alpha_0 + B_2\alpha_0^2 + B_3\alpha_0^3 \tag{5}$$

These were developed by first fitting third-degree polynomials in α_o for each specimen type (bar or rod) and each value of *W/B*. Then the coefficients of the intermediate polynomials were in turn fit to a second-degree polynomial in *W/B* to produce the final forms of Eqs 4 and 5. Values of the coefficients for Eqs 4 and 5 are given in Tables 1 and 2, respectively.

An expression for determining the relative crack length α as a function of measured displacements is

$$\alpha = C_0 + C_1U + C_2U^2 + C_3U^3 + C_4U^4 \tag{6}$$

TABLE 1—*Coefficients for Eq 1.*[a]

Specimen	Coeff.	Expression
Bar	A_0	$-0.110 + 0.354\,(W/B) - 0.088\,(W/B)^2$
	A_1	$0.268 + 1.628\,(W/B) - 0.400\,(W/B)^2$
	A_2	$1.637 - 6.358\,(W/B) + 1.872\,(W/B)^2$
	A_3	$0.075 + 4.462\,(W/B) - 1.508\,(W/B)^2$
Rod	A_0	$0.147 + 0.089\,(W/B) - 0.026\,(W/B)^2$
	A_1	$0.358 + 1.150\,(W/B) - 0.096\,(W/B)^2$
	A_2	$2.860 - 5.190\,(W/B) + 0.770\,(W/B)^2$
	A_3	$-3.610 + 5.100\,(W/B) - 0.800\,(W/B)^2$

[a]Range: $1.5 \leq (W/B) \leq 2.0$, $0 \leq \alpha_0 \leq 0.5$.

TABLE 2—*Coefficients for Eq 5.*[a]

Specimen	Coeff.	Expression
Bar	B_0	$-17.03 + 29.94\,(W/B) - 5.0\,(W/B)^2$
	B_1	$-116.00 + 141.60\,(W/B) - 29.6\,(W/B)^2$
	B_2	$1131.00 - 1304.00\,(W/B) + 342.0\,(W/B)^2$
	B_3	$-1351.00 + 1654.00\,(W/B) - 443.2\,(W/B)^2$
Rod	B_0	$5.47 + 6.29\,(W/B) + 2.46\,(W/B)^2$
	B_1	$-65.93 + 72.62\,(W/B) - 5.62\,(W/B)^2$
	B_2	$622.00 - 659.80\,(W/B) + 146.10\,(W/B)^2$
	B_3	$-541.40 + 629.10\,(W/B) - 135.20\,(W/B)^2$

[a]Range: $1.5 \leq (W/B) \leq 2.0$, $0 \leq \alpha_0 \leq 0.5$.

where U is the Saxena and Hudak form [5]:

$$U = \frac{1}{\left(\dfrac{EBV}{P}\right)^{1/2} + 1}$$

The coefficients for Eq 6 are given in Table 3. This equation lends itself to computer-controlled fracture toughness testing, since the subcritical crack growth can be determined from automated load and deflection data acquisition.

When the relative crack length α is known, the stress intensity factor Y^* and the dimensionless compliance EBV/P can be computed from the following expressions:

$$Y^* = e^{D_0 + D_1\alpha + D_2\alpha^2 + D_3\alpha^3 + D_4\alpha^4} \tag{7}$$

and

$$\frac{EBV}{P} = e^{E_0 + E_1\alpha + E_2\alpha^2 + E_3\alpha^3 + E_4\alpha^4} \tag{8}$$

The coefficients for Eqs 7 and 8 are given in Tables 4 and 5, respectively.

TABLE 3—*Coefficients for Eq 6.*[a]

Specimen	Coeff.	Expression
Bar	C_0	$3.09 - 24.12\alpha_0 + 57.12\alpha_0^2$
$W/B = 1.5$	C_1	$-109.30 + 1\,227.00\alpha_0 - 2\,876.00\alpha_0^2$
	C_2	$1\,908.00 - 22\,216.00\alpha_0 + 51\,286.00\alpha_0^2$
	C_3	$-14\,900.00 + 168\,580.00\alpha_0 - 381\,240.00\alpha_0^2$
	C_4	$41\,390.00 - 451\,059.00\alpha_0 + 987\,080.00\alpha_0^2$
Bar	C_0	$2.08 - 8.74\alpha_0 + 16.93\alpha_0^2$
$W/B = 2.0$	C_1	$-63.31 + 540.00\alpha_0 - 1\,019.00\alpha_0^2$
	C_2	$1\,086.00 - 11\,296.00\alpha_0 + 20\,043.00\alpha_0^2$
	C_3	$-9\,327.00 + 98\,493.00\alpha_0 - 158\,690.00\alpha_0^2$
	C_4	$28\,430.00 - 284\,970.00\alpha_0 + 366\,330.00\alpha_0^2$
Rod	C_0	$0.672 + 4.85\alpha_0 - 23.93\alpha_0^2$
$W/B = 1.5$	C_1	$25.670 - 361.90\alpha_0 + 1\,624.00\alpha_0^2$
	C_2	$-858.000 + 9\,512.00\alpha_0 - 39\,580.00\alpha_0^2$
	C_3	$9\,219.000 - 105\,260.00\alpha_0 + 411\,440.00\alpha_0^2$
	C_4	$-35\,145.000 + 417\,050.00\alpha_0 - 1\,550\,300.00\alpha_0^2$
Rod	C_0	$0.896 + 7.24\alpha_0 - 26.5\alpha_0^2$
$W/B = 2.0$	C_1	$21.800 - 590.40\alpha_0 + 2\,087.0\alpha_0^2$
	C_2	$-1\,192.000 + 17\,166.00\alpha_0 - 58\,980.0\alpha_0^2$
	C_3	$16\,772.000 - 213\,330.00\alpha_0 + 713\,640.0\alpha_0^2$
	C_4	$-78\,837.000 + 961\,870.00\alpha_0 - 3\,146\,400.0\alpha_0^2$

[a]Range: $0.18 \leq \alpha_0 \leq 0.22$, $\alpha_0 \leq \alpha \leq 0.8$.

TABLE 3—*Coefficients for Eq 6.*[a]

Specimen	Coeff.	Expression
Bar	C_0	$3.09 - 24.12\alpha_0 + 57.12\alpha_0^2$
$W/B = 1.5$	C_1	$-109.30 + 1\,227.00\alpha_0 - 2\,876.00\alpha_0^2$
	C_2	$1\,908.00 - 22\,216.00\alpha_0 + 51\,286.00\alpha_0^2$
	C_3	$-14\,900.00 + 168\,580.00\alpha_0 - 381\,240.00\alpha_0^2$
	C_4	$41\,390.00 - 451\,059.00\alpha_0 + 987\,080.00\alpha_0^2$
Bar	C_0	$2.08 - 8.74\alpha_0 + 16.93\alpha_0^2$
$W/B = 2.0$	C_1	$-63.31 + 540.00\alpha_0 - 1\,019.00\alpha_0^2$
	C_2	$1\,086.00 - 11\,296.00\alpha_0 + 20\,043.00\alpha_0^2$
	C_3	$-9\,327.00 + 98\,493.00\alpha_0 - 158\,690.00\alpha_0^2$
	C_4	$28\,430.00 - 284\,970.00\alpha_0 + 366\,330.00\alpha_0^2$
Rod	C_0	$0.672 + 4.85\alpha_0 - 23.93\alpha_0^2$
$W/B = 1.5$	C_1	$25.670 - 361.90\alpha_0 + 1\,624.00\alpha_0^2$
	C_2	$-858.000 + 9\,512.00\alpha_0 - 39\,580.00\alpha_0^2$
	C_3	$9\,219.000 - 105\,260.00\alpha_0 + 411\,440.00\alpha_0^2$
	C_4	$-35\,145.000 + 417\,050.00\alpha_0 - 1\,550\,300.00\alpha_0^2$
Rod	C_0	$0.896 + 7.24\alpha_0 - 26.5\alpha_0^2$
$W/B = 2.0$	C_1	$21.800 - 590.40\alpha_0 + 2\,087.0\alpha_0^2$
	C_2	$-1\,192.000 + 17\,166.00\alpha_0 - 58\,980.0\alpha_0^2$
	C_3	$16\,772.000 - 213\,330.00\alpha_0 + 713\,640.0\alpha_0^2$
	C_4	$-78\,837.000 + 961\,870.00\alpha_0 - 3\,146\,400.0\alpha_0^2$

[a]Range: $0.1 \leq \alpha_0 \leq 0.35$ (bar), $0.1 \leq \alpha_0 \leq 0.40$ (rod), $\alpha_0 \leq \alpha \leq 0.8$.

TABLE 5—*Coefficients for Eq 8.*

Specimen	Coeff.	Expression
Bar	E_0	$2.850 - 6.48\alpha_0 + 61.56\alpha_0^2$
$W/B = 1.5$	E_1	$1.177 + 26.59\alpha_0 - 349.30\alpha_0^2$
	E_2	$9.650 - 8.37\alpha_0 + 708.90\alpha_0^2$
	E_3	$-16.240 - 62.60\alpha_0 - 597.00\alpha_0^2$
	E_4	$10.450 + 56.82\alpha_0 + 167.90\alpha_0^2$
Bar	E_0	$3.885 - 17.75\alpha_0 + 94.97\alpha_0^2$
$W/B = 2.0$	E_1	$-5.160 + 123.20\alpha_0 - 624.20\alpha_0^2$
	E_2	$34.270 - 324.50\alpha_0 + 1562.00\alpha_0^2$
	E_3	$-52.330 + 386.80\alpha_0 - 1756.00\alpha_0^2$
	E_4	$27.950 - 173.20\alpha_0 + 741.40\alpha_0^2$
Rod	E_0	$3.91 - 23.18\alpha_0 + 138.4\alpha_0^2 - 91.84\alpha_0^3$
$W/B = 1.5$	E_1	$-10.01 + 237.70\alpha_0 - 1356.0\alpha_0^2 + 1325.00\alpha_0^3$
	E_2	$51.60 - 758.80\alpha_0 + 4284.0\alpha_0^2 - 4777.00\alpha_0^3$
	E_3	$-74.66 + 969.60\alpha_0 - 5480.0\alpha_0^2 + 6516.60\alpha_0^3$
	E_4	$37.83 - 433.00\alpha_0 + 2464.5\alpha_0^2 - 3043.00\alpha_0^3$
Rod	E_0	$2.92 + 0.28\alpha_0 + 26.67\alpha_0^2 + 33.27\alpha_0^3$
$W/B = 2.0$	E_1	$1.68 + 28.52\alpha_0 - 336.00\alpha_0^2 + 111.40\alpha_0^3$
	E_2	$20.59 - 135.84\alpha_0 + 1157.00\alpha_0^2 - 918.40\alpha_0^3$
	E_3	$-39.16 + 218.10\alpha_0 - 1581.00\alpha_0^2 + 1581.00\alpha_0^3$
	E_4	$22.64 - 115.78\alpha_0 + 756.60\alpha_0^2 - 837.20\alpha_0^3$

[a]Range : $0.1 \leq \alpha_0 \leq 0.35$ (bar), $0.1 \leq \alpha_0 \leq 0.40$ (rod), $\alpha_0 \leq \alpha \leq 0.8$.

Discussion

Generalized Equations

Equation 4 fits the calculated values of α_m within $0.013W$ for the bar specimens and within $0.006W$ for the rod specimens. Equation 5 fits the calculated values of Y_m^* within 1.0% for the bar specimens and within 2.7% for the rod specimens.

Within the ranges of α and α_0 specified in Tables 3 to 5, Eq 6 fits the measured values of α within $0.003W$ for the bar specimen and within $0.002W$ for the rod specimen; Eq 7 fits the calculated values of Y^* within 2.9% for the bar specimen and within 2.1% for the rod specimen; and Eq 8 fits the measured values of EBV/P within 1.4% for both the bar and the rod specimen.

Table 3 of ASTM Test for Plane-Strain (Chevron-Notch) Fracture Toughness of Metallic Materials (E 1304–89) gives values of Y_m^* and a critical slope ratio r_c. That ratio is the ratio of the compliances corresponding to α_m and α_0. For specimens with $W/B = 2.0$, the values of Y_m^* computed from Eq 5 for both the bar and rod specimens are within 0.6% of those in Ref 7. The critical slope ratio computed from Eq 8 is within 1% for the bar specimen but is 7.8% low for the rod specimen.

Problems in Determining Y_m^* and α_m

The method of data analysis used in Ref *3* was not given explicitly and could not be determined directly from archival records. In attempting to verify the numerical analysis (by duplication), several methods were tried. Each produced a significantly different value for α_m for the same data set, and this is a problem that should be discussed.

The problem is inherent in the chevron-notch specimen. It is due to the same characteristic that makes it desirable, namely the fact that Y^* has a minimum. For example, assume that we have a function f such that

$$\frac{EBV}{P} = f(\alpha)$$

where f includes the data transform (if any) and a fitting function. Substituting this into the derivative of Eq 3 and eliminating non-zero terms, we have

$$0 = \frac{1}{\alpha_m - \alpha_0} f'(\alpha_m) - f''(\alpha_m) \qquad (9)$$

where f' and f'' are the first and second derivatives and α_m is the root of this equation. Unlike simpler specimens, we need to determine the *second* derivative as well. This presents a strong challenge to the analyst.

Figure 2, from Ref *1*, shows the typical variation of Y^* with α for different values of α_0. Experimental compliance data would be expected to scatter about these lines. It is apparent from this figure that for a short initial crack (say, $\alpha_0 = 0.2$) Y^*_m will be relatively insensitive to the method of curve fitting but α_m will be very sensitive. However, for a long initial crack (say, $\alpha_0 = 0.5$) the opposite will be true.

Thus if the primary objective of the test is to determine K_{Iv}, the initial crack length should be short. This is the case in ASTM E 1304. However, a long initial crack length may be preferable if the critical crack length is important for, say, fractographic purposes.

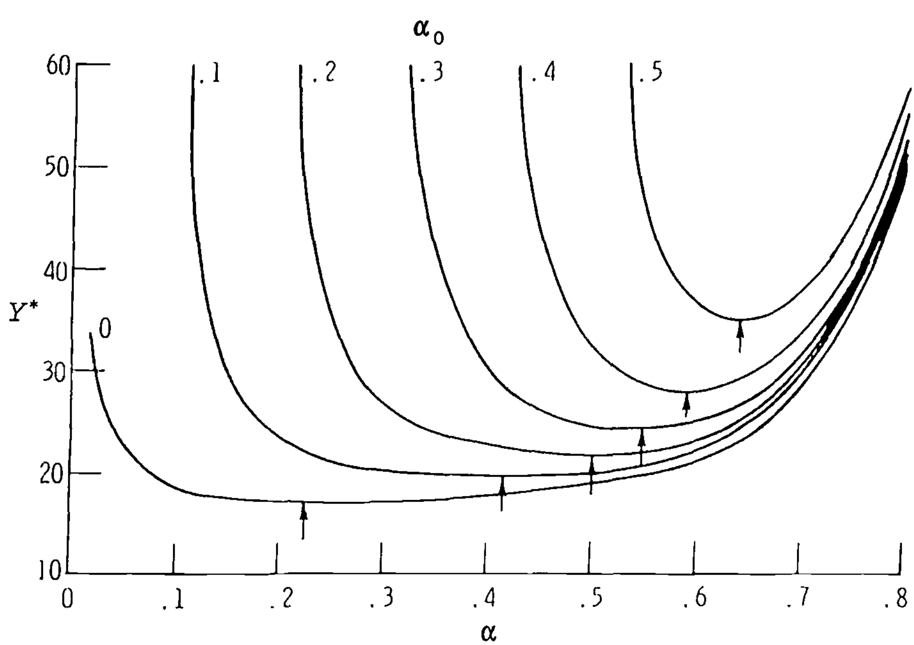

FIG. 2—*Typical variation of stress intensity factor with crack length for chevron-notch specimens* [1] *Arrows denote minima.*

It should be pointed out that numerical analyses (i.e., finite element or boundary integral methods) are subject to the same problem, although to a lesser degree. Discrete pairs of (Y^*, α_0) for several initial crack lengths must be fitted with a function to calculate a minimum. Three pairs are required; more would be preferred.

Conclusions

The equations presented here are in forms suitable for several purposes in fracture testing with chevron-notch specimens. They encompass the range of specimen geometries most commonly used and provide a good fit to the basic compliance data.

Determination of the minimum stress intensity factor and the critical crack length requires numerical differentiation. This presents a problem which is unique to the chevron-notch specimens, and that problem is discussed.

References

[1] Munz, D., Bubsey, R. T., and Srawley, J. E., "Compliance and Stress Intensity Coefficients for Short Bar Specimens with Chevron Notches," *International Journal of Fracture*, Vol. 16, No. 4, Aug. 1980, pp. 359–374.

[2] Bubsey, R. T., Munz, D., Pierce, W. S., and Shannon, J. L., Jr., "Compliance Calibration of the Short Rod Chevron-Notch Specimen for Fracture Toughness Testing of Brittle Materials," *International Journal of Fracture*, Vol. 18, No. 2, Feb. 1982, pp. 125–133.

[3] Shannon, J. L., Jr., Bubsey, R. T., Pierce, W. S., and Munz, D., "Extended Range Stress Intensity Factor Expressions for Chevron-Notched Short Bar and Short Rod Fracture Toughness Specimens," *International Journal of Fracture*, Vol. 19, No. 3, July 1982, pp. R55–R58.

[4] Bubsey, R. T., Orange, T. W., Pierce, W. S., and Shannon, J. L., Jr., "Closed-Form Expressions for Crack-Mouth Displacements and Stress Intensity Factors for Chevron-Notched Short Bar and Short Rod Specimens Based on Experimental Compliance Measurements," NASA TM 83796, 1991.

[5] Saxena, A. and Hudak, S. J., Jr., "Review and Extension of Compliance Information for Common Crack Growth Specimens," *International Journal of Fracture*, Vol. 14, No. 5, Oct. 1978, pp. 453–468.

A. R. Rosenfield[1] *and B. S. Majumdar*[1]

Fracture Toughness Evaluation of Ceramic Bonds Using a Chevron-Notch Disk Specimen

REFERENCE: Rosenfield, A. R. and Majumdar, B. S., "**Fracture Toughness Evaluation of Ceramic Bonds Using a Chevron-Notch Disk Specimen,**" *Chevron-Notch Fracture Test Experience: Metals and Non-Metals, ASTM STP 1172*, K. R. Brown and F. I. Baratta, Eds., American Society for Testing and Materials, Philadelphia, 1992, pp. 63–73.

ABSTRACT: The chevron-notched diametrally compressed disk specimen has been used to measure the fracture toughness of zirconia/zirconia bonds and zirconia/nodular-cast-iron bonds. The data are reasonably consistent with experience obtained using monolithic ceramics. In particular, the strain energy release rate increases with increasing shear:tension ratio, and the opening-mode fracture toughness measured using the disks is generally within 20% of the value obtained with bend beams. However, the shear toughnesses of the bonds investigated are approximately 2.4 times the opening toughness, a ratio somewhat higher than that for monolithic ceramics. The high ratio can be attributed to rubbing of mutually opposed crack faces, deviation of the fracture plane into higher-toughness zirconia prior to instability for the ceramic/ceramic bonds, and shear of the braze-metal interlayer in the case of the metal/ceramic bonds.

KEY WORDS: fracture toughness, compression loads, shear stresses, disk specimen, chevron-notch specimen, partially stabilized zirconia, nodular cast iron, ceramic/ceramic bonds, metal/ceramic bonds

Cylinders loaded in compression along a diameter have been used for many years to measure "splitting," i.e. tensile strength of rocks (ASTM D 3967)[2] and concrete (ASTM C 496),[3] and a comprehensive review of this test geometry has appeared recently [*1*]. The driving force for fracture in the specimen is generated from a tensile stress located at its center and normal to the loading axis, whose magnitude is one third of the principal compressive stress. Both of the existing ASTM standards employ relatively large specimens; for example, the minimum diameter in D 3967 is 47 mm and the length is typically twice the diameter. In addition, the standards call for a padding material (cardboard and/or plywood) inserted between the brittle cylinder and the loading points to distribute the load and inhibit localized crushing.

Recently there has been increasing interest in applying diametral compression of cylinders to fracture toughness testing of advanced ceramics, which have much finer microstructures than rocks and concrete. The specimens used in such experiments are considerably thinner (length:diameter $\approx$1/10) than the unnotched ASTM design. The difference in geometry arises from the need to supply the fracture toughness specimen with a notch, which is most

[1]Research leader and principal research scientist, respectively, Metals and Ceramics Department, Battelle Memorial Institute, Columbus, OH 43212-2693.
[2]Test Method for Splitting Tensile Strength of Intact Rock Core Specimens (D 3967).
[3]Test Method for Splitting Tensile Strength of Cylindrical Concrete Specimens (C 496).

easily accomplished using circular sawcuts normal to the specimen faces to produce a chevron [2]. The sharp crack is created by stable crack growth which fractures the chevron region prior to instability. The fine microstructures of advanced ceramics insure that the notch-tip stress field will sample a representative amount of material, even when the specimen is only a few millimetres thick.

An added advantage of the notched-disk specimen is that the crack plane can be rotated around the disk axis (Fig. 1*a*) to provide any desired combination of tension/longitudinal-shear loading on the notch [3], and the crack plane can also be rotated around the diameter to provide a range of tension/transverse-shear loading [4]. Because of this flexibility, a number of mixed-mode failure envelopes have been generated for brittle materials, e.g. [5], and stable crack growth has been measured in glass under combined shear and tension loadings [6]. Disks with straight-through notches have also been used to study mixed-mode failure in polymer-bonded materials [7,8].

This paper reports experiments using chevron-notched disks to measure fracture toughness of bonds, with at least one of the substrates being partially stabilized zirconia (PSZ). Opening-mode fracture toughness values for bonds, as well as that of the bulk interlayer used in PSZ/PSZ joints, were also determined using straight-notched bend bars (Fig. 1*b*). Because the interlayer has different elastic constants than the substrate, bonds present unusual analytical problems, even for the case of a material bonded to itself. Although the loading system may produce only a Mode I stress field in a homogeneous material, the

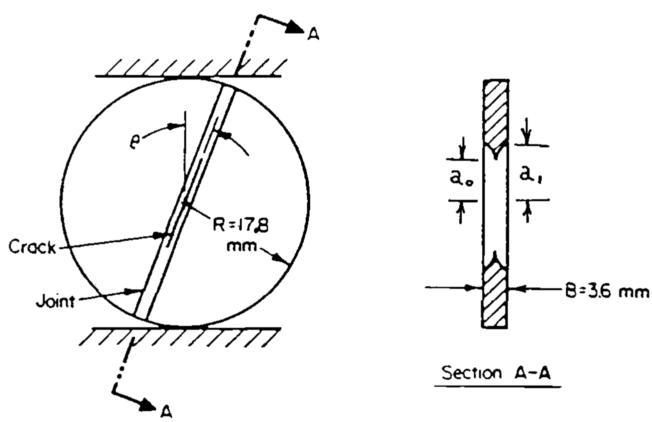

FIG. 1*a*—*Chevron-notch bonded disk specimen.*

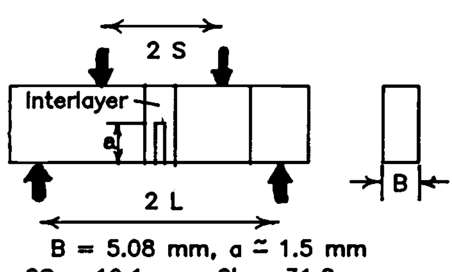

FIG. 1*b*—*Straight-notch bend bar.*

elastic mismatch at a bimaterial interface gives rise to mixed-mode stress intensity factors for a crack [9,10], and the local stress intensities generally have to be determined using the finite-element method. However, if the crack lies along the interlayer/substrate interface, a stress-intensity approach is not sufficient to characterize the local stress fields at the crack tip, and a strain-energy-release rate approach is found to be superior [11].

In the special case where two pieces of the same material are joined and there is a crack at the interlayer/substrate interface, Hutchinson [11] has used an asymptotic analysis to show that

$$G = (1 - \nu_1^2)(K_I^2 + K_{II}^2)/E_1 \tag{1}$$

where K_I and K_{II} are the far-field stress intensity factors for a homogeneous material of the same geometry and loading as the bonded specimen, while E_1 and ν_1 are the elastic constants of the substrate. The term, mixity, is denoted Ψ and is used to describe the relative shear and tensile contributions to G

$$\Psi = \tan^{-1}(K_{II}/K_I) + \omega \tag{2}$$

where ω is a known function of the elastic moduli of the substrate and bonding material and is evaluated in Ref *11*. For homogeneous specimens $\omega = 0$.

Failure envelopes can be generated either as relations between G and Ψ or as relations between K_{iq} and K_{iiq}, which are used in this paper to denote far-field stress intensity components at failure. The term, K_{Ic}, is used for opening-mode toughness, even though there is no ASTM standard for ceramics. As an example of the alternative methods of presenting the data, consider the previously reported results for alumina [5] and porcelain [12], which Fig. 2*a* shows to satisfy the relation

$$K_{iq}/K_{Ic} + (K_{iiq}/CK_{Ic})^2 = 1 \tag{3}$$

where $C = 2$ for these materials was obtained by curve-fitting the data. Figure 2*b* is a replot of the same data in G/Ψ space. The solid line in Fig. 2*b* is

$$G/G_{Ic} = 1 + (\Psi/\Psi_0)^2 \tag{4}$$

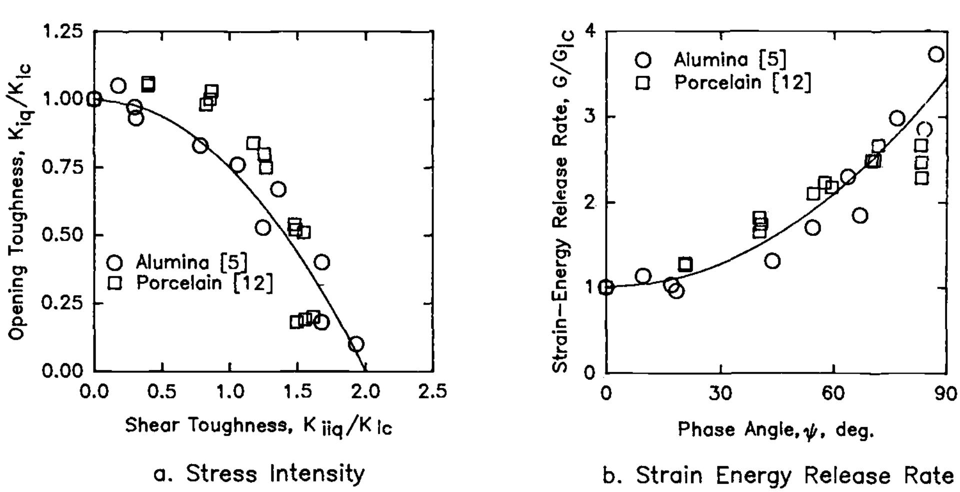

FIG. 2—*Mixed-mode failure envelopes for ceramics.*

where $\Psi_0 = 1$ radian for alumina and porcelain. Even though Eq 4 will be used to describe failure envelopes, far-field stress intensity values will be retained for reporting the relative fracture resistance at the endpoints (cracks stressed completely in tension or shear) because of the difficulty of obtaining a physical feeling for Ψ_0 or ω.

The object of this paper is to show that the chevron-notched disk specimen provides a simple, inexpensive method for evaluating mixed-mode toughness of bonds. As an initial step in developing a bonded-joint fracture-toughness test, preliminary results are reported on the measurement of toughness of zirconia/zirconia (PSZ/PSZ) and zirconia/nodular-cast-iron (PSZ/NCI) bonds, loaded both in tension and in shear. Since partially stabilized zirconia and nodular cast iron have very similar elastic moduli (202 and 163 GPa, respectively) and thermal expansion coefficients (10.3 and 14.9 $\times$ 10^{-6}/°C, respectively), residual stresses arising from bonding were found not to have any significant influence on the fracture toughness parameters [*13*] and have been neglected here.

Experimental Procedure

The disk specimen for measuring toughness of zirconia/zirconia bonds consisted of two semicircular pieces of partially stabilized zirconia (PSZ) bonded along the diameter (Fig. 1) using a thin glass-ceramic/powdered-zirconia interlayer that was molten at the joining temperature. The thickness of the bonds ranged between 100 and 150 μm. Zirconia/iron bonds were fabricated using high-quality ferritic nodular cast iron (NCI) and a braze alloy containing Ag, Cu, Ti, and In to produce bonds between 15 and 30 μm thick. Further details on bonding procedures are found in Ref *13*.

The notches were approximately 250 μm wide and were machined using a diamond-impregnated wafering wheel approximately 20 mm in diameter. Care was taken to align the notch along the center line of the joint. The notch-length ($2a$) to diameter ($2R$) ratio (a/R) was typically 0.5. Specimens were loaded in compression at a cross-head rate of 0.85 μm/s. Thin cardboard was used to inhibit crushing by cushioning the specimen/loading-platen interface. Crack-mouth-opening displacements were monitored using a strain-gage extensometer. Figure 3*a* illustrates the experimental arrangement.

For chevron-notched disk specimens, with $\theta = 0$, it has been shown [*2*] that fast fracture occurs after the crack has grown stably and completely through the chevron notch. This behavior was also inferred from markings observed on the fracture surface of bonded specimens. Therefore, the critical crack length at fracture (a_c) was set equal to a_1 for calculation of the critical stress intensity factor. On the other hand, for $\theta \neq 0$, fast fracture occurred when the crack had propagated only partway through the chevron notch. In this mixed-mode case, fracture involved complete deviation of the crack plane from the original chevron-notch plane towards the loading points (see Fig. 3*b*).[4] Therefore for $\theta \neq 0$, stress intensity factors were based on measured crack lengths at the onset of fast fracture; typically a_c/R ranged from 0.42 to 0.46 for $\theta \neq 0$ and was 0.5 for $\theta = 0$. The full thickness, B, of the specimen was used when calculating mixed-mode stress intensity factors using Atkinson's formulae [*14*], even though fast fracture occurred when the crack had grown only partially through the chevron notch in the case of $\theta \neq 0$. The reasoning was that the sudden kinking of the crack at the point of instability consumed the entire thickness, so that the strain energy release rate must be based on the full thickness of the specimen. Although concerns may exist that standard through-crack formulae are not applicable for kinked cracks, and for cracks that have not grown through the entire chevron region, we believe that the

[4]The only exception was the case of PSZ/NCI joints, where there was the normal crack-path deviation on the PSZ side; on the NCI side the crack propagated along the NCI interface instead of deviating towards the load point because of the much higher toughness of NCI.

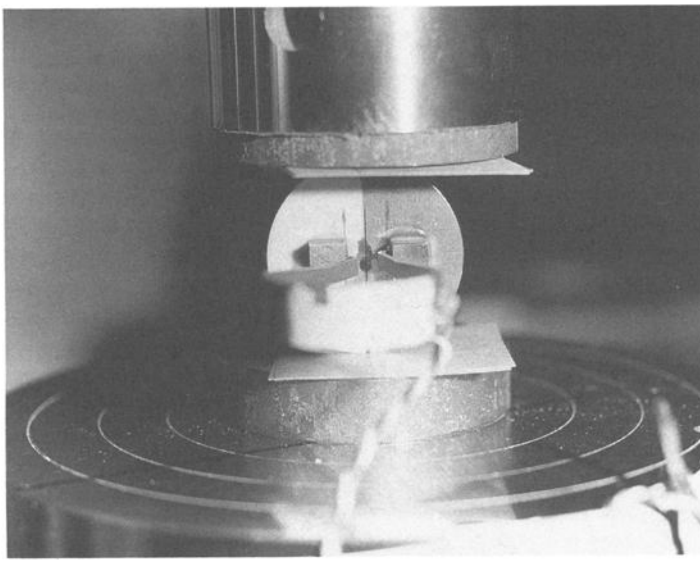

FIG. 3*a*—*Loading arrangement for PSZ/NCI bonded disk specimen with gage attached for crack-mouth-opening displacement measurement.*

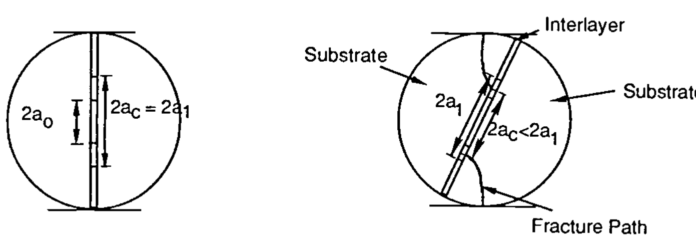

FIG. 3*b*—*Schematic diagram illustrating fracture path for opening-mode and mixed-mode fracture* ($2a_0$ *and* $2a_1$ *are point and end of chevron, respectively;* $2a_c$ *is instability length).*

approach that we have used here provides rational characterization of the crack tip at the point of fast fracture.

Specimens were oriented to produce nominal Mode I loading (notch parallel to load line), nominal Mode II loading (notch at an angle of approximately 23° to the load line), or nominal mixed-mode loading. In addition to the disk specimens, straight-notched four-point-bend bars were used to determine nominal Mode I fracture toughness for comparison with the disk-specimen results.

Results and Discussion

Failure Envelopes

Figure 4 shows a typical load/crack-mouth-opening-displacement curve for the cracked-disk specimen. From finite-element analysis it was found that stress intensity was typically within 2% of Atkinson's analytical solution for a homogeneous cracked disk [*14*]. The good match was due to the similarity of elastic modulus between PSZ (200 GPa) and the thin

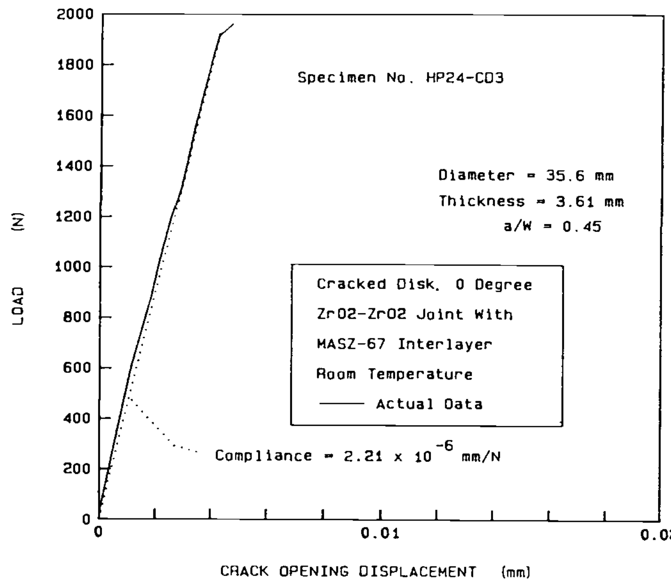

FIG. 4—*Typical load/displacement plot.*

ceramic interlayer (130 GPa) for PSZ/PSZ bonds and between PSZ and nodular cast iron (163 GPa) for the PSZ/cast-iron bonds.

Figure 5 shows the bond data on a G/G_{Ic} versus Ψ plot, where $G_{Ic} = 20.9$ J/m^2 for the PSZ/PSZ as measured independently using bend bars fabricated from bulk interlayer material, since the crack path in bonded specimens ran only through interlayer material. For PSZ/NCI joints $G_{Ic} = 238$ J/m^2 was used, as measured independently on a bend bar by cutting a notch into the reaction zone of the zirconia. A reason for this location was that cracks in PSZ/NCI joints ran largely through the reaction zone of the zirconia.

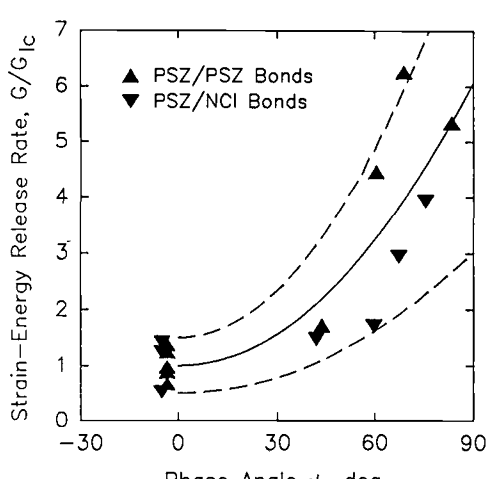

FIG. 5—*Mixed-mode failure envelope for ceramic bonds.*

The solid line in Fig. 5 is Eq 4 with $\Psi = 0.7$ radians, a smaller value (steeper curve) than for monoliths, while the dashed lines represent 50 and 150% of the solid line, reflecting the scatter usually associated with fracture of bonds.

Far-Field Mode I and Mode II Toughness

Table 1 summarizes the fracture toughness results in terms of far-field stress intensities at failure. For the PSZ/PSZ bonds the bulk interlayer data were obtained from notched bend bars machined from separately cast interlayer blocks. The PSZ/PSZ joint toughnesses were approximately half that of the PSZ substrate.

Figure 6 compares pure opening mode toughness (K_{Ic}) values obtained using the disk specimen with those obtained using other test geometries for both homogeneous and bonded specimens. This figure includes values given in Table 1, along with those tabulated in Ref *15*. As shown in Fig. 6, the Mode I (K_{Ic}) data for bonds are consistent with experience with monolithic ceramics, which has shown that fracture toughnesses measured using the disk specimen are comparable to those measured using more common technical ceramic designs, such as the double-torsion and chevron-bend specimens [*15*]. The two types of bonds exhibit opposite trends; the bend-bar result is higher than the disk for PSZ/PSZ bonds and lower than the disk for PSZ/NCI bonds. Note that these latter data can be plotted on this brittle-material graph since fractography revealed that zirconia occupied at least half of the fracture surface for all PSZ/cast-iron joints, the balance of the surface being the PSZ/braze-metal interface.

Table 2 reports the literature data while Fig. 7 compares tensile and shear toughness results, with the upper dashed line representing a 2:1 ratio ($K_{IIc} = 2\ K_{Ic}$) and the lower

TABLE 1—*Experimental results for bonded zirconia specimens used for test-method comparison.*

	Toughness, $MPa\sqrt{m}$		
	Tension[a]	Tension[b]	Shear[c]
	BULK MATERIALS		
NCI	92 [*16*][d]	...	...
PSZ (as-received)	9.7	8.6	...
PSZ (heat treated)[e]	5.6	...	...
MASZ-67 interlayer[f]	2.1	...	...
MASZ-80 interlayer[f]	2.9	...	...
	PSZ/PSZ BONDS		
MASZ-67	2.5	2.1	5.0[g]
MASZ-80	3.2	2.5	...
	PSZ/CAST-IRON BONDS		
Braze interlayer	5.9	6.6	16.2[h]

[a]Four-point bend.
[b]Diametrically compressed disk.
[c]Diametrically compressed disk.
[d]Compact specimen.
[e]Heated to produce the temperature/time history during bonding.
[f]The interlayer material is designated MASZ-XX, with XX being the weight percent of zirconia powder.
[g]Interpolated from K_I versus K_{II} plot.
[h]Extrapolated from K_I versus K_{II} plot.

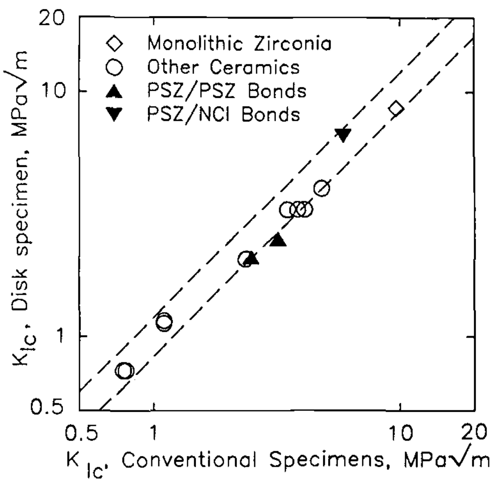

FIG. 6—*Comparison of fracture toughness test methods.*

dashed line representing a 1:1 ratio, or $K_{IIc} = K_{Ic}$. The data divide roughly into two families. Chevron-notch diametral compression results lie closer to the higher ratio because fracture instability occurs after some stable crack growth for this notch configuration ($a_1 > a_c > a_0$, see Fig. 3*b*). The associated rubbing of opposing crack faces under Mode II loading prior to instability shields the tip from the full applied shear stress intensity. In addition to the chevron-notched disks, the notched block result on mortar exhibits a high K_{IIc}:K_{Ic} ratio [*17*]. The author of that paper noted that the fracture surfaces were so rough that interference of the relative motion of the opposing faces occurred, strongly implying a shielding effect.

The rubbing effect can be ameliorated by using a straight-through notch [*15*] with the potential penalty of producing artificially high K_{Ic} values due to reduced acuity. This point was examined in Ref *15*, which reported the same K_{Ic} values for both a blunt notch and a chevron crack in porcelain specimens. As can be seen in Table 2, the Mode II:Mode I ratio is close to unity for porcelain, presumably because blunt notches was used for both opening and longitudinal shear loads, and rubbing was eliminated.

It is not clear that rubbing is undesirable. On the one hand, specimens free of rubbing provide actual notch-tip stress intensity values, while rubbing induces crack-tip screening and a resultant apparent elevation of stress intensity at failure. On the other hand, rubbing is characteristic of the sharp crack under Mode II loading and thus is a real feature of crack growth. Thus, there is a dilemma in mixed-mode fracture toughness test development, which cannot be resolved at present: either use a blunt notch, which can lead to nonconservative K_{Ic} values due to acuity effects, or use a sharp crack, which may lead to nonconservative K_{IIc} values due to crack-face interference.

Rubbing provides one reason why the critical G value (strain energy release rate) increases with an increasing ratio of shear:tension loading. Other possible contributions can be expected on the basis of microscopic examination [*13,27*]. In the PSZ/PSZ couple, mixed-mode fracture was accompanied by growth of the crack into the higher-toughness zirconia substrate during fracture of the chevron region. In the PSZ/NCI couple, shear of the braze metal was observed, indicating a plasticity contribution to fracture energy.

TABLE 2—*Published K_{Ic}/K_{IIc} data for ceramics ($MPa\sqrt{m}$).*

Material[a]	K_{Ic}	K_{IIc}	Reference
	STRAIGHT-THROUGH NOTCHED DISKS; COMPRESSION		
Glass	0.73	0.90	[18]
Graphite	0.689	0.762	[19]
Graphite	0.724	0.830	[19]
Graphite	0.943	1.09	[19]
Graphite	0.814	0.886	[19]
Plaster	0.130	0.148	[19]
Marble	0.933	1.05	[19]
Cement paste	0.271	0.298	[20]
Porcelain	1.13	1.3	[15]
WC/Co	13.4	15	[21]
	CHEVRON-NOTCHED DISKS; COMPRESSION		
Alumina	3.35	6.7	[5]
Zirconia	7.3	11	[5]
Zirconia	4.2	6.5	[5]
Zirconia	5.4	9.0	[5]
PSZ/PSZ bonds	2.1	5.0	This work
PSZ/cast-iron bonds	6.6	16.2	This work
	NOTCHED PLATES; TENSION		
Glass	0.51	0.41	[22][b]
Glass	0.75	0.60	[23][c]
	NOTCHED BLOCKS; SHEAR		
Mortar	0.7	1.82	[17]
Concrete	2.25	2.58	[24]
Concrete	2.25	2.46	[24]
Concrete	2.24	2.58	[24]
	SLOTTED TUBES; TORSION		
Silicon nitride	6.76	5.32	[25]
	SURFACE-CRACKED PLATES; BENDING + PRESSURE		
Glass	1.1	1.16	[26]

[a]Multiple entries per material indicate that several different compositions and/or heat treatments were used.
[b]Units are not clearly given; the ratio of the toughnesses is correct, however.
[c]Absolute values of toughness not reported; K_{Ic} was estimated and K_{IIc}/K_{Ic} ratio digitized from graph.

Conclusions

The notched diametrally compressed disk provides a simple, inexpensive method for evaluating bonds in ceramic/ceramic and ceramic/metal systems. As is the case for monolithic disks, the opening mode fracture toughness (K_{Ic}) values obtained using the disk are comparable to the notched-bend specimen. There are two additive components of apparent shear toughness (K_{IIc}) for the chevron-notch specimen fabricated from a monolithic material; one component arises from the crack-tip stress intensity while the second arises from crack-tip screening associated with rubbing. While the screening component may depend on material, a typical value is about equal to K_{IIc} for an unscreened crack. Bonded specimens introduce added complications for all specimen geometries; thermal-expansion mismatches lead to residual stresses, and elastic-modulus mismatches lead to a second component of screening. Additional differences arise from crack deviation from the interlayer and, in the case of the metal/ceramic bond, plastic deformation of the braze metal.

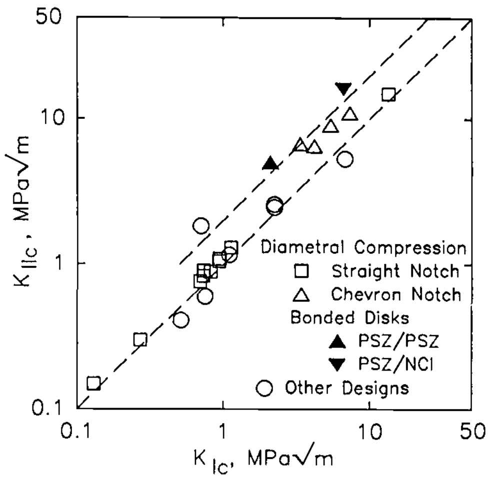

FIG. 7—*Mixed-mode fracture toughness of various brittle materials.*

Acknowledgments

This work was performed under Oak Ridge National Laboratory subcontract 86X-SB046C, the prime sponsor being the U.S. Department of Energy. Expert experimental help was provided by P. R. Held. S. L. Swartz and BSM collaborated in the PSZ/PSZ bonding, while Y. Park and J. A. Cawley (both of the Ohio State University) and D. A. Hauser (Edison Welding Institute) fabricated the PSZ/NCI bonds. We also wish to thank J. Ahmad and C. F. Shih for the finite element analysis of the bonded specimen. The nodular cast iron was kindly provided by R. Salzbrenner and K. A. Sorenson of Sandia National Laboratory.

References

[1] Darvell, B. W., "Uniaxial Compression Tests and the Validity of Indirect Tensile Strength," *Journal of Material Science*, Vol. 25, 1990, pp. 757–780.
[2] Shetty, D. K., Rosenfield, A. R., and Duckworth, W. H., "Fracture Toughness of Ceramics Measured by a Chevron-Notched Diametral Compression Specimen," *Journal of the American Ceramic Society*, Vol. 68, 1985, pp. C325–C327.
[3] Singh, D. and Shetty, D. K., "Microstructural Effects on Fracture Toughness of Polycrystalline Ceramics in Combined Mode I and Mode II Loading," *Transactions of ASME, Journal of Engineering of Gas Turbine Power*, Vol. 111, 1989, pp. 174–180.
[4] Rosenfield, A. R. and Duckworth, W. H., "Combined Tension/Transverse Shear Fracture of Glass," *International Journal of Fracture*, Vol. 32, 1987, pp. R59–R62.
[5] Singh, D. and Shetty, D. K., "Fracture Toughness of Polycrystalline Ceramics in Combined Mode I and Mode II Loading," *Journal of the American Ceramic Society*, Vol. 72, 1989, pp. 78–84.
[6] Singh, D. and Shetty, D. K., "Subcritical Crack Growth in Soda-Lime Glass in Combined Mode I and Mode II Loading," *Journal of the American Ceramic Society*, Vol. 73, 1990, pp. 3597–3606.
[7] Schmidt, R. A., Ahmad, J., and Rosenfield, A. R., "Analytical and Experimental Evaluation of Joining Ceramic Oxides to Ceramic Oxides and Ceramic Oxides to Metal for Advanced Heat Engines," *Ceramic Technology for Advanced Heat Engines Project*, Report ORNL/TM-10388, Oak Ridge National Laboratory, 1988, pp. 214–223.
[8] Wang, J.-S, and Suo, Z., "Experimental Determination of Interfacial Toughness Curves using Brazil-Nut Sandwiches," *Acta Metallurgica and Materia*, Vol. 38, 1990, pp. 1279–1290.
[9] Shih, C. F. and Asaro, R. J., "Elastic-Plastic Analysis of Cracks on Bimaterial Interfaces: Part I—Small-Scale Yielding," *Journal of Applied Mechanics*, Vol. 55, 1988, pp. 299–316.

[10] Atkinson, C., "Cracks in Bimaterial Interface—An Overview," in *Advances in Fracture Research*, Vol. 4, K. Salama et al., Eds., Pergamon, Oxford, 1989, pp. 3053–3061.

[11] Hutchinson, J. W., "Mixed Mode Fracture Mechanics of Interfaces," Report MECH-139, Harvard University, 1989.

[12] Rosenfield, A. R., "Mixed-Mode Fracture of Steel and Ceramics," *Fracture Behaviour and Design of Materials and Structures*, D. Firrao Ed., EMAS, Warley, UK, 1990, pp. 501–515.

[13] Hopper, A. T., et al., "Analytical and Experimental Evaluation of Joining Ceramic Oxides to Ceramic Oxides and Ceramic Oxides to Metal for Advanced Heat Engine Applications," Final Report from Battelle to Oak Ridge National Laboratory on Subcontract 86X-SB046C, July 1990.

[14] Atkinson, C., Smelser, R. E., and Sanchez, J., "Combined Mode Fracture via the Cracked Brazilian Disk Test," *International Journal of Fracture*, Vol. 18, 1984, pp. 279–291.

[15] Rosenfield, A. R., "Fracture of Brittle Materials under a Simulated Wear Stress System," *Journal of the American Ceramic Society*, Vol. 72, 1989, pp. 2117–2120.

[16] Salzbrenner, R. and Crenshaw, T. B., "Multiple Specimen J-Integral Testing at Intermediate Rates," *Experimental Mechanics*, 1990, pp. 217–233.

[17] Davies, J., "Fracture Behaviour of Mortar in Shear-Compression Field," *Journal of Material Science Letters*, Vol. 6, 1987, pp. 879–881.

[18] Shetty, D. K., Rosenfield, A. R., and Duckworth, W. H., "Mixed-Mode Fracture in Biaxial Stress State: Application of the Diametral-Compression (Brazilian Disk) Test," *Engineering Fracture Mechanics*, Vol. 26, 1987, pp. 825–840.

[19] Awaji, H. and Sato, S., "Combined Mode Fracture Toughness Measurement by the Disk Test," *Transactions, ASME, Journal of Engineering Materials Technology*, Vol. 100, 1978, pp. 175–182.

[20] Yatomi, C., Fujii, K., and Nakagawa, K., "Combined Stress Hypothesis for Mixed-Mode Fracture Criterion," *Engineering Fracture Mechanics*, Vol. 32, 1989, pp. 881–888.

[21] Yarema, S. Y., Ivantskaya, G. S., Maistrenko, A. L., and Zboromirskii, A. I., "Crack Development in a Sintered Carbide in Combined Deformation of Types I and II," *Strength of Materials*, Vol. 16, 1984, pp. 1121–1128.

[22] Panasyuk, V. V., Berezhnitskiy, L. T., and Kovchik, S. Y., "Propagation of an Arbitrarily Oriented Rectilinear Crack During Extension of a Plate," *Prikladi Mekhanika*, Ukranian Academy of Sciences, Vol. 1, 1965, pp. 48–55.

[23] Kordisch, H., Rietmuller, J., and Sommer, E., "The Strain Energy Density Criterion—Investigations for its Applicability," *Proceedings of the Symposium on Absorbed Specific Energy/Strain Energy Density*, G. C. Sih et al., Eds., 1984, pp. 33–43.

[24] Carpinteri, A., et al., "The Four Point Shear Test on Single Notched Specimens: An Experimental and Numerical Analysis," *Fracture Behaviour and Design of Materials and Structures*, D. Firrao, Ed., EMAS, Warley, UK, 1990, pp. 667–675.

[25] Petrovic, J. J., "Mixed-Mode Fracture of Hot-Pressed Si_3N_4," *Journal of American Ceramic Society*, Vol. 68, 1985, pp. 348–355.

[26] Ikeda, K. and Igaki, H., "Mixed-Mode Fracture Criterion in Soda-Lime Glass," *Japan Society of Mechanical Engineers International Journal*, Series I, Vol. 33, 1990, pp. 84–88.

[27] Majumdar, B. S. and Ahmad, J., "Fracture of Ceramic-Metal Joints: Zirconia/Nodular Cast Iron System," *Proceedings*, TMS/ASM Symposium on *Metal-Ceramic Joints*, Detroit, MI, October 1990.

James P. Lucas[1]

Fracture Toughness of Composite Laminates and Metallic Materials Using a Modified CNSB Specimen

REFERENCE: Lucas, J. P., "**Fracture Toughness of Composite Laminates and Metallic Materials Using A Modified CNSB Specimen,**" *Chevron-Notch Fracture Test Experience: Metals and Non-Metals, ASTM STP 1172,* K. R. Brown and F. I. Baratta, Eds., American Society for Testing and Materials, Philadelphia, 1992, pp. 74–88.

ABSTRACT: Mode I fracture toughness was determined for several unidirectional, continuous fiber reinforced polymer matrix composites and a monolithic homogeneous alloy using a modified chevron-notch short bar (CNSB) specimen. The modified short bar specimen consisted of two dissimilar materials and is, consequently, referred to as the *hybrid short bar* (HSB) specimen. The HSB specimen comprised the host material that contained the chevron notch ligament through which fracture occurred during testing. Bonded to both sides of the host material were metallic adherends. Similar geometric dimensions were maintained between the monolithic (i.e., standard) and the hybrid short bar specimens. Maintaining geometric consistency between the specimens enabled standard short bar fracture toughness analysis techniques to be used in the data reduction of all specimens. Using *metal/laminate* HSB specimens, Mode I delamination fracture toughness was determined for graphite epoxy and graphite thermoplastic polymer matrix composite laminates. Also, plane strain chevron notch fracture toughness, K_{Iv}, was determined for 6061-T651 Al using a metal/metal HSB specimen. The *metal/metal* HSB specimen consisted of Al 6061-T651 as the host material onto which Ni adherends were bonded via electroplating. Using a low-temperature electroplating process in fabricating the metal/metal HSB specimens provided two significant benefits. First, a strong metallurgical bond was achieved between the dissimilar materials of the metal/metal HSB specimen. Second, during the plating process, modification of the host material microstructure was insignificant. Maintaining consistent microstructures between the metal/metal HSB and the monolithic short bar (SB) specimens permitted direct comparison of experimental fracture toughness test results. After correcting the HSB fracture toughness data to account for effects due to *compliance mismatch* of dissimilar materials, good agreement was observed between the toughness results obtained using hybrid short bar and monolithic short bar specimens.

KEY WORDS: fracture toughness, delamination toughness, monolithic short bar, hybrid short bar, composite laminates

Understanding stable crack growth behavior in materials is of great significance in providing knowledge which can aid the materials selection process and in promoting confidence in design and analysis of fail-safe structures. Linear elastic fracture mechanics (LEFM) provides an analytical approach that enables the design of engineering materials and structures using flaw tolerance analysis. From LEFM analysis, the critical stress intensity parameter, K, which is related to the product of the critical flaw size and the applied stress of the material, can be determined, thus enabling failure limits to be calculated for materials and

[1]Associate Professor, Department of Metallurgy Mechanics and Materials Science, Michigan State University, East Lansing, MI 48824-1126. Formerly: Senior Member of Technical Staff, Organic and Composite Materials Division, Org. 8311, Sandia National Laboratories, Livermore, CA 94551-0969.

structures. Standard test methods [*1,2*] exist for determining the stress intensity parameter of fracture toughness that employ various specimen geometries. Yet, for nearly all specimen geometries, a necessary requirement is that the crack length be determined as a prerequisite to assessing fracture toughness or critical stress intensity factor of materials. Often, crack length measurement can be an arduous process depending on the specimen geometry and/or test methods. Consequently, by alleviating the necessity to measure crack length, fracture toughness testing can be simplified and made more economical. Approximately a decade ago, a fracture toughness testing technique was introduced by Barker [*3–5*] which utilized a specimen design that permitted fracture toughness determination without measurement of the crack length. The chevron notch short bar (CNSB) specimen met the criterion in that the fracture toughness could be determined without explicit knowledge of the crack length. The use of the CNSB also alleviated the need for specimen precracking. Using CNSB specimens allowed fracture toughness to be determined essentially by knowing only the applied maximum load.

Characterization of fracture in materials is frequently assessed by the analysis of fracture toughness results. Often times, however, limited material availability, non-standard geometry, and the inability to conveniently measure the crack length preclude fracture toughness determination by more conventional test methods. Alternative test methods are sometimes deemed necessary to obtain fracture toughness of materials when such *compatibility* issues arise for testing by more established methods. Attempting to address testing incompatibility issues, an alternative test specimen was fabricated and evaluated.

In this investigation, a modified version of the monolithic chevron notch short bar (SB) specimen was utilized to determine fracture toughness of a metallic alloy and of resin matrix composite laminates. The configuration of the modified short bar specimen (i.e., hybrid short bar, HSB) consists of the host material, for which the fracture toughness is determined, bonded to metallic adherends. More specifically, the delamination fracture toughness was determined for continuous carbon fiber reinforced thermoset and thermoplastic matrices composite laminates; and, plain strain chevron notch fracture toughness (K_{Iv}) was obtained for 6061-T651 Al alloy. Fabrication, testing, and data reduction and analysis associated with the HSB specimen are discussed.

Experimental Procedure

Metal/Laminate HSB Specimens

Three different composite laminates were examined. One laminate was a graphite fiber reinforced epoxy (Gr/Ep) composite which was supplied by Fiberite Corporation. The laminate layup was unidirectional, 16 plies, 2.2 mm thick consisting of T300 fibers (elastic modulus, E = 148 GPa) in a 934 epoxy matrix. The second laminate was 3.6 mm thick containing 24 plies of unidirectional AS4 fibers (E = 131 GPa) in a 938 epoxy matrix. The final laminate examined was a graphite fiber reinforced thermoplastic (Gr/Tp) composite containing IM6 fibers (E = 270 MPa) in a PEEK (polyether-etherketone) resin matrix.

The first stage of fabrication of metal/laminate hybrid short bar test specimens involved adhesively bonding metal adherends (6061-T6 aluminum) to the composite laminates to form hybrid stock panels (HSP) from which test specimens were subsequently extracted by conventional machining methods. Components of the hybrid stock panel are shown in Fig. 1. Using a hydraulic laminating press, the composite laminate was adhesively bonded to grooved, anodized, 12.5 mm thick 6061-T6 aluminum platens. Adhesive film placed on both sides of the laminate provided sufficient adhesive bonding integrity. Moreover, the adhesive bonding integrity of the adherends to the laminate was enhanced by mechanical locking provided by

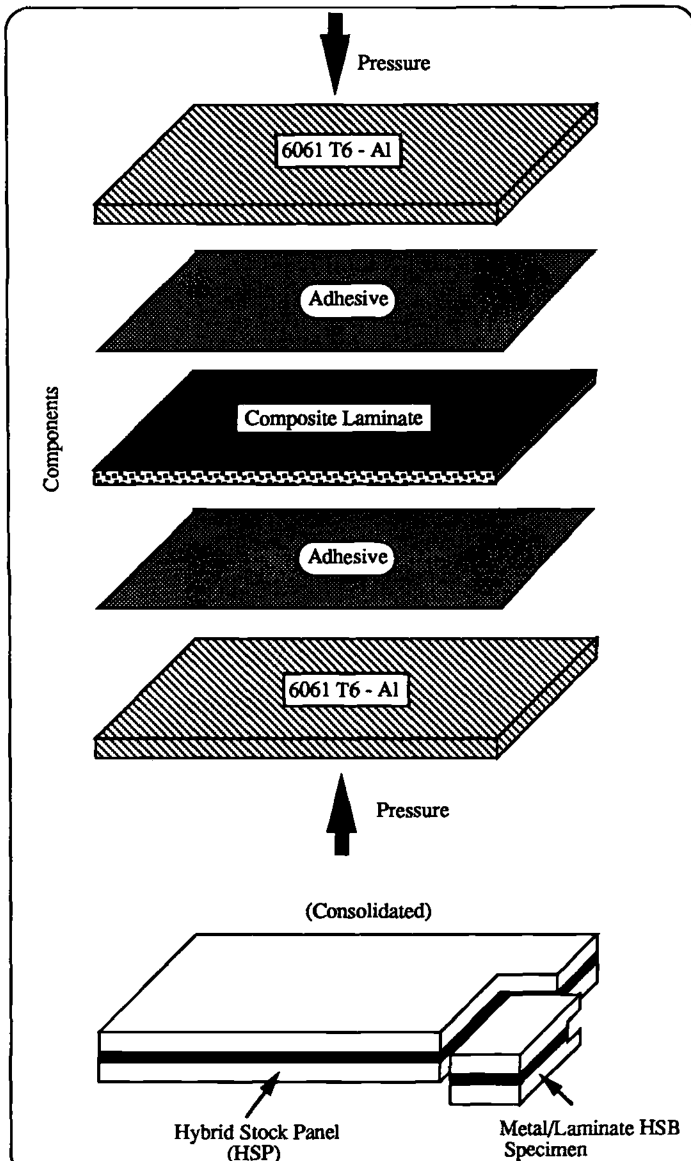

FIG. 1—*The hybrid stock panel (HSP) components are shown prior to consolidation and after consolidation. The metal/laminate HSB specimen is machined from the HSP.*

adhesive-filled grooves (~1.3 mm deep, 0.6 mm, and angled 60° with respect to the plane of the laminate) that were machined in the Al platens. Consolidation of the HSP took place under a pressure of 50 MPa at 125°C (400 K) for 5.1×10^3 s).

After consolidation, metal/laminate hybrid short bar specimens were machined from the hybrid stock panel. A metal/laminate HSB test specimen is exhibited in Fig. 2. The chevron V-notch ligament was machined into the host (laminate) material of the HSB specimen with

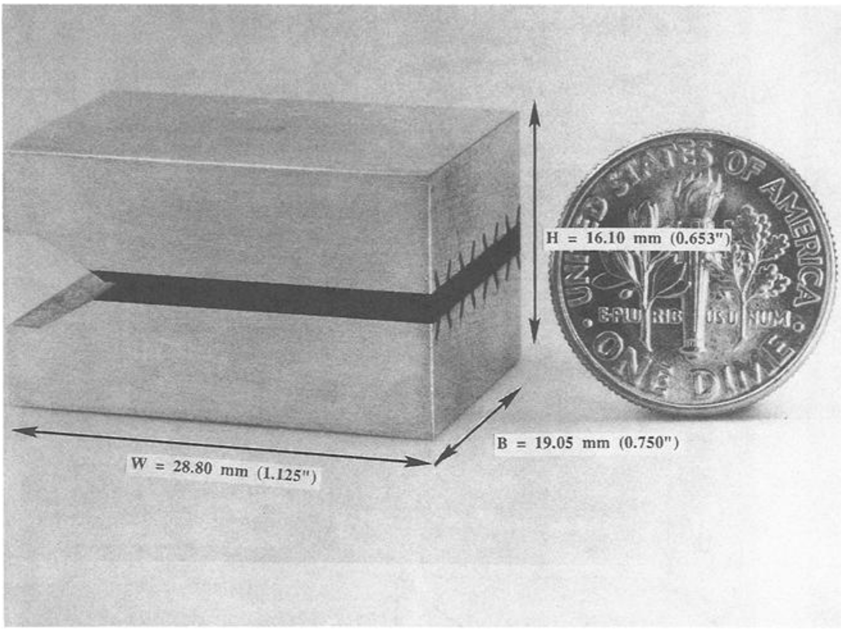

FIG. 2—*The metal/laminate HSB specimen is shown containing a carbon fiber resin matrix composite laminate as the host material and Al adherends.*

a slitting saw using a fine grit diamond-impregnated blade. The dimensions of the metal/laminate HSBs were: length (W) = 28.8 mm, width (B) = 19.1, and height (H) = 16.1 mm (Fig. 2).

Metal/Metal HSB Specimens

The metal/metal hybrid short bar specimen consisted of electrodeposited nickel adherends with 6061-T651 Al as the host material. Electrodeposition of thick Ni coating was chosen over other bonding techniques because a strong metallurgical bond was achievable between the dissimilar materials without significantly altering the microstructure of the Al host material. Surface preparation of the host material prior to electrodeposition involved surface grinding with 600-grit abrasive paper, followed by a solvent rinse, and hot vapor degreasing in trichloroethylene. The final phase of surface preparation included electroplating of copper, 0.002 mm thick, on the Al substrate. The thin copper coating was required in order to bond the Ni coating (adherends) to the Al alloy substrate (host material).

Thick (10 mm) Ni coating was deposited on the Al substrate in a heated (54°C, 327 K) Ni sulphamate plating bath in which the plating current density was 2.15×10^{-4} A/mm^2. These deposition parameters produced a Ni plating rate of approximately 1 mil/h or 4.2×10^{-4} mm/min. Upon reaching a minimum required thickness (~6.4 mm) for the Ni coating, the electrodeposition process was terminated and excess coating was machined off to meet the dimensional requirements of the standard SB specimen. Schematically depicted in Fig. 3 are various stages in the fabrication process leading to the metal/metal hybrid short bar specimen. Metal/metal HSB specimens were fabricated from the electrodeposited Al/Ni lamina construction by electrospark discharge machining. The dimensions of the metal/metal HSB specimens were as follows: B = 12.7 mm, W = 19.1 mm, and H = 11.1 mm (Fig. 4).

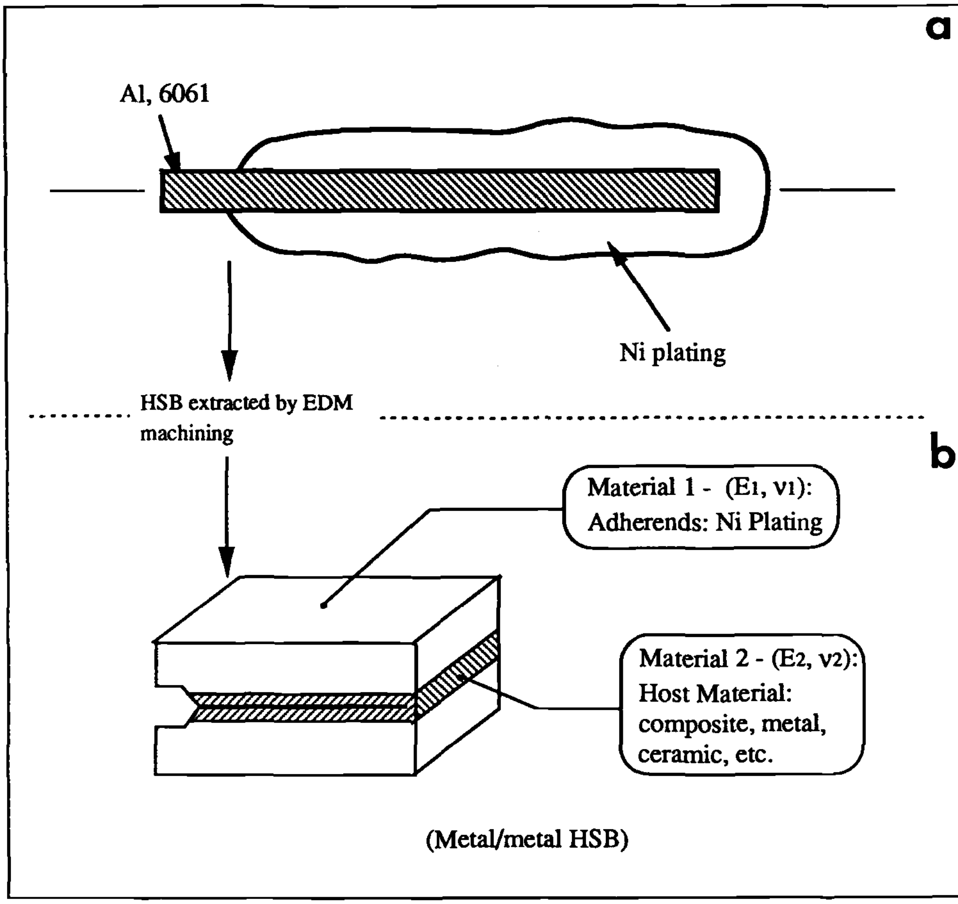

FIG. 3—*A schematic diagram of the electroplating process shows that* (a) *thick Ni coating is electrodeposited onto Al (host material) and it shows* (b) *a metal/metal hybrid short bar specimen machined from the electrodeposited Ni/Al material.*

CNSB Theory and Test Method

The theory of fracture toughness as related to the chevron notch short bar method was analyzed thoroughly by Barker [*3–5*] and others [*6*]. The expression for CNSB fracture toughness K_{Iv} is derived from basic energy principles. The energy required to advance a crack an increment, Δa, is given as

$$\Delta W = G_{Ic} \cdot b \cdot \Delta a \tag{1}$$

where G_{Ic} is the strain energy release rate or fracture energy and b is the instantaneous crack front width at crack length, $a + \Delta a$. Irrecoverable work, ΔW, when the crack advances an amount Δa can be expressed in terms of the elastic compliance change while loading the material. Thus irrecoverable work is expressed as

$$\Delta W = \frac{P^2 \Delta C}{2} \tag{2}$$

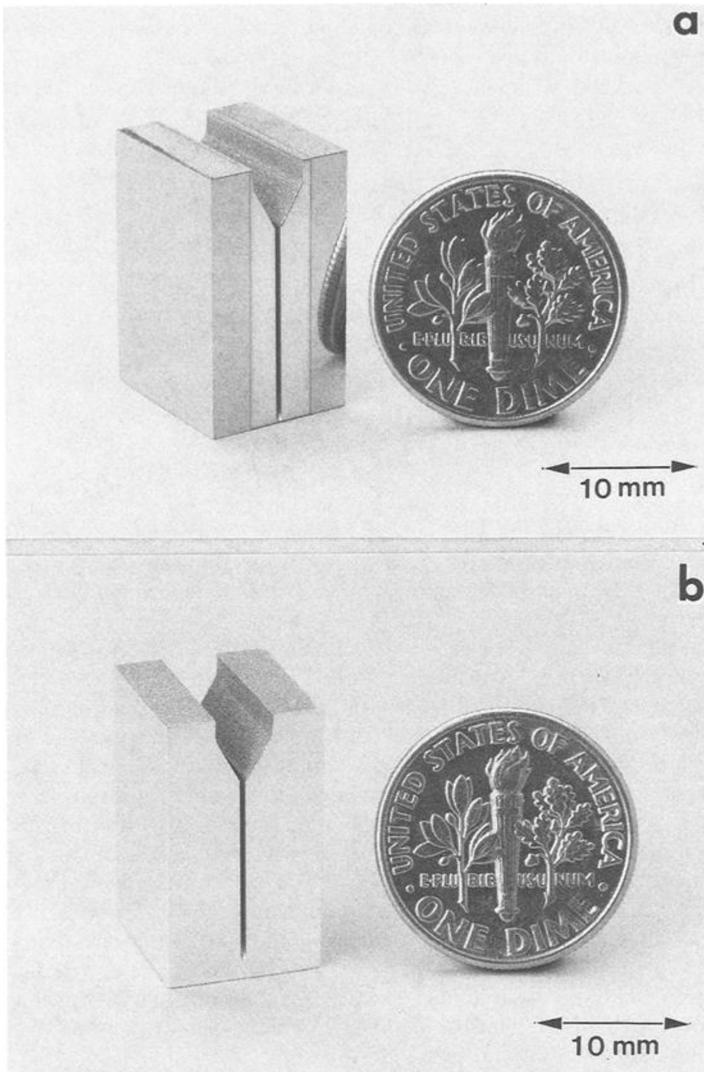

FIG. 4—*A metal/metal HSB specimen is shown* (a) *comprising 6061-T651 Al as the host material with electrodeposited, thick Ni adherends. The monolithic 6061-T651 Al SB specimen is shown* (b) *for comparison.*

where P is the applied load and ΔC is the incremental change in compliance due to crack advance, Δa. Combining Eqs 1 and 2 gives the strain energy release rate as the classical compliance equation [7] from linear elastic fracture mechanics (LEFM), That is,

$$G_{\mathrm{Ic}} = \frac{P^2}{2b} \cdot \frac{\partial C}{\partial a} \tag{3}$$

The strain energy release rate is expressed in terms of the stress intensity factor. Note that the fracture toughness is denoted as K_{Iv} to be consistent with the recent standard test procedure (ASTM E 1304-89) adopted for chevron notch short bar specimen testing. Therefore the energy release rate is given by

$$G_{\mathrm{Ic}} = \frac{K_{\mathrm{Iv}}^2(1 - \nu^2)}{E} \tag{4}$$

where E is the elastic modulus and ν is Poisson's ratio. Combining Eqs 3 and 4 gives the stress intensity [*3,4*]:

$$K_{\mathrm{Iv}} = \frac{P(1 - \nu^2)^{-1/2}}{B^{3/2}} \cdot f\left(\frac{a}{B}\right) \tag{5}$$

where B is the width of the specimen and

$$f\left(\frac{a}{B}\right) = \left(\frac{B}{2b} \cdot \frac{\partial(CEB)}{\partial(a/B)}\right)^{1/2} \tag{6}$$

The expression in parentheses is a dimensionless factor depending only on the specimen geometry. For the short bar geometry ($W/B = 1.45$), the value of $f(a/B) = 22.5$. For the short bar method, often, only the maximum load is needed to determine the fracture toughness, provided that LEFM criteria are satisfied. With the short bar geometry, it has been shown [*3,4*] that a critical crack length is reached under stable crack growth conditions that is coincident with the occurrence of the maximum load.

During testing of the HSB specimen, load is applied normal to the plane of the propagating crack front in the V-notch ligament (i.e., Mode I loading). All tests were performed in air at room temperature at 37% relative humidity. Tests were run on a commercially available chevron notch short bar test system. The specimen mouth opening displacement rate was 5.8×10^{-4} mm/s. The mouth-opening displacement was measured with a clip gage positioned in the grip slot of the SB specimen. A typical load-displacement profile obtained from testing a metal/laminate HSB specimen is shown in Fig. 5. The load-displacement response is linear on initial loading, corresponding to the elastic compliance of the test specimen before sharp crack growth initiation. However, steadily increasing the load causes deviation of the load/displacement profile from linearity, indicating the onset of stable crack growth in the chevron notch ligament. The crack grows initially in a stable manner, reaching a critical length under the influence of a high stress intensity field. At the point of maximum load, the fracture toughness can be determined using Eq 5.

Results and Discussion

Fracture Toughness of Metal/Metal HSB Specimens

As noted earlier the metal/metal hybrid CNSB specimen consisted of the host material 6061-T651 Al with Ni adherends. The experimental fracture toughness results of monolithic 6061 Al [*8*] are listed in Table 1 for both the monolithic and the hybrid short bar test specimens. Clearly, the raw data in Table 1 show that significantly higher fracture toughness values were obtained for HSB specimens than for monolithic aluminum SB specimens. Since the magnitude of fracture toughness values obtained using HSB was distinctly different from those values obtained using monolithic SB specimens, this matter was investigated in attempt to isolate and to explain the reason for the toughness disparity. Subsequent to fracture toughness testing, an examination of the crack profile and the fracture surfaces of the

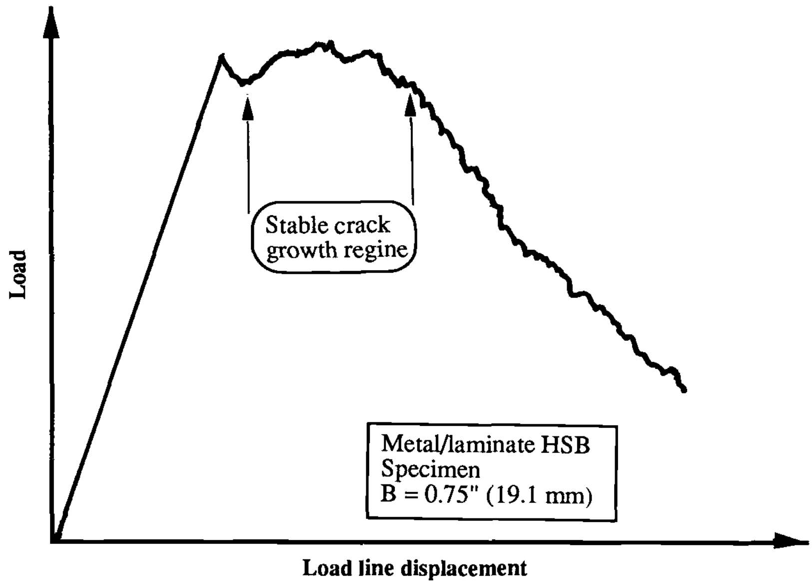

FIG. 5—*A typical load versus displacement profile is shown for metal/laminate hybrid short bar specimen. Stable crack growth in the laminate is demonstrated.*

TABLE 1—*Fracture toughness results obtained for monolithic and metal/metal short bar specimens. The HSB fracture toughness results in the right hand column have been corrected for compliance mismatch differences.*

Fracture Toughness of Metallic SB Specimens			
Specimen #ID	K_{Iv} (Monolithic) (MPa $\sqrt{m}$)	K_{Iv} (Hybrid) (MPa $\sqrt{m}$)	K_{Iv} (Al)[a] (MPa $\sqrt{m}$)
M1	34.3	...	...
M2	34.3	...	...
M3	33.0	...	...
M4	34.2	...	...
M5	32.9	...	...
M5	33.8	...	...
H1	...	43.0	34.0
H2	...	43.0	34.0
H3	...	42.2	33.4
H4	...	42.1	33.3
H5	...	43.5	34.3
H6	...	42.4	33.4
Avg. K_{Iv}	33.8	42.7	33.7
Std. Deviation	33.8 ± 0.7	42.7 ± 0.5	33.7 ± 0.4

[a]Corrected for compliance difference: $[E(\text{host})/E(\text{hybrid})]^{1/2}$.

monolithic SB and HSB specimens was conducted using light-optics and SEM microscopy. The crack profile and the fracture surfaces characteristics were remarkably similar between the two specimen types (Fig. 6). Examining the fracture surfaces, it is evident that the primary void growth size associated with fractured precipitates was virtually identical for both specimens. Also, shear ligaments failure mode on the fracture surface due to microvoid coalescence appeared to be quite similar. There was also generally consistency in the tortuosity of the crack propagation paths. Such similarity in fracture features suggested that fracture modes and microfracture mechanisms were consistent for both specimen types during the fracture process. Consequently, the observed disparity in K_{Iv} results was not caused by differences in the crack tip fracture mechanisms relative to the specimen design. In addition, for the metal/metal HSB specimen, the crack tip plastic zone size (R_p = 0.86 mm) was well within the confines of the Al host material as delineated by its thickness, T = 5 mm. Since the T/R_p ratio ~ 6, the plastic zone size was not affected (constrained) by the elastic moduli mismatch between the host material and the adherends. Thus it was surmised that neither the crack tip plasticity nor the crack tip *stress* environment experienced during fracture was responsible for the observed fracture toughness difference in the HSB and the monolithic SB specimens. It was concluded therefore that the crack tip microfracture process had essentially no effect on the disparity in fracture toughness.

However, it is recognized that the strain energy release rate G_{Ic} for the aluminum (a material property) is the same regardless of whether G_{Ic} values were obtained using the elastic moduli mismatched HSB specimen or monolithic modulus, short bar (MSB) specimen. Since the strain energy release rate, G, is related to the stress intensity factor, K, by $K = (EG)^{1/2}$, the fracture toughness of the 6061 aluminum material should be the same irrespective of test method and geometry. Therefore an adjustment factor was required in order to attain consistency between the HSB and monolithic SB fracture toughness data. Higher fracture toughness was manifested by a higher maximum load, P_{max}, observed for the HSB specimens. The difference in the maximum load between HSB and MSB specimens is illustrated by load-opening displacement profiles of Fig. 7. The increased fracture toughness observed for the HSB specimen was due to the compliance difference between the specimen arms of the monolithic and hybrid short bar specimens. Appropriately treating the arms of the SB specimens as cantilever beams, the compliance of the monolithic and the hybrid SB specimens can be compared by determining the rigidity modulus, EI, where E is the elastic modulus and I is area moment of inertia. Since the hybrid test specimen consisted of Ni adherends [elastic moduli mismatch: E_{Ni} (190 GPa) ν_{Ni} (0.35) > E_{Al} (69 GPa) ν_{Al} (0.3)], EI for the composite hybrid specimen will be greater than the monolithic Al test specimen. Also, an effective elastic modulus can be found from the rigidity modulus, EI, of the hybrid (composite) SB specimen. The fracture toughness of a hybrid specimen consisting of dissimilar materials (E_1,ν_1 and E_2,ν_2) can be corrected for the compliance difference by following an elastic analysis similar to that proposed by Wang et al. [9]. For a composite double cantilever beam (DCB) specimen, the analysis [9] suggested that the fracture toughness of the host material was dependent on the elastic moduli ratio between the host material and adherend material of the specimen. Hence, in order to determine the fracture toughness of the host material, the observed toughness values of the hybrid (composite) specimen had to be modified by an adjustment factor equivalent to the square root ratio of the respective elastic (effective) moduli of the dissimilar materials. The fracture toughness of the host material of the hybrid specimen is given by the following expression

$$K_{Iv}(\text{host}) = \left(\frac{E(\text{host})}{E(\text{hybrid})}\right)^{1/2} \cdot K_{Iv}(\text{hybrid}) \tag{7}$$

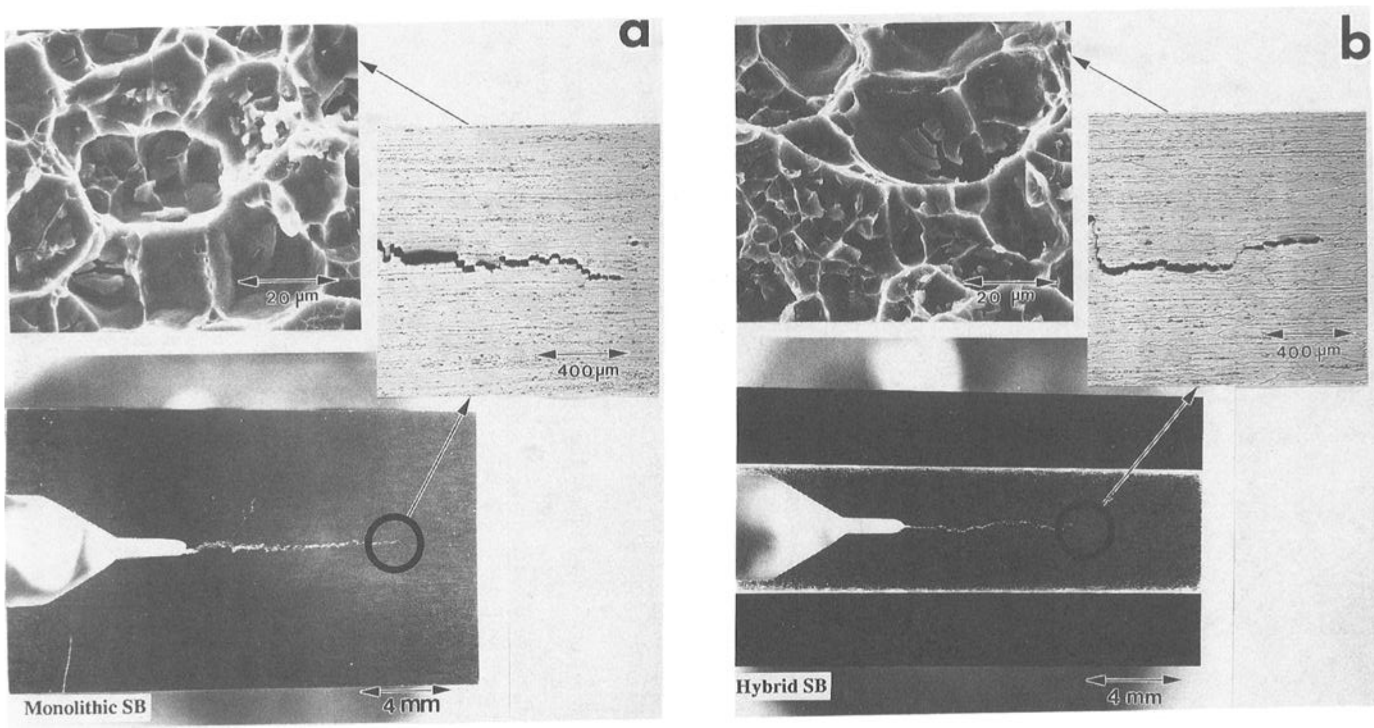

FIG. 6—*Micrographs of* (a) *the monolithic SB and* (b) *metal/metal HSB specimen are shown. Optical and SEM micrographs show that in the crack tip region the crack propagation profile and the microfracture mechanisms are similar.*

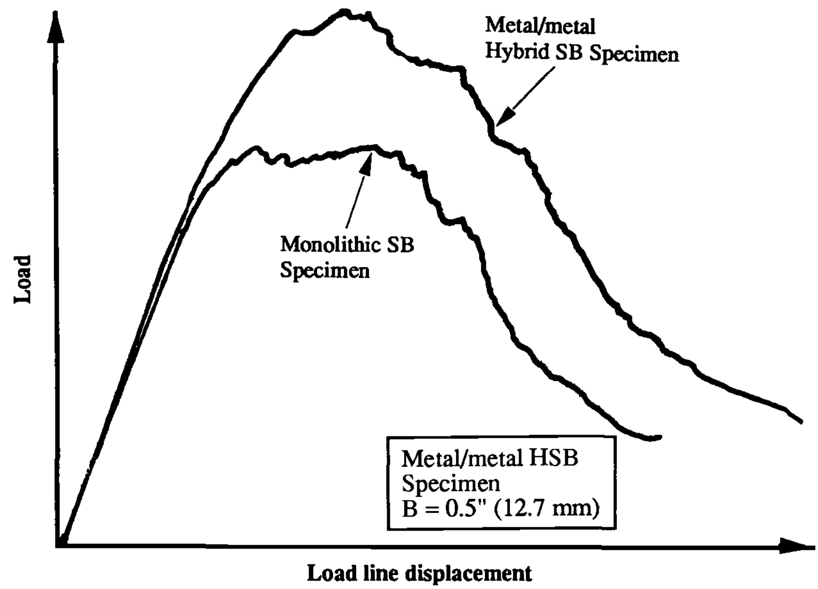

FIG. 7—*Typical load versus displacement profile is shown for a monolithic short bar specimen and for a metal/metal hybrid short bar specimen with the same specimen geometries. These profiles demonstrate that the maximum load for the HSB specimen is greater than the maximum load for the monolithic SB specimen. (Note: The elastic slopes of the load-displacement curves were electronically forced to appear similar in the graphical presentation; however, in actuality the elastic slopes are quite dissimilar due to compliance mismatch of the HSB specimen. However, this procedure does not affect the maximum loads observed for the respective specimens. The maximum load value is critical in determining the* K_{Iv}.)

where E(host) is the elastic modulus of the host materials (i.e., elastic modulus of Al and E(hybrid) is the effective elastic modulus of the hybrid beam (arm) determined from the equivalent EI of the hybrid specimen. Note that the arm of the hybrid test can be analyzed as a composite beam [*10*]. Unlike E(host), E(hybrid) will change as the thickness ratio between the host and adherend materials changes.

Fracture Toughness of Metal/Laminate HSB Specimens

Fracture toughness results obtained for metal/laminate HSB specimens are given in Tables 2 to 4. Listed in Tables 2 to 4 are K_{Iv} results for T300/934, AS4/938, and IM6/PEEK resin matrix composites, respectively. The fracture toughness values for the laminate, K_{Iv}(laminate), were calculated from experimentally observed HSB fracture toughness values, K_{Iv}(hybrid, using the compliance correction factor approach discussed previously for metal/metal HSB specimens. More specifically, the arm of the metal/laminate HSB specimen was treated as a composite beam of dissimilar materials (E_1,ν_1 and E_2,ν_2) using simple beam theory [*10*] analysis to calculated E(hybrid). Applying Eq 7 to the metal/laminate HSB specimen shows that the fracture toughness of the laminate is be given by the relationship

$$K_{Iv}(\text{laminate}) = \left(\frac{E(\text{laminate})}{E(\text{hybrid})}\right)^{1/2} \cdot K_{Iv}(\text{hybrid}) \tag{8}$$

where E(laminate) is the transverse orthotropic modulus of the laminate and E(hybrid) is

TABLE 2—*Fracture toughness results for a T300/934 graphite epoxy laminate.*

Fracture Toughness, T300/934			
Fiber orientation	K_{Iv} (Hybrid)$^{+}$ (MPa $\sqrt{m}$)	K_{Iv} (laminate)$^{++}$ (MPa $\sqrt{m}$)	$G_{Ic}{}^{++}$ (J/m^2)
0°	1.61	0.79	65
0°	1.52	0.75	61
0°	1.42	0.74	56
0°	1.61	0.79	65
Avg. K_{Iv}	1.58	0.77	62

$^{+}$Hybrid test specimen contains unidirectional fiber laminate (2.2 mm thick) with 6061 Al adherends.
$^{++}$Corrected for compliance difference.

TABLE 3—*Fracture toughness results for an AS4/938 graphite epoxy laminate.*

Fracture Toughness, AS4/938			
Fiber orientation	K_{Iv} (Hybrid)$^{+}$ (MPa $\sqrt{m}$)	K_{Iv} (laminate)$^{++}$ (MPa $\sqrt{m}$)	$G_{Ic}{}^{++}$ J/m^2
0°	2.0	1.17	131.1
0°	2.2	1.30	164.1
0°	2.1	1.23	146.9
0°	2.3	1.36	179.6
0°	2.2	1.30	164.1
0°	2.1	1.19	137.5
	Avg. = 2.15	1.31	166.3

$^{+}$Unidirectional fiber laminate (3.6 mm thick), 6061 Al adherends hybrid specimen.
$^{++}$Data corrected for compliance difference.

TABLE 4—*Fracture toughness results for an IM6/PEEK graphite thermoplastic laminate.*

Fracture Toughness, IM6/PEEK			
Fiber orientation	K_{Iv} (Hybrid)$^{+}$ (MPa $\sqrt{m}$)	K_{Iv} (laminate)$^{++}$ (MPa $\sqrt{m}$)	$G_{Ic}{}^{++}$ J/m^2
0°	5.1	3.1	995
0°	5.1	3.1	995
0°	4.9	2.9	876
0°	5.1	3.1	995
0°	4.9	2.9	876
0°	5.0	3.0	933
Avg. K_{Iv} Std. Deviation	5.0 ± 0.1	3.0	933

$^{+}$Unidirectional fiber laminate (3.5 mm thick), 6061 Al adherends hybrid specimen.
$^{++}$Data corrected for compliance difference.

the effective modulus of the composite beam calculated from the rigidity modulus, EI, of the hybrid composite beam.

The fracture energy of the laminate, G_{Ic}, was subsequently determined from the fracture mechanics relationship that exists between K versus G. That is,

$$G_{Ic}(\text{laminate}) = \frac{K_{Iv}^2(\text{laminate})}{E'} \tag{9}$$

where E' is the plane strain transverse modulus of the composite laminate.

Test data in Tables 2 to 4 show that the K_{Iv} values observed for the HSB specimen are highly reproducible but higher than the toughness results determined for the laminate host material. When the HSB fracture toughness data are corrected for compliance differences using the square root of the moduli ratio factor, the fracture toughness and fracture energy results of the laminate were found to be somewhat lower than fracture toughness results obtained in previous investigations using the SB method [*11*] or other conventional test methods like those using DCB and CN (center notched) specimens [*12–14*]. For comparison, fracture toughness (energy) results from several investigations [*12,13,15–23*] are shown in Table 5 for brittle thermoset composites and ductile thermoplastic composites. The modified CNSB test method tended to give conservative delamination fracture toughness and fracture energy values for composite laminates. Nonetheless, from this investigation it is apparent that employing the modified CNSB specimen is viable for determining delamination fracture toughness in composite laminates, and for determining plain strain fracture toughness in metallic materials.

Conclusions

1. Plane strain fracture toughness was determined for 6061-T651 aluminum alloy using a metal/metal hybrid short bar specimen. Also, delamination fracture toughness was determined for composite laminates using metal/laminate hybrid short bar specimen.

TABLE 5—*Comparison of Mode I delamination fracture energy for graphite fiber reinforced thermosets and thermoplastics composite laminates.*

Composite Laminate Fiber/matrix	G_{Ic} J/m^2	K_{Ic} or K_{Iv} MPa $\sqrt{m}$	Test Method	Reference
T300/934	90	...	DCB	12
T300/934	103	...	DCB	13
T300/5208	100	...	DCB	15
T300/1034C	77	0.96	DCB	16
T300/5208	93	...	DCB	17
T300/934	65	0.79	CNSB	This Study
AS4/938	166	1.31	CNSB	This Study
AS4/PEEK	1770	2.24	DCB	18
AS4/PEEK	1560	...	DCB	19
AS4/PEEK	1120	...	RS	16
AS4/PEEK		3.6	CN	20
AS4/PEEK	1800	5.3	DCB	21
IM6/PEEK	2150	...	DCB	22
CF/PEEK	2000	5.0	DCB	23
IM6/PEEK	995	3.1	CNSB	This Study

DCB = double cantilever beam, CN = center notch, RS = rail shear, CNSB = chevron notch short bar.

2. In general, fracture toughness results obtained using hybrid short bar specimens were consistently higher fracture toughness results obtained using monolithic short bar specimens. When compliance correction was made for hybrid short bar specimens resulting from increased stiffening by adherends due the elastic moduli mismatch, fracture toughness values were found to be in reasonable agreement with values obtained using monolithic SB test specimens.

Acknowledgments

The support of A. Gardea and T. Sage is gratefully appreciated for their assistance in specimen preparation and metallography. An expression of gratitude is also extended to J. Hachman and R. Johnson for their assistance in electroplating specimens. This investigation was supported by DOE through Contract DE-AC04-76-DP00789.

References

[*1*] ASTM E 399-74, "Standard Test Method for Plane Strain Fracture Toughness of Metallic Materials," 1974.
[*2*] ASTM E 813-81, "J_{Ic}, A Measure of Fracture Toughness," 1989.
[*3*] Barker, L. M., "A Simple Method for Measuring Plane Strain Fracture Toughness," *Engineering Fracture Mechanics*, Vol. 9, 1977, pp. 361–369.
[*4*] Barker, L. M., "Compliance Calibration of a Family of Short Rod and Short Bar Fracture Toughness Specimens," *Engineering Fracture Mechanics*, Vol. 17, No. 4, 1983, pp. 289–312.
[*5*] Barker, L. M., "Theory for Determining *K* from Small Non-LEFM Specimens Supported by Experiments on Aluminum," *International Journal of Fracture*, Vol. 15, No. 6, 1979, pp. 515–536.
[*6*] *Chevron-Notch Specimens: Testing and Analysis, ASTM STP 855*, J. H. Underwood, S. W. Frieman, and F. I. Baratta, Eds., American Society for Testing and Materials, Philadelphia, 1984.
[*7*] Irwin, G. R. and Kies, J. E., "Critical Energy Rate Analysis of Fracture Strength," *Welding Journal*, Vol. 33, 1954, pp. 193–198.
[*8*] Morrison, J., Gough, P., and KarisAllen, K. J., "Comparison of Chevron-Notched Specimen Types for Fracture Toughness Testing of Aluminum," *Journal of Testing and Evaluation*, Vol. 17, No. 1, 1989, pp. 14–19.
[*9*] Wang, S. S., Mandell, J. F., and McGarry, F. J., "An Analysis in Crack Tip Stress Field in DCB Adhesive Fracture Specimens," *International Journal of Fracture*, Vol. 14, No. 1, 1978, pp. 39–58.
[*10*] Roark, R. J. and Young, W. C., *Formulas for Stress and Strain*, 5th ed., McGraw-Hill, New York, 1975.
[*11*] Lucas, J. P. and Odegard, B. C., "Moisture Effects on Mode I Interlaminar Fracture Toughness of a Graphite Thermoplastic Matrix Composite," in *Advances in Thermoplastic Matrix Composite Materials, ASTM STP 1044*, American Society for Testing and Materials, Philadelphia, 1989, pp. 231–247.
[*12*] Saghizdel, H. and Dharan, C. H. K., "Delamination Fracture Toughness of Graphite and Aramid Epoxy Composites," *Journal of Engineering Materials and Technology*, Vol. 108, No. 4, 1986, pp. 290–295.
[*13*] Garg and Ishai, "Hygrothermal Influence on Delamination Behavior of Graphite/Epoxy Laminates," NASA Technical Memorandum 85895, 1983.
[*14*] Wang, Q. and Springer, G. S., "Moisture Absorption and Fracture Toughness of PEEK Polymer and Graphite Fiber Reinforced PEEK," *Journal of Composites Materials*, Vol. 23, 1989, pp. 434–447.
[*15*] Hunston, D. L. "Composite Interlaminar Fracture: Effect of Matrix Fracture Energy," *Composites Technology Review*, Vol. 6, No. 4, 1984, pp. 176–180.
[*16*] Donaldson, S. L., "Fracture Toughness Testing of Graphite/Epoxy and Graphite/PEEK Composites," *Composites*, Vol. 16, No. 2, 1985, pp. 103–111.
[*17*] Lee, S., Gaudert, P., Dainity, R., and Scott, R. F., "Characterization of the Fracture Toughness Property (G_{Ic}) of Composite Laminates Using Double Cantilever Beam Specimen," *Polymer Composites*, Vol. 10, 1989, pp. 305–312.
[*18*] Crick, R. A., Leach, D. C., Meakin, P. J., and Moore, D. R., "Interlaminar Fracture Morphology of Carbon Fibre/PEEK Composite," *Journal of Materials Science*, Vol. 22, 1987, pp. 2094–2104.

[19] Gillespie, J. W., Carlson, L. A., and Smiley, A. J., "Rate Dependent Mode I Interlaminar Crack Growth Mechanisms in Graphite/Epoxy and Graphite/PEEK," *Composites Science and Technology*, Vol. 28, 1987, pp. 1–15.
[20] Talbott, M. F., Springer, G. S., and Berglund, L. A., "The Effects of Crystallinity on the Mechanical Properties of PEEK Polymer and Graphite Fiber Reinforced PEEK," *Journal of Composites Materials*, Vol. 21, 1987, pp. 1056–1081.
[21] Hine, P. J., Brew, B, Duckett, R. A., and Ward, I. M., "The Fracture Behaviour of Carbon Fibre Reinforced Poly(Ether Etherketone)," *Composites Science and Technology*, Vol. 33, 1988, pp. 35–71.
[22] Davies, P., Cantwell, W., and Kausch, H. H., "Measurement of Initiation Values in IM6/PEEK Composites," *Composites Science and Technology*, Vol. 35, 1989, pp. 301–313.
[23] Friedrich, K., Gogeva, T., and Fakirov, S., "Thermoplastics Impregnated Fiber Bundles: Manufacturing of Laminates and Fracture Mechanics Characterization," *Composites Science and Technology*, Vol. 33, 1988, pp. 197–220.

Applications to Metallic Materials

Herbert J. Mueller[1]

Fracture Toughness and Fractography of Corroded Dental Amalgams

REFERENCE: Mueller, H. J., "**Fracture Toughness and Fractography of Corroded Dental Amalgams,**" *Chevron-Notch Fracture Test Experience: Metals and Non-Metals, ASTM STP 1172*, K. R. Brown and F. I. Baratta, Eds., American Society for Testing and Materials, Philadelphia, 1992, pp. 91–109.

ABSTRACT: The plane strain short-rod fracture toughness of six dental amalgams after having been aged in air or exposed to 0.1% sodium chloride for 2 years was investigated. Amalgams were also corroded by polarization. Their fractured chevron surfaces were characterized by scanning electron microscopy. Results revealed an effect from sample diameter. The 6.35 mm diameter high-copper amalgams had a fracture toughness 20–37% higher than that for 11.28 mm diameter size. Only one amalgam, one with indium revealed significantly higher toughness, this being 16% after immersion, whereas the other amalgams showed no significant differences between air and solution conditioning. Increases in toughness were also obtained by polarization-induced corrosion, which after excessive charge transfer, decreased toughness. Chlorine was detected within regions of the fractured chevron planes indicating diffusion to a depth of 300 μm and more. It was thought that chlorides were deposited along Ag-Hg matrix phase grain boundaries inhibiting their decohesive rupturing thereby enhancing toughness.

KEY WORDS: plane strain, fracture toughness, short-rod, chevron notch, crack jump, smooth crack advance, load versus mouth opening displacement, fractography, microstructure, dental amalgam, corrosion, polarization

Dental amalgam is a restorative material used for the filling of teeth. Deterioration, corrosion, and property changes occur due to environmental conditioning with the oral bioelectrolytes. Bulk and edge (margin) fractures occur with amalgam restorations requiring either repair or replacement.

The property of fracture toughness has been used to a limited extent as an indicator of the mechanical usefulness of amalgam as a restorative material [*1–3*]. The effects of deterioration and corrosion upon possible changes in fracture toughness of amalgam have not been investigated. Since amalgam restorations are continually exposed to the oral electrolytes, localized deterioration and corrosion occur routinely. Susceptible locations include interfacial crevice regions with tooth structure where stagnant conditions and differential aeration cells prevail. Some corrosion of the adjacent amalgam at the tooth-amalgam interface is beneficial, since a better sealing of the interface from the ingress of electrolytes occurs. In some instances more of the amalgam bulk becomes involved with deterioration and corrosion. In this regard, the conventional amalgams which have a low copper content are most susceptible due to the presence of the corrosion prone, tin-mercury phase. The higher copper-content amalgams, either dispersed phase or of a single particle type are more resistant to corrosion.

[1]Research Associate, Council on Dental Materials, Instruments and Equipment, American Dental Association, Chicago, IL 60611.

Microindentation [4], three-point bending [1,2], and chevron notched short-rod techniques [3] have been used to assess fracture toughness of amalgam. The microindentation technique appears to offer some favorable features, since it is possible to assess fracture toughness within surface regions that have undergone deterioration and corrosion. The chevron notch sample geometry also offers advantages, since the chevron notches can provide a means to localize the corrosion along the edges of the chevron plane, and in more advanced stages of corrosion to include most of the material contained within the chevron plane. By choosing a short rod sample with smaller diameter, bulk material contained within the chevron plane is reduced thereby increasing the percentage of corroded material. The chevron notch sample also permits easy fractographic analysis of the fractured sample halves. With the microindentation technique this is not possible, only polished cross sections are capable of analysis.

The purpose of this project was to investigate whether corrosion influences the fracture toughness of amalgam so that better predictions of amalgam's time to fracture can be made.

Materials and Methods

Amalgams and Sample Processing

Table 1 summarizes details of the amalgam alloy powders used. Six commercial alloys representing two conventional, one dispersed phase, and three single particle high-copper varieties were included.

Amalgams were processed from the powders by conventional dental procedures and by following the manufacturers' recommended instructions. The powders and recommended percentages of mercury were mechanically mixed in a plastic capsule with an amalgamator operating at 70 Hz for times from 5 to 10 s. An amalgamator operates in a back-and-forth motion over several inches of travel, thereby intimately contacting the mercury with the surface of the alloy particles. Chemical reactions begin immediately generating silver-mercury, copper-tin and tin-mercury phases. The unset amalgam plastic masses were packed into a 6.35 mm diameter stainless steel mold and placed under a load of 445 N with plungers for a duration of 2 min commencing at 3 min after the start of mixing. Mercury released while under load was collected and weighed.

Fracture Toughness

Samples—Figure 1 details the short-rod sample geometry used. It is noted that a square end groove design instead of a tapered design was used. Following removal of the samples

TABLE 1—*Amalgam alloy powders used.*

Material	Source	Type	Composition, wt%			DTS,[a] MN m^{-2}
			Ag	Sn	Cu	
Sybraloy	Kerr	Single	40.0	31.2	28.8	48.2 [6]
Unison	J & J[b]	Single	56.7	28.6	14.7	. . .
Spheraloy[c]	Kerr	Conven.	71.2	25.2	3.3	60.7 [6]
Dispersalloy[c]	J & J	Dual	69.3	18.1	18.5	48.2 [6]
Indiloy[d]	Shofu	Single	60.0	22.0	13.0	44.8 [6]
True Dentalloy	S.S. White	Conven.	70.4	25.8	3.8	63.4 [7]

[a]24 hour.
[b]Johnson & Johnson.
[c]Also contains up to 1% Zn.
[d]Also contains 5% In.

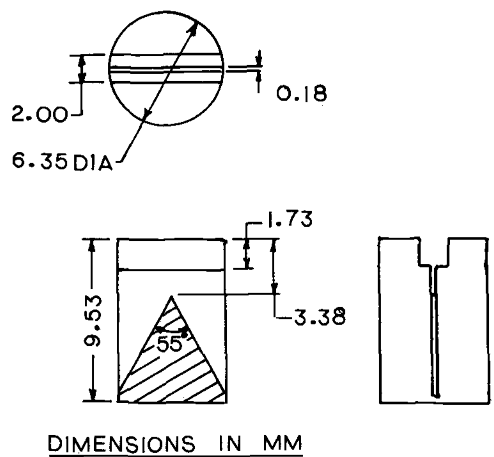

FIG. 1—*Short-rod sample geometry.*

from the mold, the lengths were ground to size on wet silicon carbide abrasive papers and ground with diamond wheels with a water soluble cutting oil. A Fractometer specimen saw model 4901 (Terra Tek) was used to cut the chevron slots and end groove. The samples were thoroughly rinsed with water followed by alcohol prior to drying.

Samples for Corrosion by Polarization—These samples were prepared in a slightly modified manner from above explanation. Samples measuring 13–15 mm in length were initially prepared. In the end opposite the ground end groove, a No. 3–48 tapped hole about 3 mm in length was formed, which served to hold the sample and make electrical contact onto and to a stainless steel electrode rod (Corrosion Cell System, Model 9700, Princeton Applied Research). Following abrasion with No. 600 grit paper, the surface of the sample was coated with several layers of a masking resin (MicroMask Stop-Off Lacquer, Michigan Chrome). After drying the sample was again ground with the 0.18 mm thick diamond wheel but only to remove masking resin overlaying the chevron slots. Hence, the samples for polarization were only exposed to electrolyte along the two chevron slots. After polarization, the resin was mechanically stripped and the samples made to length at the end containing the tapped hole.

Testing—The short-rod plane strain fracture toughness K_{IcSR} similar to but not exactly the same as K_{Iv}, which is in accordance with ASTM Standard Test Method for Plane-Strain (Chevron-Notch) Fracture Toughness of Metallic Materials (E 1304-89), was determined with a Fractometer II Model 2101A machine (Terra Tek) [*5*]. The details were the same as those used in a related report [*3*]. Applied load versus mouth opening displacement (MOD) plots were obtained for each sample during testing. Unloading-reloading cycles were initiated throughout the tests. For samples fracturing via a smooth crack advance, two cycles which bracketed the critical slope ratio, $r_c = 0.55$, were obtained. The criterion for plane strain conditions (ASTM E 1304) is

$$K_{Iv} \geq 1.25\ (K_{Iv}/\sigma_{ys})^2 \tag{1}$$

Diametrical tensile stresses [*6,7*] of the amalgams, similar to their tensile yield stresses, are presented in Table 1. K_{IcSR}, which is referred to here as K_{Iv}, was obtained from

$$K_{Iv} = AP_c(1 + p)B^{-3/2} \tag{2}$$

where

K_{Iv} = plane strain fracture toughness, MN $m^{-3/2}$,
P_c = applied load at critical slope ratio, N,
A = calibration constant, 22.0, dimensionless,
p = plasticity, dimensionless, and
B = diameter, m.

For samples fracturing via crack jumping process, K_{Ivj} was obtained from

$$K_{Ivj} = A_r P_j B^{-3/2} \tag{3}$$

where

K_{Ivj} = plane strain fracture toughness for crack jumping,
A_r = calibration related to crack jump at slope ratio r, and
P_j = load initiating a crack jump.

Corrosion

Polarization—The amalgam samples were corroded by polarization under constant current conditions in air-exposed 1 wt% sodium chloride (NaCl) solution. A Wenking potentiostat Model LP75M in combination with an external resistor controlled a constant current between amalgam working electrode and graphite counter electrodes. Currents selected corresponded to between 1–10 mA which approximated 1–10 mA/cm^2. A Wenking voltage integrator integrated the anodic output charge by means of a current to voltage converter in the potentiostat.

Environmental Conditioning—Six short-rod samples of each amalgam were processed and prepared as described and each sample conditioned in its own glass vial containing 5 mL of 0.1% NaCl solution and sealed with parafilm for 2 years at 25°C. For comparison, six similar samples of each amalgam were conditioned in air for the same time interval. Samples were also prepared and aged 1 week or less before testing. Statistical significance between means was obtained by using Tukey's multiple comparison test [*8*].

Fractography

The fractured sample halves of selected samples were submitted to scanning electron microscopy (SEM) analysis. Those samples containing non-conductive corrosion products were first coated with a thin gold film to eliminate charging. Energy dispersive spectrocopy (EDS) was also utilized on selected samples in a qualitative and semi quantitative manner. A Cambridge scanning electron microscope equipped with a Princeton Gamma Tech spectrometer and related hardware and software were used. Compositions were obtained with computer program taking into account atomic number, absorbance, and fluorescence (ZAF) interactional effects between elements.

Results

Short-Rod Diameter

Figure 2 presents the fracture toughness of 6.35 mm diameter samples for the six amalgams aged for 1 week in air. Also shown are the results on the 11.28 mm diameter samples after similar aging as previously reported [*3*]. Except for the Spheraloy amalgam, which revealed

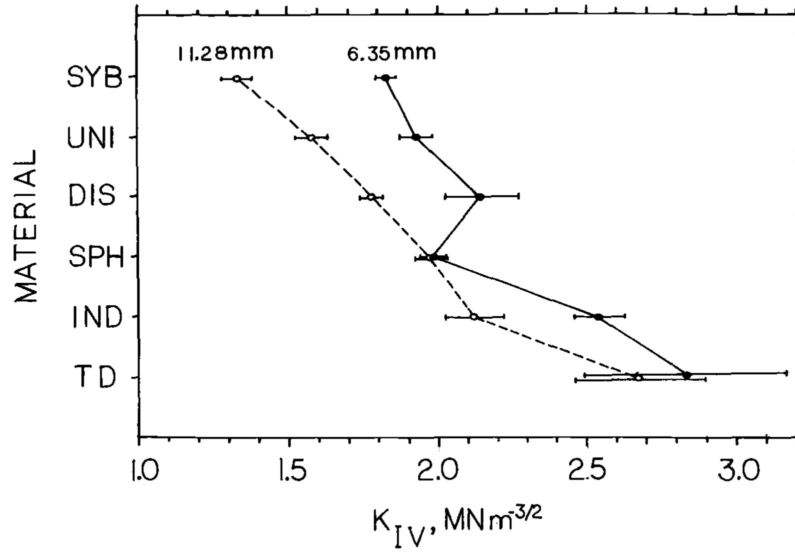

FIG. 2—*Fracture toughness versus amalgam for 6.35 and 11.28 mm diameter samples (see Table 1 for alloy identification.) Mean and standard deviation are shown.*

almost the same fracture toughness for both diameters, the other five amalgams all revealed higher mean values for the smaller diameter. Because of the large standard deviation associated with True Dentalloy, a significant difference did not occur between the two sizes.

Load Versus MOD

Except for True Dentalloy, which displayed a smooth crack advance, all other amalgams displayed a crack jumping behavior. Figures 3 and 4 represent typical plots for amalgams of each type.

Fracture Toughness

Corrosion by Immersion—Table 2 presents the fracture toughness of the amalgams after having been immersed in 0.1% NaCl or conditioned in air for 2 years. Data are also presented for similar amalgams after aging in air for only 1 week.

Corrosion by Polarization—Table 3 presents the fracture toughness of the amalgams after having been corroded by various amounts of anodic charge. Figure 5 presents load versus MOD plots for an Indiloy amalgam corroded by immersion for 2 years and another having been polarized by 90 C of charge.

Fractography

Conventional Amalgams—Figures 6 to 23 present SEM micrographs of the fractured surfaces of the short-rod samples. Figures 6 and 7 compare at low magnification two-year-old True Dentalloy samples after air and NaCl conditioning, respectively. The NaCl exposed surface readily reveals corrosion products covering most of the surface outside of the chevron plane. Figure 8 shows the chevron plane of the corroded sample directly beneath its apex,

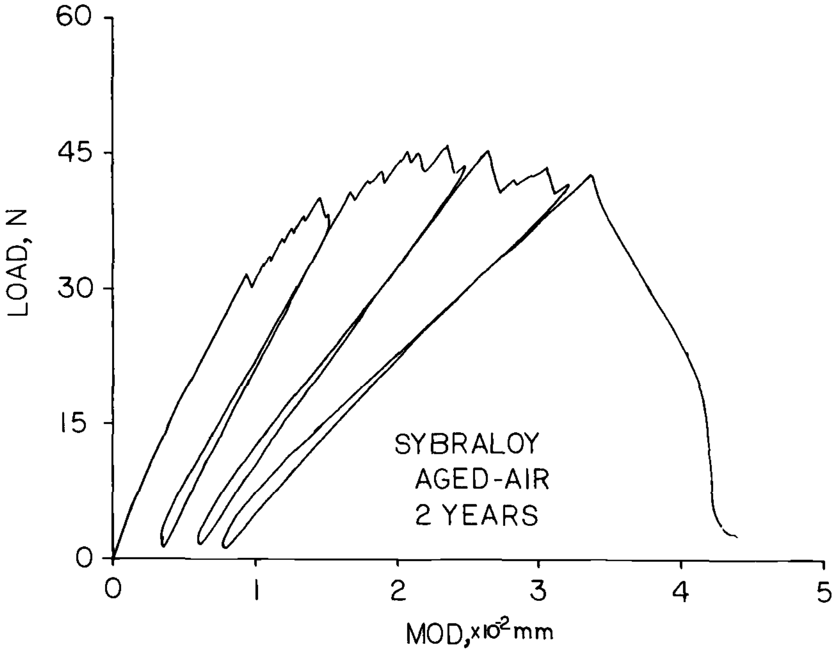

FIG. 3—*Load versus MOD for Sybraloy amalgam.*

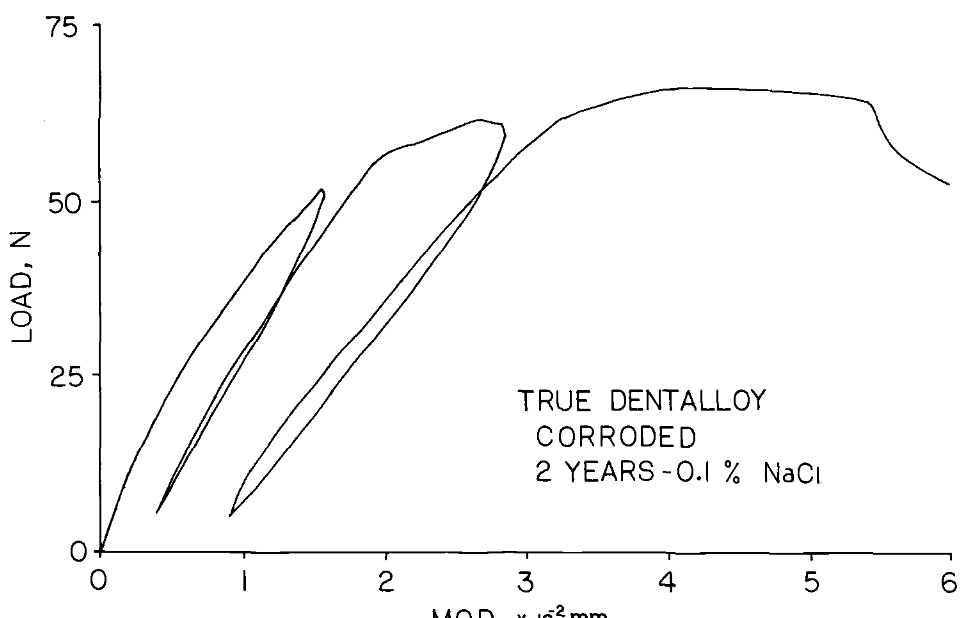

FIG. 4—*Load versus MOD for True Dentalloy amalgam.*

TABLE 2—*Short-rod fracture toughness results.*[a]

Material	K_{Ic8R}, MN $m^{-3/2}$ 1 Week-Air	2 Year-Air	2 Year-Immersion[b]
Sybraloy	1.834 ± 0.047	1.571 ± 0.042	. . .
Unison	1.931 ± 0.058	1.866 ± 0.177	1.910 ± 0.131
Spheraloy	1.918 ± 0.077	2.017 ± 0.133	2.172 ± 0.088
Dispersalloy	2.149 ± 0.124	2.085 ± 0.080	2.187 ± 0.189
Indiloy	2.548 ± 0.098	2.530 ± 0.234	2.936 ± 0.110
True Dentalloy[c]	2.841 ± 0.353	2.550 ± 0.168	2.841 ± 0.351

[a]Means and standard deviations of 5–6 samples each.
[b]In 0.1% NaCl solution.
[c]Not including plasticity in calculation.

TABLE 3—*Fracture toughness results*[a] *for polarized*[b] *amalgams.*

Material	K_{IC8R}, MN $m^{-3/2}$ 15 C	30 C	60 C	75 C	90 C
Sybraloy	. . .	1.331	. . .	. . .	[c]
Dispersalloy	. . .	. . .	1.954	2.197	1.803
Indiloy	2.971	. . .	1.804	. . .	0.769
True Dentalloy	. . .	3.076	3.112	2.812	2.636

[a]1 test per condition.
[b]Indicated as anodic charge in coulombs.
[c]Broke while handling.

indicating regions of porosity. Inspection of a central region in Fig. 8, and at higher magnification shown in Fig. 9, reveals porosity or voids (labeled "V") and that product deposition had occurred within some of the pores (labeled "P"). The rod-shaped product as shown by EDS to contain tin, mercury, and chlorine. Hence, chloride for this particular corrosion product had diffused about 100 μm. The voids revealed in Fig. 9 were a result of either true porosity contained within the amalgam or voids due to the dissolution of the Sn_7Hg phase. Figure 10 reveals the features of the fractured plane from a Spheraloy sample exposed to NaCl. No differences were obvious between this surface and that of Spheraloy aged in air. The crack has propagated intergranularly through the Ag-Hg matrix grains and around the unreacted alloy particles.

High Copper Amalgams—Figures 11 and 12 compare the fractured surfaces of Dispersalloy corroded in NaCl by either immersion for 2 years or by polarization with 90 C of charge. The surface from the polarized sample has obviously been alter by the excessive corrosion. Figure 13 presents the fractured chevron plane for Unison amalgam exposed to 0.1% NaCl for 2 years prior to testing. Flat-like features which were common to both aged and corroded surfaces were evident. Sybraloy also revealed flat-like fractured surface features. Figure 14 reveals the needle-like Cu_6Sn_5 amalgamation phase, labeled as "N," covering the unreacted alloy particles on the fractured chevron plane surface for Sybraloy amalgam. With corrosion by polarization, the fractured chevron plane for Sybraloy amalgam, shown in Fig. 15, revealed an abundance of corroded Cu_6Sn_5 phase. For Indiloy, one of the corroded samples revealed a ring around the apex of the chevron plane (Fig. 16). Chlorine was detected over much of the chevron plane. For example, the Cl concentrations for the dark background

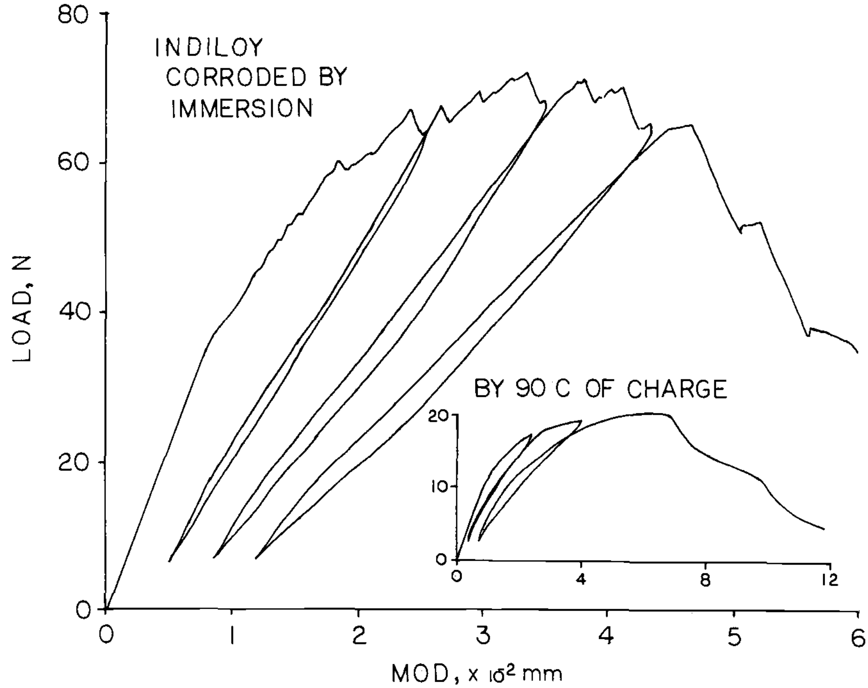

FIG. 5—*Load Versus MOD for Indiloy amalgams after corrosion by immersion for 2 years and after corrosion by polarization with the passage of 90 C of charge.*

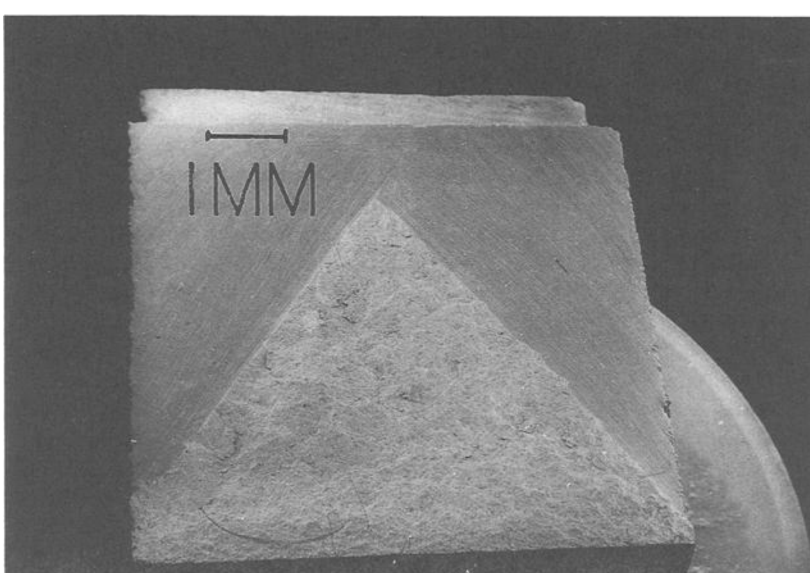

FIG. 6—*SEM micrograph of the fractured chevron plane for True Dentalloy amalgam aged in air for 2 years prior to testing.*

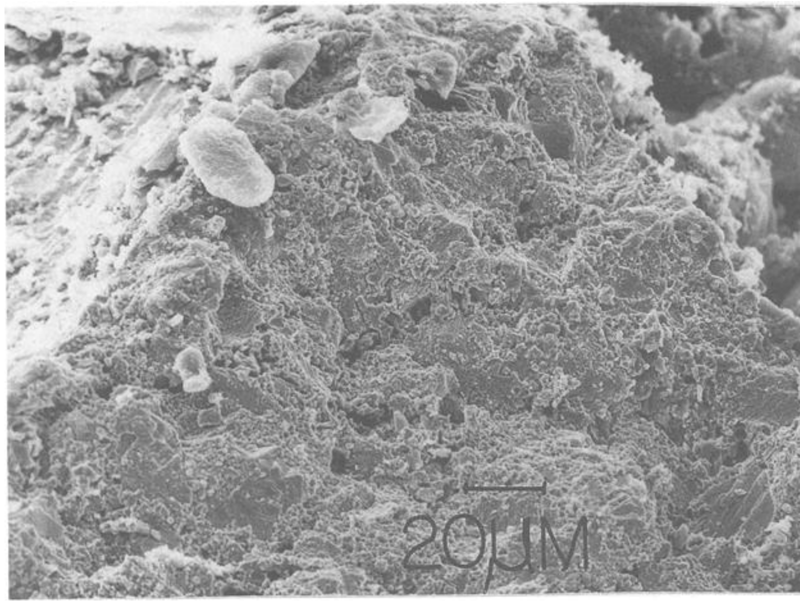

FIG. 7—*SEM micrograph of the fractured chevron plane for True Dentalloy amalgam exposed to 0.1% NaCl solution for 2 years prior to testing.*

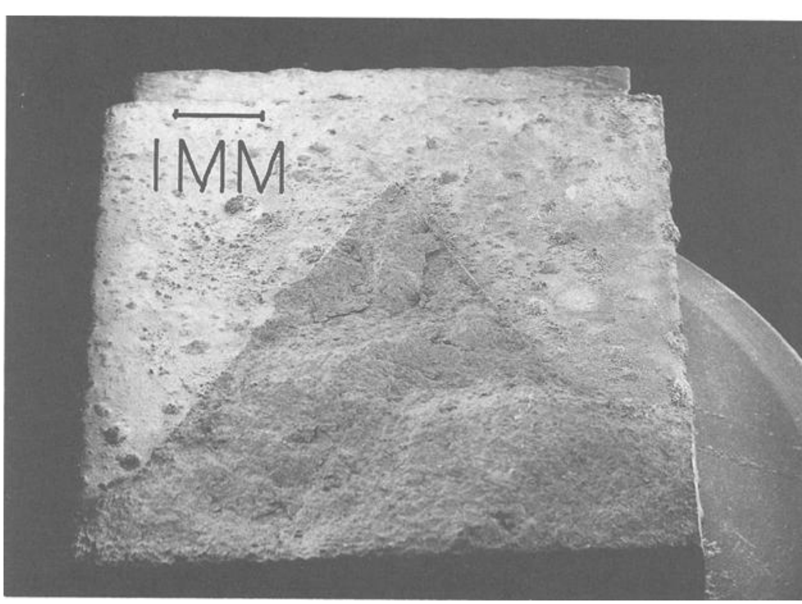

FIG. 8—*SEM micrograph of the region in Fig. 7 below the apex at higher magnification.*

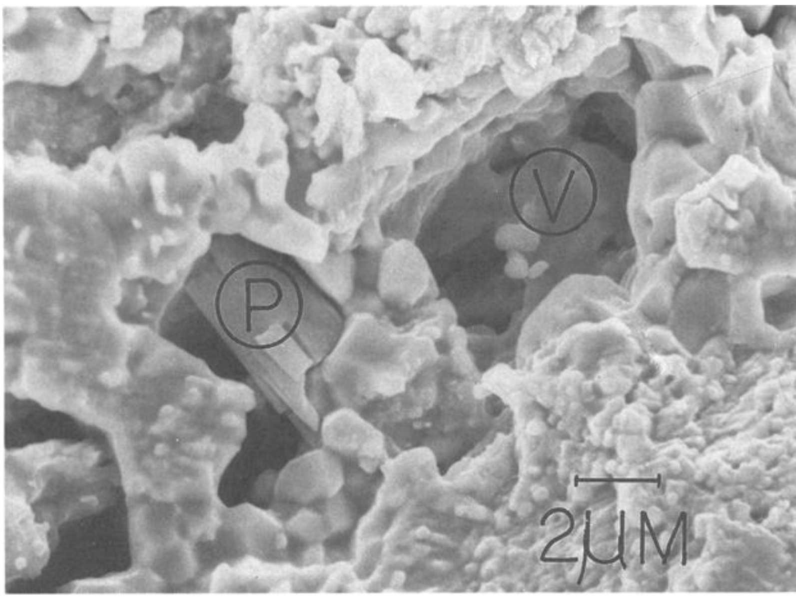

FIG. 9—*SEM micrograph of the central region in Fig. 8 at higher magnification. "V" labeled for void or pore and "P" labeled for product of corrosion.*

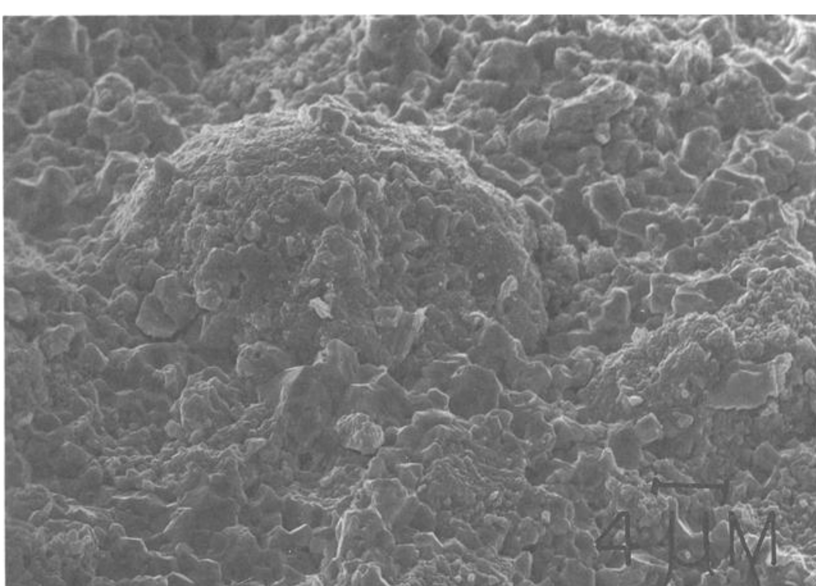

FIG. 10—*SEM micrograph of the fractured chevron plane for Spheraloy amalgam exposed to 0.1% NaCl solution for 2 years prior to testing.*

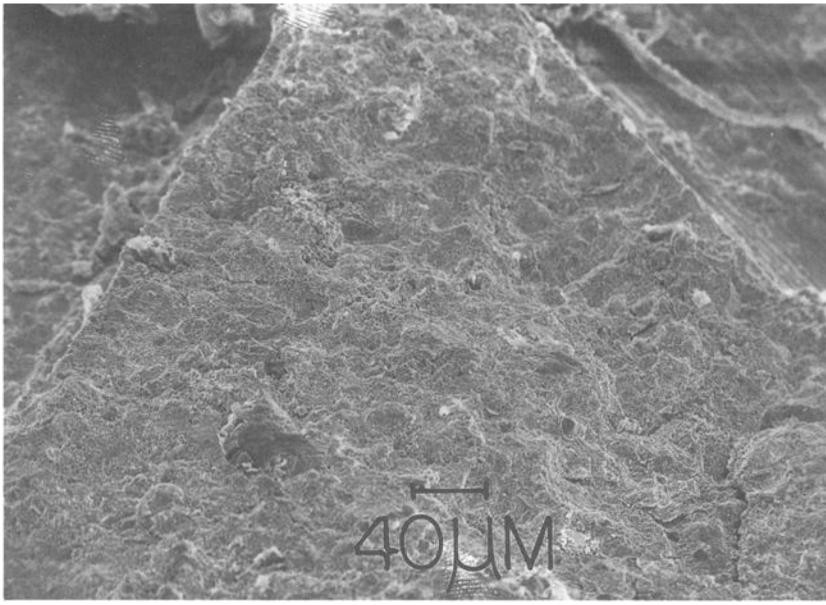

FIG. 11—*SEM micrograph of the fractured chevron plane for Dispersalloy amalgam exposed to 0.1% NaCl solution for 2 years prior to testing.*

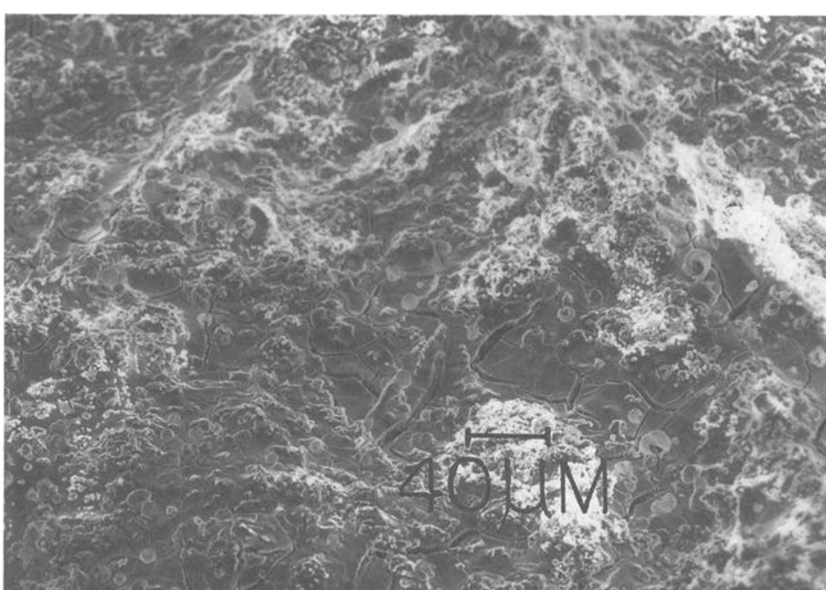

FIG. 12—*SEM micrograph of the fractured chevron plane for Dispersalloy amalgam corroded in 1% NaCl solution by polarization with 90 C of charge prior to testing.*

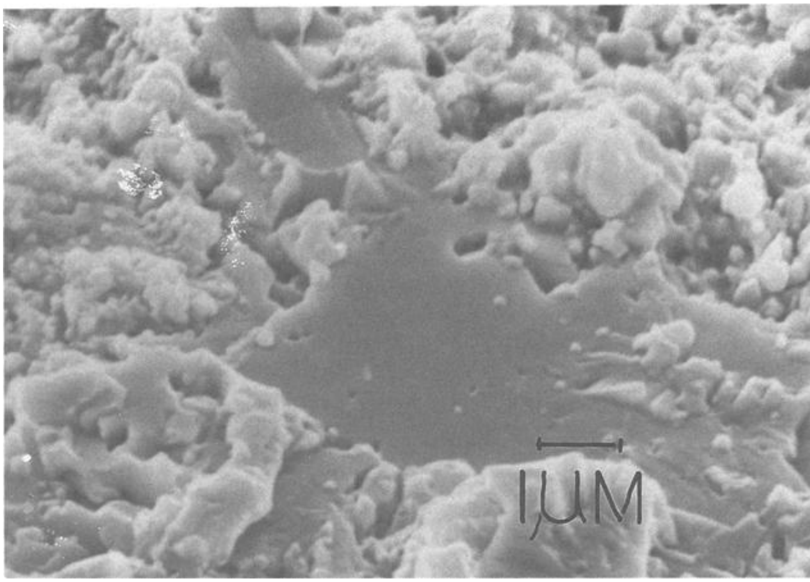

FIG. 13—*SEM micrograph of the fractured chevron plane for Unison amalgam exposed to 0.1% NaCl solution prior to testing.*

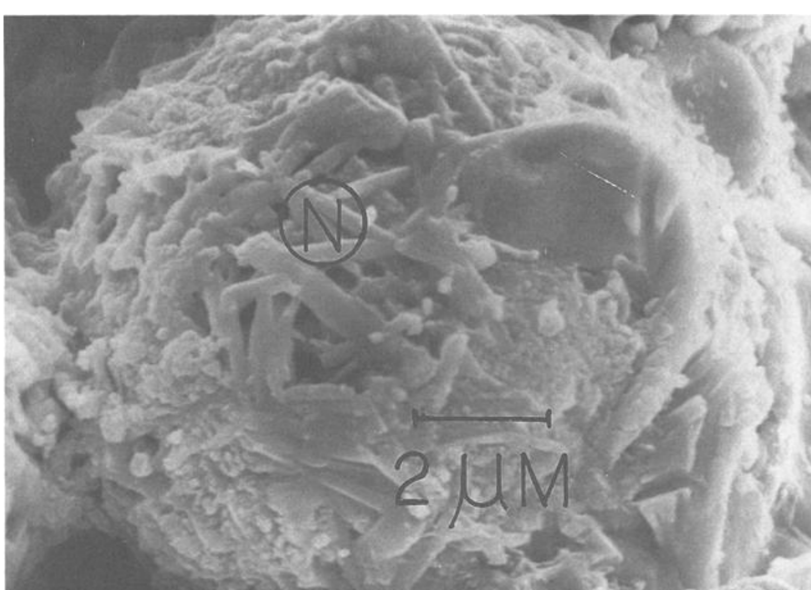

FIG. 14—*SEM micrograph of the fractured chevron plane for Sybraloy amalgam aged in air for 2 years prior to testing. "N" labeled for needle-like Cu-Sn amalgamation reaction products.*

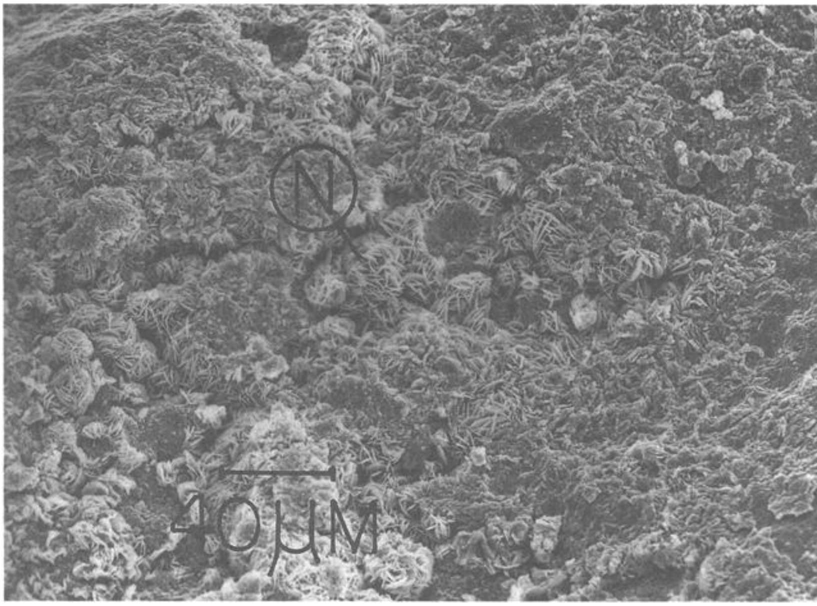

FIG. 15—*SEM micrograph of the fractured chevron plane for Sybraloy amalgam corroded in 1% NaCl solution by polarization with 90 C of charge. "N" labeled for corroded Cu-Sn amalgamation phase.*

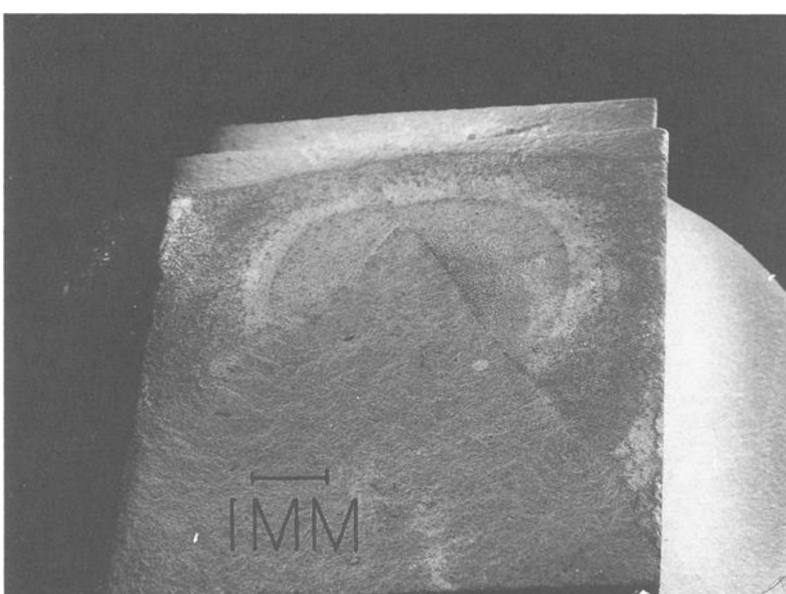

FIG. 16—*SEM micrograph of the fractured chevron plane for Indiloy amalgam after exposure to 0.1% NaCl solution for 2 years prior to testing.*

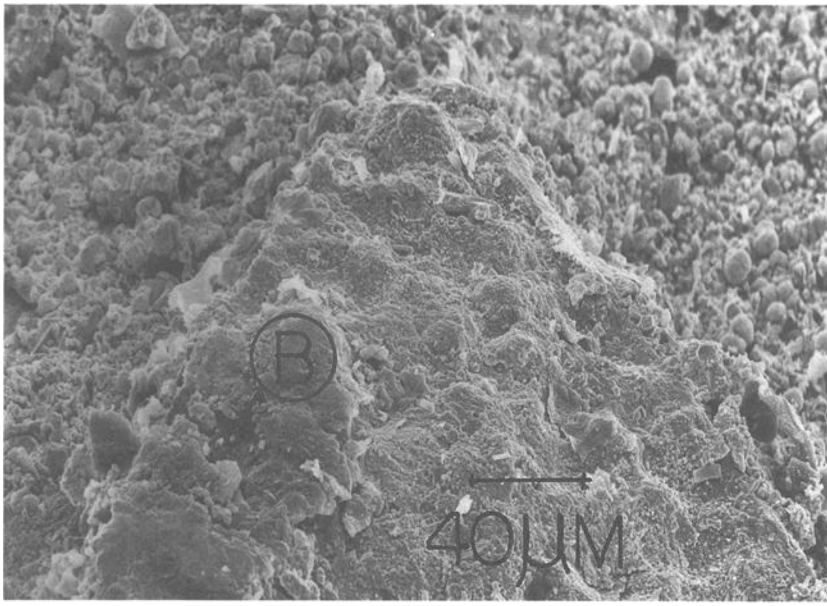

FIG. 17—*SEM micrograph of the region below the apex in Fig. 16 at higher magnification. EDS analysis of area labeled "B" contained 12 wt% Cl content.*

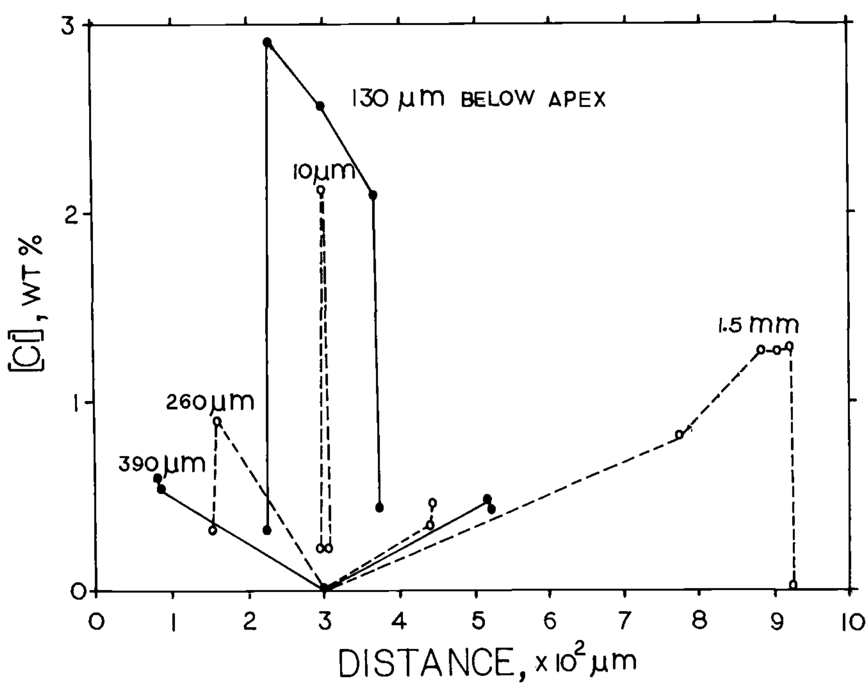

FIG. 18—*Chlorine concentration across the chevron plane in Fig. 17 at different distances from the apex.*

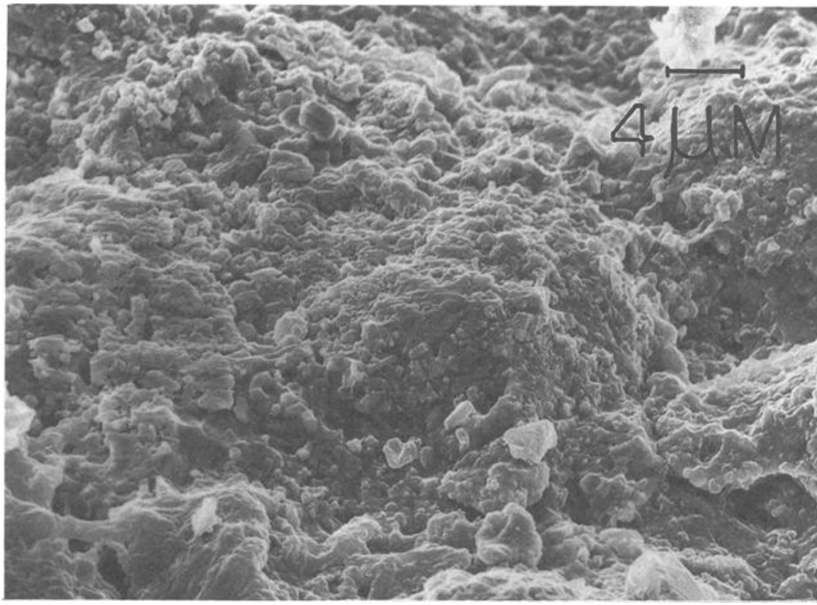

FIG. 19—*SEM micrograph of region in Fig. 17 at higher magnification.*

(labeled "B") and lighter surrounding material in Fig. 17 were 12.6 and 3.9 wt%, respectively. Figure 18 presents Cl percentages at various distances from the chevron apex. Higher magnification of the fractured plane (Fig. 19) revealed intergranular fracture of the Ag-Hg matrix phase and with a waviness to the surface. Unreacted alloy particles were not detected. A similar appearance was noted with Indiloy aged in air. Figures 20 and 21 present the fractured chevron plane surface from a polarized Indiloy sample corroded with the passage of 15 C of charge. In both figures "P" is labeled for small particle products dispersed across the fractured surface. Figures 22 and 23 present the fractured chevron plane surface again from a polarized Indiloy sample but with the passage of 90 C of charge. Larger prismatic-like products were detected as well as of evidence for the propagation of the crack to have occurred through these products.

Discussion

Short-Rod Diameter

Except for Spheraloy and True Dentalloy, K_{Iv} was dependent on the diameter of the short-rod samples. The smaller size gave higher values of K_{Iv}. Previous data [*3*] have shown this trend, but not to this magnitude. The largest increase occurred with Sybraloy (37%), followed with Unison (22%), Indiloy (20%), and Dispersalloy (20%). Interestingly, the three materials revealing between 20–22% increases in fracture toughness contained copper within a small range between 14.7–18.5%, while the one material indicating the largest increase with the smaller diameter also contained the largest copper content of 28%. Spheraloy gave the same values with both diameters, while True Dentalloy showed a mean increase by 6% with the smaller size. Because of the large standard deviations with True Dentalloy, this small increase was not significant.

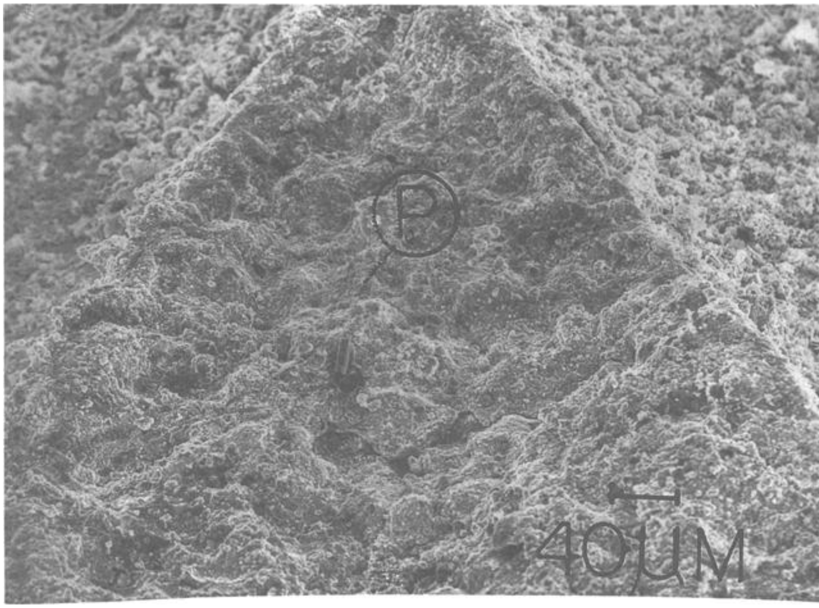

FIG. 20—*SEM micrograph of fractured chevron plane for Indiloy amalgam corroded in 1% NaCl solution by polarization with 15 C of charge prior to testing. "P" labeled for small-particle products dispersed across surface.*

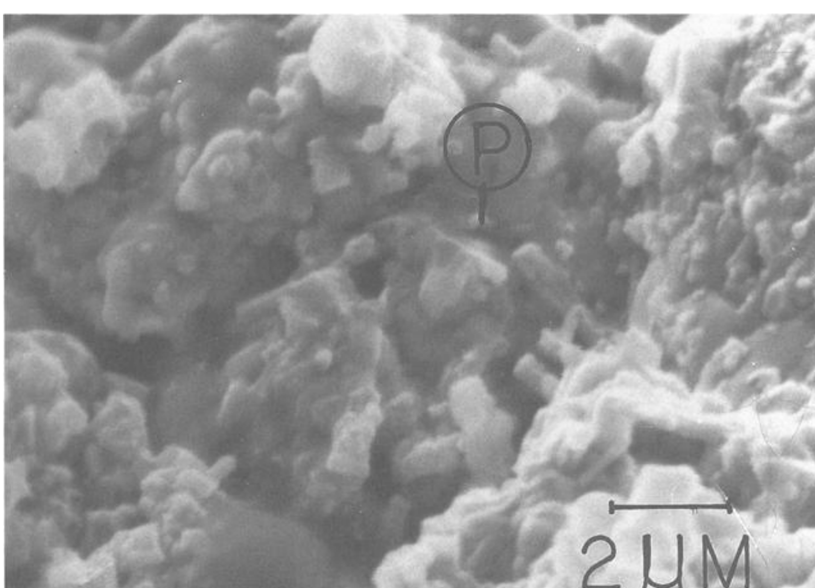

FIG. 21—*SEM micrograph of a region in Fig. 20 at higher magnification. "P" labeled for small-particle products.*

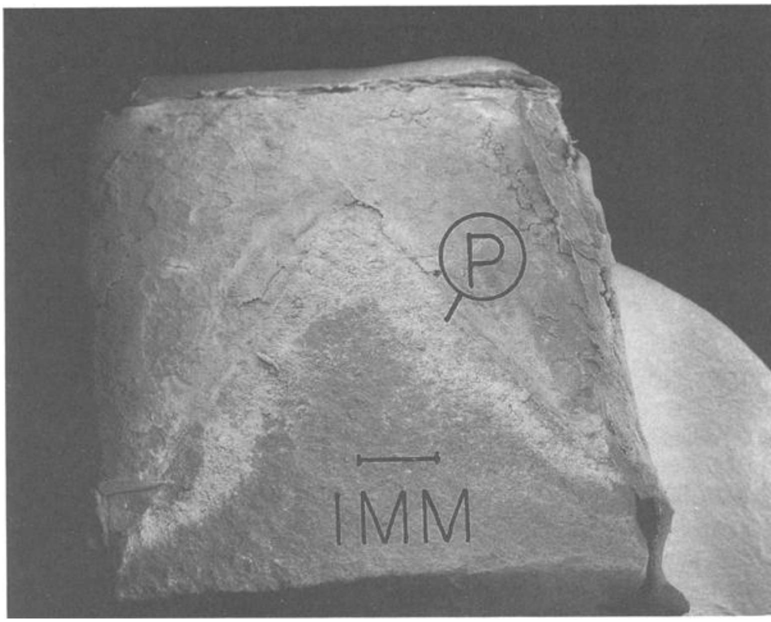

FIG. 22—*SEM micrograph of fractured chevron plane for Indiloy amalgam corroded in 1% NaCl solution by polarization with 90 C of charge. "P" labeled for larger prismatic products located along the edges of the chevron slot.*

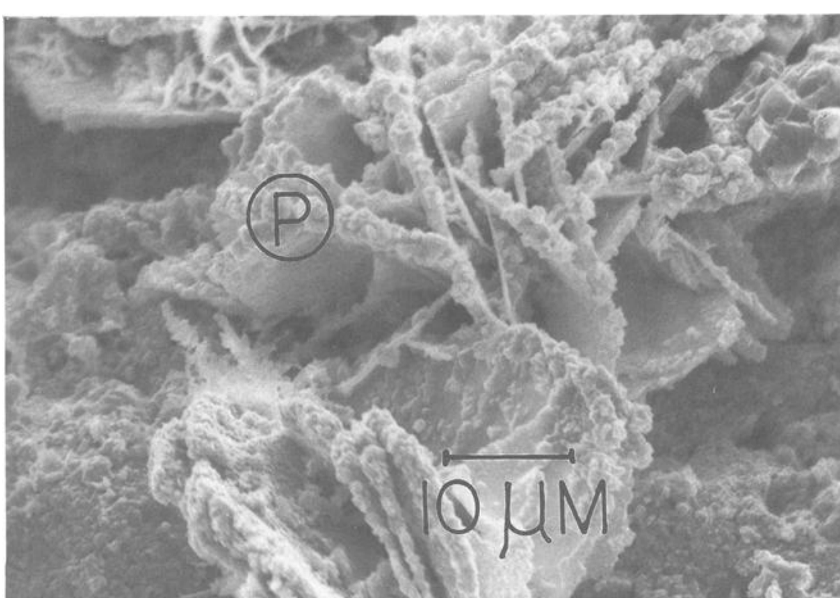

FIG. 23—*SEM micrograph of a region in Fig. 22 at higher magnification. "P" labeled for larger prismatic products.*

The two materials not showing a dependency upon diameter were conventional low-copper amalgams. Spheraloy and True Dentalloy reveal, respectively, 1.26–1.35 and 1.32–1.42 times larger diametrical tensile stresses (Table 1) than those for the high copper amalgams. It does appear, therefore, that the dependency of K_{Iv} on diameter can be explained with a consideration of Eq 1.

If the yield strengths obtained in bending [1] are used instead of the diametrical tensile stresses, then Eq 1 does not predict the effect of sample diameter on K_{Iv}. That is, the yield stresses in bending for the high copper amalgams were as high or higher than for the conventional amalgams. This anomaly, however, may then be linked to the so called "*R*-curve effect" [9]. With amalgams behaving as viscoelastic materials, this could cause an *R*-curve effect which gives rise to an increased K_{Iv} for larger diameters.

Corrosion Affecting Fracture Toughness

A comparison of the 2-year-aged amalgams in air to 1 week samples revealed no significant differences in fracture toughness except for Sybraloy which had a 14% reduction by aging in air. Because of the increased copper-content of this amalgam, it may be that oxides of copper were more easily formed with this amalgam and were detrimental to fracture toughness.

Amalgams exposed to 0.1% NaCl solution instead of air for 2 years revealed small increases in fracture toughness, but only for Indiloy was this increase significant. It was also shown for Indiloy that chloride had diffused within some regions of the chevron plane and may have been a reason for affecting fracture toughness. It was unexpected that an increase would have occurred, since any process attempting to dealloy the amalgam would be susceptible for degrading alloy properties. Besides, any products formed with chloride, such as with copper, tin, and indium would not be expected to improve fracture toughness. Since fracturing of amalgams occurs mainly by intergranular fracture of the Ag-Hg phase matrix grains, speculation is put forth that chloride products were formed along matrix grain boundaries inhibiting intergranular fracture and tending to toughen the material. It is also likely that indium may be linked to the toughening, since a significant increase in fracture toughness only occurred with an indium-containing amalgam.

It is interesting that the Indiloy amalgam corroded by polarization revealed an increase in fracture toughness after 15 C of charge had passed. Increasing the amount of charge beyond this amount also significantly decreased fracture toughness. It may be that at 60 and 90 C of charge, gross corrosion degradation had occurred which reversed any effects from a toughening process occurring at lower amounts of charge transfer.

True Dentalloy also revealed increases in fracture toughness with corrosion by polarization. Even though values began to reverse as the amount of charge reached 75 C, this amalgam, like with Dispersalloy, still showed remarkable toughness after large amounts of charge transfer. As corrosion began to consume the easily corrodable phases, Sn-Hg in True Dentalloy and Cu-Sn in Dispersalloy, the more corrosion resistant phases began to become deteriorated and began to undermine the entire structure. Sybraloy showed reduction in toughness already with 30 C of charge, and at 90 C the toughness had degraded to the point where the amalgam was able to sustain only very small loads.

Analysis of Fractured Surfaces

Even though no significant differences in fracture toughness for Dispersalloy and Unison between the air and solution exposed samples occurred, differences between their fractographic surfaces were still noted. Dispersalloy aged in air instead of solution revealed more irregular surface characteristics. Even though not as noticeable as with Dispersalloy, Unison also revealed a somewhat of a similar trend. This indicated the path by which fracturing occurred was different between the two conditions even though the toughness measurements were the same. At high magnification, Unison in both conditions revealed a flatter surface texture than that occurring with Dispersalloy in either condition.

Conclusions

1. The 6.35 mm diameter short-rod samples from four dental high-copper amalgams were 20, 20, 22, and 37% higher in toughness than for the amalgams fabricated from 11.28 mm diameter samples. For two conventional amalgams sample size effect should have been noticed but was not.
2. Differences in fracture toughnesses between air and 0.1% NaCl storage for two years were not significant except for one amalgam containing indium. In this case, NaCl storage increased fracture toughness by 16%.
3. Chlorides were detected within the fractured chevron plane showing diffusion to a distance of at least 300 μm and more.
4. The formation of chloride corrosion products along Ag-Hg phase grain boundaries was postulated as a possible mechanism for increasing fracture toughness.
5. Corrosion by polarization was also able to increase fracture toughness. However, as the amount of charge became excessive fracture toughness decreased.

Acknowledgments

A portion of this work was supported by a grant from the National Institutes of Health, DE 05761. John Lenke from the American Dental Association provided electron optical support.

References

[1] Roberts, J. C., Powers, J. M., and Craig, R. G., "Fracture Toughness and Critical Strain Energy Release Rate of Dental Amalgam," *Journal of Materials Science*, Vol. 13, 1978, pp. 965–971.
[2] Lloyd, C. H. and Adamson, M., "The Fracture Toughness(K_{Ic}) of Amalgam," *Journal of Oral Rehabilitation*, Vol. 12, 1985, pp. 59–68.
[3] Mueller, H. J., "Fracture Toughness and Fractography of Dental Amalgams," *Microstructural Science*, T. A. Place et al., Ed., International Metallographic Society, Vol. 18, 1990, pp. 486–504.
[4] Hassan, R., Vaidyanathan, T. K., and Schulman, A., "Fracture Toughness Determination of Dental Amalgams Through Microindentations," *Journal of Biomedical Materials Research*, Vol. 20, 1986, pp. 135–142.
[5] Terra Tek, "The Fractometer II Systems Manual," Terra Tek, Salt Lake City, Utah.
[6] Osborne, J. W., Gale, E. N., Chew, C. L., Rhodes, B. F., and Phillips, R. W., "Clinical Performance and Physical Properties of Twelve Amalgam Alloys," *Journal of Dental Research*, Vol. 57, 1978, pp. 983–988.
[7] Nagai, K., Ohashi, M., Habu, H., Uemura, M., Korenaga, F., Goto, N., Nagata, Y., and Fujimoto, Y., "Tensile Strength of Commercially Available Amalgam Alloys in Dental Use," *Journal of Nihon University School of Dentistry*, Vol. 12, No. 1, 1970, pp. 9–24.
[8] Analytical Software, *Statistix Manual*, Analytical Software, St. Paul, Minn., pp. 162–169.
[9] Salem, J. A. and Shannon, Jr., J. L., "Some Observations in Fracture Toughness and Fatigue Testing with Chevron-Notched Specimens," in this volume, pp. 9–25.

Patrick T. Purtscher,[1], *J. David McColskey*,[1] *and Elizabeth S. Drexler*[1]

Aluminum-Lithium Alloys: Evaluation of Fracture Toughness by Two Test Standards, ASTM Method E 813 and E 1304

REFERENCE: Purtscher, P. T., McColskey, J. D., and Drexler, E. S., "**Aluminum-Lithium Alloys: Evaluation of Fracture Toughness by Two Test Standards, ASTM Method E 813 and E 1304**," *Chevron-Notch Fracture Test Experience: Metals and Non-Metals, ASTM STP 1172*, K. R. Brown and F. I. Baratta, Eds., American Society for Testing and Materials, Philadelphia, 1992, pp. 110–130.

ABSTRACT: Fracture toughness of three aluminum-lithium alloys and Alloy 2219 (a total of nine different plates) was measured with two different types of specimens and methods: (1) compact specimens using ASTM E 813 and (2) chevron-notched short-bar specimens using ASTM E 1304. The properties were measured in two orientations (T-L and L-T) and at three temperatures (295, 76, and 4 K). In general, the short-bar specimens exhibited a higher fracture toughness than the compact specimens. The difference between the two procedures was relatively constant, independent of test orientation and strength. However, when the specimens exhibited extensive delaminations on the fracture surface, the compact specimens had a higher fracture toughness than the short bar specimens. The difference in fracture toughness measured by the two procedures is explained in terms of the alloys' crack growth behavior.

KEY WORDS: fracture toughness, aluminum-lithium alloys, delaminations, cryogenic properties, Alloy 2219

A simple, inexpensive method of measuring fracture toughness is needed to compare different materials and to evaluate the effect of processing variables on the materials. The chevron-notched specimens presented by Barker [*1*] and others [*2–3*] is applicable to a wide range of materials including metals, ceramics, polymers, and rocks.

Aluminum-lithium (Al-Li) alloys are a relatively new class of materials that have been introduced on a commercial scale within the last five years and are slowly being incorporated into manufacture and construction of aerospace structures. The properties of these new alloys have received attention because a large increase in fracture toughness has been observed with decreasing test temperature. Their use in industry has been hampered by production problems and the users' lack of familiarity with the material.

The purpose of this paper is to compare the fracture toughness of high-strength Al alloys by two different ASTM methods: (1) E 813 for J_{Ic} [*4*] specimens that was initially approved in 1981 and recently revised in 1988 and (2) E 1304 for K_{Iv} [*5*] that was adopted in 1989. These results are part of a comprehensive study of the mechanical properties of Al-Li alloys [*6*]. Alloy 2219, which does not contain Li, is included in the study for comparison purposes.

[1]Materials research engineer, physical scientist, and materials research engineer, respectively, Materials Reliability Division, National Institute of Standards and Technology, Boulder, CO 80303.

The purpose of this work is to create a data base of cryogenic material properties available for current (1989 vintage), commercial Al-Li alloys.

Materials and Procedures

The chemical compositions and alloy characterization of the aluminum alloys used in this study are shown in Table 1. The "x" in front of Alloy 2095 indicates that it is an experimental alloy. Most of the plates were 12.7 mm thick, but a 19-mm-thick plate of 2090 was also included. The T8 tempers are slightly less than peak aged. The microstructures of the plates show large pancake-shaped grains. The grain size for each alloy is shown in Table 2 along with the room temperature hardness. Undissolved intermetallic or constituent particles, 1 to 10 μm in size, were elongated along the rolling direction in all alloys. The X2095 plates had the highest volume fraction of constituent particles followed by the plates of 2219 and 8090. The 2090 plates had the lowest volume fraction of constituent particles.

The procedures used in tension testing of cylindrical specimens, 25-mm gage length and 6-mm diameter, at cryogenic temperatures are found elsewhere [6]. Fracture toughness tests on compact, C(T), and chevron-notched short-bar specimens were performed in the T-L and L-T orientations with respect to the rolling direction of the plates. The mechanical testing was performed in three different test environments: room air at approximately 295 K; liquid nitrogen, which is at a temperature of 76 K in Boulder, Colorado where the altitude is approximately 1.6 km above sea level; and liquid helium, which is at a temperature of 4 K in Boulder, Colorado. The specimen dimensions for the fracture toughness specimens are summarized in Table 3.

The tests were conducted in stroke control on a servohydraulic controlled test machine. The cryogenic tests (4 and 76 K) were precracked at 76 K. Crack growth was monitored by the unloading compliance technique. The value of J_{Ic} was determined by the intersection of the tearing and blunting lines drawn according to ASTM Test Method for J_{Ic}, a Measure of Fracture Toughness (E 813-81). The 1981 test method tends to give more conservative values for J_{Ic} than the latest version, revised in 1987, due to the different definitions of J_{Ic} used in the two methods [7]. The fracture toughness measured in the J_{Ic} test is converted to $K_{Ic}(J)$, assuming plane stress conditions, by the formula

$$K_{Ic}(J)^2 = J_{Ic} \cdot E \tag{1}$$

where E = Young's modulus measured in tension testing at the same test temperature. If plane strain conditions were assumed instead of plane stress, the fracture toughness would be slightly higher and nonconservative.

The short-bar specimens were tested at 295 and 76 K in a screw-driven test machine. At 4 K, the tests were run in the servohydraulic controlled test machine used for C(T) testing. The side slots were cut into the short-bar specimen with a diamond blade. A ring gage was placed in one of the side slots to monitor the crack opening during testing, approximately 3 mm from the mouth of the specimen. A schematic of the short-bar specimen and the testing arrangement is shown in Fig. 1. The ring gage is shown mounted at the grips for clarity only, but during testing the gage was in the side slot.

Method E 813, using C(T) specimens, requires fatigue precracking while the short-bar specimens do not. In Method E 813, the critical point on the test record where the fracture toughness is evaluated is related to the area under the load-displacement curve (absorbed energy) at a short relative crack extension. In Method E 1304, measured with chevron-notched short-bar specimens, the fracture toughness is a mechanics-based value rather than

TABLE 1—*Compositions of Al-Li alloys and Alloy 2219, mass %.*

Alloy	Cu	Li	Mg	Zr	Si	Fe	Ti	Cr	Zn	Ag	Other
8090-T8771	1.21	2.36	0.68	0.11	0.02	0.06	0.03	0.002	0.04	. . .	. . .
2090-T81-1/2	2.70	2.30	0.03	0.12	. . .	0.08	0.19	<0.01	0.01	. . .	0.01 Ni
2090-T81-3/4	2.85	2.30	0.05	0.10	. . .	0.07	0.13	<0.01	0.02	. . .	0.01 Ni
X2095-T851, T651, T351	4.72	1.28	0.42	0.12	0.02	0.03	0.02	. . .	0.02	0.35	0.01 Ni
2219-T851	5.71	. . .	. . .	0.08	0.04	0.02	0.04	0.18	. . .	. . .	0.24 Mn
2219-T37	5.72	. . .	. . .	0.03	0.04	0.02	0.03	0.02	. . .	. . .	0.22 Mn

TABLE 2—*Summary of grain size and hardness data.*

Alloy	Average Grain Size, μm			Hardness, R_B
	L[a]	T[a]	S[a]	
8090-T8151	600	380	20	70
8090-T8771	600	380	20	74
2090-T81-1/2	2000	1400	200	85
2090-T81-3/4	2000	1400	100	76
X2095-T351	1000	1000	40	76
X2095-T651	800	400	25	89
X2095-T851	4000 to 100	800 to 100	30	88
2219-T37	220	140	40	71
2219-T851	220	130	40	73

[a]L, T, and S refer to the longitudinal, long-transverse, and short-transverse orientation with respect to the rolling direction of the plate, respectively.

TABLE 3—*Dimensions for fracture mechanics specimens.*

	Width, mm	Thickness, mm	Crack Length/Width
C(T)	50.8	12.7	0.60
C(T)[a]	50.8	19.0	0.60
Chevron-notched	19.0	12.7	0.33

[a]One plate called 2090-T81-3/4.

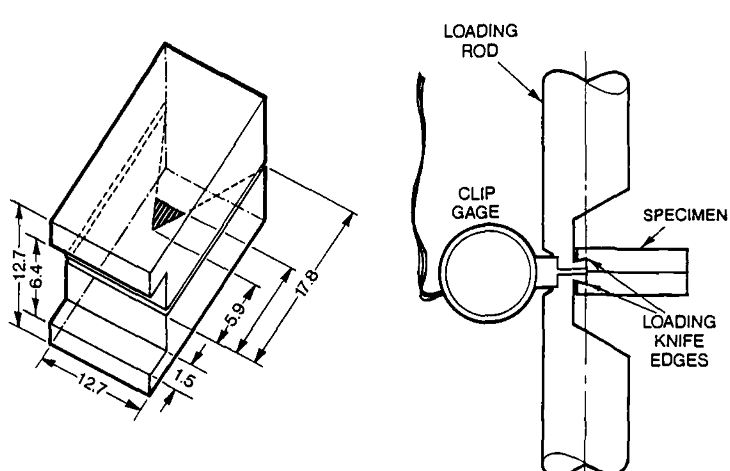

FIG. 1—*Short-bar specimen dimensions and testing arrangement.*

an energy-based toughness, and the critical point is measured after relatively large crack extension.

The toughness measured in short-bar testing is quantified by K_{Iv}, the plane-strain (chevron-notched) fracture toughness. K_{Iv} relates to crack extension resistance with respect to slowly advancing, steady-state crack advance. The main validity check on K_{Iv} is the value of p defined as

$$p = \Delta X_0 / \Delta X \tag{2}$$

where ΔX_0 is the horizontal distance between the two effective unloading lines, and ΔX is the distance between the effective unloading lines along the zero load line.

Results

The tension and fracture toughness tests are summarized in Tables 4 through 12. The yield and ultimate strengths of each alloy increase and the tensile ductility parameters (elongation and reduction in area) remain relatively constant or decrease as the test temperature is decreased. Alloy X2095-T851 has the highest strength of any alloy at each temperature, while the lowest strength material was Alloy 2219-T37.

No trends that describe the temperature dependence of the fracture toughness of these materials as a group are observed. The $K_{Ic}(J)$ values increased 20 to 30% in Alloy 2219 between room and liquid nitrogen temperatures, but did not change significantly between liquid nitrogen and helium temperatures. For Alloy 2090, $K_{Ic}(J)$ at cryogenic temperatures were appreciably higher than at room temperature, except for the thicker plate when tested at 76 K. In Alloy X2095, $K_{Ic}(J)$ of artificially aged plates, T851 and T651 tempers, showed little temperature dependence, but the deformed and naturally aged plate, T351 temper, showed a 25% decrease in $K_{Ic}(J)$ between 295 and 76 K and a 45% decrease between 295 and 4 K. For Alloy 8090, $K_{Ic}(J)$ either decreased or increased at cryogenic temperature relative to room temperature, depending upon the test orientation and temper. Clearly, the effect of temperature on the fracture toughness of high-strength aluminum alloys is complex.

Plots that compare the fracture toughness measured by the two procedures at 295, 76, and 4 K are shown in Figs. 2, 3, and 4, respectively. In many cases, the fracture toughness from the chevron-notched specimens is greater than the fracture toughness from C(T) specimens. The disparity between the two test methods does not appear to vary with the fracture toughness or test temperature.

Little data are found in the literature for Al-Li alloys where fatigue precracked C(T) specimens can be compared to chevron-notched specimens. Rao et al. [*8*] used fatigue-precracked specimens of Alloy 2090 to measure K_{Ic} by Method E 399 [*9*] in the L-T orientation. Similar data were reported by Dorward [*10*], who used the chevron-notched specimens. Comparing these two sets of data at a similar strength level, we find that the chevron-notched specimens produce lower fracture toughness (K_{Iv} = 31 and 40 MPa $\cdot \sqrt{\text{m}}$ at 295 and 88 K compared to 36 and 51 MPa $\cdot \sqrt{\text{m}}$ for K_{Ic} at 295 and 77 K, respectively). A similar comparison between fatigue-precracked C(T) specimens and chevron-notched specimens of Alloy 2090 in the S-L orientation again shows that K_{Iv} is less than K_{Ic} [*11*]. For non-Li-containing Al alloys, Brown [*2*] found that the fracture toughness of fatigue-precracked C(T) specimens and chevron-notched specimens were equal at low values of fracture toughness (20 MPa $\cdot \sqrt{\text{m}}$), and K_{Iv} was significantly higher than K_{Ic} for higher fracture toughness Al alloys (greater than 35 MPa $\cdot \sqrt{\text{m}}$).

TABLE 4—*Tensile and fracture toughness properties: X2095-T851.*

Specimen Orientation	Young's Modulus, GPa (msi)	Yield Strength, MPa (ksi)	Tensile Strength, MPa (ksi)	Elongation, %	Reduction of Area, %	Fracture Toughness, MPa $\sqrt{m}$ (ksi $\sqrt{in.}$)
			295 K			
T	71 (10.3)	581 (84)	638 (92)	11	22	
L	75 (10.9)	607 (88)	640 (93)	10	20	
						ASTM E 813, K_{Ic} (*J*)
T-L						23, 23 (21, 21)
L-T						22, 21 (20, 19)
						ASTM E 1304, K_{Iv}
T-L						28, 28, 29 (25, 25, 26)
L-T						31, 28, 34 (28, 25, 31)
			76 K			
T	84 (12.2)	677 (98)	761 (110)	9	12	
L	82 (12.0)	712 (103)	782 (113)	11	14	
						ASTM E 813, K_{Ic} (*J*)
T-L						20, 22 (18, 20)
L-T						20, 23 (20, 21)
						ASTM E 1304, K_{Iv}
T-L						29, 30 (26, 27)
L-T						45, 42 (41, 38)
			4 K			
T	84 (12.2)	744 (108)	859 (124)	8	10	
L	83 (12.0)	785 (114)	893 (129)	11	13	
						ASTM E 813, K_{Ic} (*J*)
T-L						26, 23 (24, 21)
L-T						31, 27 (28, 25)
						ASTM E 1304, K_{Iv}
T-L						35, 29 (32, 26)
L-T						50, 50 (46, 46)

NOTE: msi = million pounds/in.^{2}.

TABLE 5—*Tensile and toughness properties: X2095-T651.*

Specimen Orientation	Young's Modulus, GPa (msi)	Yield Strength, MPa (ksi)	Tensile Strength, MPa (ksi)	Elongation, %	Reduction of Area, %	Fracture Toughness, MPa $\sqrt{m}$ (ksi $\sqrt{in.}$)
			295 K			
T	77 (11.1)	543 (79)	620 (90)	10	17	
L	77 (11.1)	567 (82)	633 (92)	9	17	
						ASTM E 813, K_{Ic} (J)
T-L						20 (18)
L-T						25, 23 (23, 21)
						ASTM E 1304, K_{Iv}
T-L						30, 32, 33 (27, 29, 30)
L-T						30, 28, 30 (27, 26, 27)
			76 K			
T	83 (12)	637 (92)	744 (108)	8	11	
L	86 (12.5)	671 (97)	764 (111)	9	12	
						ASTM E 813, K_{Ic} (J)
T-L						21, 23 (19, 21)
L-T						25, 21 (23, 19)
						ASTM E 1304, K_{Iv}
T-L						23, 26 (21, 24)
L-T						39, 43 (36, 39)

NOTE: msi = million pounds/in.^{2}.

TABLE 6—*Tensile and toughness properties: X2095-T351.*

Specimen Orientation	Young's Modulus, GPa (msi)	Yield Strength, MPa (ksi)	Tensile Strength, MPa (ksi)	Elongation, %	Reduction of Area, %	Fracture Toughness, MPa $\sqrt{m}$ (ksi $\sqrt{in.}$)
			295 K			
T	76 (11.0)	412 (60)	541 (78)	14	22	
L	76 (11.0)	453 (66)	551 (80)	11	14	
						ASTM E 813, K_{Ic} (J)
T-L						61, 47 (56, 43)
L-T						53, 54 (48, 49)
						ASTM E 1304, K_{Iv}
T-L						52, 60, 58 (47, 55, 53)
L-T						57, 57, 63 (52, 52, 57)
			76 K			
T	85 (12.4)	506 (73)	671 (97)	14	13	
L	83 (12.1)	583 (84)	680 (99)	12	14	
						ASTM E 813, K_{Ic} (J)
T-L						42, 43 (38, 39)
						ASTM E 1304, K_{Iv}
T-L						54, 47 (49, 43)

NOTE: msi = million pounds/in.^{2}.

TABLE 7—*Tensile and fracture toughness properties: 8090-T8771.*

Specimen Orientation	Young's Modulus, GPa (msi)	Yield Strength, MPa (ksi)	Tensile Strength, MPa (ksi)	Elongation, %	Reduction of Area, %	Fracture Toughness, MPa $\sqrt{m}$ (ksi $\sqrt{in.}$)
			295 K			
T	83 (12)	501 (73)	566 (82)	6	12	
L	79 (11.4)	512 (74)	567 (81)	3	6	
						ASTM E 813, K_{Ic} (J)
T-L						36, 31, 24 (33, 28, 22)
L-T						33, 39, 32 (30, 35, 29)
						ASTM E 1304, K_{Iv}
T-L						22, 21, 27 (20, 19, 25)
L-T						39, 36, 43 (35, 33, 39)
			76 K			
T	86 (12.5)	537 (78)	680 (99)	6	6	
L	88 (12.8)	542 (79)	699 (101)	11	11	
						ASTM E 813, K_{Ic} (J)
T-L						25 (23)
L-T						40, 55 (36, 50)
						ASTM E 1304, K_{Iv}
T-L						34, 30 (31, 27)
L-T						53, 51 (48, 46)

NOTE: msi = million pounds/in.^{2}.

TABLE 8—*Tensile and fracture toughness properties: 8090-T8151.*

Specimen Orientation	Young's Modulus, GPa (msi)	Yield Strength, MPa (ksi)	Tensile Strength, MPa (ksi)	Elongation, %	Reduction of Area, %	Fracture Toughness, MPa $\sqrt{m}$ (ksi $\sqrt{in.}$)
			295 K			
T	80 (11.6)	405 (59)	507 (73)	6	6	
L	79 (11.4)	402 (58)	474 (69)	4	4	
						ASTM E 813, K_{Ic} (J)
T-L						44 (40)
L-T						48 (44)
						ASTM E 1304, K_{Iv}
T-L						46, 48, 42 (42, 44, 38)
L-T						47, 47, 48 (43, 43, 44)
			76 K			
T	88 (12.8)	415 (60)	642 (93)	11	10	
L	88 (12.8)	411 (60)	633 (92)	10	9	
						ASTM E 813, K_{Ic} (J)
T-L						48, 29 (44, 26)
L-T						54, 58 (49, 53)
						ASTM E 1304, K_{Iv}
T-L						47, 46, 46 (43, 42, 42)
L-T						51, 51 (46, 46)

NOTE: msi = million pounds/in.^{2}.

TABLE 9—*Tensile and fracture toughness properties: 2219-T851.*

Specimen Orientation	Young's Modulus, GPa (msi)	Yield Strength, MPa (ksi)	Tensile Strength, MPa (ksi)	Elongation, %	Reduction of Area, %	Fracture Toughness, MPa $\sqrt{m}$ (ksi $\sqrt{in.}$)
			295 K			
T	75 (10.9)	331 (48)	443 (64)	8	16	
L	72 (10.4)	342 (50)	447 (65)	8	19	
						ASTM E 813, K_{Ic} (*J*)
T-L						30 (27)
L-T						31 (28)
						ASTM E 1304, K_{Iv}
T-L						38, 38, 38 (35, 35, 35)
L-T						49, 48, 48 (45, 44, 44)
			4 K			
T	82 (11.9)	434 (63)	660 (96)	9	15	
L	81 (11.7)	439 (64)	662 (96)	10	18	
						ASTM E 813, K_{Ic} (*J*)
T-L						36 (33)
L-T						42 (38)
						ASTM E 1304, K_{Iv}
T-L						44, 43 (40, 39)
L-T						58, 54 (53, 49)

NOTE: msi = million pounds/in.^{2}.

TABLE 10—*Tensile and fracture toughness properties: 2219-T37.*

Specimen Orientation	Young's Modulus, GPa (msi)	Yield Strength, MPa (ksi)	Tensile Strength, MPa (ksi)	Elongation, %	Reduction of Area, %	Fracture Toughness, MPa $\sqrt{m}$ (ksi $\sqrt{in.}$)
			295 K			
T	70 (10.1)	303 (44)	398 (58)	11	25	
L	71 (10.3)	333 (48)	391 (57)	12	28	
						ASTM E 813, K_{Ic} (J)
T-L						26, 26 (24, 24)
L-T						31, 26 (28, 24)
						ASTM E 1304, K_{Iv}
T-L						35, 36, 34 (32, 33, 31)
L-T						39, 38, 40 (35, 35, 36)
			76 K			
T	77 (11.2)	381 (55)	518 (75)	16	21	
L	77 (11.2)	420 (61)	510 (74)	17	27	
						ASTM E 813, K_{Ic} (J)
T-L						32, 33 (29, 30)
L-T						41, 39 (37, 35)
						ASTM E 1304, K_{Iv}
T-L						45, 45 (41, 41)
L-T						57, 51 (52, 46)
			4 K			
T	80 (11.6)	447 (69)	668 (97)	14	16	
L	72 (10.4)	516 (75)	671 (97)	17	23	
						ASTM E 813, K_{Ic} (J)
T-L						33, 33 (30, 30)
L-T						35, 42 (32, 38)
						ASTM E 1304, K_{Iv}
T-L						51, 57 (46, 52)
L-T						47, 41 (43, 37)

NOTE: msi = million pounds/in.^{2}.

TABLE 11—*Tensile and fracture toughness properties: 2090-T81-3/4, 19.1-mm plate.*

Specimen Orientation	Young's Modulus, GPa (msi)	Yield Strength, MPa (ksi)	Tensile Strength, MPa (ksi)	Elongation, %	Reduction of Area, %	Fracture Toughness, MPa $\sqrt{m}$ (ksi $\sqrt{in.}$)
			295 K			
T	79 (11.4)	559 (81)	597 (86)	6	13	
L	77 (11.2)	578 (84)	608 (88)	8	17	
						ASTM E 813, K_{Ic} (J)
T-L						25 (23)
L-T						37 (34)
						ASTM E 1304, K_{Iv}
T-L						32, 34, 29 (29, 31, 26)
L-T						44, 45, 43 (40, 41, 39)
			76 K			
T	87 (12.6)	624 (90)	693 (100)	3	4	
L	86 (12.5)	649 (94)	738 (107)	10	2	
						ASTM E 813, K_{Ic} (J)
T-L						24 (22)
L-T						33 (30)
						ASTM E 1304, K_{Iv}
T-L						34, 37 (31, 34)
L-T						50, 50 (46, 46)

NOTE: msi = million pounds/in.^{2}.

TABLE 12—*Tensile and fracture toughness properties: 2090-T81-1/2, 12.7-mm plate.*

Specimen Orientation	Young's Modulus, GPa (msi)	Yield Strength, MPa (ksi)	Tensile Strength, MPa (ksi)	Elongation, %	Reduction of Area, %	Fracture Toughness, MPa $\sqrt{m}$ (ksi $\sqrt{in.}$)
			295 K			
T	78 (11.3)	507 (73)	546 (79)	2	4	
L	77 (11.2)	501 (73)	530 (77)	7	9	
						ASTM E 813, K_{Ic} (*J*)
T-L						34, 29 (31, 26)
L-T						35, 49 (32, 45)
						ASTM E 1304, K_{Iv}
T-L						23, 28, 28 (21, 25, 25)
L-T						48, 49, 47 (44, 45, 43)
			76 K			
T	89 (12.9)	570 (83)	6[illegible] (88)	1	4	
L	87 (12.6)	550 (80)	616 (89)	9	9	
						ASTM E 813, K_{Ic} (*J*)
T-L						27, 50 (25, 46)
L-T						74, 64 (67, 58)
						ASTM E 1304, K_{Iv}
T-L						31, 35 (28, 32)
L-T						53, 59 (48, 54)
			4 K			
T	89 (12.9)	621 (90)	669 (97)	1	4	
L	88 (12.8)	600 (87)	688 (100)	10	17	
						ASTM E 813, K_{Ic} (*J*)
T-L						41, 51 (37, 46)
L-T						58, 71 (53, 65)
						ASTM E 1304, K_{Iv}
T-L						36, 45 (33, 41)
L-T						51, 55 (46, 50)

NOTE: msi = million pounds/in.^{2}.

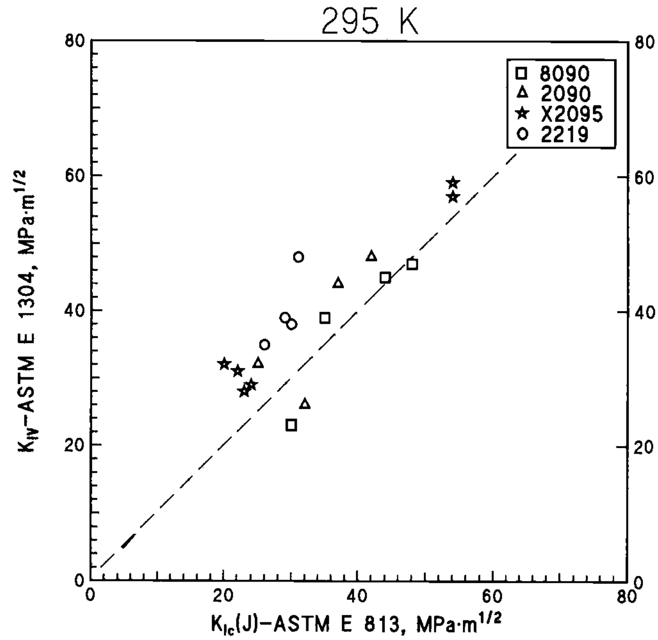

FIG. 2—*Comparison of fracture toughness calculated by Method E 813 and E 1304 at 295 K.*

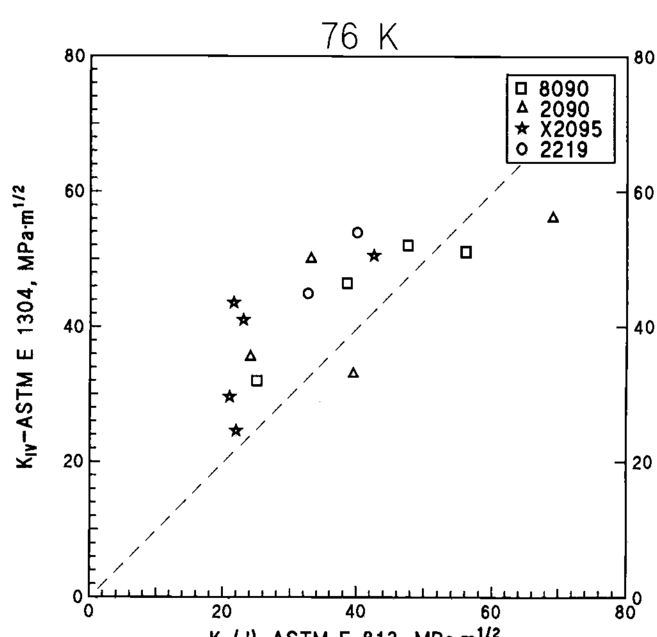

FIG. 3—*Comparison of fracture toughness calculated by ASTM E 813 and E 1304 at 76 K.*

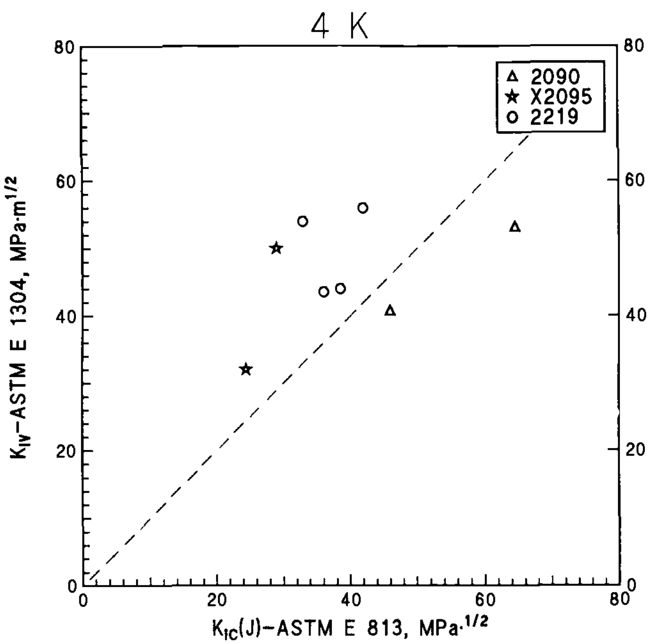

FIG. 4—*Comparison of fracture toughness calculated by ASTM E 813 and E 1304 at 4 K.*

Exceptions to this trend occur for Alloys 8090 and 2090, which exhibit extensive delaminations on the fracture surface. For these alloys, the fracture toughness from *C*(T) specimens is usually larger than the fracture toughness from the chevron-notched specimens. The behavior of Alloys 8090 and 2090 is tied to delaminations along the pancaked grain boundaries that form free surfaces perpendicular to the crack front. An example of the size and frequency of delaminations are shown in Fig. 5, which is a scanning electron microscope photograph of the fracture surface of alloy 2090-T81-1/2 tested at 4 K.

The appearance of the curves of load (*P*) versus crack mouth opening displacement (CMOD) in the fracture toughness tests was a function of the material's tendency to delaminate. The delaminations produce an increase in the CMOD reading without an appreciable change in unloading compliance. In this way, the formation of a delamination resembles plastic deformation, adding to the fracture toughness in the J_{Ic} test. In the chevron-notched specimens, if the load-displacement curve shows extensive displacement before maximum load, that displacement does not directly add to the fracture toughness as in the J_{Ic} test.

Representative *P*-versus-CMOD curves for both test methods from a plate that delaminated (Alloy 2090-T81-1/2) and one that did not (Alloy X2095-T851) are shown in Figs. 6 and 7. The curves for Alloy 2090 from the two test procedures, Figs. 6*a* and 7*a*, are similar in that they both show relatively large CMOD values before the maximum load is reached. The curves for Alloy X2095, Figs. 6*b* and 7*b*, show less CMOD than observed for Alloy 2090.

The influence of delaminations on the determination of J_{Ic} can be seen by comparing Fig. 6*a* and *b*. The fracture toughness of the C(T) specimen by Method E 813 is approximated by the area under the curve up to the point where the compliance increases significantly, marked as J_{Ic} on the curve. If the *P*-versus-CMOD curves of C(T) specimens were analyzed by Method E 399, the critical load that corresponds to the intersection of the curve with

FIG. 5—*Fracture surface of C(T) specimen from Alloy 2090-T81-1/2 tested at 4 K.*

the 5% secant is marked as K_{Ic}. For Alloy 2090, the critical points on the curve are significantly different, while for Alloy X2095, the points are nearly the same.

For Alloy X2095, there is little evidence for delaminations on the fracture surface. The *P*-versus-CMOD curve for the C(T) specimen, shown in Fig. 6*b*, is nearly linear-elastic with a relatively small CMOD to reach the maximum load. The C(T) curve can also be evaluated by Method E 399 [*9*] for K_{Ic}, but in general the ratio of P_{max}/P_q is greater than 1.10, so a

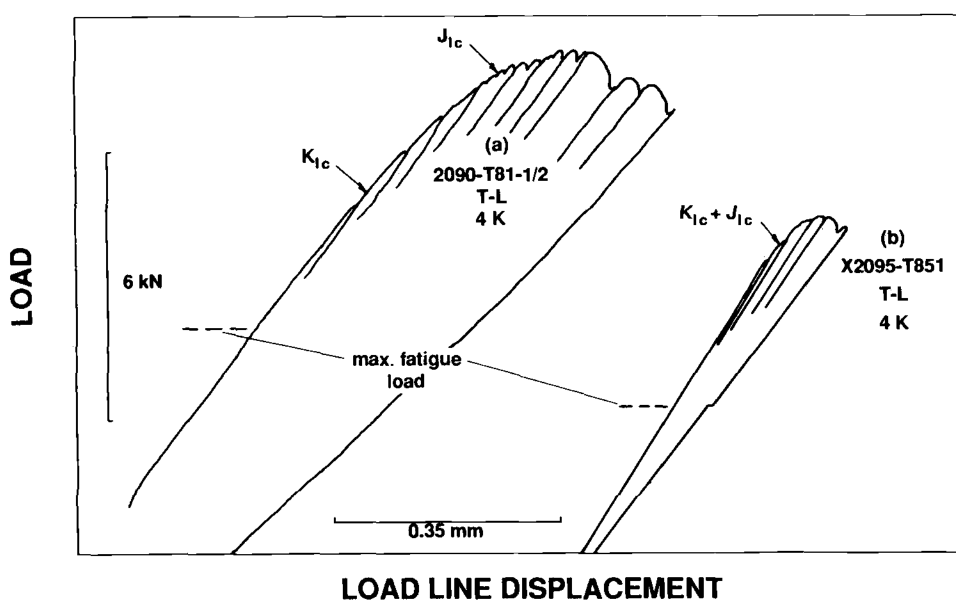

FIG. 6—*P-versus-CMOD curves for C(T) specimens of alloys* (a) *2090-T81-1/2 and* (b) *X2095-T851.*

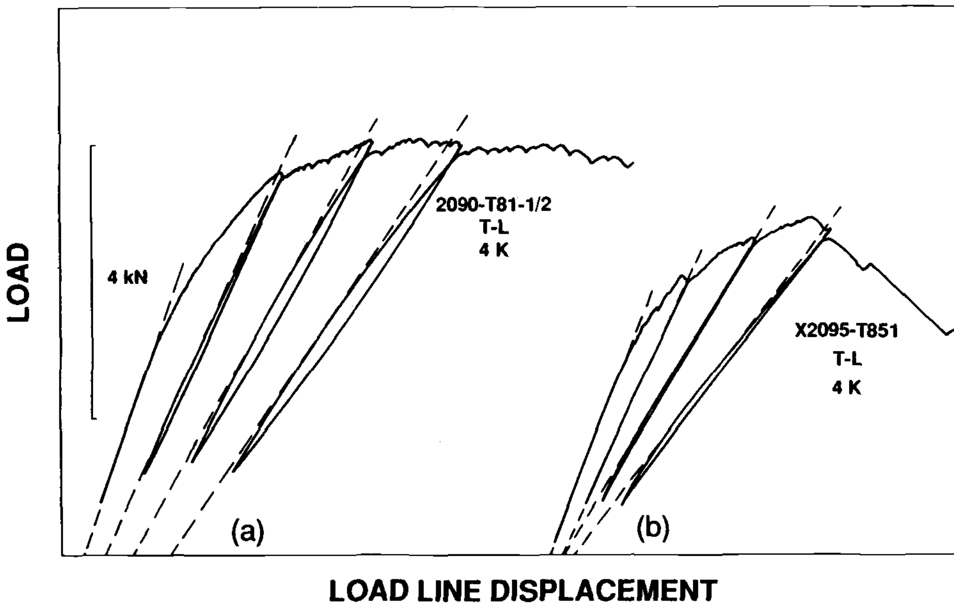

FIG. 7—*P-versus-CMOD curves for chevron-notched specimens of alloys* (a) *2090-T81-1/2 and* (b) *X2095-T851.*

K_{Ic} analysis is not always valid for the X2095 specimens. An *R*-curve analysis for each *P*-versus-CMOD curve from a C(T) specimen would show that the maximum *K* is increasing with crack growth, but for Alloy X2095 the increasing *R*-curve is particularly significant because the fracture toughness is relatively low and plane strain conditions are maintained at the crack front (evidenced by small shear lips).

In the chevron-notched specimen, the fracture toughness is proportional to the load at the critical point on the curve. Alloy 2090 in Fig. 7 shows larger hysteresis in the unloading portions of the curve than in alloy X2095. If the value of p (as defined by Eq 2) is calculated, the test for Alloy 2090 is invalid. Normally, the value of p is a measure of the plastic zone, but in this case, the large hysteresis and value of p are indications of delaminations. The value of p for Alloy X2095 is nearly zero at all crack length, indicating that the plastic zone remains relatively small throughout the test and plane strain conditions are maintained.

Discussion

The behavior of the aluminum alloys in fracture toughness testing is complex. The two tests, Methods E 1304 and E 813, do not always give equivalent results for characterizing the fracture toughness of this new class of materials. The differences between the two test methods can be understood by looking closely at the material behavior with respect to the test.

At the lowest fracture toughness, Alloy X2095-T851 and T651 show a large relative discrepancy between the two tests where the fracture toughness of chevron-notched specimens can be 100% greater than that of C(T) specimens (Alloy X2095-T851 at 76 K in the L-T orientation). At similar K_{Ic} toughness, Brown found good agreement between fatigue precracked C(T) and chevron-notched specimens [9]. The X2095-T851 and -T651 show a rising crack growth resistance under plane strain conditions similar to that observed in Al_2O_3

by Munz et al. [3]. The maximum K that can be calculated from Fig. 6*b* is about 10% greater than $K_{Ic}(J)$, but in other specimens from alloy X2095, it was as large as 100% larger. Because $K_{Ic}(J)$ is evaluated at a relatively short crack extension and K_{Iv} is evaluated at a relatively long crack extension, one might expect K_{Iv} to be higher than $K_{Ic}(J)$.

When delaminations form in a C(T) specimen before the critical point on the P-versus-CMOD curve, the local stress state at the crack front is no longer plane strain. The relative influence of delaminations on fracture toughness is critically linked to the point the delaminations nucleate and their size. Rao et al. [8] sectioned interrupted C(T) specimens and found that the load for delaminations was about 85% of the critical load measured in Method E 399 testing. For these results, we assume that the delaminations form in the C(T) specimen soon after the P-versus-CMOD curve departs from linearity, then the plastic component of the CMOD at J_{Ic} can be attributed to delamination. The ability of the 2090 and 8090 alloys to plastically deform is relatively low, as seen in the tension test results (Table 4), so the assumption that delamination starts when the P-versus-CMOD curve becomes inelastic seems appropriate. For the curve shown in Fig. 6*a*, the delamination contribution to $K_{Ic}(J)$ can be estimated to be 50% of the total. If $K_{Ic}(J)$ is reduced by 50%, then K_{Iv} is greater than $K_{Ic}(J)$, similar to the correlation for other alloys. Also, the delamination toughening varies from specimen to specimen because the location of the weak grain boundaries varies with respect to the fatigue precrack, contributing to the scatter in $K_{Ic}(J)$ for Alloys 2090 and 8090.

These comparisons between the two test methods are informative because they highlight the differences between the methods and the materials' fracture behavior. Method E 813 is best used when the material shows significant plastic deformation prior to crack growth (elastic-plastic behavior). The energy dissipated through plastic deformation before crack growth can be converted to an equivalent elastic stress intensity by Eq 1. The problem arises when the material shows extensive delamination toughening that is treated in the data analysis the same as plastic deformation. There is no equivalent elastic stress intensity factor to account for delamination toughening. For this reason, the $K_{Ic}(J)$ values reported here for 2090 and 8090 cannot be considered plane-strain, lower-bound estimates of fracture toughness. The E 1304 method is not based on the area under the P-versus-CMOD curve and is therefore not influenced by delamination toughening to the same degree as the E 813 method. The K_{Iv} values appear to be better estimates for design purposes of the lower-bound fracture toughness than the $K_{Ic}(J)$ values when the alloy exhibits extensive delaminations.

These considerations of the results highlight the need to understand the limitations of a test before the results are used. We can consider that the fracture toughness measured in a test under given conditions is composed of intrinsic and extrinsic components. The intrinsic part is the material property and the extrinsic part depends upon the given set of test conditions, like specimen width and thickness. The standard test methods for fracture toughness are set up so that if the guidelines are followed, the extrinsic component is minimized. However, in forming the guidelines, certain assumptions are made with regard to how the material will behave. If the material shows unusual behavior, the guidelines may not insure that the extrinsic contribution to the measured fracture toughness, the delamination toughening, is small compared to the material property. The behavior seen here for Alloys 2090 and 8090 are good examples of how delaminations complicate the evaluation of fracture toughness.

In summary, the two methods discussed in this paper for measuring fracture toughness do not always agree. Each has its advantages and disadvantages. The short-bar specimen is smaller and requires lower loads to test. The procedure is simpler and faster, and when the material exhibits delaminations, K_{Iv} is lower than $K_{Ic}(J)$ and may be a better engineering estimate of the lower-bound fracture toughness. In the end, we must agree with Brown [9] and consider that the short-bar specimen is useful for screening purposes even when there is no 1:1 correlation with $K_{Ic}(J)$. The fatigue-precracked C(T) specimen tested for J_{Ic} is a widely used technique to measure plane-strain fracture toughness in elastic-plastic materials. However, high-strength Al-Li alloys are not elastic-plastic at cryogenic temperatures and, depending upon composition and temper, exhibit extensive delaminations that can lead to an overestimation of the lower-bound fracture toughness.

Conclusions

1. For high-strength Al alloys, K_{Iv} measured with chevron-notched short-bar specimens does not have a 1:1 correlation to $K_{Ic}(J)$ measured with a fatigue-precracked compact specimen. Typically, K_{Iv} is higher than $K_{Ic}(J)$.
2. The exception to the trend is for materials that exhibit extensive delaminations on the surface, Alloys 2090 and 8090. In this case, K_{Iv} is lower than $K_{Ic}(J)$, and $K_{Ic}(J)$ does not represent a lower-bound, plane-strain fracture toughness.
3. Alloys X2095 and 2219 in T8 and T6 tempers have relatively low $K_{Ic}(J)$, and much higher K_{Iv}. The difference in fracture toughness between the two test procedures is thought to be due to an increase in the crack growth resistance in plane strain conditions.
4. The chevron-notched short-bar specimen is useful for ranking different alloys and correlating the effects of thermomechanical processing with respect to fracture toughness.

Acknowledgments

This work was done for the Air Force Systems Command, Edwards Air Force Base, Contract No. 99011. Reynolds Metals, ALCOA, ALCAN, and Kaiser aluminum companies supplied the materials used in this study. Special thanks to David Mason of NIST-Boulder for his help in specimen preparation.

References

[1] Barker, L. M., "Short Rod and Short Bar Fracture Toughness Specimen Geometries and Test Methods for Metallic Materials," *Fracture Mechanics, ASTM STP 743*, 1981, p. 456.
[2] Brown, K. R., "The Use of the Chevron-Notched Short-Bar Specimen for Plane Strain Toughness Determinations in Aluminum Alloys," *Chevron-Notched Specimens: Testing and Stress Analysis, ASTM STP 855*, American Society for Testing and Materials, Philadelphia, 1984, p. 237.
[3] Munz, D., Bubsey, R. T., and Shannon, Jr., J. L., "Performance of Chevron-Notch Short Bar Specimen in Determining the Fracture Toughness of Silicon Nitride and Aluminum Oxide," *Journal of Testing and Evaluation*, Vol. 8, No. 3, May 1980, p. 103.
[4] ASTM Standard E 813-89: Test Method for J_{Ic}, a Measure of Fracture Toughness, American Society for Testing and Materials, Philadelphia, 1990, p. 700.
[5] ASTM Standard E 1304-89: Test Method for Plane-Strain (Chevron-Notch) Fracture Toughness of Metallic Materials, American Society for Testing and Materials, Philadelphia, 1990, p. 927.
[6] Reed, R. P., Purtscher, P. T., McColskey, J. D., Walsh, R. P., Berger, J. R., Drexler, E. S., Santoyo, R., and Simon, N. J., "Aluminum Alloys for ALS Cryogenic Tanks: Comparative Measurements of Cryogenic Mechanical Properties of Al-Li Alloys and Alloy 2219," to be published as internal report, Boulder, CO.
[7] Rosenthal, Y. A., Tobler, R. L., and Purtscher, P. T., "J_{Ic} Data Analysis Procedure with a 'Negative Crack Growth' Correction," *Journal of Testing and Evaluation*, 1990, p. 301.
[8] Rao, K. T. V., Yu, W., and Ritchie, R. O., "Cryogenic Toughening of Commercial Aluminum-Lithium Alloys—Role of Delamination Toughening," *Metallurgical Transactive, A*, Vol. 20A, 1989, p. 485.
[9] ASTM Standard E 399-83: Test Method for Plane-Strain Fracture Toughness of Metallic Materials, American Society for Testing and Materials, Philadelphia, 1900, p. 488.

[10] Dorward, R. C., "Cryogenic Toughness of Al-Cu-Li Alloy AA 2090," *Scripta Metallurgica*, Vol. 20, 1986, p. 1379.

[11] Purtscher, P. T. and Drexler, E. S. "Through-Thickness Toughness Properties of High-Strength Aluminum Alloy Plates for Cryogenic Applications," *Proceedings*, Symposium on Light Weight Alloys for Aerospace Applications, New Orleans, E. W. Lee and N. J. Kim, Eds., February 1991, The Metallurgical Society, Warrendale PA, 1991, pp. 65–76.

Jack W. Bray[1]

Use of the Chevron-Notched Short Bar Test to Guarantee Fracture Toughness for Lot Release in Aluminum Alloys

REFERENCE: Bray, J. W., "**Use of the Chevron-Notched Short Bar Test to Guarantee Fracture Toughness for Lot Release in Aluminum Alloys,**" *Chevron-Notch Fracture Test Experience: Metals and Non-Metals, ASTM STP 1172*, K. R. Brown and F. I. Baratta, Eds., American Society for Testing and Materials, Philadelphia, 1992, pp. 131–143.

ABSTRACT: Chevron-notched short bar fracture toughness (K_{IvM} per ASTM E 1304) has been correlated with plane strain fracture toughness (K_{Ic} or K_Q per ASTM E 399 or ASTM B 645) for commercial 2124-T851, 7050-T7451, 7050-T7651, and 7475-T7351 plate.

It was found that the chevron-notched and $K_{Ic}(K_Q)$ test methods correlated regardless of alloy, orientation, or temper. However, larger scatter in the higher toughness materials resulted in expected retest rate advantages (% of time the correlative test would fail and the referee test would pass lot release) when separating the results into "low" and "high" toughness databases. An *A* value minimum approach, via computation of derived properties (as defined in paragraphs 9.2.10 and 9.2.11 of *Military Handbook 5E*), was used to calculate the lot release correlations between K_{IvM} and $K_{Ic}(K_Q)$. In addition, statistical correlations were performed on the entire database in order to utilize the chevron-notched short bar test more effectively for research and development programs.

KEY WORDS: fracture toughness, chevron-notch short bar, fracture test invalidity, aluminum alloys, correlations, *A* minimums, K_{Ic}, K_Q, K_{IvM}, K_{Iv}, 2124, 7050, 7475, lot release

Background

The use of fracture mechanics to guarantee the damage tolerance of high-strength aluminum aerospace materials has grown steadily since the early 1960s. The fracture toughness characterization parameter of preference for linear elastic materials is K_{Ic}, the plane-strain fracture toughness, which is generated per ASTM E 399, Standard Test Method for Plane-Strain Fracture Toughness of Metallic Materials. The fatigue-precracked compact tension K_{Ic} test (specimen shown in Fig. 1) is relatively expensive to perform, however, and various tests have been utilized to predict K_{Ic}, most notably the notched tensile strength test [*1*]. Unfortunately, this test often correlates poorly with K_{Ic} and is sensitive to the acuity of the notch root radius and the load train alignment. Recently, ASTM Subcommittee E24.01 has developed a chevron-notched fracture test method (Standard Test Method for Plane-Strain (Chevron-Notch) Fracture Toughness of Metallic Materials, ASTM E 1304), for which the specimen does not require fatigue precracking and is therefore less expensive to evaluate. Unlike the notch tensile test, the short bar specimen provides a relative measure of the plane-strain fracture toughness [*2,3*]. Thus, the chevron-notched test is expected to provide a better prediction of plane strain fracture toughness K_{Ic}. Indeed, with sufficiently brittle

[1]Supervisor, Mechanical Metallurgy Section, Reynolds Metals Company, Metallurgy Laboratory, Richmond, VA 23219.

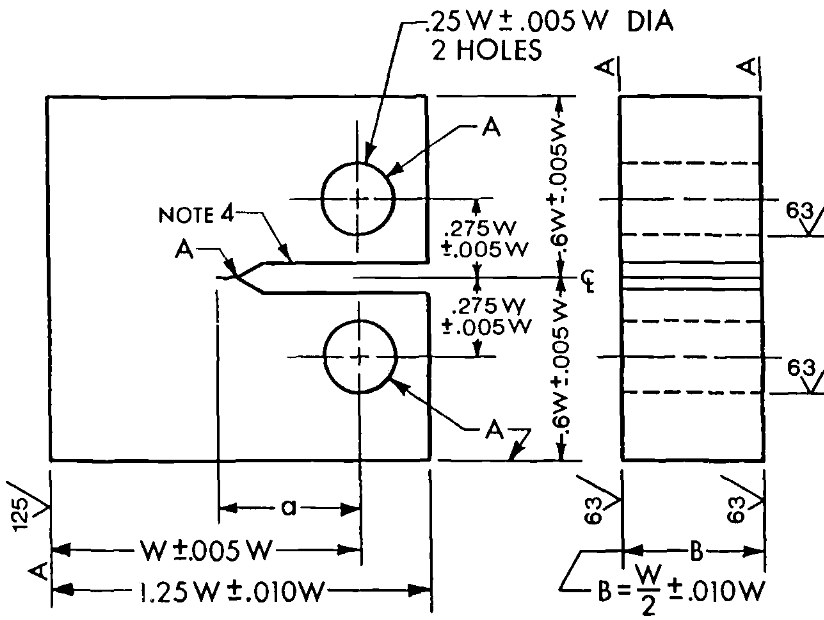

FIG. 1—*Compact tension test specimen (ASTM E 399).*

materials it can be shown that the short bar test result (K_{Iv}) generated per ASTM E 1304 is numerically equivalent to K_{Ic} [*4*]. In addition to K_{Iv}, a simplified (based on the maximum load) test parameter K_{IvM} can be calculated from the chevron-notched load-displacement curves. K_{IvM} is simpler to analyze and requires only a thickness validity check (Table 1). Thus, the short bar test can also be advantageous from a standpoint of providing invalidity alleviation. The chevron-notched short bar specimen is shown in Fig. 2. Further details of the mechanics of the short bar test can be found elsewhere [*4–6*].

For heavier section aluminum alloy plate, K_{Ic} is typically generated via ASTM B 645 (Standard Practice for Plane-Strain Fracture Toughness Testing of Aluminum Alloys). B 645-90 allows some alleviation from the E 399 requirements for excess plasticity and specimen thickness (which ensure that plane strain conditions are met). Certain results calculated per B 645 estimate K_{Ic} and are considered "meaningful" and acceptable for lot release. For relatively high toughness aluminum alloys (such as 7475-T7351) K_Q results often cannot be considered meaningful [7]. However, under certain testing conditions (paragraph 11.2.5 of B 645-90) the invalid K_Q results can be utilized for lot release. Therefore, in accordance with ASTM B 645-90, test results are used in this study which fall into the category of valid K_{Ic}, meaningful K_Q, and invalid K_Q. The invalid K_Q results met the B 645-90 criteria for lot release and were thus included in order to establish the $K_{Iv}(K_{IvM})$ and $K_{Ic}(K_Q)$ relationships over the full range of K_{Ic}-tested commercial aluminum aerospace alloys.

The purpose of this study was twofold: (1) to establish correlative database(s) whereby the short bar $K_{Ivm}(K_{Iv})$ could be utilized to guarantee $K_{Ic}(K_Q)$ for lot release purposes; and (2) to determine the feasibility of using the chevron-notched fracture test results to predict $K_{Ic}(K_Q)$. Lot release K_{Ic} (or K_Q) and short bar $K_{IvM}(K_{Iv})$ data pairs were generated independently by multiple producers (Reynolds Metals, Kaiser Aluminum, Ravenswood Aluminum) on a variety of aluminum alloys, plate thicknesses, and directions. The relationships

TABLE 1—*Validity requirements for fracture toughness tests.*

Parameter	ASTM Test Method	Validity Check
K_{Ic}	E 399	1. $P_{max}/P_Q <= 1.10$ Ensures that plane strain conditions are met. 2. $a,B >= 2.5\ (K_Q/YS)^2$ Ensures that plane strain conditions are met.
K_Q	B 645	1. $a >= 2.5\ (K_Q/YS)^2$ Ensures that the plastic zone is small compared to the crack length. 2. $P_{max}/P_Q <= 1.15$, depending upon B/W ratios. Ensures that K_Q approximates K_{Ic}.
K_{Iv}	E 1304	1. $P_M/P_c <= 1.10$ Ensures that plane strain conditions are met. 2. $B >= 1.25\ (K_{Iv}/YS)^2$ Ensures that plane strain conditions are met. 3. $-0.05 <= p <= 0.10$ Ensures that residual stresses are low or absent.
K_{IvM}	E 1304	1. $B >= 1.25\ (K_{IvM}/YS)^2$ Ensures that plane strain conditions are met.

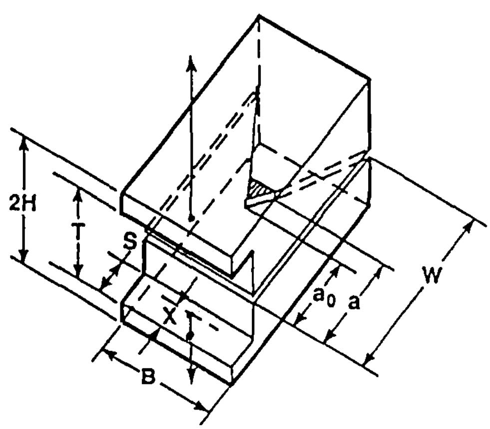

FIG. 2—*Chevron-notched short bar test specimen (ASTM E 1304).*

between $K_{Ic}(K_Q)$ and $K_{IvM}(K_{Iv})$ were examined utilizing linear regression statistical techniques. For correlative purposes, the "Direct Computational Procedure" given in chapter 9.2.11.1 of *Military Handbook, 5E* [*8*] was applied. This model identifies the short bar toughness level to guarantee a particular $K_{Ic}(K_Q)$ with 99% compliance at 95% confidence.

Experimental Procedures

Data Generation

Lot release K_{Ic} tests were performed on commercial aluminum aerospace materials, using the compact tension specimen, to ASTM E 399 or B 645 for the range of alloys, directions, and tempers shown in Table 2. All specimen sizes and sample locations were in accordance to the aerospace specification for which the plate was produced. In some circumstances valid (E 399) or meaningful (B 645) K_{Ic} or K_Q values could not be achieved; in these cases the material was released on the basis of: (*a*) K_Q being acceptable for lot release per B 645-90, and (*b*) following the acceptance of the invalidity or invalidities by the user(s). Therefore, the invalid K_Q results were included in the correlative database, as the primary goal was to utilize the short bar test for lot release.

Short bar specimens with $B = 1.0$ in., and a W/B ratio of 1.45, were machined from either the broken K_{Ic} specimen halves or adjacent material. The sample location was chosen such that the fracture planes of the compact tension and the short bar specimen were identically located (e.g., L-T K_{Ic} at $t/2$ paired with L-T $K_{IvM}(K_{Iv})$ at $t/2$, etc.). The short bar tests were performed and analyzed in accordance with ASTM E 1304. Similarly to the K_{Ic} test results, the short bar $K_{IvM}(K_{Iv})$ results were not excluded from the database due to invalidity issues.

$K_{Ic}(K_Q)$ and $K_{Ivm}(K_{Iv})$ data were generated as described above independently by multiple aluminum companies on materials produced at their respective plate mills. Subsequent combining of these database(s) ensured that the correlation would not be a function of the plate processing route.

Statistical Analysis

An A value correlation statistical approach for determining design allowables by regression analysis was applied in order to calculate the $K_{IvM}(K_{Iv})$ values to guarantee $K_{Ic}(K_Q)$. Known as the "Direct Computational Procedure," it is applicable when the relationship between the dependent and independent variables is linear. (Note: The assumption is made that the Y's are normally distributed around the mean for a given value of X.) This approach is outlined in Chapter 9 (in particular 9.2.11) of *MIL-Hdbk-5E* [*8*] and is described in detail by Ruff [*9*]. In essence, this approach allows identification of the short bar fracture toughness level which guarantees a particular $K_{Ic}(K_Q)$ (typically the specification minimum) at 95% confidence with 99% compliance. The regression analysis procedure is summarized as follows:

1. Perform (least squares) linear regression on the X $(K_{IvM}(K_{Iv}))$, Y $(K_{Ic}(K_Q))$ data pairs.
2. Utilize analysis of variance ($F_{statistics}$) to verify the linearity of the regression equation.
3. Calculate the A value lower bound (99% conforming with 95% confidence) according to:

$$A = (\text{Dep. Var.}) - k_A * s' * \{1 + 1/n + [x_0 - \text{sum}(x)/n]^2/[\text{sum}(x^2) - ((\text{sum}(x))^2/n)]\}^{1/2} \quad (1)$$

TABLE 2—*Materials evaluated.*

Alloy-Temper	Directions	Gages
2124-T851	L-T, T-L	2.75″–6.00″
7050-T7451	L-T, T-L	1.00″–6.00″
7050-T7651	L-T, T-L	1.00″–2.50″
7475-T7351	L-T, T-L, S-L	1.00″–4.25″

where

$$\text{Dep. Var.} = K_{Ic}(K_Q)$$

k_A = one-sided tolerance-limit factor corresponding to a proportion at least 0.99 of a normal distribution and a confidence coefficient of 0.95,
s' = standard error of estimate,
x_0 = K_{IvM} calculated from the linear regression for the particular dependent variable K_{Ic},
n = number of observations, and
sum(x) = summation of dependent variables ($K_{IvM}(K_{Iv})$).

This analytical technique provides the construction of a parabolic lower bound to the linear regression of the dependent and independent variables. This lower bound represents the value of the independent variable (in this case, short bar fracture toughness K_{IvM}) necessary to guarantee a specific level of the dependent variable (in this case K_{Ic} or K_Q) at the confidence level of 95% with 99% conformance. (Note: This lower bound, referred to in the figures as *A* Value Minimums," is not to be confused with the *A* basis mechanical property values of *MIL-Hdbk-5*, which are calculated from a normally distributed population of a *single* variable.) An *X-Y* plot showing both the linear regression and the *A* value lower bound allows the user (graphically) to ascertain the necessary *A* correlation value minimum at the dependent variable level of interest.

Figure 3, using demonstration data, illustrates graphically the *A* correlation value approach. From the referee value of interest (typically a specification minimum), a horizontal line is drawn to the *A* value lower confidence band in order to establish the *A* correlative test value. This graph also demonstrates, through the marked quadrants, the effectiveness of the correlation test in replacing the referee test.

Prior to performing the *A* correlation value calculation, the "$Y = bX + c$" linear regres-

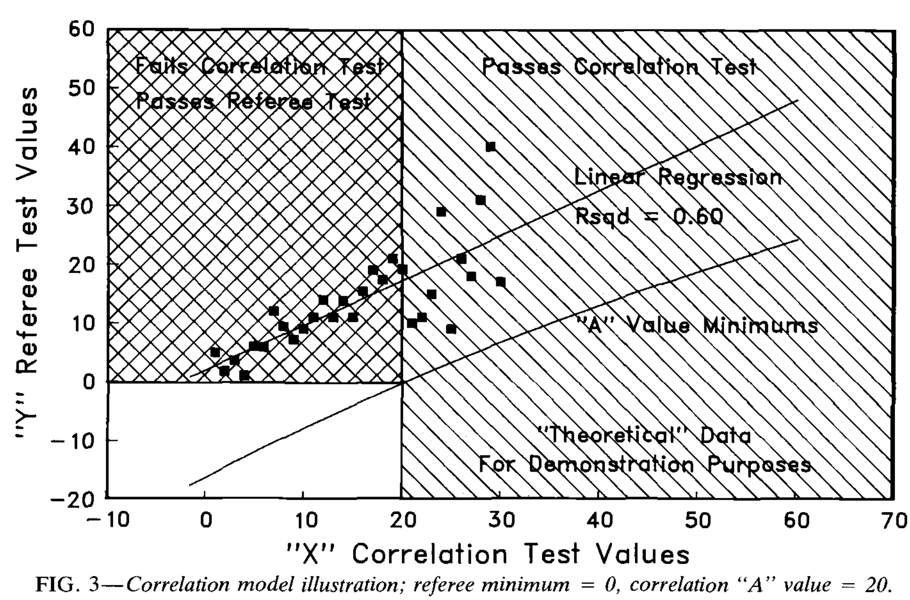

FIG. 3—*Correlation model illustration; referee minimum = 0, correlation "A" value = 20.*

sion was performed both with $b = K_{IvM}(K_{Iv})$ and b = Natural Logarithm ($K_{IvM}(K_{Iv})$). The logarithmic model was forced, as previous researchers have shown that the relationship between K_{Ic} and $K_{IvM}(K_{Iv})$ is curvilinear at higher toughness [*10*].

Results and Discussion

General

Preliminary analysis of the data showed that a slightly better regression (based on the linear regression R^2) was obtained when the K_{IvM} parameter was correlated with $K_{Ic}(K_Q)$, as opposed to K_{Iv}. As the K_{IvM} parameter is easier to generate and requires fewer validity checks than K_{Iv}, subsequent correlation efforts centered on it.

A plot of all data pairs regardless of alloy, direction, or plate thickness is shown in Fig. 4. It is evident from this plot that the correlation between K_{IvM} and $K_{Ic}(K_Q)$ exists essentially on the basis of the *test methods* and is not a function of material; thus, various alloys, directions, and plate thicknesses can be grouped together for correlative purposes. It is noted, however, that greater scatter is present in the higher toughness 7475 alloy. Therefore, in order to reduce retest rates when using the *A* correlation value K_{IvM} to guarantee $K_{Ic}(K_Q)$, the lower toughness 2124-T851, 7050-T7451, and 7050-T7651 were analyzed as one database and 7475-T7351 was analyzed as another (discussion following).

Use of K_{IvM} *to Predict* $K_{Ic}(K_Q)$

It was found that selecting a logarithmic data model (described earlier) resulted in essentially the same R^2 value as did a linear fit (0.928 versus 0.929) when utilizing K_{IvM} to predict $K_{Ic}(K_Q)$ for the entire database. The linear and logarithmic models are shown in Fig. 5. The equation coefficients are as follows:

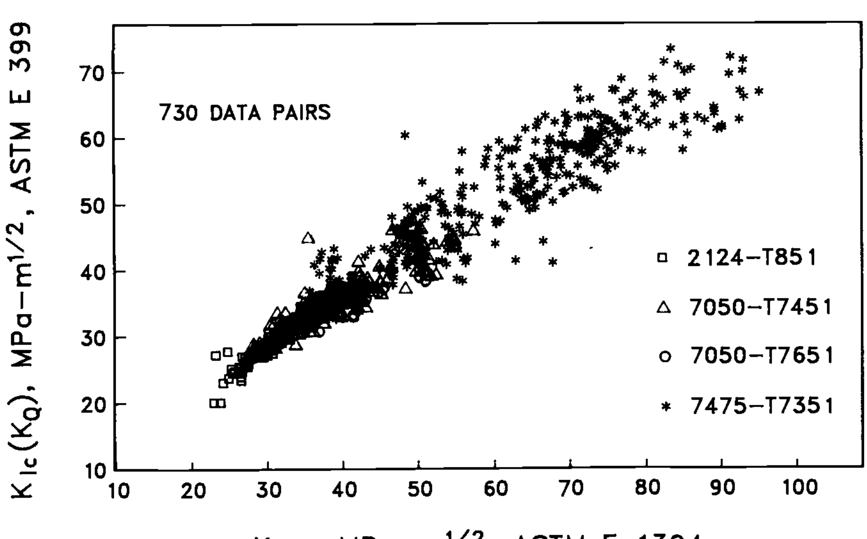

FIG. 4—K_{Ic} *or* K_Q *vs.* K_{IvM}; *all alloys, directions, plate thicknesses.*

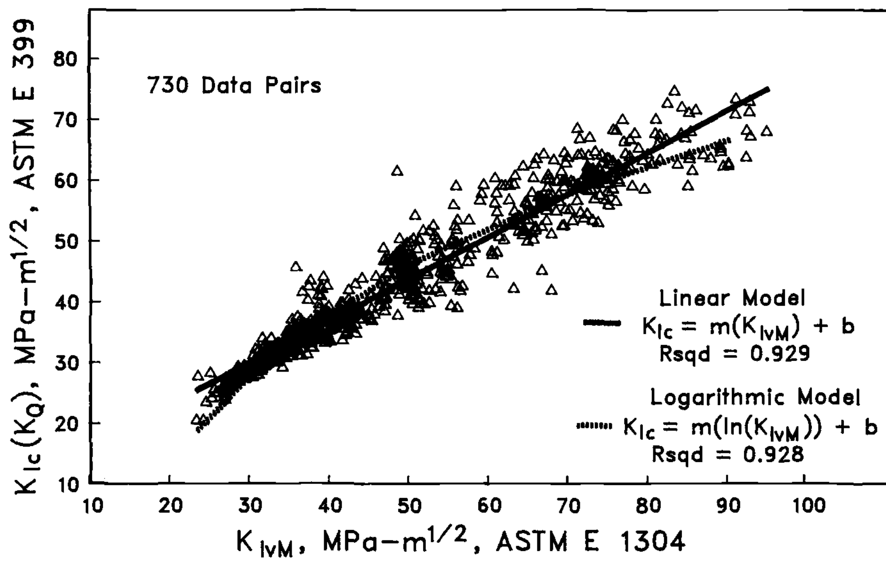

FIG. 5—*Models of* K_{Ic} *or* K_Q *as a function of* K_{IvM}; *all alloys, directions, plate thicknesses.*

- *Linear Regression:*

$$K_{Ic} = 0.681\ (K_{IvM}) + 9.259 \tag{2}$$

$$R^2 = 0.929$$

- *Forced Logarithmic (Linear) Regression:*

$$K_{Ic} = 34.13\ (\ln\ (K_{IvM})) - 88.19 \tag{3}$$

$$R^2 = 0.928$$

It is well established that R-curve and/or thickness heterogeneity effects cause K_{IvM} to overpredict K_{Ic} (using absolute magnitude) at K_{Ic} values higher than, roughly, 40 MPa-m$^{1/2}$ [*10,11*]. One researcher has found that a logarithmic correction can be used to collapse K_{IvM} to K_{Ic} [*10*]. However, the data analyzed in this report indicate that, over the range, specimen size, and validity of the $K_{Ic}(K_Q)$ results evaluated, the linear model was as good as the logarithmic model in utilizing the independent variable X (K_{IvM}) to explain the variance in the dependent variable Y ($K_{Ic}(K_Q)$). It is not proposed that the current data are in conflict with earlier findings; indeed, close examination of Figs. 5 and 6 indicates that, at lower toughness, K_{IvM} and $K_{Ic}(K_Q)$ converge. It is proposed that, under the conditions mentioned above, a linear regression model of $K_{Ic}(K_Q)$) versus K_{IvM} is as effective for a correlative lot release procedure as one involving more complicated mathematics. Thus, the linear regression model, which has been used previously for correlating K_{Ic} with notch tensile/yield strength ratios [*12*], was utilized for the K_{IvM} A correlation value analysis. The linear regression model listed above (Eq 2) is recommended for use to predict $K_{Ic}(K_Q)$) from K_{IvM} data.

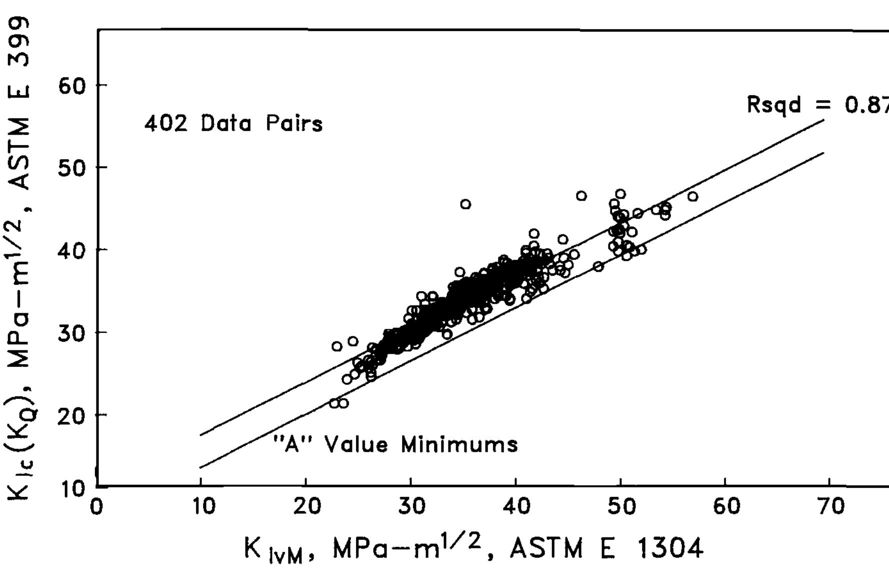

FIG. 6—K_{Ic} *vs.* K_{IvM} *correlation; 2124-T851, 7050-T7451, 7050-T7651.*

Use of K_{IvM} *to Guarantee a Minimum* $K_{Ic}(K_Q)$

As noted previously, more scatter was apparent in the 7475-T7351 $K_{IvM}/K_{Ic}(K_Q)$ data pairs than for lower toughness alloys. In order to optimize the effectiveness of the *A* value minimum approach, the data pairs were separated into "lower toughness" alloys (2124-T851, 7050-T7451, and 7050-T7651) and "higher toughness" alloys (7475-T7351). Subsequently, an analysis of variance approach was applied to establish the validity of the linear regression by calculating the $F_{\text{probability}}$ (unexplained/explained variance). It was found that each database gave good linear regression results, with $F_{\text{probability}} < 0.0001$ (Table 3).

Lower-Toughness Alloys

The correlation plot with calculated *A* correlation value K_{IvM} minimum for alloys 2124-T851, 7050-T7451, and 7050-T7651 is shown in Fig. 6. All K_{IvM} results in this database are valid. The K_{Ic} and/or K_Q results were valid (E 399) or meaningful (B 645). At the lower toughness of these alloys, no appreciable scatter was noted due to alloy, temper, direction, or plate thickness.

TABLE 3—*Analysis of variance statistics.*

Database	No. of Observations	*F*	Probability
Low Toughness	402	2707	<0.0001
High Toughness	328	1284	<0.0001

Higher-Toughness Alloys

The correlation plot with calculated A value K_{IvM} minimums for 7475-T7351 is shown in Fig. 7. Most K_{IvM} results in this database were valid, while some failed the thickness check of ASTM E 1304. The K_{Ic} and/or K_Q values represented valid (E 399), meaningful (B 645), and invalid (albeit acceptable for lot release per B 645-90) results.

Representative data were further analyzed to ascertain the reasons for the higher scatter in the "high toughness" database. Figures 8, 9, and 10 show respectively the influences of validity, orientation, and plate thickness on the $K_{Ic}(K_Q)/K_{IvM}$ relationships. Validity issues and test orientation did not account for data scatter. However, as shown in Fig. 10, it was found that thinner plate thicknesses (for the L-T and T-L orientations) produced generally higher K_{IvM} values for the same range of $K_{Ic}(K_Q)$) values. This phenomenon has been investigated in aluminum alloys by Brown [*11*], who found that the shift in K_{IvM} values with plate thickness is attributed primarily to through-thickness fracture toughness variations, and to a lesser degree R-curve and K_{Ic} specimen size effects. The plate thickness effect arises when the short bar specimen (with an effective width of essentially $B/3$) samples material which has an average toughness greater than the average toughness of the wider sampling path of the larger K_{Ic} test specimen. This phenomenon is shown graphically in Fig. 11. The rising R-curve phenomena (which causes K_{IvM} to overpredict K_{Ic}) is well established [*13*]. More recently, Barker [*14*] has proposed that it is the $K_{Ic}(K_Q)$) which is influenced by the R-curve effect, with the hypothesis that, if large enough specimens are tested, K_{Ic} and the short bar result should be in agreement. It is interesting to note that, in Fig. 10, where the 7475-T7351 L-T 4.25 in. K_Q results were generated with an unusually large compact tension specimen (W = 8.5 in., compared to W = 6.0 in. maximum for lighter gage L-T tests), the trend for K_{IvM} to more closely approximate K_Q is indeed observed.

Regardless, due to availability of data, all "high toughness" plate thicknesses were grouped together for the calculation of the A correlation value minimums. As additional data become available, it may prove beneficial to further subdivide this database into "thin" and "thick" original plate thicknesses in order to improve the statistics and retest rates.

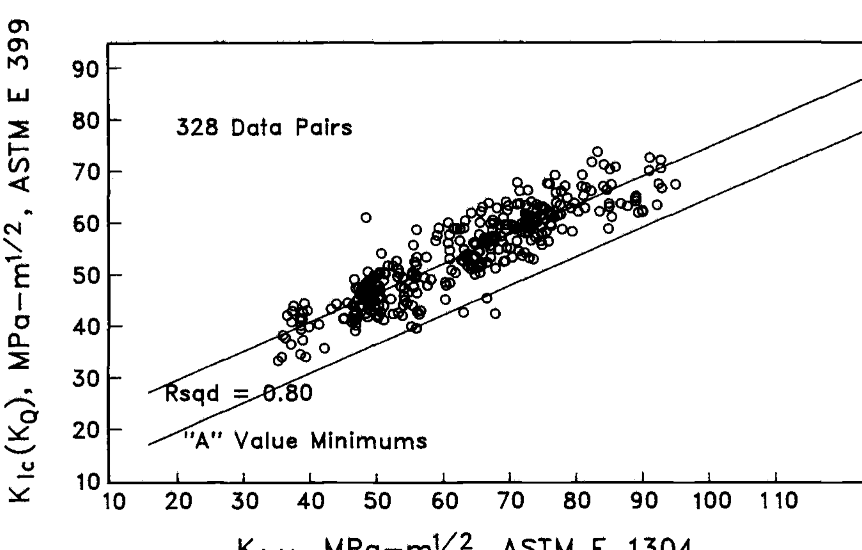

FIG. 7—K_{Ic} (K_Q) *vs.* K_{IvM} *correlation; 7475-T7351, all directions, plate thicknesses.*

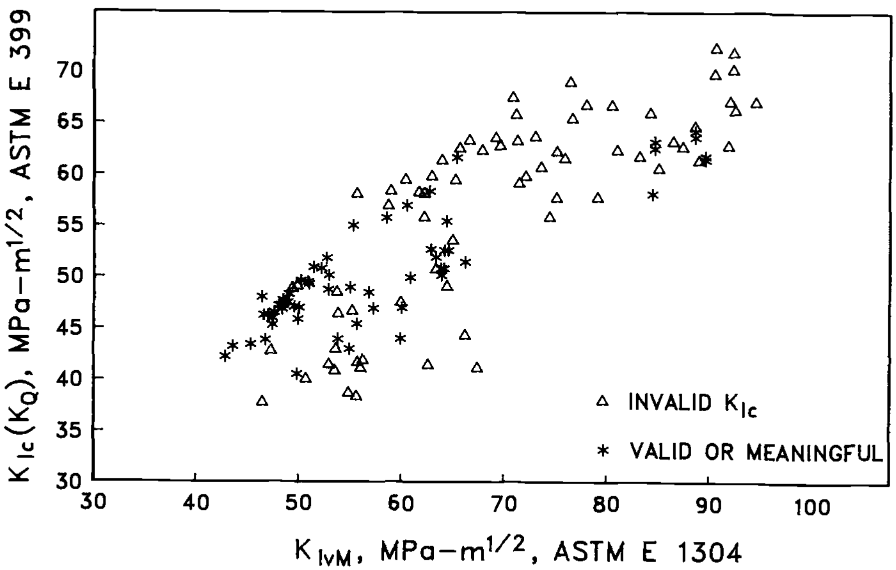

FIG. 8—K_{Ic} *or* K_Q *as a function of* K_{IvM}; *7475-T7351, all directions, by validity.*

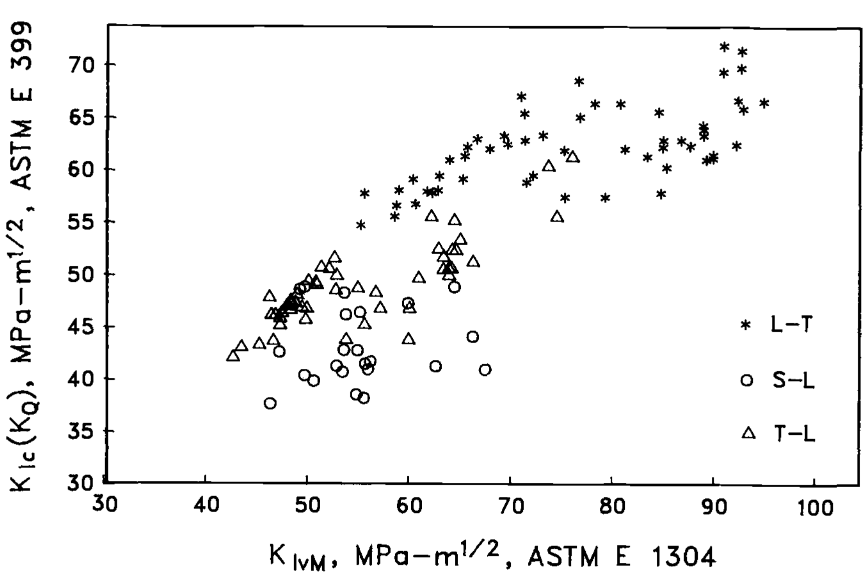

FIG. 9—K_{Ic} *or* K_Q *as a function of* K_{IvM}; *7475-T7351 L-T, T-L, S-L.*

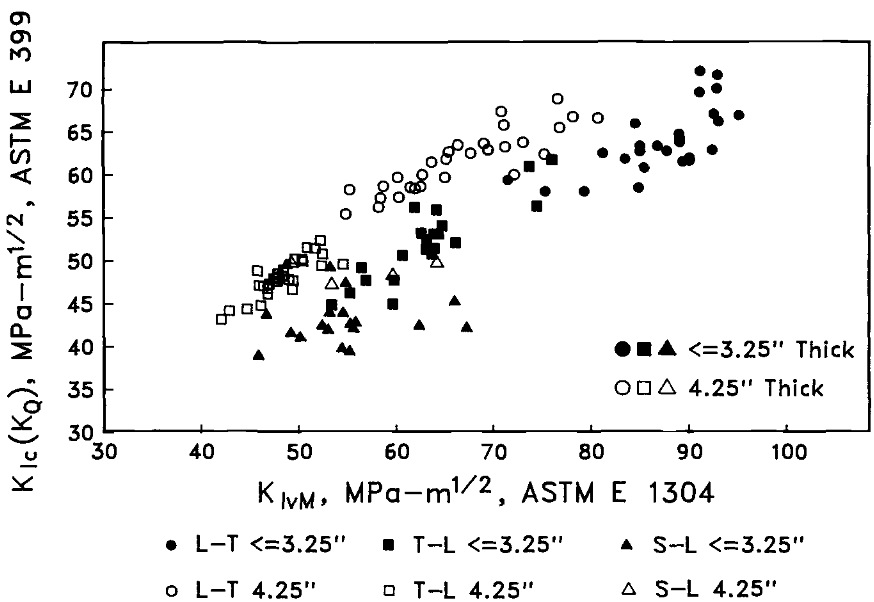

FIG. 10—K_{Ic} *or* K_Q *as a function of* K_{IvM}; *7475-T7351 by direction and plate thickness.*

Conclusions

A linear regression approach is successful in using K_{IvM} to predict $K_{Ic}(K_Q))$ in commercial aluminum aerospace alloys; it is proposed, where appropriate, that this relationship (Eq 2) be applied as a resource-saving measure.

Short bar K_{IvM} (ASTM E 1304) has been successfully correlated with $K_{Ic}(K_Q)$ (ASTM B 645 or E 399) to guarantee fracture toughness minimums for lot release purposes for commercial aluminum aerospace materials.

It has been shown that a correlation exists between the two test methods and is independent of alloy, direction, or temper. In higher toughness materials (notably 7475) heterogeneity in fracture toughness through the plate thickness can introduce data scatter when differing original plate thicknesses are grouped together. Due to this inherent scatter in higher toughness materials, it is advantageous, when utilizing K_{IvM} to guarantee $K_{Ic}(K_Q)$ in aluminum alloys for lot release, to separate the data by higher-toughness alloys (7475) and lower toughness alloys (2124-T851, 7050-T7X51).

A correlation value minimums for utilizing K_{IvM} for lot release have been calculated for (relatively) "low" and "high" toughness aluminum alloy databases; it is proposed that they be applied, respectively, for (lower-toughness) alloys 2124 and 7050, and higher toughness alloy 7475.

Acknowledgments

The provision of valuable technical input and data by Dr. Kevin R. Brown, Aircraft/Aerospace Technical Liaison Manager for Kaiser Aluminum and Chemical Corporation, is gratefully acknowledged, as is the assistance of the Mechanical Metallurgy technical staff of Reynolds Metals Company in performing the chevron-notch short bar tests.

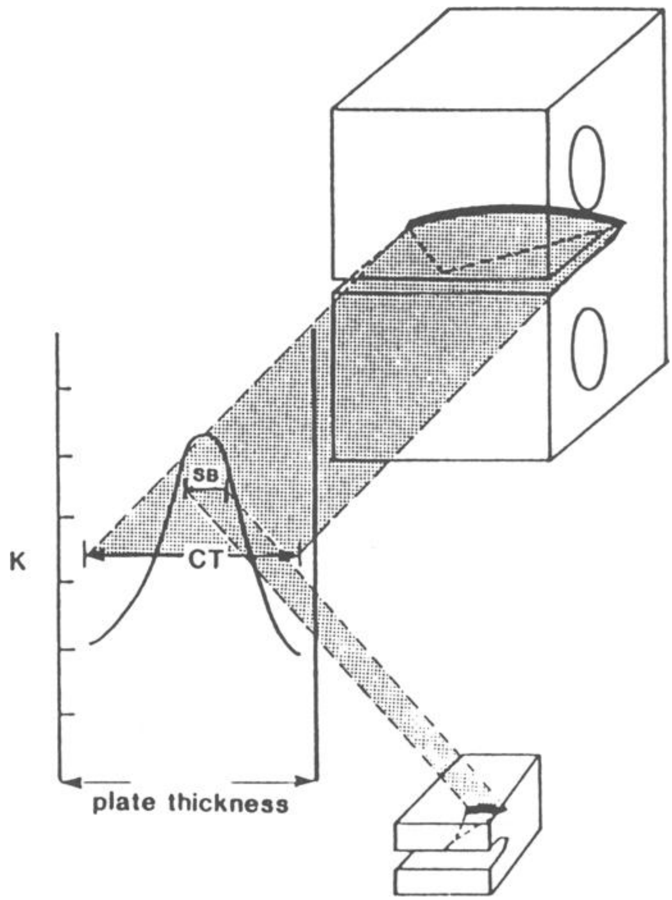

FIG. 11—*Schematic representation of through-thickness toughness effects when correlating short bar and compact tension test results (Courtesy Kaiser Aluminum).*

References

[1] Kaufman, J. G., Sha, G. T., Kohm, R. F., and Bucci, R. J., "Notch-Yield Ratio as a Quality Control Index for Plane-Strain Fracture Toughness," in *Cracks and Fracture, ASTM STP 601*, American Society for Testing and Materials, Philadelphia, 1976, pp. 169–190.

[2] Barker, L. M., "A Simplified Method for Measuring Plane Strain Fracture Toughness," *Engineering Fracture Mechanics*, Vol. 9, 1977, pp. 361–369.

[3] Barker, L. M., "Theory for Determining K_{Ic} from Small, Non-LEFM Specimens, Supported by Experiments on Aluminum," *International Journal of Fracture*, Vol. 15, 1979, pp. 515–536.

[4] Newman, J. C., Jr., "A Review of Chevron-Notched Fracture Specimens," in *Chevron-Notched Specimens, Testing and Stress Analysis, ASTM STP 855*, J. H. Underwood, S. W. Freiman, and F. I. Baratta, Eds., American Society for Testing and Materials, Philadelphia, 1984, pp. 5–31.

[5] Brown, K. R., "The Chevron Notched Fracture Toughness Test," *ASTM Standardization News*, Nov. 1988, pp. 66–69.

[6] Munz, D., Bubsey, R. T., and Srawley, J. E., "Compliance and Stress Intensity Coefficients for Short Bar Specimens with Chevron Notches," *International Journal of Fracture*, Vol. 16, No. 4, Aug. 1980, pp. 359–374.

[7] Kaufman, J. G., "Experience in Plane-Strain Fracture Toughness Testing per ASTM Method E 399," in *Developments in Fracture Mechanics Test Methods Standardization, ASTM STP 632*, W. F. Brown, Jr., and J. G. Kaufman, Eds., American Society for Testing and Materials, Philadelphia, 1976, pp. 3–24.

[8] Chapter 9.2.11, *Military Handbook 5E, Metallic Materials and Elements for Aerospace Vehicle Structures*, Naval Publications and Forms Center, Philadelphia, pp. 9-24–9-27.

[9] Ruff, P. E., "Design Allowables for Static Metallic Material Properties," *Metals Handbook, Ninth Edition, Volume 8, Mechanical Testing*, American Society for Metals, Metals Park, Ohio, 1985, pp. 662–677.

[10] Eschweiler, J., Marci, G., and Munz, D., "Fracture Toughness of an Aluminum Alloy from Short-Bar and Compact Specimens," in *Chevron-Notched Specimens, Testing and Stress Analysis, ASTM STP 855*, American Society for Testing and Materials, Philadelphia, 1984, pp. 255–269.

[11] Brown, K. R., "The Use of the Chevron-Notched Short-Bar Specimen for Plane-Strain Toughness Determination in Aluminum Alloys," in *Chevron-Notched Specimens, Testing and Stress Analysis, ASTM STP 855*, American Society for Testing and Materials, Philadelphia, 1984, pp. 237–254.

[12] Zinkham, R. E., "7475-T7351 Fracture Toughness and Quality Assurance Values," Report No. ML 84-9, Reynolds Metals Company, 1984.

[13] Munz, D., "Determination of Fracture Toughness of High Strength Aluminum Alloys With Chevron Notched Short Rod and Short Bar Specimens," *Engineering Fracture Mechanics*, Vol. 15, No. 1–2, 1981, pp. 231–236.

[14] Barker, L. M., "Chevron-Notched Specimens for Fracture Toughness Measurements Independent of R-Curve Effects," *Journal of Testing and Evaluation*, Vol. 17, No. 4, July 1989, pp. 218–223.

Charles W. Marschall,[1] *Paul R. Held,*[1] *and Fred J. Dolan*[2]

Using Chevron-Notch, Short-Bar Specimens for Measuring the Fracture Toughness of a Martensitic Stainless Steel at High Hardness

REFERENCE: Marschall, C. W., Held, P. R., and Dolan, F. J., "**Using Chevron-Notch, Short-Bar Specimens for Measuring the Fracture Toughness of a Martensitic Stainless Steel at High Hardness,**" *Chevron-Notch Fracture Test Experience: Metals and Non-Metals, ASTM STP 1172,* K. R. Brown and F. I. Baratta, Eds., American Society for Testing and Materials, Philadelphia, 1992, pp. 144–156.

ABSTRACT: Fracture toughness tests were conducted at room temperature and at −196°C on a martensitic stainless steel that had been quenched and tempered to a hardness of Rockwell C 61–63. The fracture toughness specimens were chevron-notch, short-bar specimens for which B was 12.7 mm and W was 25.4 mm. Tests were conducted in accordance with ASTM Test Method for Plane-Strain (Chevron Notch) Fracture Toughness of Metallic Materials (E 1304-89).

Five tests were conducted at each temperature, and each test produced a valid K_{Iv} result. Test results were unusually reproducible for plane-strain fracture toughness tests; the standard deviation for room temperature tests was approximately ±5% and for −196°C tests was approximately ±2% of the mean value of K_{Iv}.

For comparison with the chevron-notch test results, three standard K_{Ic} tests were conducted on fatigue-precracked compact (tension) specimens at room temperature. The tests were conducted in accordance with ASTM Test Method for Plane-Strain Fracture Toughness of Metallic Materials (E 399). As was the case for the K_{Iv} tests, the K_{Ic} tests produced very reproducible results: the standard deviation for three tests was approximately ±2% of the mean value. However, it was found that the mean K_{Iv} values for this high-hardness steel were approximately 18% greater than the mean K_{Ic} values. That result confirms the warning included in ASTM E 1304 that K_{Iv} values may be larger than K_{Ic} values in some materials.

KEY WORDS: fracture toughness, martensitic stainless steel, cryogenic testing, chevron-notch specimens, short-bar specimens, ultra-high-strength steel

In a program conducted at Battelle for NASA Marshall Space Flight Center, fracture toughness tests were conducted on CRB-7 martensitic stainess steel that had been quenched and tempered to a hardness of Rockwell C 61–63. It was decided initially that the tests would utilize chevron-notch, short-bar specimens, partly because similar specimens had been used previously in testing other martensitic stainless steels and partly because difficulties were anticipated in fatigue precracking compact-tension or bend specimens at these high hardness levels. However, because ASTM Test Method for Plane-Strain (Chevron Notch) Fracture Toughness of Metallic Materials (E 1304-89) warns that the toughness value obtained from this method, K_{Iv}, may be larger than K_{Ic} obtained from ASTM Test Method for Plane-Strain Fracture Toughness of Metallic Materials (E 399), it was decided that several

[1]Senior research scientist and researcher, respectively, Metals and Ceramics Department, Battelle, 505 King Avenue, Columbus, OH 43201.

[2]Deputy division chief, Engineering Physics, NASA, Marshall Space Flight Center, Huntsville, AL 35812.

additional tests would be conducted to determine K_{Ic} so that the two fracture toughness parameters could be compared directly. Of course, the success of these additional tests required that fatigue precracking could be accomplished in reasonable times at appropriate ΔK levels.

A total of ten chevron-notch (short-bar) specimens and three compact-tension specimens were fabricated and tested. Five of the chevron-notch specimens were tested at 20°C (68°F) and five were tested at −196°C (−320°F). The three compact-tension specimens were tested at 20°C (68°F).

Material Investigated

The material investigated was a cylinder of CRB-7 martensitic stainless steel, furnished to Battelle in the spheroidized annealed condition by NASA/MSFC. Its diameter was 114 mm (4.5 in.), and its length was 31.8 mm (1.25 in.). The chemical composition furnished by the manufacturer, Carpenter Technology Corporation, is given in Table 1. Also shown in Table 1 is the composition specified in AMS 5900A to which the material was purchased. The reported chemical composition of the cylinder is seen to meet the specification.

Hardening of the steel was accomplished after specimen blanks had been machined from the cylinder. Blanking, hardening, and finish machining are described in the next section.

Experimental Procedures

Details of specimen fabrication, heat treatment, and testing have been included so that the reader can judge the validity of the comparisons made between experimentally determined K_{Iv} and K_{Ic} values.

Blanking and Finish Machining of Specimens

Specimen blanks were machined from the stainless steel cylinder as described in Appendix A. Specimens included ten short-bar fracture toughness specimens and three compact specimens; in both types of specimens, B was 12.7 mm (0.5 in.) and W was 25.4 mm (1 in.). The orientation of the fracture-toughness specimens was C-R, as defined in ASTM E 399. Dimensions of the short-bar specimens are shown in Fig. 1. Compact specimens were of

TABLE 1—*Chemical composition of CRB-7 bearing steel (Heat No. 99067) tested in this investigation.*

	Chemical Composition, wt%	
Element	Heat No. 99067	AMS 5900A
Carbon	1.12	1.05–1.15
Manganese	0.40	0.25–0.50
Silicon	0.30	0.20–0.40
Phosphorus	0.015	0.015 max
Sulfur	0.006	0.010 max
Chromium	14.14	13.75–14.75
Molybdenum	2.07	1.90–2.25
Columbium	0.29	0.25–0.35
Vanadium	1.01	0.90–1.15
Nickel	0.13	0.35 max
Copper	0.03	0.35 max

Symbol	Name	Value, inch	Tolerance, inch
B	Thickness	0.500	± 0.001
W	Length	1.000	± 0.005
a_0	Distance to chevron tip	0.200	± 0.0025
S	Grip groove depth	0.075	± 0.005
X	Distance to load line	0.050	± 0.0015
T	Grip groove width	0.175	± 0.0025
2H	Height	0.500	± 0.0025

To convert inches to mm, multiply by 25.4

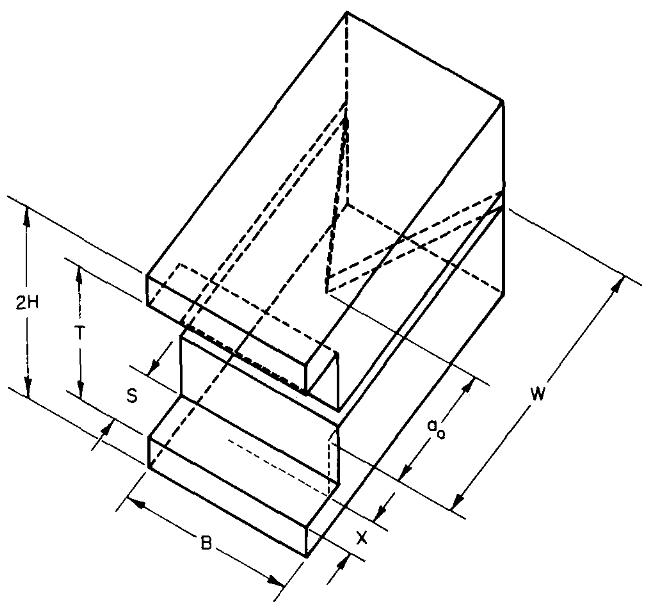

FIG. 1—*Chevron-notch short-bar specimen used in this investigation.*

the design specified in ASTM E 399. Specimen blanks were prepared 0.25-mm (0.010-in.) oversize to allow for possible oxidation and/or decarburization during heat treatment.

Following heat treatment of the blanks, described in the next section, the specimens were ground to final dimensions by removing approximately 0.13 mm (0.005 in.) from each surface. Notching of the short-bar and compact specimens and introducing holes in the compact specimens were accomplished using electric-discharge wire cutting. Each specimen was inspected to ensure that its dimensions were in compliance with specifications.

Although electric-discharge machining (EDM) can produce a damaged surface layer of recast metal, it was the authors' opinion that such a layer would be inconsequential in testing both the compact specimens and the short-bar specimens. In the compact specimens, the notch formed by EDM was subsequently sharpened by fatigue precracking, thereby negating any harmful effect of the EDM-damaged layer on the measured toughness. In the short-bar specimens, K_{Iv} was determined at a point in the test at which a stable crack had grown approximately one third of the length of the chevron; hence, even though the material at the very tips of that crack may have been damaged by the EDM process, it is likely that the net effect was simply to sharpen the grooves which formed the chevron and guarantee plane-strain conditions during the test.

Heat Treatment of Specimen Blanks

Prior to being heat treated, the specimen blanks were degreased and then were encapsulated in two separate Vycor™ tubes that were evacuated and back filled with approximately one third atmosphere of argon gas. Capsules 1 and 2 contained the following specimen blanks:

Capsule 1	Capsule 2
Short-bar specimens nos. 1, 3, 4, 5, 7, and 9	Short-bar specimens nos. 2, 6, 8, and 10
Compact specimen no. 3	Compact specimen nos. 1 and 2

The capsules were used to protect the specimen blanks from oxidation and decarburization during the austenitization portion of the heat treatment. When the capsules were removed from the austenitizing furnace, they were fractured immediately over the oil-quench bath so that the specimens fell directly into a wire basket suspended within the bath.

The heat treatment procedure followed at Battelle was specified by NASA/MSFC. Details of that procedure can be found in Appendix B.

Rockwell C hardness tests were conducted on each of the specimens after they had been ground to final dimensions. Individual hardness readings ranged from C 61 to 63; the average value for all the readings on all the specimens was C 62.3 and the standard deviation was C 0.5. Therefore, each specimen met the heat treatment specification for hardness of C 61 to 64.

Fatigue Precracking of Compact Specimens

Fatigue precracking of compact specimens was conducted in a servohydraulic testing machine at a minimum-load/maximum-load ratio of 0.1. Maximum loads ranged from 1225 to 1780 N (275 to 400 lbf), and the number of cycles to initiate and grow the fatigue crack was slightly in excess of one million. Initiation and growth of the fatigue crack were monitored using Krak Gages™ bonded to both sides of the compact specimens. These gages are capable of detecting small changes in crack length through changes in electric resistance of the gage.

It was intended that the fatigue crack would be grown approximately 1.25 mm (0.05 in.) beyond the original notch tip. However, because of an error in setting the calibration factor for the Krak Gages™, the actual growth of the fatigue crack was slightly in excess of 2.5 mm (0.100 in.). That result produced specimens having a/W ratios slightly in excess of 0.55, where a is crack length and W is specimen width. Actual values of a/W for the three specimens ranged from 0.554 to 0.563. The range of a/W values specified in ASTM E 399 is 0.45 to 0.55. Thus, the compact specimens used in this investigation fell slightly outside that specification. However, it is believed that the slight deviation from specifications that existed in these specimens did not have a significant effect on the K_{Ic} results [1]. Calculation of K_I for these specimens employed the expression in Paragraph A4.5.3 of ASTM E 399.

Testing of Short-Bar Specimens

Testing of chevron-notch short-bar specimens was conducted in accordance with instructions set forth in ASTM E 1304 to obtain a value for P_c, the load required to advance the crack when the crack was at the critical crack length. A conditional value, K_{Qv}, of the plane-strain toughness was first calculated as follows

$$K_{Qv} = Y_m^* P_c/(B\sqrt{W})$$

where Y_m^* is the minimum stress intensity factor coefficient (equal to 29.90 for the specimens used in this investigation) and B and W have the values shown in Fig. 1. If $B \geq 1.25(K_{Qv}/\sigma_{YS})^2$, and if P_M (the maximum-load value) was less than $1.10P_c$, and if certain requirements regarding the unloading slopes were satisfied, and if all other validity criteria were met, then the test was valid, and $K_{Qv} = K_{Iv}$. In all ten specimens tested in this investigation, each of the validity requirements was satisfied and K_{Qv} was equal to K_{Iv}.

For short-bar tests conducted at $-196°C$ ($-320°F$), the entire specimen and the displacement gage were submerged in liquid nitrogen and held there for a time sufficient to allow temperatures to equilibrate prior to loading the specimen.

Testing of Compact Specimens

ASTM E 399 was used to determine the value of K_{Ic}, believed to represent a lower, limiting value of fracture toughness. Specimens were tested under displacement control in a screw-driven Instron testing machine at a loading rate such that the rate of increase of stress intensity was within the range from 0.55 to 2.75 $MPa\sqrt{m}/s$ (30 to 150 $ksi\sqrt{in.}/min$). A test record of load versus displacement was obtained autographically after first adjusting the load (y axis) and displacement (x axis) sensitivities of the recorder to obtain a convenient-size trace and an initial elastic-loading slope between 0.7 and 1.5. Loading was continued until the specimen fractured.

In order to establish that a valid K_{Ic} value was determined, it was necessary first to calculate a conditional result, K_Q, which involved a construction on the test record, and then to determine whether this result was consistent with the size and yield strength of the specimen. In all three compact-specimen tests, the load-displacement record was Type 1 (see ASTM E 399) and the calculated values of K_{Ic} satisfied the validity requirements of ASTM E 399.

Experimental Results

Chevron-Notch Short-Bar Tests

Each of the five short-bar specimens tested at room temperature and each of the five short-bar specimens tested at $-196°C$ ($-320°F$) produced valid K_{Iv} results. Representative load-displacement curves for room-temperature and cryogenic-temperature tests are shown in Figs. 2 and 3, respectively.

Results of the tests are summarized in Table 2. In addition to showing P_c and K_{Iv} values, Table 1 shows P_M and K_{IvM} values, where the M subscript refers to values at maximum load in the test. In all ten tests, the difference between K_{Iv} and K_{IvM} was small. At room temperature, the average value of K_{IvM} was 2.3% greater than the average value of K_{Iv}, while at $-196°C$ ($-320°F$), K_{IvM} values exceeded K_{Iv} values by an average of 1.2%.

As was anticipated, the K_{Iv} values at room temperature were significantly greater than those at $-196°C$ ($-320°F$). The values were consistent among five tests, displaying a standard deviation of approximately 5 and 2% of the mean value, respectively, for room-temperature and cryogenic-temperature tests.

Compact Specimen Tests

Each of the three compact specimens tested at room temperature gave valid K_{Ic} results. A representative load-displacement curve is shown in Fig. 4. K_{Ic} values are given in Table 3. As was the case for the K_{Iv} values in Table 2, K_{Ic} values exhibited little scatter among replicate tests; the standard deviation was approximately 2% of the mean value.

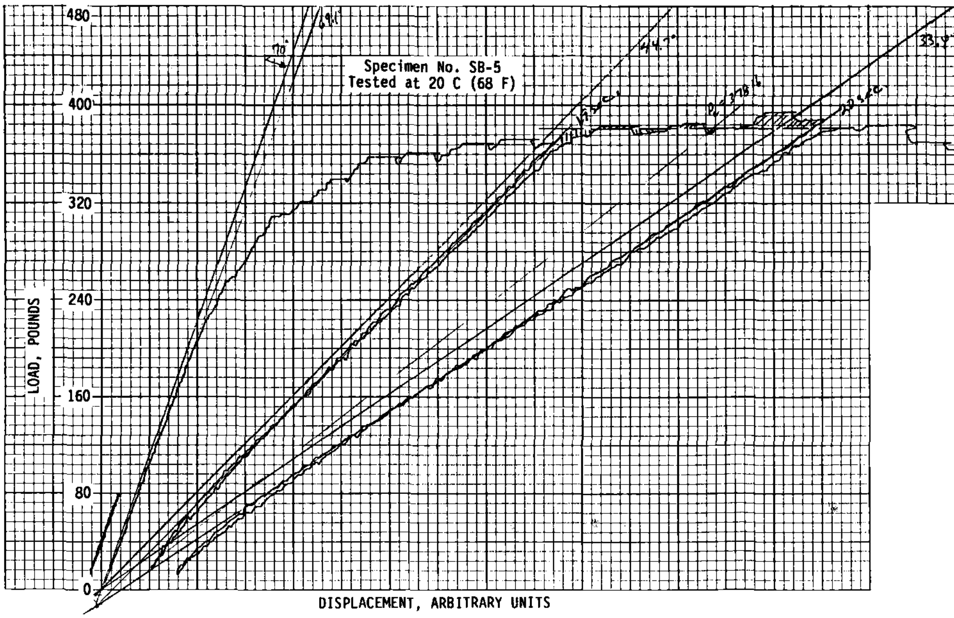

FIG. 2—*Copy of the test record for short-bar specimen SB-5, tested at room temperature.*

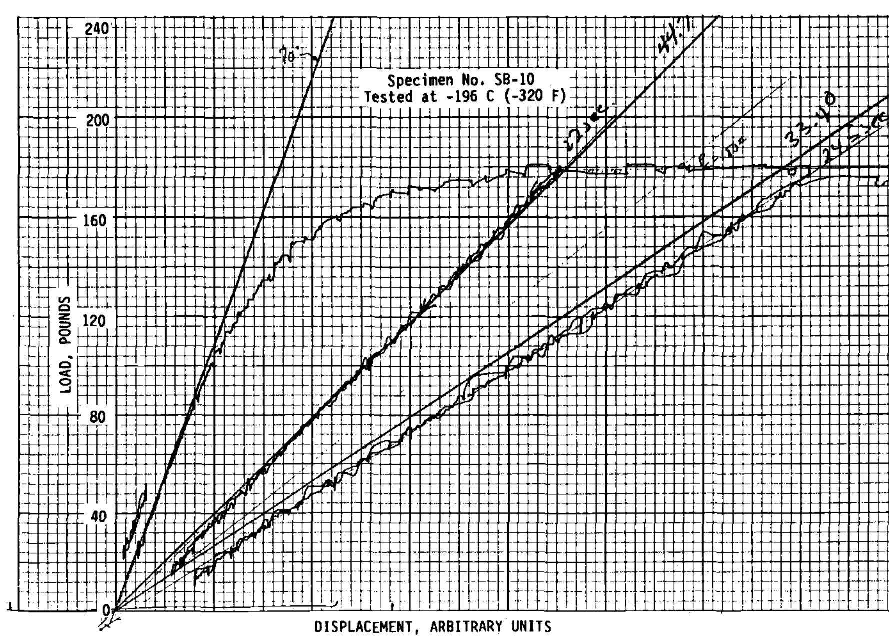

FIG. 3—*Copy of the test record for short-bar specimen SB-10, tested at −196°C (−320°F).*

TABLE 2—*Results of chevron-notch short-bar tests on hardened CRB-7 bearing steel.*

Specimen Number	Hardness, Rockwell C	Test Temperature		P_c		P_M		K_{Iv}		K_{IvM}	
		°C	°F	N	lb	N	lb	MPa $\sqrt{m}$	ksi $\sqrt{in.}$	MPa $\sqrt{m}$	ksi $\sqrt{in.}$
SB-1	62.0	20	68	1542	347	1591	358	22.8	20.8	23.5	21.4
SB-3	62.0	20	68	1716	386	1716	386	25.3	23.1	25.3	23.1
SB-5	62.3	20	68	1680	378	1751	394	24.8	22.6	25.9	23.6
SB-7	62.3	20	68	1778	400	1805	406	26.3	23.9	26.7	24.3
SB-9	62.0	20	68	1645	370	1685	379	24.3	22.1	24.9	22.7
Average	62.1							24.7	22.5	25.3	23.0
Std. Dev.	±0.2							±1.3	±1.2	±1.2	±1.1
SB-2	62.4	−196	−320	791	178	796	179	11.7	10.6	11.8	10.7
SB-4	62.6	−196	−320	813	183	818	184	12.0	10.9	12.1	11.0
SB-6	62.9	−196	−320	791	178	796	179	11.7	10.6	11.8	10.7
SB-8	62.5	−196	−320	809	182	831	187	12.0	10.9	12.3	11.2
SB-10	62.5	−196	−320	800	180	805	181	11.8	10.8	11.9	10.8
Average	62.6							11.8	10.8	12.0	10.9
Std. Dev.	±0.2							±0.2	±0.2	±0.2	±0.2

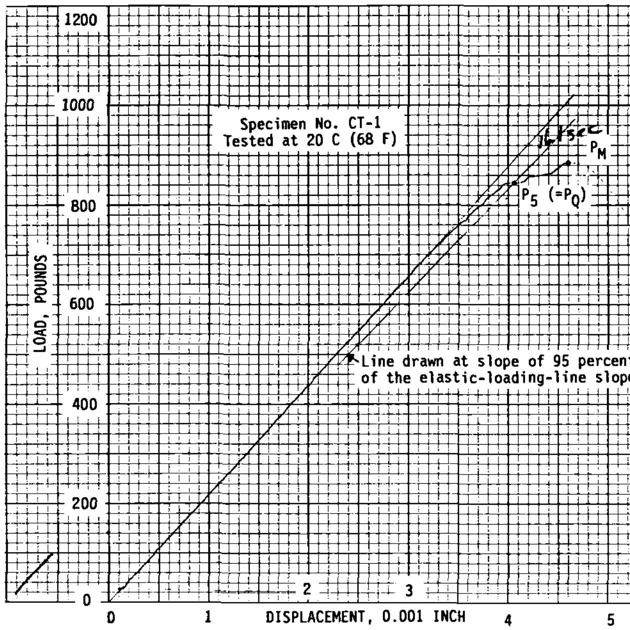

FIG. 4—*Copy of the test record for compact specimen CT-1, tested at room temperature.*

Comparison of K_{Ic} *and* K_{Iv} *Values*

Comparison of the mean K_{Iv} value (Table 2) with the mean K_{Ic} value (Table 3) at room temperature reveals that K_{Iv} for this high hardness steel is approximately 18% greater than K_{Ic}. Because of the way that the specimens were prepared from the starting cylinder of steel, the authors consider it unlikely that the difference in results is due to metallurgical differences at the crack tip in the two specimen types. Rather, the difference between K_{Iv} and K_{Ic} is thought to be due to the different nature of the crack extension process in the two specimens. In the K_{Iv} test, fracture toughness is relative to a slowly advancing, steady state crack initiated at a chevron-shape notch and propagating in a chevron-shaped ligament. In the K_{Ic} test, on the other hand, attention is centered on the start of crack extension from a fatigue precrack.

The authors are not aware of a body of statistical data comparing K_{Ic} and K_{Iv} values for ultrahigh-strength steels. Barker and Baratta [*2*] performed limited testing of two quenched-and-tempered low-alloy steels that were substantially tougher than the steels tested in this study. For 4340 steel, they found that K_{Ic} values were approximately 6% less than K_{Iv} values. For D6AC steel, on the other hand, they found the opposite result, i.e., K_{Ic} values were approximately 6% greater than K_{Iv} values.

Most of the statistical comparisons between the two test methods are for high-strength aluminum alloys. For example, Brown [*3*], in a statistical study of high-strength heat-treated aluminum alloys, found that K_{Iv} correlated well with K_{Ic}, especially when differences arising from metallurgical heterogeneity were eliminated from the data comparisons. For a variety of aluminum alloys and temper designations, Brown reported that

$$K_{Iv} = 1.017\ (\pm 0.014) K_{Ic}$$

TABLE 3—*Results of* K_{Ic} *tests on 0.5T compact specimens of hardened CRB-7 bearing steel.*

Spec. No.	Hardness Rockwell C	a		P_c		P_Q		P_M		K_{Ic}	
		mm	in.	N	lb	N	lb	N	lb	MPa $\sqrt{m}$	ksi $\sqrt{in.}$
CT-1	61.8	14.06	0.5536	3756	845	3756	845	3934	885	21.3	19.4
CT-2	62.3	14.20	0.5589	3534	795	3534	795	3565	802	20.4	18.6
CT-3	62.3	14.31	0.5632	3556	800	3556	800	3689	830	20.9	19.0
									Average	20.9	19.0
									Std. Dev.	±0.5	±0.4

with a standard deviation of 1.97 and a correlation coefficient of 0.998 for values of K_{Ic} up to 40.7 MPa$\sqrt{m}$ (37 ksi$\sqrt{in.}$).

The limited data reported here for ultrahigh-strength steel indicate that K_{Iv} and K_{Ic} values for these materials do not agree as well as has been reported for high-strength aluminum alloys by Brown. Numerous additional tests would be required to establish a statistical correlation between the two toughness parameters for these types of materials. As a small step in that direction, Battelle is currently conducting both K_{Iv} and K_{Ic} tests on another high hardness bearing steel.

Conclusions

Based on the experimental work reported here, the following conclusions can be drawn for CRB-7 martensitic stainless steel quenched and tempered to a hardness of 61 to 63 Rockwell C:

1. At room temperature, the mean value of K_{Iv} from chevron-notch short-bar specimens (C-R orientation) was 24.7 ± 1.3 MPa$\sqrt{m}$ (22.5 ± 1.2 ksi$\sqrt{in.}$).
2. At room temperature, the mean value of K_{Ic} from compact specimens (C-R orientation) was 20.9 ± 0.5 MPa$\sqrt{m}$ (19.0 ± 0.4 ksi$\sqrt{in.}$). Thus, K_{Iv} for this material was approximately 18% greater than K_{Ic}.
3. At −196°C (−320°F), the mean value of K_{Iv} from chevron-notch short-bar specimens (C-R orientation) was 11.8 ± 0.2 MPa$\sqrt{m}$ (10.8 ± 0.2 ksi$\sqrt{in.}$). That value is approximately 48% of the K_{Iv} value at room temperature.

Acknowledgments

Appreciation is expressed to K. R. Brown at Kaiser Aluminum and Chemical Company for supplying both a draft copy and a final copy of Test Method E 1304, and for providing helpful comments regarding interpretation of E 1304 during the course of the Battelle investigation. Thanks are due also to W. F. Brown, Jr., and J. L. Shannon at NASA Lewis Research Center for helpful discussions.

APPENDIX A

Instructions for Blanking and Finish Machining of Test Specimens from CRB-7 Steel Disk

MACHINING OF TEST SPECIMENS FROM CRB-7 STEEL DISK

Material:

CRB-7 martensitic stainless steel, 114 by 31.8 mm (4½ diameter by 1¼ in.) long.

Specimens Required:

10 short-bar fracture toughness specimens [B = 12.7 mm (0.500 in.)].
3 compact-tension specimens (B = 0.5 in., W = 1.0 in.).

Instructions:

1. Slice the disk provided to obtain two disks (Disks A and B), each about ⅝ in. thick.

2. From Disk A (Fig. A-1) prepare 10 short-bar specimen blanks (Spec. Nos. SB-1 through SB-10).

   Note:

   (a) Blanks must line up with a radius, as in Sketch 1.
   (b) Mark the top of each short-bar specimen blank as shown in Fig. A-1 to maintain proper orientation of subsequent notch plane.
   (c) Blanks should be 12.95 by 12.95 by 26.92 mm (0.510 by 0.510 by 1.060 in.) prior to heat treatment; later they will be finish machined to 12.7 by 12.7 by 26.67 mm (0.500 by 0.500 by 1.050 in.).
3. From Disk B (Fig. A-2) prepare 3 compact-tension specimen blanks (Spec. Nos. CT-1 through CT-3).

   Note:

   (a) Blanks must line up with a radius, as in Fig. A-2.
   (b) Mark the top of each compact-specimen blank as shown in Fig. A-2 to maintain proper orientation of subsequent notch plane.
   (c) Compact specimen blanks should be 30.73 by 32.00 by 12.95 mm (1.210 by 1.260 by 0.510 in.) prior to heat treatment; later they will be finish machined to 30.48 by 31.75 by 12.7 mm (1.200 by 1.250 by 0.500 in.).
4. Return all blanks for heat treatment to Rockwell C 61 to 64. Also return all leftover material.
5. After the heat-treated blanks are returned to the shop, complete final machining as shown in Fig. 1 (short bar specimens) and in ASTM E 399 (compact tension specimens). Take special care in ensuring that the short bar and compact tension specimens have the proper orientation.
6. Inspect the specimens for compliance with dimensional and perpendicularity requirements.

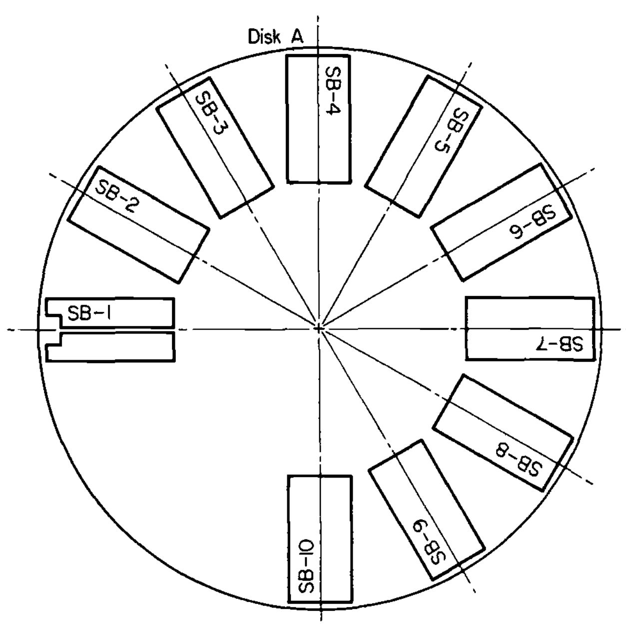

FIG. A-1—*Cutting pattern for machining short-bar-specimen blanks from disk of CRB-7.*

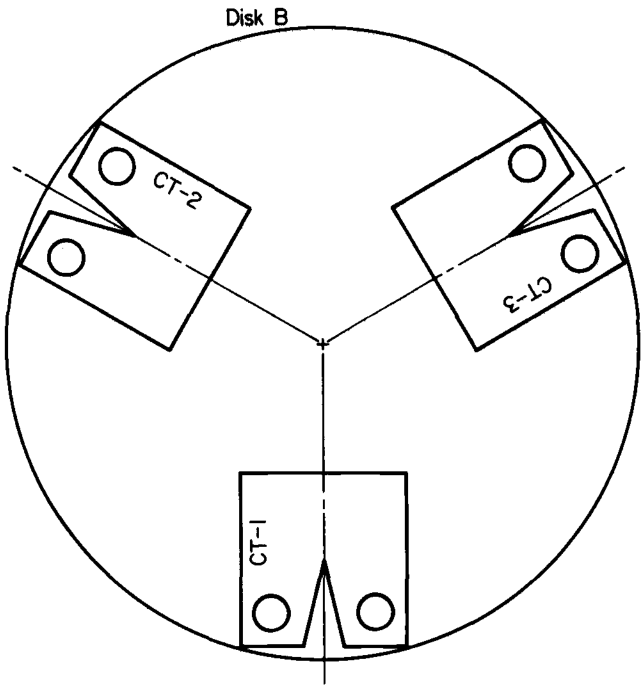

FIG. A-2—*Cutting pattern for machining compact specimen blanks from disk of CRB-7.*

APPENDIX B

Detailed Requirements for Heat Treatment of CRB-7, AMS 5900 (Requirements Supplied by NASA/MSFC)

The procedure given here was obtained from notes on Rockwell International Drawing 7R032203.

1. Preheat at 815 ± 15°C (1500 ± 25°F) to equalize temperature.
2. Austenitize at 1150 ± 15°C (2100 ± 25°F) for 30 min minimum.
3. Quench in an acceptable medium at a temperature not to exceed 480°C (900°F). (Note: Battelle, acting upon instructions from the NASA/MSFC project monitor, quenched the specimen blanks in oil that had been heated to 60°C (140°F).
4. Cool in air to room temperature.
5. Stress relieve at 150 ± 15°C (300 ± 25°F) for 60 ± 5 min.
6. Cool in air to room temperature.
7. Stabilize at −196°C (−320°F) in liquid nitrogen for 30 min minimum.
8. Warm in air to room temperature.
9. Temper at 525 ± 8°C (975 ± 15°F) for 2 h, ±15 min.
10. Cool in air to room temperature.
11. Repeat temper cycle in Steps 9 and 10.

Time Tolerance: The bearing details shall be subjected to a time tolerance of 2 h or less between Steps 3 and 6 and between Steps 6 and 8 during heat treatment.

Hardness Test: A hardness test shall be performed on item surfaces in accordance with ASTM E 18 to determine conformance with the hardness requirement. The hardness of the material after final tempering shall be within the range of Rockwell C 61–64. Failure to meet the hardness requirement shall be cause for rejection.

References

[1] Brown, W. F., Jr., NASA Lewis Research Center, private communication, 13 Sept. 1990.

[2] Barker, L. M. and Baratta, F. I., "Comparisons of Fracture Toughness Measurements by the Short Rod and ASTM Standard Method of Test for Plane-Strain Fracture Toughness of Metallic Materials (E 399 78)," *Journal of Testing and Evaluation*, JTEVA, Vol. 8, No. 3, May 1980, pp. 97–102.

[3] Brown, K. R., "The Use of the Chevron-Notched Short-Bar Specimen for Plane-Strain Toughness Determination in Aluminum Alloys," *Chevron-Notched Specimens: Testing and Stress Analysis, ASTM STP 855*, J. H. Underwood, S. W. Frieman, and F. I. Baratta, Eds., American Society for Testing and Materials, Philadelphia, 1984, pp. 237–254.

Applications to Non-Metallics

Michael G. Jenkins,[1] *Mattison K. Ferber,*[2] *Asish Ghosh,*[3] *Jouko T. Peussa,*[4] *and Jonathan A. Salem*[5]

Chevron-Notched, Flexure Tests for Measuring the Elevated-Temperature Fracture Resistance of Structural Ceramics

REFERENCE: Jenkins, M. G., Ferber, M. K., Ghosh, A., Peussa, J. T., and Salem, J. A., "**Chevron-Notched, Flexure Tests for Measuring the Elevated-Temperature Fracture Resistance of Structural Ceramics,**" *Chevron-Notch Fracture Test Experience: Metals and Non-Metals, ASTM STP 1172,* K. R. Brown and F. I. Baratta, Eds., American Society for Testing and Materials, Philadelphia, 1992, pp. 159–177.

ABSTRACT: Chevron-notched, three-point flexure specimens were used to study the quasi-static fracture behaviour of a variety of structural ceramics at temperatures to 1400°C. Types of materials tested included monolithic ceramics (SiC, Si_3N_4, $MgAl_2O_4$), self-reinforced monoliths (acicular-grained Si_3N_4, acicular-grained mullite), and ceramic matrix composites (SiC whisker/Al_2O_3 matrix, TiB_2 particulate/SiC matrix, SiC fibre/CVI SiC matrix, Al_2O_3 fibre/CVI SiC matrix).

Fracture resistance behavior of the materials was quantified as three distinct regimes of the fracture histories. At the initial part of the crack propagation, the apparent fracture toughness was evaluated as the critical stress intensity factor for the chevron notch, K_{IvM}. During stable crack propagation, the crack growth resistance was characterized by the instantaneous strain energy release rate, G_R, using a compliance method assuming linear-elastic unloading to calculate the effective crack lengths. At final fracture, the complete fracture process was quantified using the work-of-fracture, γ_{WOF}, which can be equated to the fracture surface energy for linear-elastic materials.

Results indicate that the chevron-notched, three-point flexure specimen facilitates the study of fracture behaviour in a wide range of brittle and quasi-brittle materials at elevated temperatures. The unique features of the chevron geometry, which are automatic crack initiation and inherent stable crack growth, are crucial to the successful evaluation of the fracture tests.

KEY WORDS: elevated temperature, fracture resistance, *R*-curve, work-of-fracture, ceramics, stable crack growth, chevron notch

Complete and accurate knowledge of the elevated-temperature fracture resistances of structural ceramics is an important requisite for the successful implementation of these materials into advanced heat engine components [*1,2*]. Although ceramics are traditionally considered to fracture in a brittle, catastrophic fashion, pioneering experimental evidence

[1]Development staff member, Oak Ridge National Laboratory, P.O. Box 2008, MS 6064, Oak Ridge, TN 37831-6064.

[2]Group leader, Oak Ridge National Laboratory, P.O. Box 2008, MS 6064, Oak Ridge, TN 37831-6064.

[3]Senior engineer, Philips Display Components Co., P.O. Box 963, Ann Arbor, MI 48106-0963.

[4]Director, technology, Federation of Finnish Metal, Engineering, and Electro-Technical Industries, Etelaranta 10, SF-00130 Helsinki, Finland.

[5]Research engineer, NASA Lewis Research Center, 21000 Brookpark Road, MS 49-7, Cleveland, OH 44135.

[3] on aluminum oxide showed the existence of increasing fracture resistance with increasing crack extension. The existence of this so-called R-curve effect has complicated the evaluation of what had been assumed to be a brittle fracture process. Indeed, the strict application of linear elastic fracture mechanics (LEFM) and the single parameter, fracture toughness, K_{IC}, can no longer be so easily accomplished in these materials, which have been assumed to fracture catastrophically at a given flaw size and applied stress.

Therefore, it has become necessary to characterize the fracture behaviour of each material more completely at the design conditions. Rather than using a single parameter such as K_{IC} to describe the fracture behaviour only at crack initiation, the entire fracture process can be divided into three regimes (crack initiation, stable crack growth, and final fracture), thus conveniently characterizing the whole fracture process using three different parameters which describe each regime as shown in Fig. 1. The chevron-notched geometry offers a simple, single-specimen method for determining these parameters. Automatic crack initiation eliminates the need for and difficulty of precracking the notched specimen, therefore allowing the determination of critical stress intensity factors, K_0 at the beginning of the R-curve for an assumed crack extension, $\Delta a = 0$, where $K_{IC} \approx K_0$. The inherent stable growth of the crack as it traverses the chevron section facilitates the determination of the crack growth resistance, G_R (R-curve). Complete, controlled fracture of the specimen allows the determination of the energy required for the entire fracture process, γ_{WOF}.

This paper describes a single-specimen, fracture testing technique which has been applied to a wide range of brittle and quasi-brittle materials at temperatures from 20 to 1400°C. First, the chevron-notched flexure geometry and testing arrangement are described. Then the monolithic and composite materials employed in the tests are detailed. The data reduction techniques, including numerical modeling and algorithms, for determining the fracture parameters are presented. Finally the test results which describe the various fracture behaviours are shown.

Chevron-Notched Geometry and Test Setup

Various chevron-notched geometries have been used for fracture testing for more than two decades [4–9]. While some applications of partially chevron-notched geometries have

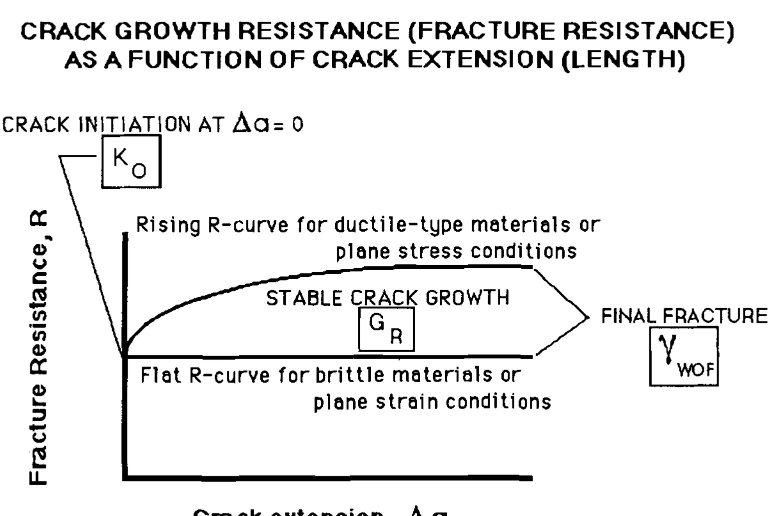

FIG. 1—*Schematic illustration of regimes of fracture resistance characterization.*

been described for ductile materials such as metals, the most general applications of full chevron-notched sections have been to brittle materials such as glasses and ceramics.

A difficulty with applying LEFM to any test geometry is the determination of the stress intensity factor and compliance relations. The determination of such relations for the chevron notch is complicated by the three-dimensional stress state in the chevron section. However, numerous approximate relations have been developed for these relations for a number of chevron-notched geometries [*4,9–13*].

The chevron-notched geometry used in the present study employed a three-point flexure loading arrangement. The flexure bar was chosen for its simplicity of fabrication and efficient use of material. Three-point flexure was chosen for the simplicity of loading, which was an important consideration at elevated temperatures where uneven loading of the components of the four-point flexure arrangement may produce unquantifiable fracture behaviour.

A full chevron section was employed across the width of the flexure bar where the chevron section depth $\alpha_1 = a_1/W$, was 1.0 for all specimens and all materials and the initial notch depth, $\alpha_0 = a_0/W$, ranged from 0.35 to 0.44 depending upon the test material. Nomenclature and a drawing of the chevron geometry are shown in Fig. 2.

Specimens were generally square in cross section with dimensions of $B \approx W = 6$ to 7 mm and length, $L = 50$ to 75 mm. Specimen material was usually tested in the as-received condition with the chevron notches fabricated with a water-cooled, diamond-grit circular saw blade 0.25 mm thick yielding notch widths of ~0.30 mm.

Elevated temperature testing was conducted in a resistance-heated furnace insulated with refractory brick. The upper part of the load fixture consisted of a single, solid, α-SiC push rod machined to a single loading line at one end and attached to the water-cooled load cell at the opposite end. The lower part of the loading fixture consisted of a single, α-SiC tube (44-mm outer diameter, 6-mm wall thickness, 325 mm long) machined to produce two fixed "knife" edges of 41-mm span, S. This lower fixture was attached to the moveable crosshead of the displacement-controlled, electro-mechanical test machine. In conducting a fracture test, the specimen was first positioned on the lower load fixture outside the furnace and then slowly raised (~10 mm/min) into test position within the hot furnace where testing was conducted at a displacement rate of 0.01 mm/min.

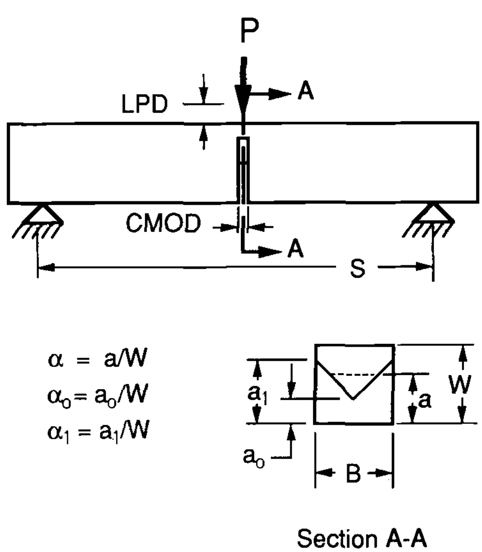

FIG. 2—*Chevron-notched, three-point flexure test geometry.*

A laser interferometric displacement gage (LIDG) [*9,14–16*], with an estimated resolution of ~0.25 μm, was employed to accurately determine specimen displacement (crack mouth opening displacement, CMOD) at all temperatures. The interference relation and a schematic diagram of the LIDG are illustrated in Fig. 3 in which a method of bonding reflective platinum targets near the mouth of the notch is also shown. Details of the use of the LIDG on ceramics at elevated temperatures are contained elsewhere [*9,14–16*]. Accurate measurement of specimen displacement was necessary for use in compliance relations for determination of the instantaneous crack length during stable crack growth. In addition, load point displacements (LPDs) as determined from the measured CMODs were used in the fracture energy calculations. Nondimensional CMOD compliance relations and CMOD/LPD relations for the particular chevron-notched geometry used in this study were determined from three-dimensional finite element analyses (FEA) [*11*] as shown in Figs. 4*a* and 4*b*, respectively. These relations, which had not been reported in previous FEA studies of this geometry [*12,13*] were nondimensionalized using the specimen dimensions width W, thickness B, and crack length a, as well as the appropriate elastic modulus E', in addition to the applied load P, and the respective displacements LPD and CMOD.

The quasi-static, fracture tests of the chevron-notched flexure bars yielded load-displacement curves displaying stable crack growth behavior. Normally, the measured displacement

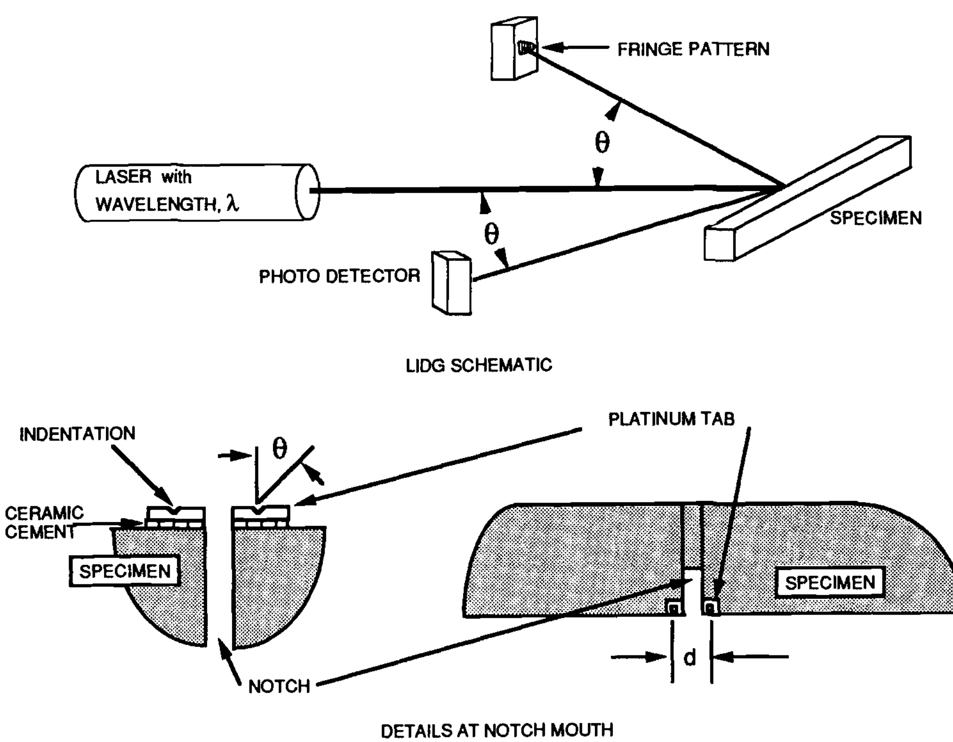

$$\text{CMOD} = \Delta d = \frac{\Delta m_1 + \Delta m_2}{2} \; \frac{\lambda}{\sin\theta}$$

FIG. 3—*Schematic illustration of LIDG.*

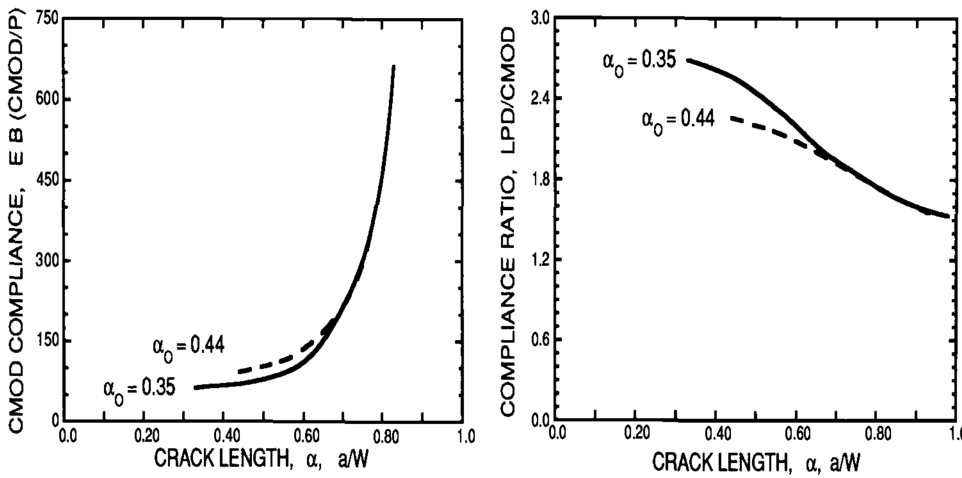

a) Dimensional compliance versus crack length relation

b) Load point displacement / crack mouth opening displacement relation

FIG. 4—*Compliance relations for chevron-notched, three-point flexure specimen.*

was CMOD, although some tests [*17*] determined LPD from the cross-head motion by subtracting the total machine/fixture compliance from total measured compliance. The fracture parameters were determined for each test from these load-displacement curves and knowledge of the specimen geometry and dimensions. Tests were usually conducted under constant, monotonically increasing, cross-head displacement rates. All tests were conducted in ambient air with test temperatures ranging from 20 to 1400°C in ~200°C increments.

Test Materials

All the materials referenced in this study were commercially available at the time of the fracture testing. In certain cases, the materials were given post-processing treatments after receipt from the manufacturer so as to elucidate certain characteristics in the specific studies. The types of materials are roughly classified as monolithic ceramics and composite ceramics and are briefly described in the following subsections.

Types of materials tested included monolithic ceramics (SiC, Si_3N_4, $MgAl_2O_4$), self-reinforced monoliths (acicular-grained Si_3N_4, acicular-grained mullite), and ceramic matrix composites (SiC whisker/Al_2O_3 matrix, TiB_2, particulate/SiC matrix, SiC fibre/CVI SiC matrix, Al_2O_3 fibre/CVI SiC matrix). The materials and material designators are summarized in Table 1.

Monolithic Ceramics

For the purposes of this paper, the term *monolithic ceramics* refers to ceramic materials in which no deliberate attempt has been made to include a second phase in a single-phase material for the purpose of structural reinforcement. By this definition, single-phase materials which are treated so as to produce acicular or elongated grain structure for the purpose of reinforcement (self-reinforced) are still considered monolithic ceramics owing to their single-phase nature.

The polycrystalline mullites ($3Al_2O_3 \cdot 2SiO_2$) presented here were obtained from two different sources and are examples of self-reinforced monolithic ceramics after proper heat

TABLE 1—*Summary of test materials.*

Type of Material	Material Designator	Material Description
	MONOLITHS	
Mullite ($3Al_2O_3{\cdot}2SiO_2$)	Mullite KM1[a] [17]	As-processed mullite
	Mullite KM3[a] [17]	KM1 + 1800°C heat treat [17]
	Mullite MM1[b] [17]	As-processed mullite
	Mullite MM3[b] [17]	MM1 + 1800°C heat treat [17]
Spinel ($MgAl_2O_4$)	Spinel[c] [18]	Dense; bimodal grain size, optically transparent
α-silicon carbide (SiC)	Hexoloy SA[d] [19]	Dense; fine, equiaxed grains
Silicon nitride (Si_3N_4)	A2Y6[e] [20]	Dense; duplex grain size distribution, hot pressed
Silicon nitride (Si_3N_4)	SN251[f] [21, 22]	Acicular grain structure; cold isostatically pressed, sintered
	COMPOSITES	
Silicon carbide whiskers in alumina matrix (SiC_w/Al_2O_3)	SA-25[g] [23, 24]	25 wt% SiC whiskers in dense Al_2O_3 matrix
Titanium diboride particles in silicon carbide matrix (TiB_2/SiC)	Hexoloy ST[h] [25]	16 vol% TiB_2 particles in dense SiC matrix
Silicon carbide fibres in silicon carbide matrix	Nicalon/CVI SiC III[i] [26]	30–34 vol% fibre/30–40 vol% CVI β-SiC
Alumina fibres in silicon carbide matrix	FP-Alumina/CVI SiC V[i] [26]	30–34 vol% fibre/30–40 vol% CVI β-SiC

[a]Mullite, Kyocera Corporation, Kyoto, Japan, 1989.
[b]Mullite (7% free silica), McDanel Corporation, Beaver Falls, Pennsylvania, 1989.
[c]Spinel, Coors Ceramic Company, Golden, Colorado, 1986.
[d]Hexoloy SA, Carborundum Co., Niagara Falls, New York, 1985.
[e]A2Y6 Silicon Nitride, GTE Laboratories, Inc., Waltham Massachusetts, 1985.
[f]SN251 Silicon Nitride, Kyocera Corporation, Kyoto, Japan, 1990.
[g]SA-25, Greenleaf Corporation, Saegertown, Pennsylvania, 1985.
[h]Hexoloy ST, Carborundum Co., Niagara Falls, New York, 1986.
[i]CVI-β-Silcion Carbide, Refractory Composites, Inc., Whittier, California, 1986.

treatments. Mullite KM[6] [17] was stoichiometric at an Al_2O_3:SiO_2 ratio of 1.5. Mullite MM[7] [17] was silica-rich, containing ~7% free SiO_2. The as-received materials contained a duplex microstructure in which 6 to 9 volume percent (vol%) acicular grains (mean dimensions of 14 × 4 μm) were dispersed in the equiaxed grain structure (~1 to 2 μm mean diameter). Two heat treatments [17] were applied to the materials in which both the dimensions and the vol% of the acicular grains increased. The first heat treatment of 1750°C for 5 h yielded 18 to 27-μm-long acicular grains at vol% of 9 to 13. The second heat treatment of 1800°C for 5 h yielded 27 to 32-μm-long acicular grains at vol% of 28 to 33.

The polycrystalline magnesium aluminate spinel[8] ($MgAl_2O_4$) [18] discussed here was essentially 100% pure with no non-stoichiometric phase present. The material was densified under a proprietary process to near 100% density, resulting in a optically transparent product with a bimodal type of grain diameter distribution ranging from 15 to 100 μm with a mean of ~35 μm.

[6]Mullite, Kyocera Corporation, Kyoto, Japan, 1989.
[7]Mullite (7% free silica), McDanel Corporation, Beaver Falls, Pennsylvania, 1989.
[8]Spinel, Coors Ceramic Company, Golden, Colorado, 1986.

The polycrystalline silicon carbide[9] (SiC) [*19*] was nearly 100% pure α-SiC. The material was sintered in argon gas at 2000°C, resulting in an essentially 100% dense product with a fine equiaxed microstructure and a grain diameter distribution ranging from 2 to 10 μm with a mean of 5 μm.

One of the polycrystalline silicon nitrides[10] (Si_3N_4) [*20*] was composed of nearly 100% β-Si_3N_4 grains (occasional α-Si_3N_4 grains present) surrounded by an amorphous, aluminum-yttrium silicate, intergranular phase. This intergranular phase was a byproduct of the sintering aids (2% Al_2O_3 and 6% Y_2O_3) which, during hot pressing at ~1750°C, promote the production of a virtually 100% dense material. The morphology of the Si_3N_4 ranged from needle-shaped to equiaxed grains with typical grain diameters on the order of 1 to 2 μm.

The other polycrystalline silicon nitride[11] (Si_3N_4) [*21,22*] was composed of a deliberate acicular grain structure and is an example of a commercially available self-reinforced material. The material of nearly 100% β-Si_3N_4 grains (occasional α-Si_3N_4 grains present) surrounded by a partially crystallized, ytterbium silicate rich, intergranular phase. This intergranular phase was a byproduct of the sintering aids, which during sintering at ~1750°C promote the production of a virtually 100° dense material and the selective growth of β-Si_3N_4 so as to provide the acicular grain structure. The morphology of the Si_3N_4 ranged from acicular (nominally 10 × 1 μm) to equiaxed (nominally 1 to 2 μm).

Composite Ceramics

For the purposes of this paper, composite ceramics refer to ceramic materials in which a deliberate attempt has been made to include a second phase in a single-phase material for the purpose of structural reinforcement. This second phase usually takes the form of a distinct structure such as particles, whiskers, or fibres but may also include a large amount of dispersed polycrystalline phase.

The polycrystalline aluminum oxide matrix composite[12] [*23,24*] discussed here was reinforced with 29 vol% single-crystal, silicon carbide whiskers. Although the exact processing parameters for this material were proprietary, it was known that the composites (SiC_W/Al_2O_3) were produced by a hot-pressing operation. The F-9 type whisker reinforcements were derived from a rice hull production process and tended to have high aspect ratios with typical dimensions of 1 × 30 μm. The polycrystalline matrix was composed of generally equiaxed grains averaging ~10 μm in diameter.

The polycrystalline silicon carbide matrix composite[13] [*25*] was reinforced with 16 vol% single-grain, titanium diboride particles. This composite (TiB_2/SiC) was processed similar to the monolithic SiC previously discussed in which sintering was performed in argon at 2000°C. The TiB_2 particles were generally well disbursed and equiaxed, averaging ~5 μm in diameter. The polycrystalline α-SiC matrix was composed of nearly equiaxed grains averaging ~7 to 8 μm in diameter.

Two composites[14] with chemical vapor infiltrated (CVI) matrices [*26*] are presented here. In both composites the infiltrated matrix was β-SiC with vol% of about ~30 to 40 and fibre vol% of ~30 to 34 arranged in continuous fibre, two-dimensional (four and eight harness satin weaves) laminates. Two polycrystalline fiber types, SiC (Nicalon) and Al_2O_3 (FP-alumina), were used with similar mean diameters (7 to 15 μm). The materials contained a

[9]Hexoloy SA, Carborundum Co., Niagara Falls, New York, 1985.
[10]A2Y6 Silicon Nitride, GTE Laboratories, Inc., Waltham Massachusetts, 1985.
[11]SN251 Silicon Nitride, Kyocera Corporation, Kyoto, Japan, 1990.
[12]SA-25, Greenleaf Corporation, Saegertown, Pennsylvania, 1985.
[13]Hexoloy ST, Carborundum Co., Niagara Falls, New York, 1986.
[14]CVI-β—Silcion Carbide, Refractory Composites, Inc., Whittier, California, 1986.

large amount of porosity with a large degree of inhomogeneity in the distribution of the matrix.

Fracture Parameters

During quasi-static, stable crack growth, the fracture history can be generally divided into three regimes: (1) critical condition at the onset of the stable propagation of the macrocrack; (2) extensive stable crack growth in which the material may exhibit increasing resistance to crack propagation; and (3) final fracture at which point the total energy dissipated during the fracture process causes the complete separation of the component.

The critical condition at the onset of stable crack propagation can be generally described by the critical stress intensity factor under plane-strain conditions, K_{IC}, although other energy-related terms such as the critical strain energy release rate, G_{IC}, or the critical nonlinear parameter, J_{IC} (J-integral), can also be used. For chevron-notched geometries, the apparent K_{IC} is normally calculated such that [*4,7–9*]

$$K_{IC} = Y_{min}P_{max}/(BW^{1/2}) \tag{1}$$

where P_{max} is the maximum applied load, Y_{min} is the minimum geometry correction factor, and B and W are as shown in Fig. 2. Strictly speaking, this relationship is only valid for materials with flat R-curves [*4,27*]. In the present study it was convenient for comparison purposes to apply Eq 1 to all materials regardless of whether or not the R-curves were flat. Therefore, the following relationship was used to designate the critical stress intensity factor for the chevron-notched geometry as determined from the maximum load although with no unloading-reloading cycles [ASTM Method for Plane-Strain (Chevron Notch) Fracture Toughness of Metallic Materials (E 1304-89)] as was the case for all the tests in this study

$$K_{IvM} = Y_{min}P_{max}/(BW^{1/2}) \tag{2}$$

where K_{IvM} is termed the chevron-notch fracture toughness for purposes of this study, and the other terms remain the same as previously defined.

As previously discussed, stable crack growth behaviour can be described as an R-curve. The R-curve is readily calculated as the strain energy release rate, G_R, plotted as a function of the incremental crack extension, Δa. A global energy approach was used in which G_R^i, for each Δa, was calculated from the change in strain energy, ΔU_i, required to create an incremental fracture area, ΔA_i, such that [*28*]

$$G_R^i = \Delta U_i/\Delta A_i \tag{3}$$

as shown schematically in Fig. 5*a*. Advantages of this technique are that it is valid regardless of the conditions at the crack tip and that it tends to average and smooth the spontaneous run-arrest crack growth behaviour of certain ceramic composites, thus yielding more "well-behaved" R-curves (i.e., realistic, energy-based R-curves).

At the point of complete fracture through the chevron section, the work-of-fracture [*5,6*] can be determined from the total energy consumed during the entire fracture process divided by the total, projected fracture area, 2 A_T, of the specimen such that

$$\gamma_{WOF} = (1/2\,A_T)\int_0^{LPD_f} Pd\,(\mathrm{LPD}) \tag{4}$$

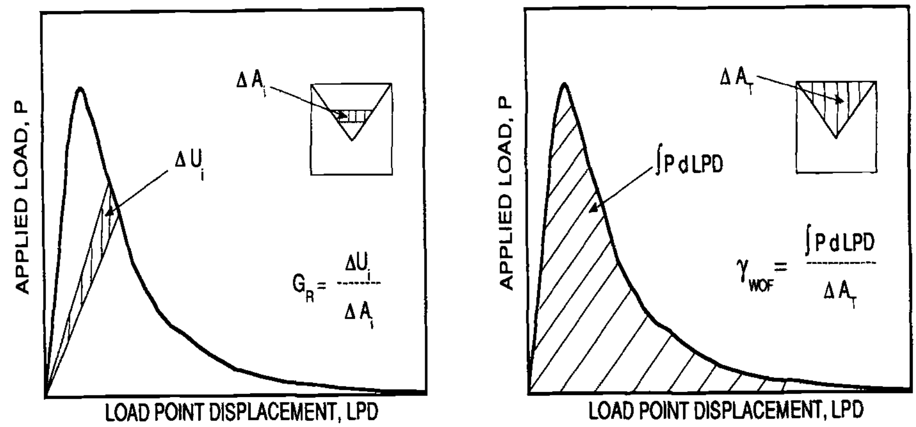

a) Schematic of R-curve determination. b) Schematic of work-of-fracture determination

FIG. 5—*Schematic illustrations for determining* G_R *(R-curve) and work-of-fracture,* γ_{WOF}.

as shown schematically in Fig. 5*b* and where LPD_f is the value of the final LPD when the applied load, P, is zero. Note that the determination of the load-LPD curve from the load-CMOD curves is necessary for the calculation of both the *R*-curves and work-of-fracture. In brittle, linear elastic materials the work-of-fracture can be used as an estimate of the fracture surface energy of a material [*5,6*]. However, for materials which display extensive non-linear fracture processes, the work-of-fracture is dependent on the stability of the crack propagation, the crack velocity (hence applied load or displacement rate), size of the fractured area, and other testing conditions. Therefore, the work-of-fracture becomes a non-linear fracture parameter meaningful primarily for comparative purposes, such as those employing various specimen sizes.

Test Results

The basic information acquired for each fracture test was a plot of applied load versus CMOD or LPD, as shown by example in Fig. 6. Note that no unloading-reloading cycles for compliance measurement checks were introduced in these curves due to the difficulties associated with such techniques at elevated temperatures and the dubious usefulness of these compliance techniques in ceramics with developed, crack-wake effects [*29*]. This load-displacement information was then digitized and used along with the specimen dimensions and testing geometry data as the input file for a computer program [*15*], which automatically calculated the apparent K_{IvM}, G_R versus Δa (assuming linear-elastic unloading), and γ_{WOF}.

Figure 7 illustrates K_{IvM} as a function of temperature for various ceramic materials. Note that K_{IvM} generally decreases with increasing temperature, although K_{IvM} of α-SiC, while relatively low compared to the other materials, appears to be nearly temperature independent. Table 2 contains the K_{IvM} values of all the various materials over the range of temperatures used in the studies.

Figures 8 and 9 show *R*-curve results for some representative materials. The *R*-curves shown are polynomial least-squares curve fits of at least three complete *R*-curves generated at each test condition, where each complete *R*-curve was generated from a single-specimen test. Linear-elastic materials such as α-SiC display flat *R*-curves with fracture resistance

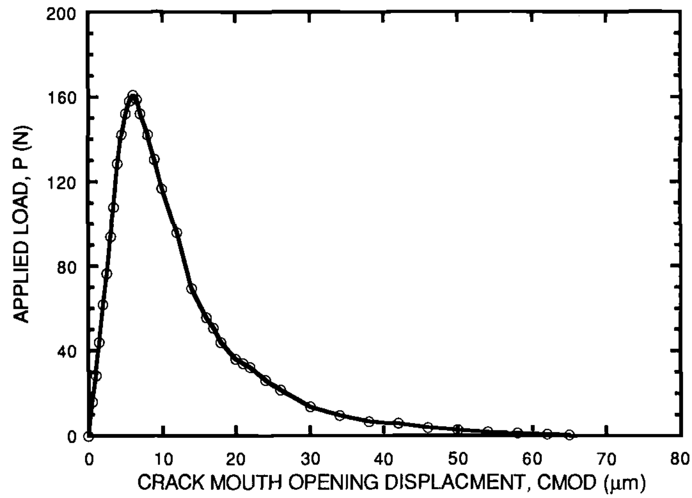

FIG. 6—*Example of load-displacement for a stable crack growth fracture test of silicon nitride (A2Y6) at room temperature.*

independent of crack length as shown in Fig. 8. Nonlinear-elastic materials such as the spinel, the self-reinforced monoliths, the SiC_W/Al_2O_3, and the CVI composites exhibit rising *R*-curves with increasing crack growth resistance for increasing crack length, as shown in Fig. 9, indicative of fracture mechanisms which develop in the wake region as the crack propagates.

Examples of work-of-fracture as a function of temperature are shown in Fig. 10. It was

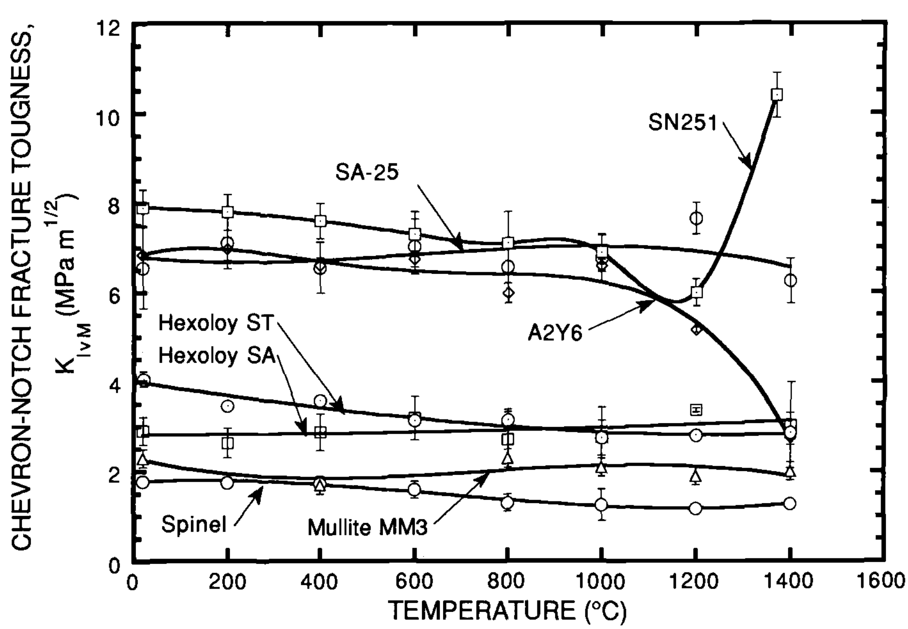

FIG. 7—*Chevron-notch fracture toughness, K_{IvM}, versus temperature for various materials.*

TABLE 2—K_{IvM} (*MPa $m^{1/2}$*) *at various temperatures.*

Material	Test Temperature, °C 20	200	400	600	800	1000	1200	1400
MONOLITHS								
Mullite KM1 [*17*]	2.2 ± 0.3	...	1.9 ± 0.2	...	1.9 ± 0.5	1.7 ± 0.2	2.0 ± 0.3	2.3 ± 0.3
Mullite KM3 [*17*]	2.3 ± 0.3	...	1.8 ± 0.2	...	1.7 ± 0.2	2.1 ± 0.1	2.1 ± 0.2	1.9 ± 0.2
Mullite MM1 [*17*]	1.9 ± 0.3	...	2.0 ± 0.2	...	2.1 ± 0.2	1.9 ± 0.2	2.1 ± 0.2	2.2 ± 0.2
Mullite MM3 [*17*]	2.3 ± 0.2	...	1.7 ± 0.2	...	2.3 ± 0.2	2.1 ± 0.2	1.9 ± 0.2	2.0 ± 0.2
Spinel [*18*]	1.8 ± 0.1	1.8 ± 0.1	1.7 ± 0.1	1.6 ± 0.2	1.3 ± 0.2	1.3 ± 0.4	1.2 ± 0.1	1.3 ± 0.1
Hexoloy SA [*19*]	2.9 ± 0.3	2.6 ± 0.3	2.9 ± 0.4	3.2 ± 0.5	2.7 ± 0.7	2.8 ± 0.7	3.4 ± 0.1	3.0 ± 0.9
A2Y6 [*20*]	6.9 ± 0.1	7.0 ± 0.3	6.6 ± 0.2	6.8 ± 0.2	6.0 ± 0.2	6.6 ± 0.1	5.2 ± 0.1	2.8 ± 0.1
SN251 [*21,22*]	7.9 ± 0.4	...	...	...	7.1 ± 0.7	6.9 ± 0.4	6.0 ± 0.3	10.4 ± 0.5[a]
COMPOSITES								
SA-25 [*23,24*]	6.6 ± 0.9	7.1 ± 0.6	6.6 ± 0.6	7.0 ± 0.6	6.6 ± 0.4	6.8 ± 0.5	7.7 ± 0.4	...
Hexoloy ST [*25*]	4.1 ± 0.2	3.5 ± 0.1	3.6 ± 0.1	3.1 ± 0.1	3.2 ± 0.2	2.8 ± 0.4	2.8 ± 0.1	2.9 ± 0.3
Nicalon/CVI SiC III [*26*]	2.9 ± 0.3	2.6 ± 0.3	2.5 ± 0.5	2.5 ± 0.4	2.4 ± 0.6	3.0 ± 0.7	2.8 ± 0.4	2.8 ± 0.4
FP-Alumina/CVI SiC V [*26*]	7.2 ± 0.8	...	5.8 ± 0.8	...	...	3.8 ± 0.5	2.9 ± 0.4	2.2 ± 0.4

NOTE: Values shown are mean values ± one standard deviation.
[a]Temperature = 1371°C.

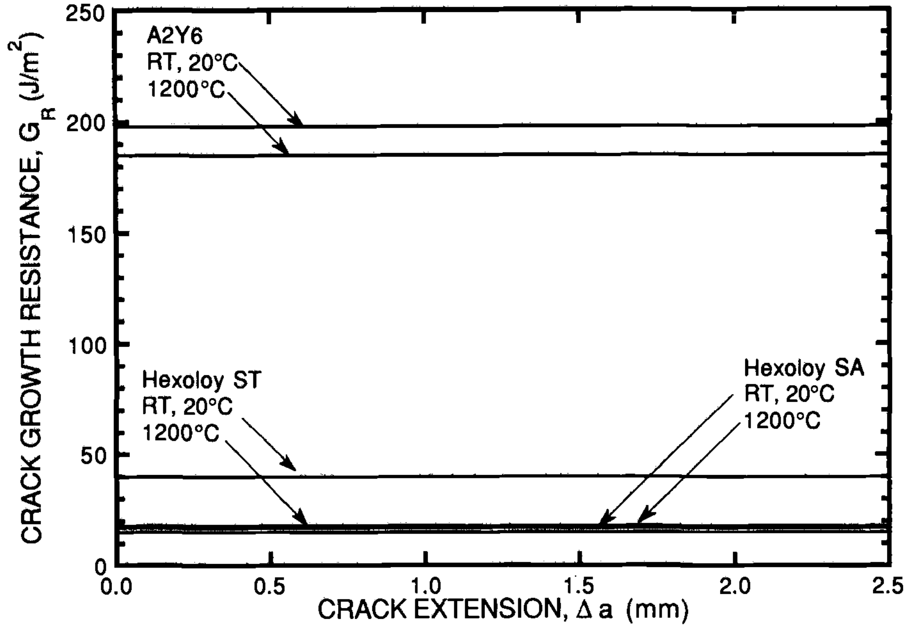

FIG. 8—*Crack growth resistance (*R*-curve)* G_R*, at two temperatures for various materials displaying linear elastic behaviour.*

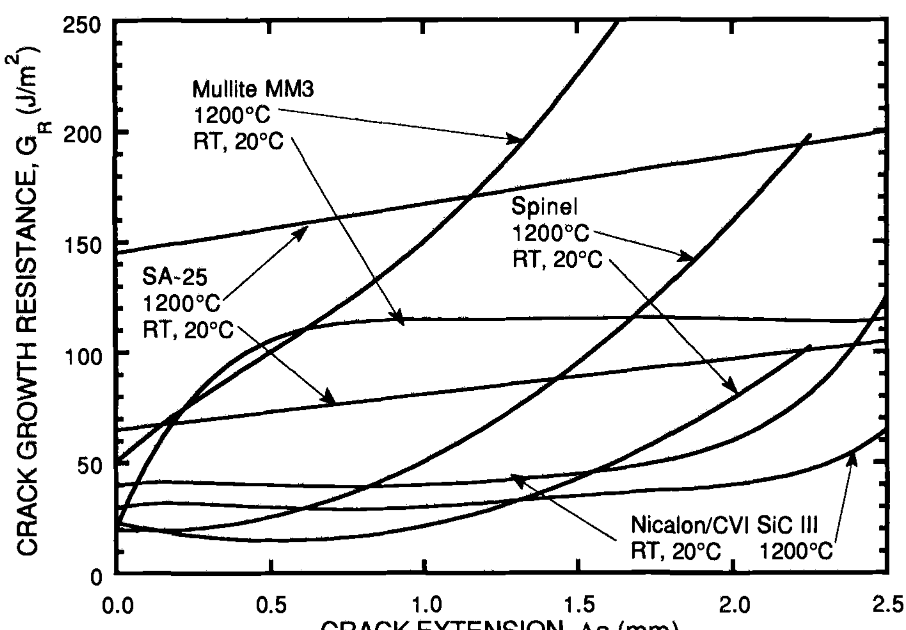

FIG. 9—*Crack growth resistance,* R*-curves,* G_R*, at two temperatures for various materials displaying nonlinear elastic behaviour.*

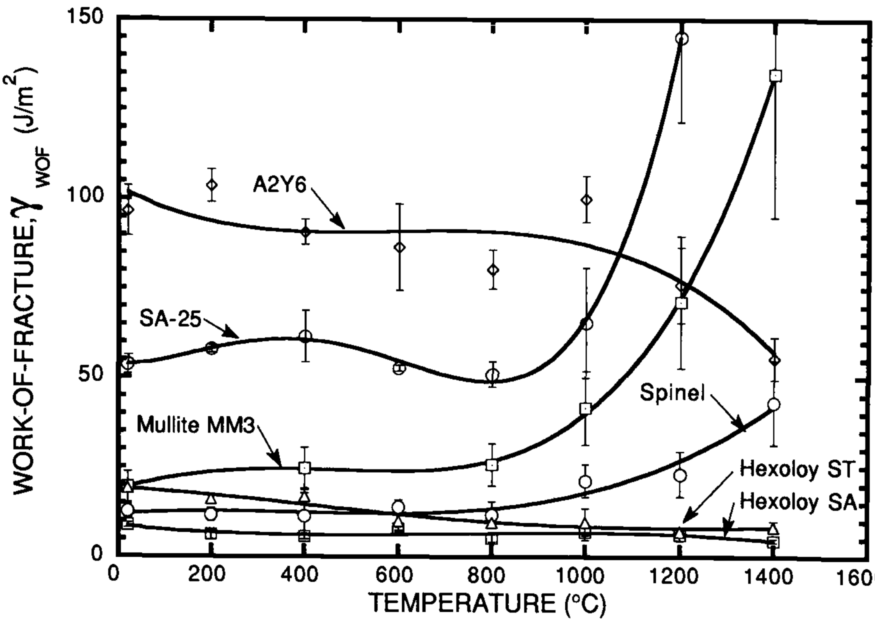

FIG. 10—*Work-of-fracture, γ_{WOF}, versus temperature for various materials.*

observed that linear elastic materials (e.g., α-SiC) display work-of-fracture values approximately equal to the fracture surface energy of the material. However, for materials which display nonlinear elastic fracture behavior (e.g., SiC_W/Al_2O_3,CVI composites) the work-of-fracture values are much greater than either the values calculated from the fracture initiation energy ($\gamma_{WOF} = G_{IC}/2$) or the values calculated from the rule-of-mixtures of the fracture surface energies of the constituent materials. Table 3 contains the γ_{WOF} values of all the various materials over the range of temperatures used in the studies.

Discussion

Generally, the chevron-notched geometry provides fracture behaviour information comparable to other methods employing sharp crack techniques (i.e., techniques in which controlled, atomistically sharp crack are introduced into the material). As mentioned previously, one of the advantages of the chevron notch is the automatic crack initiation, which eliminates the time consuming and tedious task of precracking the specimens. Sharp cracks are particularly important for determining the fracture parameter, K_{IC}, at crack initiation, where blunt crack tips will cause an overestimation of the sharp crack K_{IC}.

In a comparison *[19]* of various sharp crack techniques applied to the model, brittle, polycrystalline α-SiC, K_{IvM} at room temperature determined from the chevron-notched geometries (2.8 to 3.6 MPa $m^{1/2}$) compared well with measured fracture toughness values from techniques such as the controlled flaw, Knoop indentation flexure specimens (2.7 to 3.5 MPa $m^{1/2}$), precracked double cantilever beam specimens (2.5 MPa $m^{1/2}$) and precracked double torsion specimens (3.0 to 4.6 MPa $m^{1/2}$). Tests on this same material using unprecracked, blunt notches yielded calculated fracture toughness values of 3.5 to 4.8 MPa $m^{1/2}$ for single edge-notched bend beams and 3.9 MPa $m^{1/2}$ for a Charpy impact specimen. The

TABLE 3—γ_{WOF} *(J/m^2) at various temperatures.*

Material	Test Temperature, °C							
	20	200	400	600	800	1000	1200	1400
MONOLITHS								
Mullite KM1 [*17*]	10.5 ± 3.8	...	9.6 ± 2.8	...	10.0 ± 3.6	11.7 ± 3.8	17.0 ± 5.5	26.2 ± 9.1
Mullite KM3 [*17*]	18.5 ± 4.1	...	20.9 ± 5.2	...	18.2 ± 4.1	22.9 ± 4.6	40.1 ± 12.3	90.5 ± 32.6
Mullite MM1 [*17*]	17.4 ± 4.1	...	20.4 ± 5.5	...	20.2 ± 4.1	23.6 ± 5.2	26.4 ± 7.3	29.8 ± 8.5
Mullite MM3 [*17*]	19.5 ± 4.3	...	24.7 ± 5.9	...	25.8 ± 5.9	41.7 ± 10.3	71.3 ± 18.5	135.2 ± 40
Spinel [*18*]	12.7 ± 1.8	11.8 ± 1.8	11.5 ± 6.4	14.1 ± 1.8	11.8 ± 3.6	21.4 ± 4.6	23.2 ± 6.4	43.2 ± 11.8
Hexoloy SA [*19*]	8.8 ± 0.6	6.4 ± 1.4	5.8 ± 0.8	8.0 ± 0.5	5.3 ± 1.0	7.1 ± 2.2	6.3 ± 1.7	4.6 ± 0.5
A2Y6 [*20*]	96.7 ± 6.9	103.2 ± 5	90.9 ± 3.5	86.7 ± 12	80.5 ± 5.5	100.8 ± 6.4	76.1 ± 10.7	55.5 ± 6.0
SN251 [*21,22*]	84.5 ± 8.3	...	...	...	...	...	...	...
COMPOSITES								
SA-25 [*23,24*]	53.7 ± 2.7	58.1 ± 1.1	61.6 ± 7.2	52.8 ± 0.8	51.1 ± 3.6	65.5 ± 15.4	145.3 ± 24	...
Hexoloy ST [*25*]	19.2 ± 1.5	16.2 ± 0.8	16.9 ± 2.3	10.1 ± 3.0	9.8 ± 1.4	9.9 ± 3.8	7.3 ± 0.1	8.5 ± 1.6
Nicalon/CVI SiC III [*26*]	...	...	...	...	...	...	...	...
FP-Alumina/CVI SiC V [*26*]	...	...	...	...	...	...	...	...

NOTE: Values shown are mean values ± one standard deviation.

chevron-notched geometry provides a simple, spontaneous method for producing a sharp crack for the proper determination of the apparent fracture toughness.

While the chevron-notched geometry provides a good means for sharp crack initiation, a limitation exists in the application of the K_{IC} calculation (Eq 1) as applied to materials which display nonlinear elastic fracture behaviour, i.e., rising *R*-curve. In the case of the SiC_w/Al_2O_3 composite [*21*,*22*], K_{IvM} at room temperature determined from the chevron-notched geometry (sharp crack) was 6.6 MPa $m^{1/2}$, while for the straight notch geometry (blunt notch) the measured fracture toughness was 6.2 MPa $m^{1/2}$. As shown in Eq 2, the calculation of K_{IvM} is made at the maximum load, which occurs in the chevron-notched geometry after a small amount of stable crack growth. Thus, since the *R*-curve for this material is rising (i.e., increasing with increasing crack extension) the stress intensity factor calculated as K_{IvM} at P_{max} actually represents the fracture resistance on the developing *R*-curve rather than at crack initiation. This can result in an overestimation of the fracture toughness, which is an even greater value than that determined from the blunt notch specimen. This empirical result is just as anticipated analytically for materials with rising *R*-curves [*4*,*28*] and limits the use of the chevron-notched specimen for determining the fracture toughness in these types of materials, thus making the *R*-curve necessary for evaluating fracture behavior.

The inherent stable crack growth in the chevron-notched geometry is crucial to the determination of the crack growth resistance. If the relations for the compliance versus crack length are known, either numerically or empirically, then it is a straightforward matter to determine the instantaneous crack length at any point along the load-displacement curve. The use of the global energy fracture parameter, *G* (linear strain energy release rate), simplifies the analysis by allowing the instantaneous change in the strain energy to be easily determined from the load-displacement curve. The assumption of linear-elastic unloading allows the use of monotonic loading, which avoids the difficulty and complication of attempting to unload and reload the specimen in order to determine the unloading compliance [*29*]. This assumption appears to be valid for many of the ceramics presented here which display linear-elastic behaviour such as shown in Fig. 8 in which the crack lengths for the flat *R*-curves were calculated using the compliances determined assuming linear-elastic unloading rather than compliances determined from unloading-reloading cycles. Errors which might develop from this assumption for nonlinear elastic ceramics are not considered directly in this study but have been addressed by other researchers [*15*,*29*]. In summary, for a given crack length the compliance values obtained from the slopes of the unloading paths can be expected to be different from those obtained from numerical or empirical evaluations. The reason for this is that during unloading the energy dissipation must be accompanied by some hysteresis in the fracture process zone and the crack wake region, including strong frictional interaction effects between the fractured main crack surfaces. Such frictional interaction is especially significant in ceramic composites (such as those with fibre, whisker, or particle reinforcements) where very rough fracture surfaces or even crack-bridging ligaments exist. The magnitude of compliance errors resulting from crack surface interactions during unloading may be expected to vary depending on material type as well as specimen geometry [*29*]. Therefore, the assumption of linear-elastic unloading offers a simple yet effective method of estimating crack length and avoids the complication and dubious benefit of unloading-reloading, especially for elevated-temperature fracture tests. Studies involving the direct comparison of various compliance methods (e.g., unload-reload cycles, monotonic loading, etc.) for determining crack lengths in ceramics will be the subject of further research.

However, for nonlinear elastic materials, the shapes of the *R*-curves are indicative of fracture mechanisms which may be influenced by the specimen geometry. For example, as shown in Fig. 9 for mullite MM3, at room temperature the *R*-curve assumes the classic power law shape noted in Fig. 1 for ductile materials. At 1200°C, for this same material, the R-curve shape is inverted and rises steeply at larger crack lengths where the crack tip approaches the back side of the specimen. Such sharply rising behaviour has been noted in other materials, as shown in Fig. 9, which display large frontal process zones which interact with the compressive stresses in the hinged, remaining ligament of the flexure specimen. In other cases, such as the SiC_W/Al_2O_3 composite at both room temperature and 1200°C, the rising R-curve never appears to reach a plateau, indicating that the size of the fracture process zone behind the main crack tip has not reached a finite size within the dimensions of the specimen (~2.5 mm). Thus, for some materials and some conditions the specimen dimensions may not be sufficiently large to allow the fracture process zone to fully develop and thus allow the crack growth resistance to reach the fully developed fracture resistance value on a plateau. However, the initial rising parts of the R-curves are still indicative of developing crack growth resistance, hence rising R-curve behaviour.

Complete and stable fracture of the specimen is necessary for the calculation of γ_{WOF}. The inherent stability of the fracture process in the chevron-notched, flexure specimen allows the controlled fracture of the entire chevron section. In linear elastic materials, such as the α-SiC, γ_{WOF} can be used as an estimate of the fracture surface energy, γ_F. Extending the assumption of linear elastic behaviour to LEFM, the apparent fracture toughness can be calculated from the γ_{WOF} such that [*5,6,28*]

$$K_{IC}^{a} = \sqrt{E' \, (2\gamma_{WOF})} \tag{5}$$

where K_{IC}^{a} is the apparent fracture toughness, E' is the elastic modulus of the material. Applying Eq 5 to the α-SiC at room temperature where $E' = 427$ GPa [*19*] and $\gamma_{WOF} = 8.8$ J/m^2 yields a K_{IC}^{a} of 2.7 MPa m$^{1/2}$, which is in very good agreement with the K_{IvM} of 2.9 MPa m$^{1/2}$ calculated from Eq 2. For nonlinear elastic materials such as the SiC_W/Al_2O_3 composite at room temperature, the use of Eq 5 to predict the K_{IC}^{a} yields a value of 6.5 MPa m$^{1/2}$ ($E' = 392$ GPa [*24*], $\gamma_{WOF} = 53.7$ J/m^2) compared to the K_{IvM} of 6.6 MPa m$^{1/2}$ calculated from Eq 2 which is also in good agreement.

However at elevated temperatures such as 1200°C where the nonlinear elastic behaviour of the composite is more in evidence, Eq 5 predicts a K_{IC}^{a} value of 9.5 MPa m$^{1/2}$ ($E' = 310$ GPa [*24*], $\gamma_{WOF} = 145.3$ J/m^2) compared to the K_{IvM} of 7.7 MPa m$^{1/2}$ calculated from Eq 2. The α-SiC at 1200°C where $E' = 427$ GPa [*19*] and $\gamma_{WOF} = 6.3$ J/m^2 yields a K_{IC}^{a} of 2.3 MPa m$^{1/2}$ using Eq 5, which is still in reasonable agreement with the K_{IvM} of 2.8 MPa m$^{1/2}$ calculated from Eq 2. Thus if the energy consumed by the nonlinear fracture processes of the composite is too large, total work-of-fracture cannot be used to predict the LEFM K_{IC}. In addition, because the work-of-fracture is related to nonlinear fracture mechanisms its determination will be dependent upon such conditions as crack velocity (displacement or loading rate), size of the chevron section, and other testing variables. Despite these limitations in non-LEFM materials, γ_{WOF} is still a useful nonlinear elastic fracture parameter for comparative purposes for the same material and test conditions.

Values of γ_{WOF} for the CVI composites were not reported due to a limitation of the flexure bar in testing fibrous composites. This limitation is that the crack front "stalls out" as it encounters the compression region of the remaining ligament where fibre buckling and other stress interactions as well as localized crushing of the material by the push rod have altered the stress distributions in that area of the specimen. The stalling of the crack is manifested in the load-displacement diagram as a constant load with increasing displacement [*26*]. In the case of specimens tested with the LIDG, the load remained constant even beyond the range of the LIDG (~1 mm). Thus complete fracture of the chevron section could not be achieved and γ_{WOF} could not be calculated.

Conclusions

Three important characteristics of the chevron-notched geometry, atomistically sharp crack initiation, inherent stable crack growth, and suitability for use at elevated temperatures, allow the study of the stable crack growth behaviour of brittle and quasi-brittle materials. Automatic crack initiation is especially important for testing at elevated temperatures where precracked specimens may experience difficulties with crack healing and blunting. Inherent stable crack growth is required for determining the crack growth resistance from single specimens of materials with flat R-curves which would fracture catastrophically in straight-through crack specimens. Suitability for use at elevated temperatures eliminates complications associated with precracking fracture specimens prior to testing or possible crack healing of the precracks during the elevated temperature tests.

The evaluation of the fracture resistance as three regimes—crack initiation, stable crack growth, and final fracture, elucidates the evolution of micro-mechanical fracture mechanisms which may be not only inherent to the material system but may also be highly dependent on processing. In addition, the three fracture parameters thus generated, K_{IvM}, G_R, γ_{WOF}, can be linked through LEFM for materials which behave in a linear elastic fashion, thus confirming the application of LEFM. If the material fractures in a nonlinear elastic manner, the three parameters are essential to more clearly characterize the fracture behaviour of the material under the given conditions.

Finally, the utility of the technique is shown in its applicability to a wide range of materials systems over a wide range of elevated temperatures. The test temperature ranged from 20 to 1400°C, while materials systems ranged from monolithic ceramics to self-reinforced monolithic ceramic to fibre-, particle-, or whisker-reinforced ceramic composites.

Acknowledgments

The authors wish to acknowledge the assistance and guidance of R. C. Bradt and A. S. Kobayashi as well as the facilities at the College of Engineering, University of Washington, in the completion of much of the work described here. Research funded as part of the Ceramic Technology for Advanced Heat Engines Project of the Advanced Materials Development Program and partially performed in the High Temperature Materials Laboratory User Facility, both sponsored by the U.S.-DOE, Assistant Secretary for Conservation and Renewable Energy, Office of Transportation Technologies, under contract DE-AC05-84OR21400 managed by Martin Marietta Energy Systems, Inc.

References

[1] Vaccari, D. L. and Khandelwal, P. K., "Life Prediction Methodology," Element 3.2.2.2, *Ceramic Technology for Advanced Heat Engines Project Semiannual Progress Report for October 1989 through March 1990*. ORNL/TM-11586, Oak Ridge National Laboratory, Oak Ridge, TN, 1990, pp. 397–401.

[2] Comfort, A., Cuccio, J., and Fang, H., "Life Prediction Methodology for Ceramic Components of Advanced Engines," WBS Element 3.2.2.3, *Ceramic Technology for Advanced Heat Engines Project Semiannual Progress Report for October 1989 through March 1990*. ORNL/TM-11586, Oak Ridge National Laboratory, Oak Ridge, TN, pp. 402–411.

[3] Steinbrech, R., Knehans, R., and Schaarwachter, W., "Increase of Crack Resistance During Slow Crack Growth in Al_2O_3 Bend Specimens," *Journal of Materials Science*, Vol. 18, No. 1, 1983, pp. 265–270.

[4] Newman, J. C., Jr., "A Review of Chevron-notched Fracture Specimens," *Chevron-Notched Specimens: Testing and Stress Analysis, ASTM STP 855*, J. H. Underwood, S. W. Freiman, and F. I. Baratta, Eds., American Society for Testing and Materials, Philadelphia, 1984, pp. 5–31.

[5] Nakayama, J., "Bending Method for Direct Measurement of Fracture Energy of Brittle Materials," *Japan Journal of Applied Physics*, Vol. 3, No. 7, 1964, pp. 422–423.
[6] Tattersal, H. G. and Tappin, G., "The Work of Fracture and Its Measurement in Metals, Ceramics, and Other Materials," *Journal of Materials Science*, Vol. 1, 1966, pp. 296–301.
[7] Pook, L. P., "An Approach to a Quality Control K_{IC} Testpiece," *International Journal of Fracture*, Vol. 8, 1972, pp. 103–108.
[8] Munz, D. G., Shannon, J. L., Jr., and Bubsey, R. T., "Fracture Toughness Calculation from Maximum Load in Four-Point Bend Tests of Chevron Notch Specimens," *International Journal of Fracture*, Vol. 16, 1980, pp. R137–R141.
[9] Ghosh, A., Jenkins, M., White, K. W., Kobayashi, A. S., and Bradt, R. C., "The Chevron-Notched Bend Bar Technique for Fracture Resistance Measurements of Ceramics," *Ceramic Materials and Components for Engines. Proceedings of the Third International Symposium*. V. J. Tennery, ed., The American Ceramic Society, Westerville, OH, 1989, pp. 592–603.
[10] Sakai, M. and Yamasaki, K. K., "Numerical Fracture Analysis of Chevron Notches: I and II," *Journal of the American Ceramic Society*, Vol. 66, 1983, pp. 371–375.
[11] Jenkins, M. G., Kobayashi, A. S., White, K. W., and Bradt, R. C., "A 3-D Finite Element Analysis of a Chevron-notched, Three-point Bend Fracture Specimen for Ceramic Materials," *International Journal of Fracture*, Vol. 34, 1987, pp. 281–295.
[12] Joch, J., Zemankova, J., and Kazda, J., "Analysis of a Chevron-Notched Four-Point-Bend Specimen by the Three-Dimensional Finite-Element Method," *Journal of the American Ceramic Society*, Vol. 71, No. 3, 1988, pp. C-154–C-155.
[13] He, M.Y. and Evans, A. G., "Three-Dimensional Finite Element Analysis of Chevron-Notched, Three-Point and Four-Point Bend Specimens," to be published in the proceedings of the ASTM 22nd National Fracture Symposium held in Atlanta, Georgia, June 1990.
[14] Jenkins, M. G., Kobayashi, A. S., Sakai, M., White, K. W., and Bradt, R. C., "Fracture Toughness Testing of Ceramics Using a Laser Interferometric Strain Gage," *American Ceramics Society Bulletin*, Vol. 12, No. 6, 1987, pp. 1734–1738.
[15] Jenkins, M. G. "Ceramic Crack Growth Resistance Determination Utilizing Laser Interferometry," Ph.D. dissertation, Department of Mechanical Engineering, University of Washington, Seattle, WA, 1987.
[16] Jenkins, M. G., Kobayashi, A. S., Peussa, J. T., Salem, J. A., and Okura, A., "Laser Interferometry for Measuring Elevated Temperature Fracture Resistance of Ceramics," *Proceedings of the International Conference on Advanced Experimental Mechanics*, Tianjin University, Tianjin, People's Republic of China, 16–20 May 1988, pp. C66–C71.
[17] Ghosh, A., "Effect of Microstructure and Temperature on the Fracture Resistance of Duplex Microstructure Mullite," Ph.D. dissertation, Department of Materials Science and Engineering, University of Washington, Seattle, WA, 1989.
[18] Ghosh, A., White, K. W., Jenkins, M. G., Kobayashi, A. S., and Bradt, R. C., "Fracture Resistance of a Transparent $MgAl_2O_4$," accepted for publication by the American Ceramic Society, 1990.
[19] Ghosh, A., Jenkins, M. G., Kobayashi, A. S., White, K. W., and Bradt, R. C., "Elevated Temperature Fracture Resistance of a Sintered α-Silicon Carbide," *Journal of the American Ceramic Society*, Vol. 72, No. 2, 1989, pp. 242–274.
[20] Ghosh, A., Jenkins, M. G., Kobayashi, A. S., and Bradt, R. C., "Elevated Temperature Fracture Resistance of a Hot Pressed Si_3N_4," unpublished work, University of Washington, Seattle, WA, 1989.
[21] Salem, J. A., Manderscheid, Freedman, M. R., and Gyekenyesi, J. P., "Reliability Analysis of a Structural Ceramic Combustion Chamber," NASA Technical Memorandum 103741, August 1990.
[22] Salem, J. A., Choi, S. R., Freedman, M. R., and Jenkins, M. G., "Mechanical Behaviour and Failure Phenomenon of an In-Situ-Toughened Silicon Nitride," NASA Technical Memorandum 103741, February 1991.
[23] Jenkins, M. G., White, K. W., Ghosh, A., Kobayashi, A. S., and Bradt, R. C., "The R-Curve Behavior of SiC Whisker Polycrystalline Alumina Matrix Composite to 1400° C," *Whisker- and Fiber-Toughened Ceramics. Proceedings of an International Conference*. R. A. Bradley, D. E. Clark, D. C. Larsen, and J. O. Stiegler, Eds., ASM International, 1988, pp. 281–288.
[24] Jenkins, M. G., White, K. W., Kobayashi, A. S., and Bradt, R. C., "Elevated Temperature Fracture Characteristics of a SiC Whisker/Al_2O_3 Matrix Composite," *Engineering Fracture Mechanics*, Vol. 30, 1988, pp. 505–510.
[25] Jenkins, M. G., Salem, J. A., and Seshadri, S. G., "Fracture Resistance of a TiB_2 Particle/SiC

Matrix Composite at Elevated Temperatures," *Journal of Composite Materials*, Vol. 23, No. 1, 1989, pp. 77–91.

[26] Peussa, J. T., "Elevated Temperature Fracture Properties of CVI Silicon Carbide Matrix Continuous Ceramic Fiber Composites," M. Sc. thesis, Department of Materials Science and Engineering, University of Washington, Seattle, WA, 1987.

[27] Shannon, J. L., Jr. and Munz, D. G., "Specimen Size and Geometry Effects on Fracture Toughness of Aluminum Oxide Measured with Short-Rod and Short-Bar Chevron-Notched Specimens," *Chevron-Notched Specimens: Testing and Stress Analysis, ASTM SPT 855*, J. H. Underwood, S. W. Freiman, and F. I. Baratta, Eds., American Society for Testing and Materials, Philadelphia, 1984, pp. 270–280.

[38] Hellan, K., *Introduction to Fracture Mechanics*, McGraw-Hill Book Co., New York, 1984.

[29] Sakai, M. and Bradt, R. C., "Graphical Methods for Determining the Nonlinear Fracture Parameters of Silica and Graphite Refractory Composites," *Fracture Mechanics of Ceramics*, Vol. 7: *Composites, Impact, Statistics, and High-Temperature Phenomena*, R. C. Bradt, A. G. Evans, D. P. H. Hasselman, and F. F. Lange, Eds. Plenum Press, New York, 1986, pp. 127–142.

Sushil K. Bhambri[1] *and Leslie N. Gilbertson*[1]

Short Bar Chevron-Notch Fracture Toughness of Bone Cement

REFERENCE: Bhambri, S. K. and Gilbertson, L. N., "**Short Bar Chevron-Notch Fracture Toughness of Bone Cement,**" *Chevron-Notch Fracture Test Experience: Metals and Non-Metals, ASTM STP 1172*, K. R. Brown and F. I. Baratta, Eds., American Society for Testing and Materials, Philadelphia, 1992, pp. 178–190.

ABSTRACT: Poly(methylmethacrylate) is used as a grouting agent in total joint arthroplasty. Fracture toughness of the relatively brittle bone cement is an important property determining the reliability and defect tolerance capability of the material. In the present study, fracture toughness of bone cement and commercial PMMA has been determined using a short bar chevron-notch test method. Chevron-notched short bar specimens were prepared with a notch molded-in during the polymerization process or by machining techniques. Specimen size and other test parameters were varied to determine variability of the results. In addition, parameters were also varied to simulate clinical practices.

A peak load test method following ASTM E 1304-89 was used to estimate fracture toughness. The load-displacement curves obtained were independent of the displacement rates within the recommended peak load time range. Wide variation of displacement rates had no effect on the fracture toughness values. No plasticity-induced effects on fracture toughness were evident in the slow rate regime up to a peak load time of 300 s for 12.7-mm-thick short bar specimens. The results of this study indicate that the ASTM Test Method E 1304-89 can be successfully used in determining fracture toughness of bone cements.

KEY WORDS: fracture toughness, brittle material, displacement rates, PMMA, bone cement, chevron-notch, fractography

Cemented total joint replacements in hip and knee surgery utilize poly(methylmethacrylate) (PMMA) or a styrene-based copolymer as a grouting agent. These polymers, commonly referred to as bone cement, are brought into the operating room as polymer powder and monomer. The two components are mixed together, positioned in the body in a viscous state, and fully polymerized in vivo. Sometimes the bone cement may form voids due to mixing and the polymerization process. The voids may act as sites for initiation of microcracks, which may propagate and lead to fracture of the cement, resulting in loosening and subsequently failure of metal prosthetic devices [*1,2*]. The bone cement, therefore, plays a vital role in determining the life of cemented total hip and knee replacement systems. The reliability and life of bone cement, like other material systems, is compared using fracture mechanics principles. In the case of bone cement, an increased fracture toughness would indicate that a cement will inherently exhibit a greater degree of resistance to propagation of cracks. Considering the in vivo situation, once the bone cement is positioned in the body it cannot be inspected or removed without significant trauma to the patient. Fracture toughness, therefore, has value in determining the inherent crack tolerance capacity of the material.

[1]Senior research engineer and manager, respectively, Engineering Test Laboratory, Zimmer, Inc., a division of Bristol-Myers Squibb Co., Warsaw, IN 46581-0708.

Various types of specimen geometry and test methods, such as compact tension [*3–6*]. Three-point bending [*6–9*], short rod [*10–12*], and double torsion [*13*] specimens have been used by different authors in the characterization of bone cement for fracture toughness. Difficulty in producing an even crack front in fatigue precracking has been reported with compact tension and three-point bending specimens [*4*]. Attempts have been made to obviate the fatigue precracking by resorting to other techniques for generating a precrack [*4,14*].

In the present investigation, a chevron-notch fracture test method with short bar specimens was used to determine fracture toughness. The ASTM Test Method for Plane-Strain (Chevron-Notch) Fracture Toughness of Metallic Materials (ASTM E 1304-89) was followed for testing and calculation of fracture toughness using the maximum load method. The short bar chevron-notched specimen was selected because it requires no fatigue precracking; the testing is quick, and data analysis is simple. This facilitates extensive testing during material development and quality control. Extensive testing is required in the development of bone cement because fracture toughness can be strongly dependent on its chemical composition and processing parameters.

Experimental Procedures

Material and Specimens

Zimmer® Dough-Type[2] bone cement was prepared by mixing methyl methacrylate powder (polymethylmethacrylate 89.25 wt%, benzoyl peroxide 0.75 wt%, and barium sulfate 10%) and liquid monomer (methyl methacrylate 97.25%,*N*, *N*-Dimethyl-p-toluidine 2.75%, and hydroquinone 75 ppm) in the ratio of 2:1. Mixing was carried out either in vacuum or air. For vacuum mixing, the monomer was chilled prior to mixing to delay polymerization, and mixing was carried out under vacuum using an Osteobond® Vacuum Mixer.[2] For mixing in air the cement and monomer were stored in laboratory air at about 22°C. The powder was placed in a polyethylene beaker, monomer was poured into the powder, and mixing was done with a spatula by hand.

In both cases, the cement was mixed until the powder was completely wetted out. When the mixture turned fully into a viscous liquid, the cement was filled into special molds for shaping as 12.7-mm-square short bar specimens with a molded-in chevron notch. These molds were fabricated from acrylic material, and thin acrylic sheet shims were used to form a 0.35-mm-wide notch. After the cement had completely polymerized, about 20 to 25 min, the mold was disassembled and the samples removed. To simulate clinical practice, a group of specimens was prepared in molds preheated to 37°C. At the 37°C mold temperature, a higher heat of polymerization is available which may result in greater expansion and, hence, a larger number of voids in the specimens. Voids are also formed in air-mixed bone cement specimens due to air entrapped during mixing. This problem was addressed by applying a load of approximately 10 N at the top of the mold. All samples were allowed to remain in the laboratory air environment until testing commenced. A short bar chevron-notched specimen is shown schematically in Fig. 1. Dimensions of all the sample configurations used are shown in Table 1. A few bars, 6.35 mm thick, were also cast from bone cement to machine small-size chevron-notched samples. A typical normal-size bone cement specimen is shown in Fig. 2 along with one of the 6.35-mm-thick specimens. As observed in Fig. 2, the 12.70-mm-square specimens with molded chevron notch were made with a larger grip groove depth than the dimensional requirements of ASTM Test Method E 1304-89 to ensure that no pores or voids were formed near the load-line of the specimen.

[2]Zimmer, Inc., Warsaw, IN.

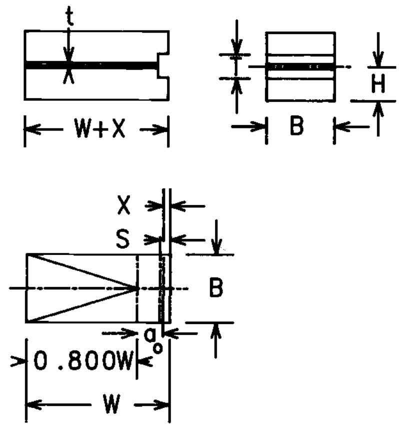

FIG. 1—*Schematic representation of a short bar Chevron-notched specimen.*

Commercially available PMMA sheet was used to prepare reference specimens. The reference samples eliminated any variations due to variation in preparation of bone cement specimens, particularly in the study related to the effect of specimen size. Both square and rectangular short bar samples with thicknesses (B) of 12.70, 11.68, and 6.35 mm were prepared in accordance with all the recommended specimen dimensions in ASTM Test Method E 1304-89 except tor the grip groove depth in 11.80-mm-square specimens with $W/B = 2.0$. In the 11.80-mm-square specimens with $W/B = 2.0$, the grip groove depth was kept similar to the 12.70-r1m-square bone cement specimens prepared with a molded-in chevron notch. The configurations and dimensions of commercial PMMA specimens are also given in Table 1, and representative specimens are shown in Fig. 3.

Test Method

The tests were carried out on an Instron universal testing machine. The grips with the knife-edges used for testing are shown in Fig. 4. The specimens were loaded at different displacement rates within the lower and upper bounds of the recommended range in order for the peak loads to occur within 15 to 60 s. The crosshead speed was varied between 0.50 to 12.7 mm/s, and a load-displacement curve was recorded for each test. Six specimens were tested for each variable parameter.

Fractography

The fracture surfaces of tested specimens were examined for characteristic fracture micromechanisms using a Cambridge S 360 scanning electron microscope. The examination was also intended to determine if any defects influenced the fracture toughness results.

Results and Discussion

Fracture toughness was calculated based on the peak load in the load-displacement curve using the following expression

$$K_{Ic} = \frac{Y_m^* P_m}{B\sqrt{W}}$$

TABLE 1—*Configurations and dimensions of short Chevron-notched specimen in Fig. 1.*

Specimen Type	Material	Preparation Method	B, mm	W, mm	a_0, mm	H, mm	X, mm	T, mm	S, mm	t, mm
Square	Bone cement	Molded	12.70	25.40	5.08	6.35	1.270	4.45	1.90	0.35
Rectangular	PMMA	Machined	12.70	18.41	6.10	5.52	1.270	4.45	1.90	0.35
Square	PMMA	Machined	11.80	23.60	4.72	5.90	1.180	4.13	1.77	0.35
Square	Bone cement	Machined	6.35	12.70	2.60	3.17	0.635	2.22	0.95	0.20
Square	PMMA	Machined	6.35	9.20	3.05	2.76	0.635	2.22	0.95	0.20
Rectangular	PMMA	Machined	6.35	9.20	3.05	2.76	0.635	2.22	0.95	0.20

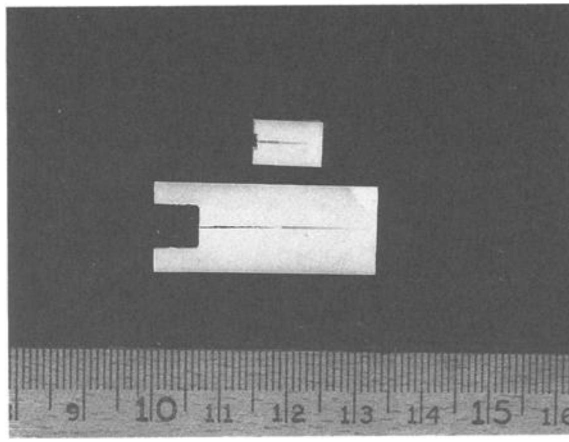

FIG. 2—*Representative bone cement specimens.*

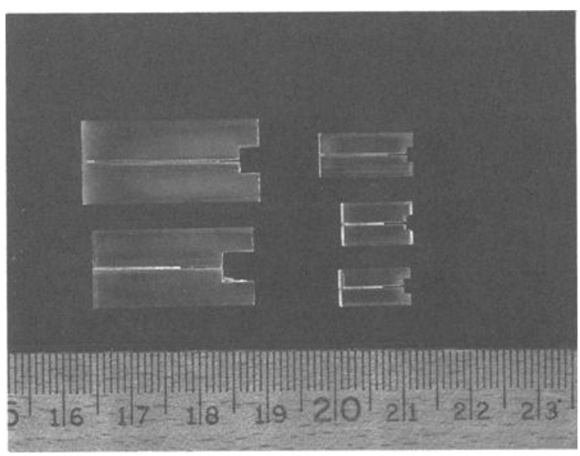

FIG. 3—*Representative commercial PMMA specimens.*

where

K_{Ic} = fracture toughness,
Y^*_m = minimum stress intensity factor coefficient,
P_m = maximum test load,
B = specimen thickness, and
W = specimen length.

The specimen configurations used in the present study are in ASTM E 1304-89. The minimum stress intensity factor coefficient values used in the calculations for each type of specimen employed in testing are given in Table 2. The corresponding values of critical slope ratio (r_c) are also shown in Table 2.

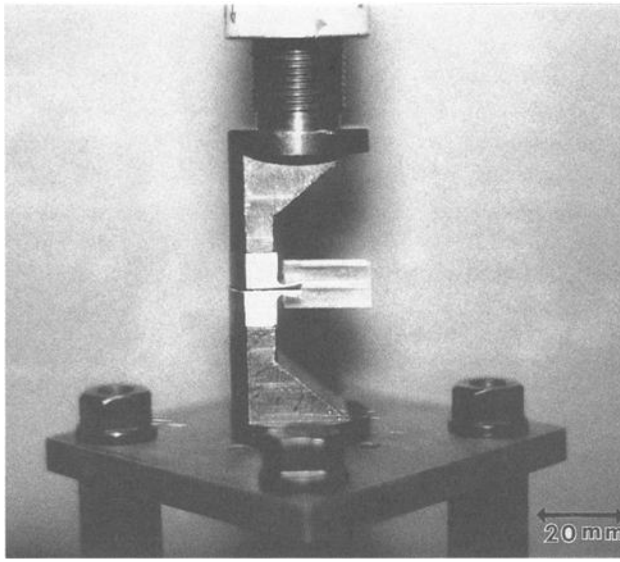

FIG. 4—*Test setup showing grips and knife edges used for testing.*

TABLE 2—*Minimum stress intensity factor coefficients used for various specimen configurations.*

Specimen Type	B, mm	W/B	a_0/W	H/B	Y^*_m	r_c
Square	12.7	2.0	0.2	0.5	29.90	0.30
Square	11.8	2.0	0.2	0.5	29.90	0.30
Rectangular	12.7	1.45	0.332	0.435	28.22	0.52
Square	6.35	2.0	0.2	0.5	29.90	0.30
Square	6.35	1.45	0.332	0.5	25.11	0.52
Rectangular	6.35	1.45	0.332	0.435	28.22	0.52

Representative load-displacement traces for bone cement and commercial PMMA are given in Fig. 5*a–c*. In general, load-displacement curves for the bone cement were flat (Fig. 5*a*). At high displacement rates, they tended to be less flat (Fig. 5*b*). The load-displacement curves for commercial PMMA were nonflat (Fig. 5*c*). Prior to calculations, a validity check was done to confirm that the peak load occurred after the 1.2 r_c point on the load-displacement curve. The fracture toughness values estimated for bone cement mixed in vacuum at 22°C and commercial PMMA are given in Fig. 6.

Representative fractured bone cement specimens tested at different loading rates are shown in Fig. 7. The fracture plane in most of the specimens was flat without any indication of deviation from the plane normal to the applied load. Some of the specimens showed some minor crack plane deviation. Two of the specimens had the fracture plane turned almost 90°, such that the crack plane was nearly parallel to the load axis. These fractures were closely examined for any flaws. While one fracture showed obvious voids, no significant defects could be detected in the other fracture, which could be responsible for the fracture behavior. On both of these specimens there was no crack plane deviation up to one third of crack plane width. Hence, the fracture toughness values calculated from the peak loads

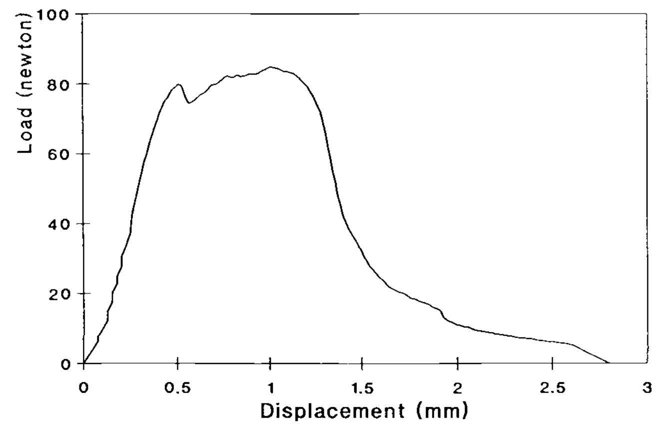

FIG. 5a—*Load-displacement trace for bone cement fracture toughness test at 0.085 mm/s displacement rate.*

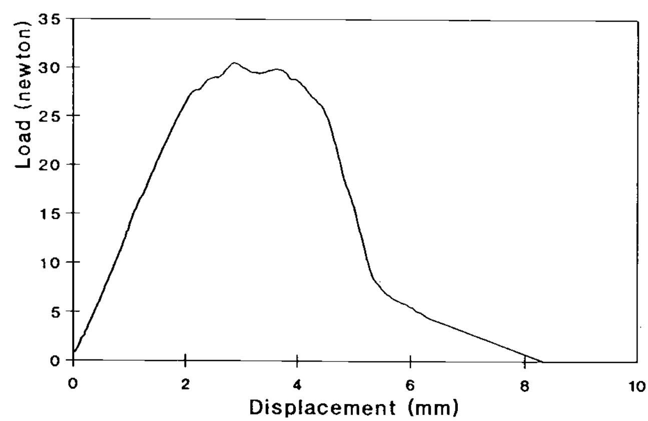

FIG. 5b—*Load-displacement curve for bone cement specimens at 0.211 mm/s displacement rate.*

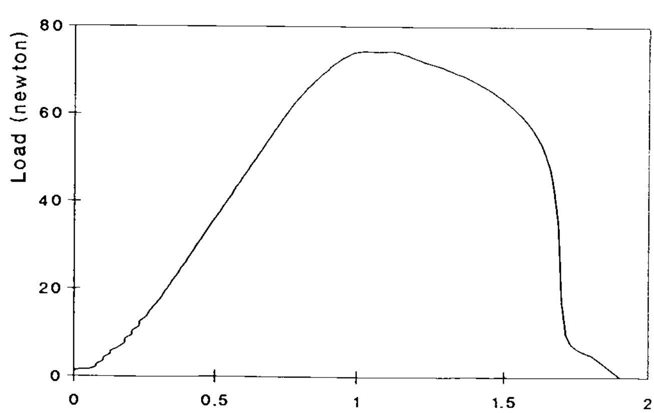

FIG. 5c—*Load-displacement curve for commercial PMMA specimens at 0.0211 mm/s displacement rate.*

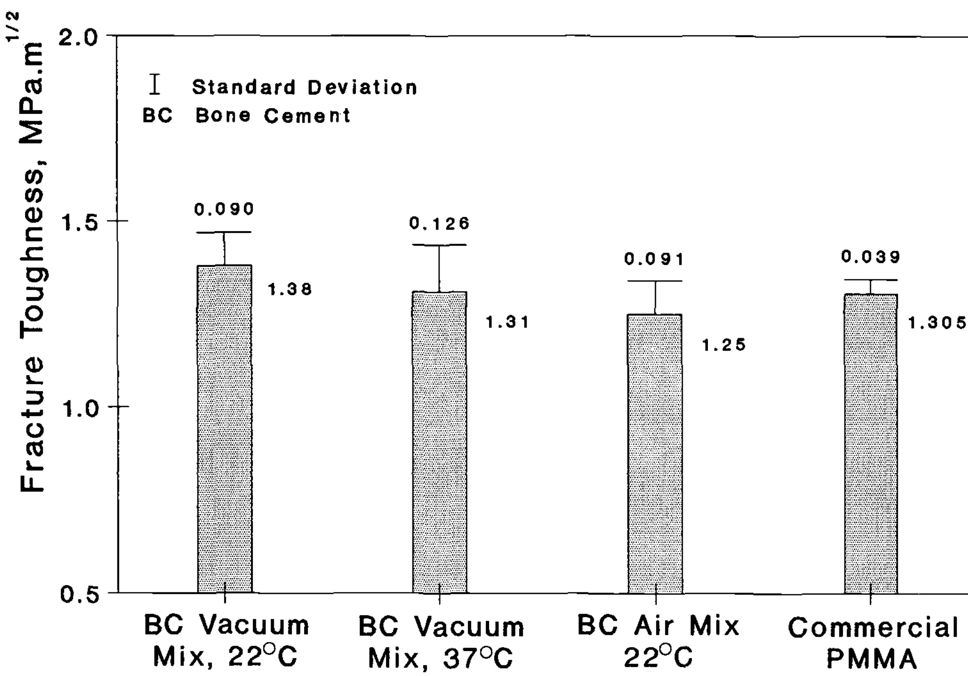

FIG. 6—*Fracture toughness of bone cement specimens for various conditions.*

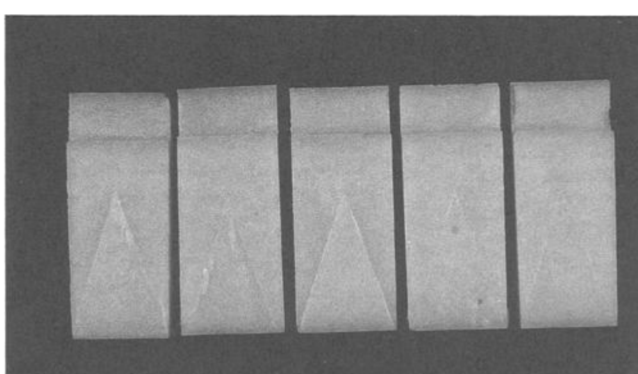

FIG. 7—*Representative fractured bone cement specimens tested at different displacement rates, left to right: 0.0084, 0.02116, 0.042, 0.085, and 0.211 mm/s.*

are still valid. Fracture toughness values, grouped separately for specimens showing different fracture planes, with and without crack plane deviations, were found to be comparable. The reason for the crack plane turning parallel to the load axis is not clearly understood. However, crack plane deviation due to friction or misalignment in experimental setup is ruled out since all specimens were tested under identical conditions and only a few showed crack plane deviation.

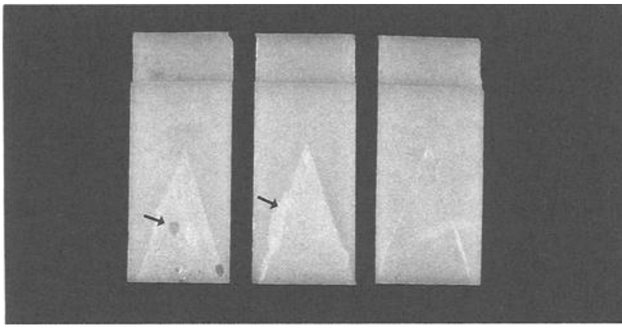

FIG. 8—*Fracture surfaces of bone cement specimens mixed in air, with and without load applied on the mold: left, no load; middle, 5-N load; right, 10-N load. Arrows point to the macroscopic defects.*

The bone cement specimens mixed in air had a fracture appearance that depended upon the pressure applied on the molds. Specimens without any pressure applied during polymerization showed a large number of voids on the fracture surface (Fig. 8). Load-displacement curves for specimens with voids showed crack jump behavior associated with a large drop in load level. Application of a pressurization load during polymerization resulted in a macroscopically flat fracture, free of large voids. This difference in fracture morphology is clearly evident from Fig. 8. In case of the specimens prepared in molds preheated to 37°C, the fracture surfaces did not show any defects which would render the tests invalid. However, large voids were frequently observed on the fracture surfaces. The fracture toughness values estimated for specimens prepared by mixing in air and in preheated molds are also shown in Fig. 6. These values are marginally lower than the specimens prepared at 22°C by vacuum mixing. The fracture toughness values in this study are consistent with the reports of other investigators for other specimen geometries [*3,15*].

The fracture toughness of acrylic polymethylmethacrylate is strongly dependent on its chemistry. The bone cement contains barium sulfate, 10% by weight, as a radiopaque agent. Barium sulfate has been reported to reduce the fracture toughness of bone cement [*3*]. It was surmised that some of the barium sulfate particles don't bond to the PMMA and consequently reduce the fracture toughness by acting as sites for crack initiation. The present results indicate no significant difference in fracture toughness values of bone cement with barium sulfate and commercial PMMA without barium sulfate. The fracture toughness of commercial PMMA varied over a wide range and was 10% higher than the values reported by other authors [*3,4*]. This could be due to the difference in manufacturing source for the commercial PMMA.

The effect of specimen size is better compared from the results of commercial PMMA testing, since a larger number of specimen sizes was investigated for this material. Fracture toughness values obtained for different sizes of specimens are shown in Fig. 9 for the commercial PMMA. The effect of size on fracture toughness of bone cement is also compared in Fig. 9. No appreciable difference in the values is observed. This indicates that fracture toughness of bone cement in small thickness specimens, close to real life situations, can be obtained with a great degree of certainty using short bar chevron-notched specimens. Reducing the specimen thickness further has limitations due to the difficulty in maintaining the dimensional accuracies within the permissible tolerances.

The effect of displacement rates on the fracture toughness of bone cement is shown in Fig. 10. Variations in displacement rates did not appear to influence the character of load-displacement traces when the displacement rates used yielded peak loads within the time intervals recommended in the ASTM Standard. At higher displacement rates, which resulted

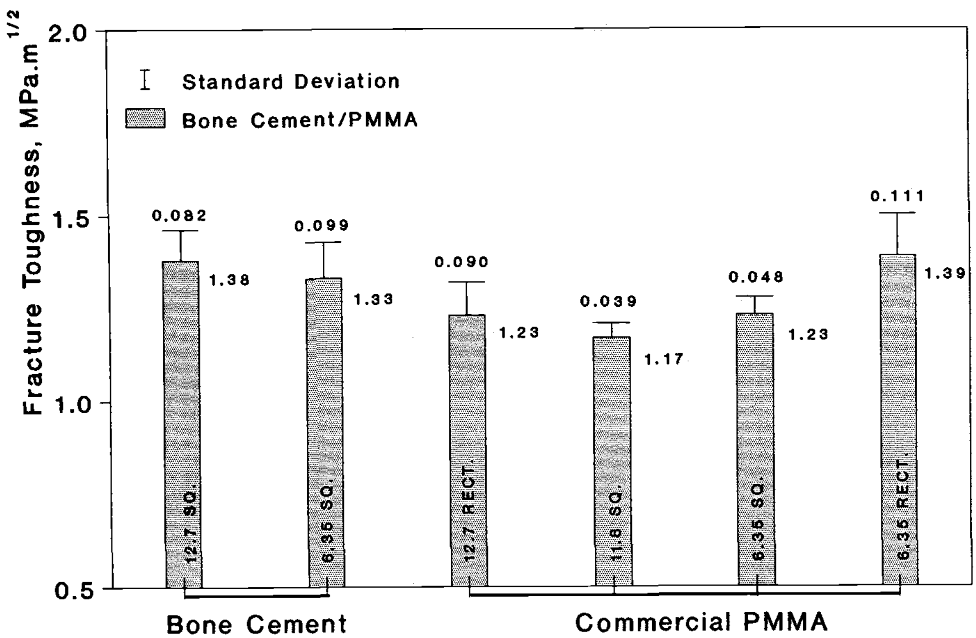

FIG. 9—*Fracture toughness of bone cement and commercial PMMA as a function of specimen size.*

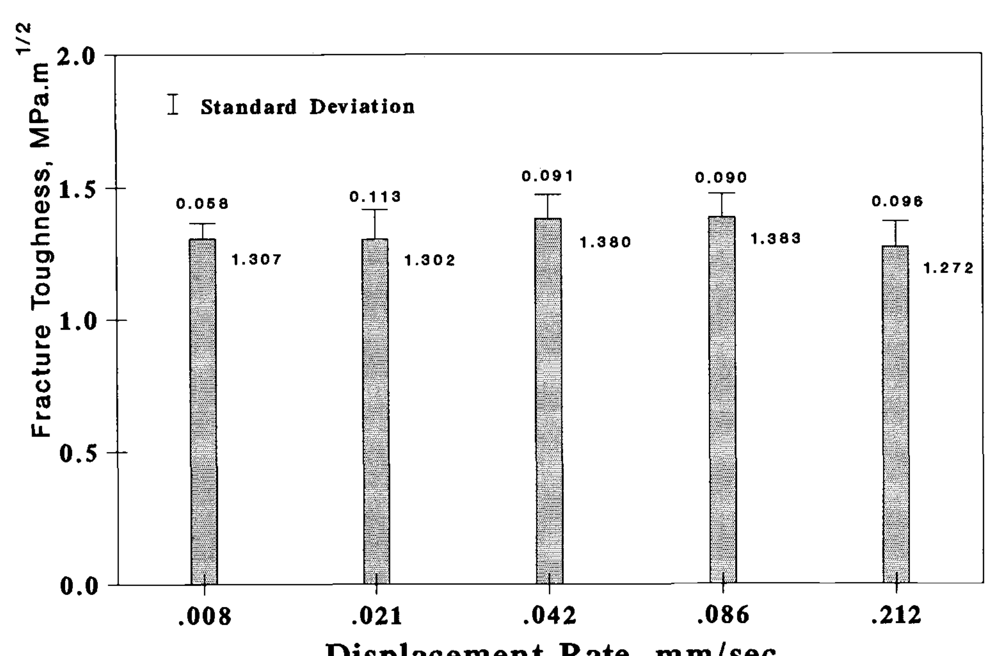

FIG. 10—*Fracture toughness of bone cement and commercial PMMA as a function of displacement rates.*

in the peak load occurring with 3 to 7, the fracture toughness values were slightly lower. On the other hand, no plasticity-induced effects were noted in the slow displacement rate regime, even when tests were run to yield peak loads at 300 s for the 12.7-mm-thick specimens. To confirm plasticity effects in this regime, specimens were loaded to a 15-N load, and the machine was turned off. Continuous load relaxation and displacement were monitored for 30 min. No viscoelastic effect was noted, and the load drop was insignificant, within the sensitivity limits. It is, however, recommended that displacement rates in the slow rate regime (longer time to reach peak load) should be used with caution for polymeric materials.

Fractographic examination of the fracture surfaces of the bone cement samples revealed microporosity and occasionally separation of prepolymerized beads from the cement matrix (Fig. 11). Crack propagation through the prepolymerized beads was the primary fracture mechanism (Fig. 12). Microporosity, considered as a microstructural parameter, has been shown to have no influence on fracture toughness [*15*]. Rimnac et al. [*15*] varied the mi-

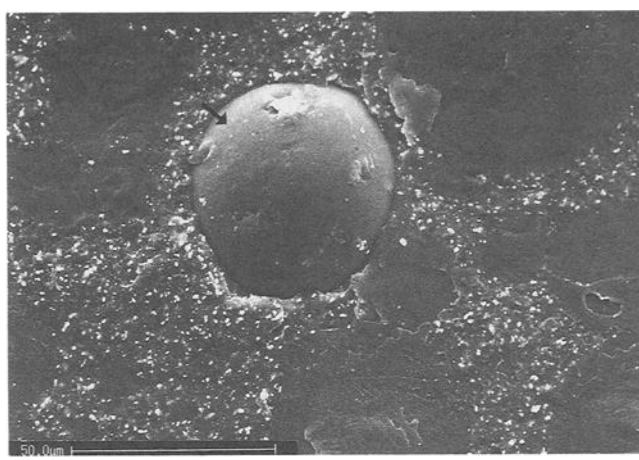

FIG. 11—*Scanning electron fractograph showing separation of prepolymerized bead from the cement matrix.*

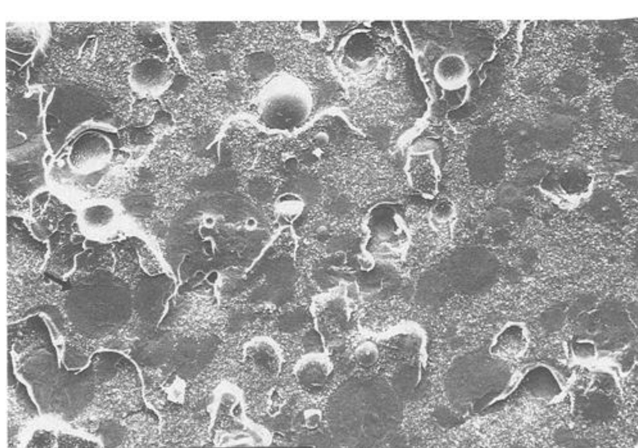

FIG. 12—*Scanning electron fractograph showing fracture through prepolymerized beads.*

croporosity in different bone cements and observed no effect on fracture toughness. The observed microporosity in these specimens also did not effect the fracture toughness values.

Although rare, barium sulfate particles were observed, which were not adherent to the matrix. These rare particles appeared to have acted as sites for crack formation during the fracture process (Fig. 13), but there was no noticeable effect on the toughness values of the specimens with these occurrences. Cleavage type brittle fracture (Fig. 14) and secondary cracking was the other fracture micromechanism observed.

Conclusions

Acrylic bone cement and commercial PMMA were tested for fracture toughness using short bar chevron-notched specimens following ASTM Test Method E 1304-89. The variable

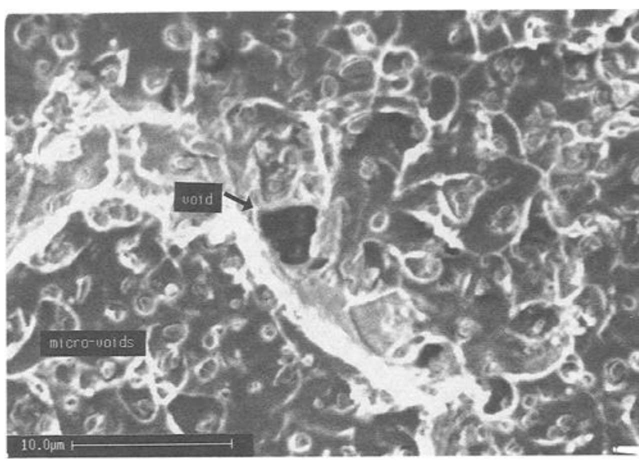

FIG. 13—*Scanning electron fractograph showing microvoids formed at barium sulfate particles during fracture of bone cement.*

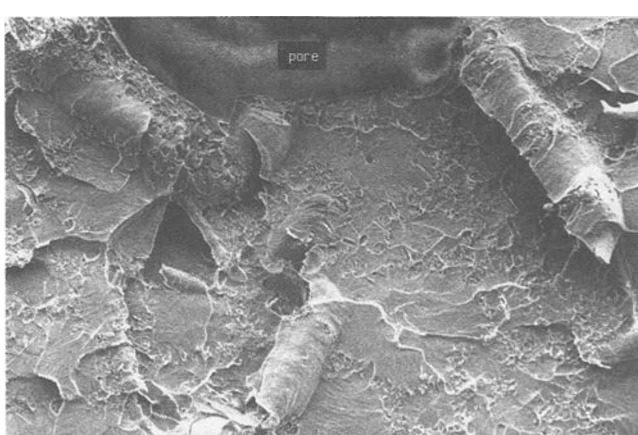

FIG. 14—*Scanning electron fractograph showing typical cleavage-like fracture mode near a large pore in the bone cement.*

test parameters were the specimen size and the displacement rates. The results indicated that the test method is applicable in evaluation of fracture toughness of bone cement. The fracture toughness values obtained in this study are consistent with those of other investigators, reported for other specimen geometries. The bone cement displayed insignificant load relaxation, and the fracture toughness of bone cement at displacement rates in the slow rate regime was not affected by plasticity effects. However, displacement rates in the slow rate regime should be used with caution for tests on bone cements.

Acknowledgments

The authors would like to thank Tom Morehouse, Marshall Sparks, and Jennifer Price for their assistance in specimen preparation and experimental work.

References

[*1*] Miller, J., Burke, D. L., Stachrewicz, J. W., and Kelebay, L. C., "Pathophysiology of Loosening of Femoral Components in Total Hip Arthroplasty," *The Hip*, C. V. Mosby, St. Louis, 1978, pp. 64–86.
[*2*] Harrington T. P., Karch J. A., and Harris W. H., "A Failure Criterion Based on Crack Initiation at Pores in Cement Applied to Loosening of Femoral Stems," *Proceedings*, 16th Annual Meeting of the Society of Biomaterials, 20–23 May 1990, Charleston, SC.
[*3*] Sih, G. C. and Berman, A. T., *Journal of Biomedical Materials Research*, Vol. 14, No. 3, 1980, p. 311.
[*4*] Freitag, T. A. and Cannon, S. L., *Journal of Biomedical Materials Research*, Vol. 10, No. 5, 1976, p. 805.
[*5*] Wright, T. M. and Trent, P. S., *Journal of Materials Science*, Vol. 14, No. 2, 1979, p. 503.
[*6*] May, T. C., Krause, W. R., Smith, M. J. V., Cardia, J. A., and Davenport, J. M., *Proceedings*, 16th Annual Meeting of Society for Biomaterials, 20–23 May 1990, Charleston, SC.
[*7*] Hashemi, S. and Williams, J. G., *Journal of Materials Science*, Vol. 19, No. 11, 1984, p. 3746.
[*8*] Stafford, D., Hugget, R., and Causton, B. E., *Journal of Biomedical Materials Research*, Vol. 14, No. 4, 1980, p. 359.
[*9*] Robinson, R. P., Wright, T. M., and Burstein, A. H., *Journal of Biomedical Materials Research*, Vol. 15, No. 2, 1981, p. 203.
[*10*] Wang, C. T. and Pillar, R. M., *Journal of Materials Science*, Vol. 24, No. 7, 1989, p. 2391.
[*11*] Boblitz, F. F., Luna, V. R., Glenn, J. F., DeVries, K. L., and Draughn, R. A., *Polymer Engineering and Science*, Vol. 19, 1979, p. 607.
[*12*] Watson, T., Jollies, M., Peyser, P., and Motoroy, S. *Journal of Materials Science*, Vol. 22, No. 4, 1987, p. 1249.
[*13*] Beaumont, P. W. R. and Young, R. T., *Journal of Biomedical Materials Research*, Vol. 9, No. 5, 1975, p. 423.
[*14*] Cayard, M. S. and Bradley, W. L., "The Effect of Various Precracking Techniques on the Fracture Toughness of Plastics," *Advances in Fracture Research*, Vol. 4, K. Salama et al., Eds., Pergamon Press, Elmsford, NY, 1989, p. 2713.
[*15*] Rimnac, C. M., Wright T. M., and McGill, D. L., *Journal of Bone and Joint Surgery*, Vol. 68-A, No. 2, 1986, p. 281.

Wang Qizhi[1] *and Xian Xuefu*[1]

Rock Fracture Toughness Determination with Chevron-Notched and Straight-Through-Notched Three-Point Bend Round Bar Specimens

REFERENCE: Qizhi, W. and Xuefu, X., "**Rock Fracture Toughness Determination with Chevron-Notched and Straight-Through-Notched Three-Point Bend Round Bar Specimens,**" *Chevron-Notch Fracture Test Experience: Metals and Non-Metals, ASTM STP 1172*, K. R. Brown and F. I. Baratta, Eds., American Society for Testing and Materials, Philadelphia, 1992, pp. 191–197.

ABSTRACT: Chevron-notched and straight-through-notched three-point bend round bar specimens were used to test fracture toughness of a Chongqing limestone. Comparable values were obtained from these two kinds of specimens, but the chevron-notched specimens had the merits of easiness for deducing and detecting overloading, less the possibility for deviation of crack growth from notch plane, and a included nonlinear correction factor in fracture toughness calculation. However, there was some size effect for chevron-notched specimens; the test values increased with increment in crack length and diameter.

KEY WORDS: chevron notch, straight-through notch, three-point bend, round bar, rock fracture toughness, stable crack growth, nonlinear correction factor, size effect

The fracture toughness of rock is needed for studies of rock cutting, hydrofracture and explosive fracture, etc. The evaluation of rock fracture toughness has been important in recent years due to the increasing demand for geothermal energy extraction and other energy-recovery schemes (e.g., gas and oil), where hydraulic fracturing and fragmentation of *in situ* rock masses is frequently used.

Chevron-notched specimens are now widely applied in fracture toughness testing for both metals and non-metals, but a review of published references revealed that most studies focused on chevron-notched short rod/bar specimens [*1*]. Investigations on chevron-notched three-point bend round bar (abbreviated as CB) were relatively scarce [*2*]. This paper reports the authors' experience in testing a Chongqing limestone with CB specimens. CB specimens with different diameters and initial crack lengths were tested to study size effects. Tests with straight-through-notched three-point bend round bar (abbreviated as SB) were also performed in order to compare these two kinds of core-based specimens and find the merits of chevron-notched bend specimens in rock fracture toughness testing.

Test Material and Procedures

The test rock was a Chongqing limestone. CB specimens (Fig. 1) were prepared by coring blocks taken from a mine near Chongqing. The specimen configurations were basically the

[1]Associate Professor and Professor, respectively, Department of Resources and Environmental Engineering, Chongqing University, Chongqing 630044, People's Republic of China.

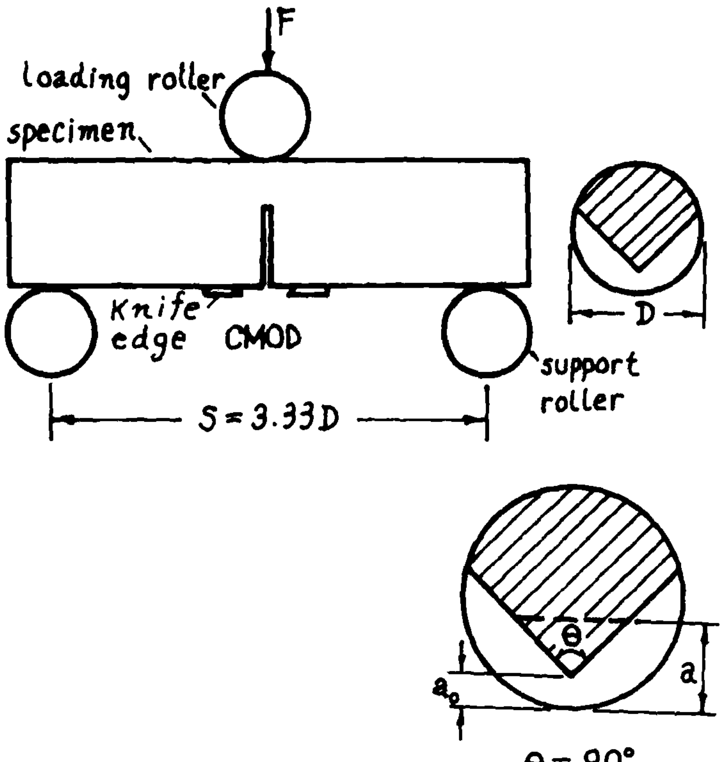

FIG. 1—*Chevron-notched three-point bend round bar with test fixture (a—crack length, a_0—initial crack length, dimensionless forms: $\alpha = a/D$, $\alpha_0 = a_0/D$).*

same as those prescribed by the International Society for Rock Mechanics (ISRM) [*3*]. The chevron notch was cut with a 1.2 mm thick by 120 mm diameter diamond saw and a universal milling machine. Then a razor blade was used to score a sharp notch at the tip of chevron notch formed by the diamond saw. This razor blade technique gave a notch tip radius estimated to be less than 0.01 mm. The specimens were marked before testing at the three points where the central load and two cylindrical supports would be acting. Specimen diameters were 56 and 72 mm, respectively, and initial crack length (α_0 in Fig. 1) varied as 0.15, 0.2, and 0.3 (for ISRM suggested specimen, α_0 = 0.15). A total of 16 CB specimens were prepared and tested. The SB specimens (cross section shown in Fig. 2) were prepared in a similar way with the diamond saw and razor blade. They had different crack lengths, while the span diameter ratio (*S*/*D*) was the same 3.33 as that of the CB specimens.

The servohydraulic test machine had four vertical columns and a stiffness of 11×10^4 kg/mm. The high stiffness of the test machine reduces stored energy that might otherwise be placed on the specimen due to unwanted load frame deflection. This condition is important in testing rocks, especially when specimens are loaded in bending. A clip gage was used to measure the crack-mouth-opening-displacement (CMOD) during testing. The gage should have enough sensitivity, since CMOD was very small for the test rock. The test was performed by controlling the CMOD rate at 0.01 mm/min. The authors noted that CMOD solely reflected specimen deformation, excluding the deformation of test machine and those on the contact points. The authors also noted that rock fracture toughness was not sensitive to

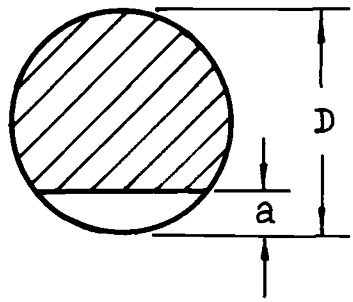

FIG. 2—*Cross section of a straight-through-notched three-point bend round bar (span and loading fixture are the same as shown in Fig. 1, dimensionless crack length $\alpha = a/D$).*

strain rate [*4*], so a low CMOD rate would be preferable to promote stable crack growth and avoid overloading.

About three or four unloading-reloading cycles were performed during the process of testing. Ideally, maximum load should be spanned between these cycles. Load versus CMOD diagrams were plotted by a computer interfaced to the test machine. Figure 3 shows a typical record of load versus CMOD plot for a CB specimen. This plot is important in two aspects: (*a*) to check whether stable crack growth is realized, which is demonstrated by a curve connecting the initial straight line and the point of maximum load; and (*b*) to subsequently obtain a nonlinear correction factor from unloading-reloading cycles.

Discussion and Results

The following equations were used to calculate fracture toughness for a CB specimen:

$$K_{CB} = A_{min} \cdot F_{max}/D^{1.5} \tag{1}$$

$$K^{P}_{CB} = K_{CB}\sqrt{(1 + p)/(1 - p)} \tag{2}$$

where A_{min} is the minimum dimensionless stress intensity factor, F_{max} is the maximum load, D is diameter, and p is nonlinear correction factor.

A_{min} was given in Ref *3* as

$$A_{min} = (1.835 + 7.15\alpha_0 + 9.85\alpha_0^2) \cdot (S/D) \tag{3}$$

where the definitions of α_0, S, and D are as shown in Fig. 1.

The degree of nonlinear behavior of the specimen p is defined by the equation

$$p = x_u/x_l \tag{4}$$

where x_u and x_l are determined by the two lines shown in Fig. 3, the two unloading lines should span F_{max}, and x_l is determined by a horizontal line representing the average load. It should be pointed out that in many references [*1*] p was defined by a load versus load-point-displacement (LPD) plot; here CMOD was used instead of LPD. The variable p reflects the severity of grain interlocking as well as the effect of crack tip fracture process zone in a rock specimen. The inclusion of the p-factor in Eq 2 is more realistic than Eq 1, which neglects the p-factor. Test results with CB specimens are listed in Table 1.

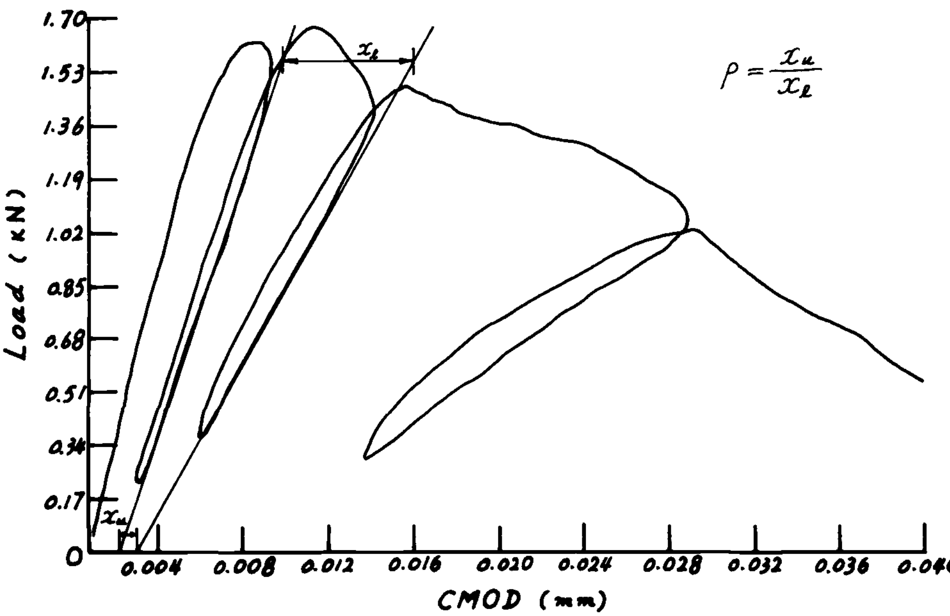

FIG. 3—*Typical load-CMOD record for a chevron-notched three-point bend round bar.*

TABLE 1—*Test results of fracture toughness for a limestone with chevron-notched three-point bend round bars.*[a]

D (mm)	α_0 (a_0/D)	p	K_{CB} (MPa $\sqrt{m}$)	K^p_{CB} (MPa $\sqrt{m}$)
56	0.15	0.14	1.15	1.33
56	0.20	0.16	1.21	1.42
56	0.30	0.20	1.33	1.61
56	0.20	. . .	2.02*	(overload)
72	0.15	0.18	1.28	1.54
72	0.20	0.20	1.38	1.69
72	0.30	0.25	1.45	1.87

[a]Excluding * average values of at least two tests are given.

The fracture toughness of an SB specimen was calculated with the stress intensity factor expression given in Ref *5*:

$$K_{SB} = (F/D^{1.5}) \cdot (S/D) \cdot (\alpha^{0.5}/(1 - \alpha)^2)$$

$$\times (3.75 - 11.98\alpha + 24.40\alpha^2 - 25.69\alpha^3 + 10.02\alpha^4) \qquad (5)$$

$$(0 < \alpha < 1, \qquad S/D = 3.33)$$

where $\alpha = a/D$, F is load, and F_{max} was applied in fracture toughness determination. The test results are listed in Table 2.

TABLE 2—*Test results of fracture toughness for a limestone with straight-through-notched three-point bend round bars.*[a]

D (mm)	α (a/D)		K_{SB} (MPa $\sqrt{m}$)
56	0.288		1.42
72	0.255		1.60
56	0.253	(crack deviation from notch plane)	1.08

[a]Single test values are given.

Phenomena Observed During Testing

Overload

At the preparatory testing, the CB specimen often broke abruptly as soon as the load tip touched the specimen; this was unsatisfactory. The authors finally succeeded in avoiding catastrophic failure by sharpening the notch tip with a razor blade and keeping the CMOD rate as low as 0.01 mm/min.

The maximum load which a CB specimen could sustain was only several kilonewtons; sudden load shock could destroy the specimen easily. Since CMOD control was effective only when there was a value of CMOD, and at the very beginning of loading there was essentially no control, the initial load should be applied with care. The notch tip should be sufficiently sharp, so the manual sharpening of the notch tip with a blade must be done with care and patience. If overload took place for a CB specimen, stable crack growth would not precede F_{max} in Fig. 3. Such tests were discarded, since it violated the basic principle of chevron-notched specimen. For an SB specimen, stable crack growth was not a prerequisite and was only possible with a deeply cracked specimen [*6*], so a sharp turn in the load-CMOD plot (shown in Fig. 4) was also allowed. It is obvious that the possibility of overloading is greater for an SB specimen than for a CB specimen, and the situation becomes even worse for an SB specimen since overload cannot be detected with the same ease as with a CB specimen from load-CMOD plot.

Deviation of Crack Growth from Notch Plane

This behavior was observed for both CB and SB specimens. Because the chevron notch had some constraint for crack growth direction, CB specimens had less possibility and severity for such deviation. Furthermore, if such deviation took place after a critical crack length α_c (e.g., $\alpha_c = 0.337$ for $\alpha_0 = 0.15$ [*7*]), the test could still be considered valid. For an SB specimen, there was no side-groove to guide the crack growth, and the deviation from the notch plane may be as large as approximately 20°. Usually this behavior corresponds to a very low value of K_{SB}. Apart from specimen configuration, material heterogeneity was also an important reason for such deviation of crack growth. Heterogeneity may be observed visually from the fractured cross section, which was composed of distinct layers of different rock composition.

Unloading-Reloading Cycles

It was not easy to perform unloading-reloading cycles with an SB specimen in the same manner as with a CB specimen, so that a nonlinear correction factor was not obtained. Many investigations have shown that the role of the fracture process zone ahead of the

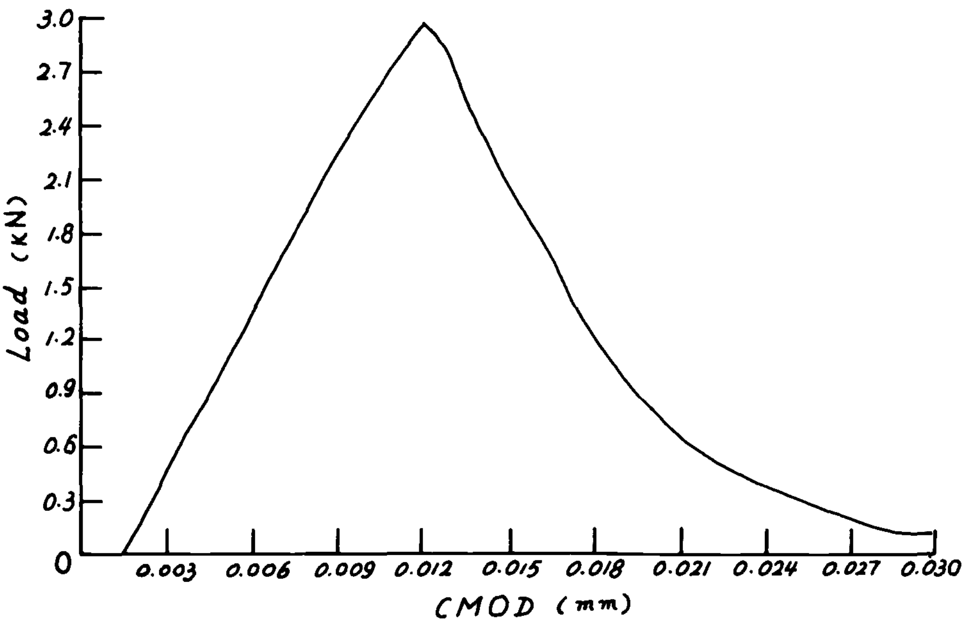

FIG. 4—*Typical load-CMOD record for a straight-through-notched three-point bend round bar.*

crack tip of a rock specimen could not be ignored in fracture toughness testing of rock, and that the p-factor was a reasonable consideration in this respect. However, it cannot be taken into consideration for an SB specimen.

Size Effect

Size effect was studied for CB specimens for which initial crack length and diameter were varied. It can be concluded from Table 1 that K_{CB} increases with increasing α_0 and D, and this trend does not change for K_{CB}^P, in which fracture toughness value is corrected by a nonlinear p-factor. An explanation for this fact is the rising R-curve effect which this limestone exhibits. Further investigation should be accomplished before a solid conclusion is reached. The size effect was not studied for SB specimens.

Conclusions

(1) Both CB and SB specimens can be used in fracture toughness testing of a Chongqing limestone. These two kinds of core-based specimens are convenient in preparation for rock, and they gave comparable toughness values, generally.

(2) CB specimen has some merits as compared with its straight-through counterpart SB specimen: (*a*) It is easy to realize a stable crack growth in the initial stage of loading before maximum load; (*b*) Constraint of chevron notch makes deviation of crack growth from the notch plane less possible or serious; (*c*) It is easier to perform unloading-reloading cycles and to obtain a nonlinear correction factor.

(3) There is some size effect for CB specimens. Test values increase with increment in initial crack length and diameter.

(4) A record of the load-CMOD plot is important for CB specimens but may be optional for SB specimens. The CMOD solely reflects the cracking and deformation of the specimen; hence loading under CMOD control is more stable than under LPD control.

References

[1] *Chevron-Notched Specimens: Testing and Stress Analysis, ASTM STP 855*, J. H. Underwood, S. W. Freimen, and F. I. Baratta, Eds., American Society for Testing and Materials, Philadelphia, 1984.

[2] Chiuder Hsiao and A. Wadood El-Rabaa, "Fracture Toughness Testing of Rock Cores," in *Proceedings*, 28th U.S. Symposium on Rock Mechanics, 1987, pp. 141–148.

[3] Ouchternony, F. (co-ordinator), "Suggested Methods for Determining the Fracture Toughness of Rock," *International Journal of Rock Mechanics and Mining Science & Geomechanics Abstracts*, Vol. 25, No. 2, 1988, pp. 71–96.

[4] Haberfield, C. M. and Johnston, I. W., "Determination of the Fracture Toughness of a Saturated Soft Rock," *Canadian Geotechnical Journal*, Vol. 27, No. 3, 1990, pp. 276–284.

[5] Underwood, J. H. and Woodward, R. L., "Wide Range Stress-intensity-factor Expression for an Edge-cracked Round Bar Bend Specimen," *Experimental Mechanics*, Vol. 29, No. 6, 1989, pp. 166–168.

[6] Wang, Q. and Xian, X. "Compliance and Stability Factors of an Edge-Cracked Three-Point Bend Round Bar Specimen," *International Journal of Fracture*, Vol. 50, No. 4, 1991, pp. R61–R67; also *Corrigenda*, Vol. 54, No. 1, 1992.

[7] Wang, Q. and Xian, X., "A Method for Calculating Stress Intensity Factors of Chevron Notched Three-Point Bend Round Bars," *International Journal of Fracture*, Vol. 45, No. 3, 1990, pp. R37–R41.

ISBN 0-8031-1480-X